Effects of cold glacier ice crystal anisotropy on seismic data

Zur Erlangung des akademischen Grades eines

DOKTORS DER NATURWISSENSCHAFTEN

der Fakultät für Physik des
Karlsruher Instituts für Technologie (KIT)

genehmigte

DISSERTATION

von

Dipl.-Geophys. Anja Diez
aus Mainz

Tag der mündlichen Prüfung: 13. Dezember 2013

Referent: Prof. Dr. Thomas Bohlen

Korreferent: Prof. Dr. Olaf Eisen

Abstract

Knowledge about crystal anisotropy is mainly provided by crystal orientation fabric (COF) data from ice cores. To gain a broader understanding about the distribution of crystal anisotropy in ice sheets and glaciers seismic data from Antarctica and the Swiss Alps are analysed here. Two effects are important: (i) sudden changes in COF lead to englacial reflections and (ii) the anisotropic fabric induces an angle dependency on the seismic velocities and, thus, also recorded traveltimes. A framework is presented here to connect COF data with the elasticity tensor to determine seismic velocities and reflection coefficients for cone and girdle fabrics from ice-core data. These results are compared to vertical seismic profiling (VSP) measurements form Antarctica to validate the overall approach. The best agreement between measured velocities from the VSP survey and theoretically calculated velocities from COF eigenvalues is obtained using the elasticity tensor of Gammon et al. (1983).

Reflection coefficients calculated for layers of different anisotropic ice fabrics and ice-bed interfaces show the weak influence of the anisotropic fabric on the reflection coefficient. Therefore, the focus is set on the analysis of the anisotropic ice fabric using the two-way traveltimes of englacial and bed reflections. Two approaches are applied: (i) the analysis of anisotropic normal moveout velocities (NMO) velocities from normal-spread seismic data (offset/depth-ratio ≤ 1) in combination with other data sets determining the depth of reflectors and (ii) the analysis of the anisotropy parameter η determined from long-spread seismic data (offset/depth-ratio > 1). These anisotropic NMO velocities determined for the stacking process differ from the zero-offset velocities needed for the depth conversion. For the Antarctic and Alpine site, it is found, that this difference is up to 9% for the P-wave but only up to 2% for the SH-wave. This sensitivity of the P-wave velocity to the anisotropic ice fabric is used to derive information about the COF from NMO analysis.

An improved understanding of COF-induced reflections is gained by the combination of seismic, radar and ice-core data. Use is made of the fact that the common reflection mechanism of seismic and radar data in cold glacier ice below the firn ice-transition is an abrupt change in the distribution of the anisotropic ice crystals. Thus, englacial reflectors in seismic and radar data can be identified as COF induced. Additionally, a new S-wave–density relationship is derived by analysing continuously refracted SH-waves of the firn from the Alpine field site.

The results show the great potential that is within the combined interpretation of seismic and radar data to identify COF-induced reflections. It is shown, that the analysis of normal spread reflection seismic data in combination with radar data and of long-spread seismic data alone gives a tool to determine the anisotropic ice fabric of glaciers and ice sheets. This is an important contribution to constrain results from the upcoming generation of ice-flow models with anisotropic rheology by remotely sensed data.

Contents

1 Introduction

> *'Die vorstehenden Ausführungen, die einen ersten Versuch darstellen,... lassen es als sicher erkennen, dass die seismische Methode neben der Dickenbesetimmung des Inlandeises eine grössere Bedeutung gewinnt für allgemeine glaziologische Fragestellungen, insbesondere für die Untersuchung der elastischen Konstanten und der Temperaturverhältnisse im Inlandeis...'*
> *Brockamp (1935)*

When the first seismic measurements were carried out on glaciers (Mothes, 1926, 1927) as preparation for the 'German Greenland Expedition Alfred Wegener' in the early 20th century the interest was to deploy a new method for the determination of the ice thickness of the Greenland ice sheet (Brockamp, 1933). However, their interest was also to use seismics for the determination of englacial temperatures. From the analysis of seismic data Brockamp (1935) draws the conclusion that the seismic method will gain importance in the future to answer general glaciological questions particularly to determine the temperature regime and the elastic constants in ice sheets (quote at the top). However, after recognizing the characteristics of the propagation of electromagnetic waves in ice the focus was set on the development and application of the radar method, especially for the determination of ice thickness and bed topography. Less effort was put in the application of the more labor intensive seismic method.

Since then climate change has become one of the big topics of our time concerning not only scientists but also the general public. One component that plays an important role in the change of the planet under changing climate conditions is the cryosphere. Glaciers and ice sheets show direct reaction to changing temperatures and precipitation by adjusting mass balance (IPCC AR5, Vaughan and Comiso, 2013). They contribute, for example, to sea level rise due to melting ice masses but force also further changes in the climate, e.g., for the dynamic processes in oceans Thus, the understanding of the dynamics of glaciers and ice sheets plays an important role in the prediction of the consequences of future climate change.

The dynamic behaviour of glaciers and ice sheets is controlled by processes at the surface and the bed, as well as the ice itself. A lot of focus is put on the understanding of the processes at the bed including the analysis of the bed properties, sliding over the bed, deformation of till or the subglacial hydrology systems. Especially the determination of the properties of the ice-bed interface has become a target for seismic methods, including the identification of water layers and channels (e.g., King et al., 2004; Smith and Murray, 2008; Horgan et al., 2013). Here, the usefulness of radar methods is limited due to high reflection coefficients for ice–bed and ice–water interfaces as well as the strong attenuation of radar waves by water (Navarro and Eisen, 2009).

An important role for the dynamics of glaciers, next to the deformation process at the bed, is the flow behaviour of the ice itself. Ice is a non-Newtonian fluid. With increasing strain the

ice becomes softer and deforms more easily until stiffening mechanisms start to dominate. Important for the strength of the ice is, among others, the orientation of the anisotropic ice crystals. The ice crystal is a hexagonal crystal. The longest axis is called c-axis and is normal to the basal plane. With the existing stresses in the ice sheet or glacier the ice crystal c-axes align. In this process the c-axes orient towards the main compression axis, away from the axis of dilatation (e.g., Gow and Williamson, 1976). This developed anisotropic fabric influences the viscosity of the ice as shear strength can be several orders of magnitude less parallel to the basal plane of an ice crystal than perpendicular to it (Ashby and Duval, 1985; Cuffey and Paterson, 2010). Thus, a preferred orientation of the anisotropic ice crystals influences the flow behaviour of the ice (Alley, 1992).

The knowledge of the distribution of the crystal orientation fabric (COF) is mainly provided from the deep ice cores from Antarctica and Greenland located at or in the vicinity of ice domes (e.g., Thorsteinsson et al., 1997; Diprinzio et al., 2005; Motagnat et al., 2012). Along ice cores, the main orientation of the ice crystals is measured on thin sections under polarised light (Wilson et al., 2003). Typical, observed fabrics include cone fabric distributions and girdle fabric distributions. The information about the fabric is often given in form of the eigenvalues of the momentum of inertia (Wallbrecher, 1986). Thus, the development and the change of the anisotropic ice fabric over depth can be investigated.

These information about the COF are important to model the flow behaviour of ice, not only to predict changes in the future but also for paleoclimate reconstructions. Ice from glaciers and ice sheets is an unique climate archive. Ice cores are analysed for the chemical concentration of, e.g., carbon dioxide (CO_2) or methane (CH_4) in air bubbles in the ice or isotopes like the $^{18}O/^{16}O$-ratio. These concentrations of greenhouse gases (CO_2, CH_4) or the $^{18}O/^{16}O$-isotope ratio, as temperature proxy, help to reconstruct past climate conditions. Here, a reliable depth–age conversion for the ice core is needed to interpret these data. Possibilities to determine a depth–age scale for ice cores include layer counting or the identification of events like volcanic eruptions. Especially, if the ice core is from the flanks and not the ice dome itself flow law models are needed to determine the age of the ice core layers accounting for the flow path of material deposited at the surface (Cuffey and Paterson, 2010). For a reliable depth–age conversion the anisotropy present at the bore location should be incorporated in the modeling of the flow.

For a better understanding of the paleoclimate, but also the behaviour of glaciers and ice sheets under changing climate conditions an increased understanding of the distribution of the anisotropic ice fabric is required. The analysis of COF from ice cores gives only a local information for the special stress regime at the bore location. Most of the deep ice cores where COF measurements have been carried out are, however, located at ice domes. The knowledge about COF distribution in flank flow regimes is still limited. Thus, a method is needed that derives information about the distribution of COF with depth over larger areas on glaciers and ice sheets.

Here, geophysical methods like seismics and radar can help. Seismic as well as radar wave propagation is influenced by a preferred orientation of ice crystals. As the surveys are carried out on the snow surface these methods allow to map englacial and bed reflections over larger areas. However, COF induced reflections need to be identified and interpreted to gain information about the existing anisotropy and, thus, the orientation of the ice crystals. Some studies exist that use radar methods to investigate the COF distribution (Fujita et al., 2006; Eisen et al., 2007; Matsuoka et al., 2009) also over larger areas (Matsuoka et al., 2003).

The biggest problem in the analysis of radar signals is to distinguish reflection signatures from changing COF from reflections due to contrasts in acidity or density. A possibility is the analysis of multi-polarisation or multi-frequency data (Matsuoka et al., 2012).

Seismic wave propagation in ice depends on density (Kohnen, 1972) and temperature (Gammon et al., 1983; Kohnen, 1974) next to the influence of the developed anisotropic ice fabric on the seismic wave propagation (Robertson and Bentley, 1990). The most extensive study on the influence of anisotropy on seismic wave propagation and the calculation of seismic velocities for different cone fabrics was done by Bennett (1968) and applied to seismic measurements from Dome C, Antarctica, by Blankenship and Bentley (1987). Englacial seismic reflections were observed in seismic surveys from Antarctica (Horgan et al., 2012; Hofstede et al., 2013) and Greenland (Horgan et al., 2008) and have been interpreted as arising from abrupt changes in the orientation of the ice crystal fabric. However, no definite conclusion was drawn on how the fabric changed to cause these seismic reflections.

The main focus of this work is to investigate the influence of the COF on the seismic wave propagation, beyond the limit of velocities for cone fabrics, including the analysis of reflection coefficients and velocities for cone but also for girdle fabrics. Further, information about the COF distribution from seismic data are derived by analysing the velocity profile gained from normal-spread seismic data (offset/depth-ratio$\leq$1) in combination with radar data and by analysing the velocity profile gained from long-spread seismic data (offset/depth-ratio$>$1) alone.

To investigate the influence of anisotropic ice fabric, for cone and girdle fabrics, on the seismic wave propagation the elasticity tensor is calculated from the COF eigenvalues gained from ice cores. Here, a new method is developed for the calculation of the polycrystal elasticity tensor for different fabric distributions from the COF eigenvalues and a monocrystal elasticity tensor following the basic idea of Nanthikesan and Sunder (1994). This gives the possibility to analyse the influence of the anisotropic ice fabric on the velocities and reflection coefficients of seismic waves in glaciers and ice sheets. Here, the influence of seismic waves on the density in the firn and the temperature regime are taken into account as well.

The evaluation of the method was possible by analysing data from a vertical seismic profiling (VSP) measurement carried out at Kohnen station, Antarctica within the borehole of the EDML ice core (EDML: EPICA Dronning Maud Land, EPICA: European Project of Ice Coring in Antarctica). This gave the possibility to directly compare velocities derived from the VSP survey with velocities calculated from the EDML COF eigenvalues. A better understanding of the reflection origin could be gained by comparing seismic and radar data with COF and density measurements of close-by ice cores. This shows the large potential of the combination of seismic and radar data for the identification and analysis of COF induced reflections. Further, the combination of seismic SH-wave data and ice-core densities made it possible to derive a new S-wave–density relationship similar to the P-wave–density relationship of Kohnen (1972).

For the derivation of anisotropy the velocity profile over depth is derived from the seismic data, analysing the moveout of traveltimes with increasing offset. The concept of normal moveout (NMO) correction in anisotropic material for normal-spread (offset/depth-ratio$\leq$1) and long-spread seismic data (offset/depth-ratio$>$1) is used here (Tsvankin, 2001). For the derivation of the anisotropy use is made of the difference between the NMO velocities,

derived from the seismic data, and the zero-offset velocities, determining the depth of reflections. Data from Antarctica and the Swiss Alps show a difference of up to 9% between NMO and zero-offset velocities for P-waves, but only 1-2% differences for SH-waves. For the derivation of the anisotropy the Thomsen parameters are used. In case of normal-spread (offset/depth-ratio$\leq$1) seismic data the anisotropy is derived by combining the seismic data with radar data, giving the depth of the reflections and, thus, deriving the anisotropic Thomsen parameter. In case of long-spread seismic data (offset/depth-ratio$>$1) the anellipticity parameter is derived directly. Thus, information about the existing anisotropic regimes at Colle Gnifetti, Switzerland and Kohnen station, Antarctica could be gained. The results derived from the seismic data are validated with help of the ice core data. Hence, this work gives a framework to derive information about anisotropic ice fabric form the analysis of seismic traveltimes, deriving velocities and Thomsen parameter during the NMO correction.

The thesis is divided into two main parts. In the first part, Chapter 2–5, the physical basis is introduced focusing on the seismic wave propagation in the anisotropic ice fabric. In the second part, Chapter 6–9, the seismic data sets from the Swiss Alps and Antarctica are introduced and analysed with focus on the determination of the COF. Variables and abbreviations will be explained in the text when they appear for the first time. Additionally, they are listed after the bibliography.

Chapter 2 will give an introduction into the main properties of ice that influence the propagation of seismic waves: the temperature, the density and a preferred orientation of the ice crystal. Within the firn part a strong density gradient influences the wave speed. Melt layers or ice lenses may cause englacial reflections. Below the firn-ice transition the seismic wave propagation is mainly influenced by the COF. To understand possible effects of COF in seismic data, the seismic wave propagation in anisotropic media is introduced in Chapter 3. This includes the concepts of vertical transversely isotropic (VTI) and horizontal transversely isotropic (HTI) media with the introduction of the Thomsen parameters. Further, the calculation of seismic velocities and reflection coefficients for orthorhombic media and the influence of anisotropy on the velocity analysis from traveltimes of reflections is explained. Additionally, the calculation of seismic velocities in anisotropic ice (cone fabric, VTI media) that was derived by Bennett (1968) is introduced.

The focus of Chapter 4 is on the influence of seismic wave propagation in anisotropic ice and the calculation of velocities and reflection coefficients for different COF distributions. In the beginning (sec. 4.1) an overview about the application and results gained from active-source seismic measurements carried out on glaciers and ice sheets until now is given. Fabric measurements on ice cores from Antarctica and Greenland show developed anisotropy including cone as well as girdle fabric distributions (sec. 2.1). The equations given by Bennett (1968) are, however, limited to the calculation of velocities for cone fabrics. To be able to take girdle fabric distributions into account and investigate the influence of the anisotropic ice fabric on velocities as well as reflection coefficients the elasticity tensor for the different existing anisotropic fabrics is needed. Thus, a method is derived in section 4.2 to calculate the elasticity tensor for the existing fabric from the eigenvalues describing the COF measured on ice cores. This is followed by the investigation of the influence of different anisotropic fabrics in ice on the seismic velocities and englacial reflection coefficients as well as bed reflection coefficients. In addition to the anisotropic ice fabric the seismic velocities are influenced by the temperature gradient and density distribution in the firn. These influences are discussed in section 4.3 and 4.4, respectively. As the seismic data is compared to radar

data for a better understanding of the origin of reflections in the seismic and in the radar data an introduction is given in Chapter 5 on the propagation of radar waves in anisotropic material. Section 5.2 discusses the main differences in the sensitivity of seismic and radar waves. Thus, the advantages of both methods can be combined in the following analysis of seismic data.

The seismic, radar, and ice-core data used here for the analysis of existing anisotropic fabrics from locations in Dronning Maud Land, Antarctica, and the Swiss Alps are discussed in Chapter 6. Colle Gnifetti (sec. 6.1) is located at a high altitude alpine saddle serving as test site. As this is an extensively studied area the seismic data can be put in relation to ice core and radar data. The Antarctic sites include the Halvfarryggen and Kohnen location. Halvfarryggen (sec. 6.2) is a local dome on the coast about 150 km inland from the German overwintering station Neumayer III where seismic wideangle and profile surveys were carried out. Kohnen (sec. 6.3) is located on the Antarctic plateau. With the deep ice core drill site EDML in the vicinity of the seismic survey this location gives fantastic possibilities in comparing ice core data to seismic wideangle and VSP measurements.

The following chapters show the analysis of the data sets introduced in Chapter 6 with focus on the anisotropic ice fabric. This includes the analysis of the VSP data set from Kohnen in Chapter 7, the combination of seismic, radar and ice-core data from Colle Gnifetti and Kohnen in Chapter 8. The analysis of the velocity variation with depth in Chapter 9 gives the option to derive information about the anisotropic ice fabric.

The VSP survey (Ch. 7) gave the possibility to directly compare picked seismic velocities with velocities calculated following the concepts of the derivation of the elasticity tensor introduced in Chapter 4. Further, the elasticity tensors measured by different authors could be analysed with the seismic data. The comparison of seismic, radar and ice-core data in Chapter 8 shows the great potential of the combination of seismic and radar data for the identification of reflectors origin. Here the different sensitivities of seismic and radar data to density, acidity or COF complement each other very well. The concepts of NMO correction for seismic data in anisotropic material (sec. 3.5) are applied in Chapter 9. Here, the challenges of a tilted bed topography for the determination of the COF distribution become obvious analysing the Halvfarryggen data. However, information about the existing anisotropy are derived from the seismic data at Kohnen and Colle Gnifetti. The main conclusions and open questions will be discussed in Chapter 10.

Part 1:

Theory and methodology

2 Ice properties

The dynamic processes in glaciers and ice sheets are driven by the accumulation, the flow, the gravity and the ablation. Accumulation is mainly provided by precipitation in form of snow. The densification of snow to ice depends strongly on the temperature regime and the amount of meltwater. The prevailing ablation process differs depending on the different glacier and ice sheet settings and regions, including actual melting at the surface, melting at the base or calving processes of glacier tongues and ice shelves in lakes or oceans.

During time the ice is transported from the accumulation area to the ablation area. Here, the flow of the ice depends on different factors, e.g., the bed and surface topography or geothermal heat flux, but also the ice properties itself. Ice is a highly viscous, non-Newtonian fluid. With increasing strain the ice becomes softer. Additionally, it is influenced by the temperature regime, hydrostatic pressure, water content, density, grain size, impurities and by the orientation of the anisotropic ice crystals (Cuffey and Paterson, 2010).

Seismic waves in ice are mainly influenced by the density distribution within the firn, the temperature distribution within the ice and the orientation of the anisotropic ice crystals. The sections below give a brief introduction into the developed anisotropic crystal orientation fabric (sec. 2.1) and the density and temperature distribution (sec. 2.2) of glaciers and ice sheets.

2.1 Crystal orientation fabric

The ice crystal on earth, under the existing atmospheric pressure and normal temperatures below the freezing point of water as well as under the existing pressure in ice sheets and glaciers, is an hexagonal crystal (ice I_h). This structure results from the bonding of the H_2O molecules. The two hydrogen atoms (H) bond to the oxygen atom (O) of two neighboring water molecules (hydrogen bonds). The water molecule also bonds to two hydrogen atoms of another two neighboring hydrogen molecules, so that each water molecule has four neighboring water molecules building a tetrahedral structure (Figure 2.1, a). These tetrahedral structures can be arranged in cubic and hexagonal form. However, the cubic form is not a stable crystal structure under the conditions on earth. Thus, it is transformed into the stable hexagonal crystal. Here, six oxygen atoms form a hexagonal shaped ring in two closely spaced planes (Figure 2.1, b). This plane is called the basal plane of the ice crystal with the c-axis, the longest axis of the ice crystal being perpendicular to this basal plane.

Due to the existing stresses within glaciers and ice sheets these anisotropic, hexagonal ice crystals can be forced to align in one specific direction. The crystal's c-axis is then oriented perpendicular to the main direction of stress. Depending on the stress regime different crystal orientation fabrics (COF) develop (Figure 2.2). The different kind of fabrics were

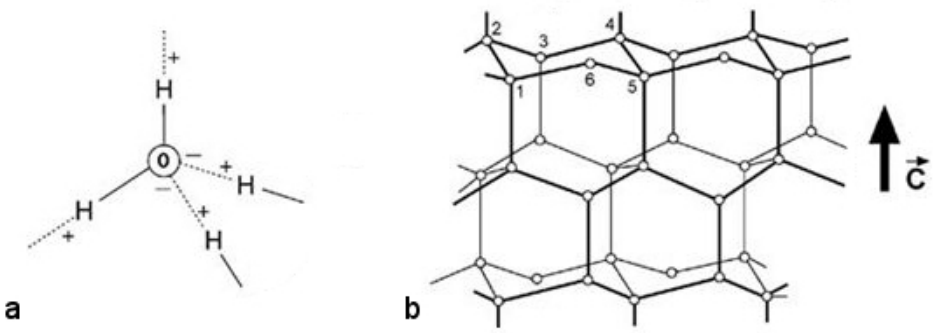

Figure 2.1: Oxygen atom with hydrogen bonds in (a). Two hydrogen bonds (solid lines) are from the two hydrogen atoms to neighboring oxygen atoms, the other two hydrogen bonds (dashed lines) are between the oxygen atom and hydrogen atoms of neighboring water molecules. Thus, a tetrahedral structure is built. The tetrahedrons are then arranged in a hexagonal structure (b). The hexagonal ring of oxygen atoms defines the basal plane with the c-axis perpendicular to this basal plane. Figure from Cuffey and Paterson (2010).

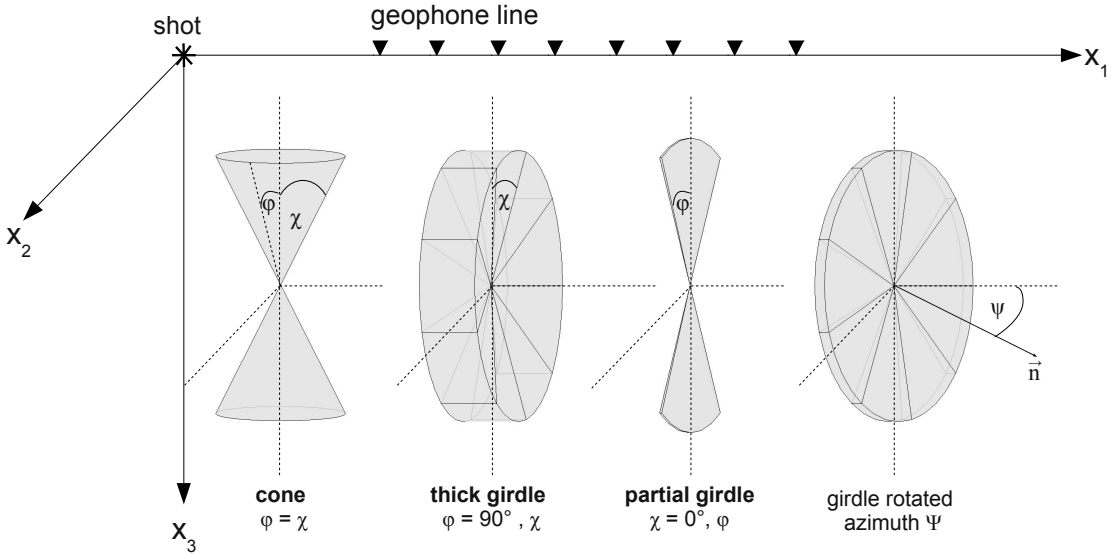

Figure 2.2: Enveloping of different COF distributions used in the following analysis of seismic data within the used coordinate system. It is distinguished between cone fabric, thick and partial girdle. The cone fabric, seismically a vertical transversely isotropic (VTI) medium, includes the two extreme forms of single vertical maximum and isotropic state. The two girdle fabrics are within the $[x_2, x_3]$-plane, a horizontal transversely isotropic (HTI) medium and can be turned around the azimuth ψ. Introduction to the different seismic anisotropies will be given in section 3.1.

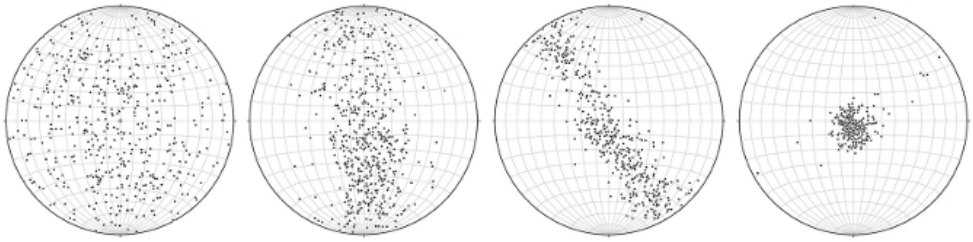

Figure 2.3: Example of Schmidt plots for different fabrics plotted onto a Schmidt net. The different distributions shown are: (a) a uniform distribution, (b) and (c) a girdle distributions, (d) a cluster distribution or cone fabric (I. Weikusat, pers. comm.).

discussed by Wallbrecher (1986). He distinguishes between 8 different kind of fabrics:

- uniform distribution - isotropic,
- cluster distribution,
- bimodal distribution,
- small circle distribution,
- (thick) girdle distribution,
- partial girdle distribution,
- cross girdle distribution,
- random distribution.

Figure 2.2 shows the fabrics that are used in the following analysis of seismic data, distinguishing between the uniform, the cluster and the thick and partial girdle distribution. The sketches of the different fabrics give the enveloping of the specific c-axes distribution for these fabrics.

The standard method of measuring COF distributions is by analysing thin sections from ice cores under polarized light using an automatic fabric analyser (Wilson et al., 2003; Peternell et al., 2010). Thus, the c-axis orientation of each single crystal is determined and can be given as a unit vector ($\vec{c}$). These orientations can be presented in so called Schmidt plots, an equal-area projection of a sphere on to a plane (Figure 2.3). The c-axes are plotted as points at their intersection point on this sphere, projected onto the plane.

Another way to describe the COF distribution is by calculating the eigenvalues of the orientation tensor of the fabric. Here the three main moments of inertia resulting from all crystals are determined. By solving the characteristic polynomial

$$\det(A_{ij} - \lambda\delta_{ij}) = 0 \tag{2.1}$$

the eigenvalues $\lambda_1, \lambda_2, \lambda_3$ of the weighted orientation tensor A_{ij}, with $i, j = 1, 2, 3$, are calculated. The weighted orientation tensor can be calculated from the c-axes orientation of the single crystals

$$A_{ij} = W \sum_{l=1}^{n} (c_i c_j)_l \tag{2.2}$$

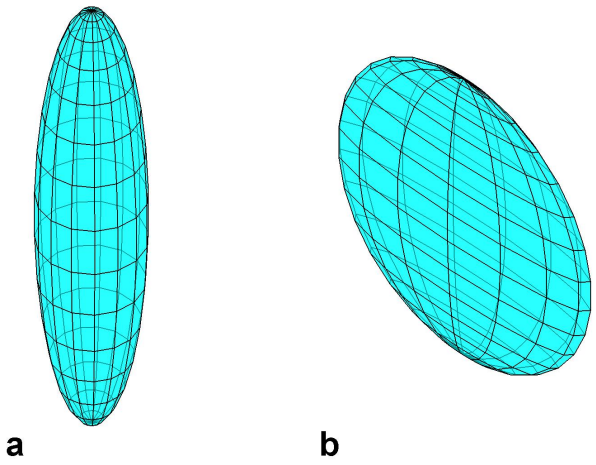

Figure 2.4: Example for the ellipsoid spanned up by the three eigenvalues $\lambda_1, \lambda_2, \lambda_3$. (a) is the prolate spheroid of a cone fabric with $\lambda_1 = \lambda_2 = 0.15$ and $\lambda_3 = 0.7$ corresponding to an opening angle for the enveloping of the c-axes of $\varphi = \chi \approx 46^\circ$, (b) is the oblate spheroid of a thick girdle fabric with $\lambda_1 = 0.06$ and $\lambda_2 = \lambda_3 = 0.47$, thus, $\varphi = 90^\circ$ and $\chi \approx 24^\circ$.

where n gives the number of grains and W is a weighting function, with weighting, e.g., by the grain ($W = 1/n$) or by the area. The three eigenvalues, with $\lambda_1 \leq \lambda_2 \leq \lambda_3$ and $\sum \lambda_i = 1$, span up a rotation ellipsoid (Figure 2.4). From these eigenvalues the corresponding eigenvectors can be calculated, giving the direction of the three main moments of inertia. However, in case of the ice core analysis, it usually does not help to derive the eigenvectors, as the orientation, the azimuth, of the ice core is often not measured.

Beside describing the fabric distribution by means of the COF eigenvalues it is also possible to give angles around a main direction determining the enveloping of the c-axis distributions. For the consideration of seismic wave propagation in anisotropic media the description of the enveloping by two opening angles in x_1- and x_2-direction in a coordinate system with the x_3-axis pointing downwards is used in this study (Figure 2.2).

As mentioned above, four of the distributions defined by Wallbrecher (1986) are taken into account here to analyse the effects of the anisotropic fabric on the seismic data (Figure 2.2). Firstly, the uniform distribution is used where all eigenvalues are equal ($\lambda_1 = \lambda_2 = \lambda_3 = 1/3$). Secondly, the cluster distribution, with a vertical symmetry axis is considered. Here all ice crystals are oriented within a cone opening angle ($\varphi = \chi$). The largest eigenvalue is λ_3 with $\lambda_1 = \lambda_2$. The extrema of this distribution are a cone opening angle of 90° which corresponds to the uniform distribution and a cone opening angle of 0°, which correspond to a vertical single maximum (VSM)-fabric. For a VSM-fabric the eigenvalues are $\lambda_1 = \lambda_2 = 0$ and $\lambda_3 = 1$, hence, all ice crystals are oriented vertically. The other two considered distributions are girdle fabrics, which are divided in the thick and partial girdle distribution. The thick girdle is a distribution where the c-axes are distributed between two planes with a certain distance, so that the opening angle φ in x_2-direction is 90° and χ in x_1-direction then gives the thickness of the girdle. The partial girdle is a distribution where all ice crystal c-axes are in one plane, but only within a slice of this plane, so that the opening angle χ in the x_1-direction is 0° and φ in x_2-direction gives the size of the slice within the plane. A partial girdle with $\chi = 0^\circ$ and $\varphi = 90^\circ$ would correspond to the eigenvalues $\lambda_1 = 0$ and $\lambda_2 = \lambda_3 = 0.5$.

The influence of anisotropic ice fabric onto the flow behaviour of ice can directly be observed in radio-echo sounding (RES) profiles from ice domes. At ice domes and divides a prominent

feature of flow under isotropic conditions is a so called Raymond bump (Raymond, 1983). As ice is a non-Newtonian fluid, it is softer and deforms more easily on the flanks of the ice dome or divide due to the higher deviatoric stress there compared to the center of the dome. Thus, the vertical flow is slower on the dome than on the flanks which leads to an upwelling of the isochronous layers, hence, a Raymond bump. Martin et al. (2009) showed that only under anisotropic conditions a double bump can develop here with synclines on the flanks. These double bumps and synclines are features often observed in RES profiles (sec. 5.1) and, thus, presently considered a direct evidence of the existence of a developed anisotropic fabric and the influence of this anisotropy onto the flow behaviour of ice.

2.2 Density and temperature profiles

Within the accumulation area of a glacier or ice sheet the net mass balance at the surface is positive. Thus, the snow can slowly be transformed into ice. Snow that lasts more than one year is referred to as firn. The areas investigated in this study are from the dry-snow-zone, as well as from the percolation zone (Cuffey and Paterson, 2010), so from regions without melting and from regions with only some melt percolating a certain distance into the snow pack, respectively. The time the densification process takes strongly depends on the amount of meltwater availability. Without melting the transformation from snow to ice is a sintering process.

Freshly fallen snow in conditions without wind can have densities as low as 50 kg m^{-3}. Due to mechanical altering of the snow, often due to wind, the branches of the dendritic ice crystals brake. Thus, the grains are rounded. This minimizes the free surface area so that the fabric reaches an energetically more favorable state. The rounded grains are afterwards packed in the densest possible way, which corresponds to a porosity of 40%, as experiments have shown, and a density of 550 kg m^{-3}. Further densification is obtained, first by sublimation processes and afterwards, if the pressure increases, by recrystallisation of the ice crystals. The firn has become glacier ice when no connection between air bubbles exists any longer, which happens at a density of 830 kg m^{-3}, referred to as pore close-off. By compression of these air bubbles the glacier ice is further densified until it reaches a density of about 917 kg m^{-3}. In presence of melt water, these processes are taking place much faster as altering of the grains is obtained by the melting process, so that large grains can easily grow on the expense of smaller ones.

The viscosity of ice is also influenced by the temperatures within the glacier or ice sheet, with the lowest temperatures at the base. Seasonal temperature signals normally propagate into the firn down to a depth of $\sim$15 m. Further down the temperatures are not influenced by seasonal temperature variations. For cold glaciers the temperatures of the ice are everywhere below the pressure melting point, in contrast to polythermal glaciers were parts of the ice are at the pressure melting point.

For more detailed explanation for the processes of firn densification and temperature regimes the text book by Cuffey and Paterson (2010) is an excellent choice.

3 Seismic wave propagation in anisotropic media

The propagation of seismic waves can be described by solving the wave equation. Therefore the relationship between stress and strain by the elasticity tensor described by Hooks law is used. In the case of anisotropic media this solution becomes complicated as simplifications of the elasticity tensor are limited. Hence, symmetries of the media are used and approximations made, e.g., with help of the Thomsen parameter, to find analytical solutions for the description of wave propagation in anisotropic media.

The following section gives an introduction into the seismic wave propagation in anisotropic media, with focus on orthorhombic media, followed by the concept of the Thomsen parameter for a simplified description of velocities. Afterwards, the calculation of seismic velocities and reflection coefficients in orthorhombic media used in the analysis of the seismic data in this study, is introduced. In the last sections the influence of seismically anisotropic material on the traveltimes is shown, especially with increasing offset, explained on an example for a single layer VSM-fabric.

3.1 Anisotropic fabrics – propagation of wavefronts

In the anisotropic case the properties of the material are not the same for the different directions in space. In the general case of an anisotropic medium the linear relationship between tensors of stress σ and strain τ is described by Hook's law

$$\sigma_{mn} = c_{mnop}\tau_{op}, \tag{3.1}$$

with the elasticity tensor c_{mnop} and $m, n, o, p = 1, 2, 3$. In the isotropic case these 81 components of the elasticity tensor can be reduced to the two well-known Lamé parameters. The symmetry consideration of strain and stress tensor that are used in the isotropic case for the reduction of the 81 unknowns are still valid in the anisotropic case,

$$c_{mnop} = c_{nmop} \text{ and } c_{mnop} = c_{mnpo}, \tag{3.2}$$

as well as the thermodynamic consideration (Aki and Richards, 2002) that lead to

$$c_{mnop} = c_{opmn}. \tag{3.3}$$

Thus, the unknowns of the elasticity tensor reduce to 21 elements in the general anisotropic case, referred to as triclinic anisotropy.

The wave equation for homogeneous, linear elastic media, without external forces and with

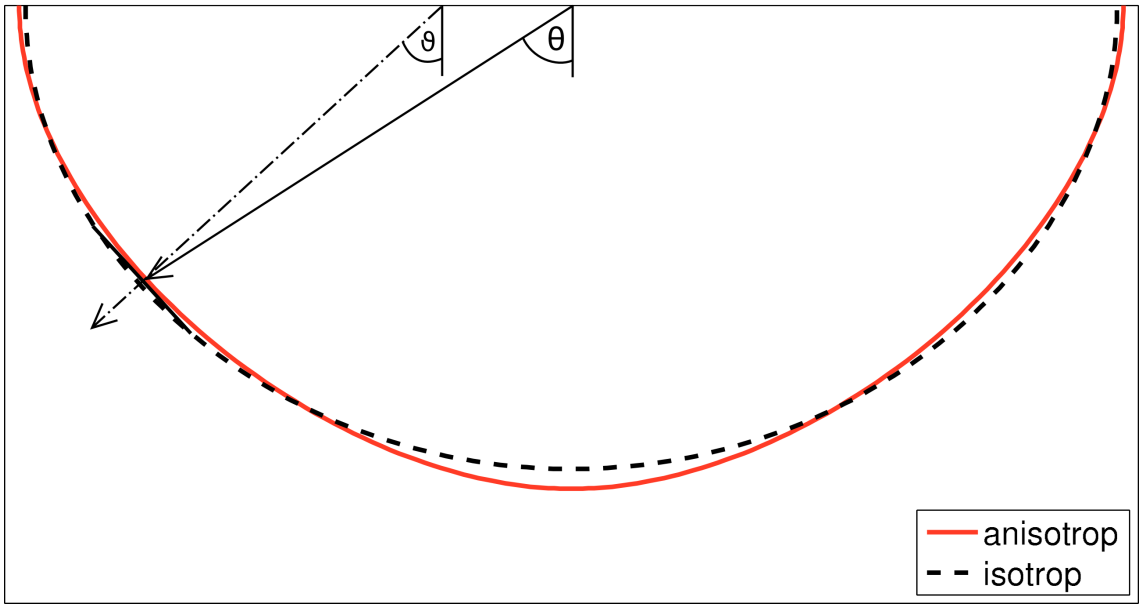

Figure 3.1: Wavefront of a P-wave traveling in isotropic ice fabric (dashed line) and in an VSM-fabric (red line), thus, a VTI media. The solid arrow shows the group velocity with group angle θ, the dashed arrow the phase velocity with phase angle ϑ.

triclinic anisotropy is then given by

$$\rho \frac{\partial^2 u_m}{\partial t^2} - c_{mnop} \frac{\partial^2 u_o}{\partial x_n \partial x_p} = 0, \tag{3.4}$$

with the density of the material ρ and the derivation of the components of the displacement vector $\vec{u}$ in time t and space $\vec{x}$. To solve this equation a trial solution of a harmonic plane wave for the displacement u_o (equivalent for u_m) is used

$$u_o = U_o \mathrm{e}^{i\omega(n_n x_n / v_{\mathrm{ph}} - t)}, \tag{3.5}$$

with the angular frequency ω, the phase velocity v_{ph}, U_o the components of the polarisation vector $\vec{U}$ and n_n the components of the unit vector $\vec{n}$ normal to the wavefront. By inserting this trial solution into the wave equation the Christoffel equation can be derived

$$\left[c_{mnop} n_n n_p - \rho v_{\mathrm{ph}}^2 \delta_{mo} \right] U_o = 0, \tag{3.6}$$

with the Kronecker delta δ_{mo}. Three non-trivial solutions exist for this eigenvalue problem, giving the three phase velocities and vectors for the quasi compressional (qP), the quasi vertical (qSV) and the quasi horizontal shear (qSH) wave. The phase vectors are orthogonal to each other. However, qP- and qSV-wave are coupled, so the waves are not necessarily pure longitudinal or shear waves outside of the symmetry planes. As the following analyses are mostly within the symmetry planes the waves will from now on be denoted as P-, SV- and SH-waves. Nevertheless, outside of the symmetry planes this term is not strictly correct. For a detailed derivation of the Christoffel equation see, e.g., Tsvankin (2001).

In case of wave propagation in anisotropic media, the description of wave velocities, transmission and reflection angles, as well as reflection coefficients becomes more complicated

compared to the isotropic case. The propagation of wavefronts in the anisotropic case is no longer spherical. Figure 3.1 shows the anisotropic wavefront for a P-wave traveling in a VSM-fabric (red line) and the spherical wavefront for a P-wave in isotropic ice fabric (dashed black line). For the anisotropic case group and phase velocity, as well as group angle θ and phase angle ϑ, are no longer the same. The group velocity determines the traveltime. The phase velocity vector is normal to the wavefront and, thus, the phase velocity and phase angle ϑ is needed for the calculation of reflection and transmission angles as well as reflection coefficients.

To simplify calculations with the elasticity tensor and due to the existing symmetries of strain and stress tensor a 6×6-matrix notation, the Voigt notation (Voigt, 1910), for the elasticity tensor C_{ij} can be used. Therefore the index combinations of mn and op are replaced by indices between 1 and 6 (11$\hat{=}$1, 22$\hat{=}$2, 33$\hat{=}$3, 23$\hat{=}$4, 13$\hat{=}$5, 12$\hat{=}$6).

To be able to find analytical solutions of the Christoffel matrix the anisotropic materials are distinguished by their different symmetries. Hence, the unknowns of the elasticity tensor C_{ij} can be reduced further. Here, the fabrics of cone, thick and partial girdle fabric are considered (sec. 2.1). A partial girdle corresponds to an orthorhombic medium, with 9 unknowns,

$$C_{ij} = \begin{pmatrix} C_{11} & C_{12} & C_{13} & 0 & 0 & 0 \\ C_{12} & C_{22} & C_{23} & 0 & 0 & 0 \\ C_{13} & C_{23} & C_{33} & 0 & 0 & 0 \\ 0 & 0 & 0 & C_{44} & 0 & 0 \\ 0 & 0 & 0 & 0 & C_{55} & 0 \\ 0 & 0 & 0 & 0 & 0 & C_{66} \end{pmatrix}. \tag{3.7}$$

In case of orthorhombic media three symmetry planes, i.e., orthogonal planes of mirror symmetry exist. The number of unknowns can be reduced further if transversely isotropic media exist, resulting in an anisotropy with a single axis of rotation symmetry. Most seismic studies have been done on vertical transversely isotropic media (VTI), where the rotation symmetry axis is vertical. In this case, the elasticity tensor consists of 5 unknowns,

$$C_{ij}^{VTI} = \begin{pmatrix} C_{11} & C_{12} & C_{13} & 0 & 0 & 0 \\ C_{12} & C_{11} & C_{13} & 0 & 0 & 0 \\ C_{13} & C_{13} & C_{33} & 0 & 0 & 0 \\ 0 & 0 & 0 & C_{55} & 0 & 0 \\ 0 & 0 & 0 & 0 & C_{55} & 0 \\ 0 & 0 & 0 & 0 & 0 & (C_{11} - C_{12})/2 \end{pmatrix}. \tag{3.8}$$

Horizontal transversely isotropic (HTI) media has a rotation symmetry as well. The rotation axis is now oriented horizontally. Again, the number of unknowns is 5. However, different components of the elasticity tensor are equal compared to the VTI case,

$$C_{ij}^{HTI} = \begin{pmatrix} C_{11} & C_{13} & C_{13} & 0 & 0 & 0 \\ C_{13} & C_{33} & C_{23} & 0 & 0 & 0 \\ C_{13} & C_{23} & C_{33} & 0 & 0 & 0 \\ 0 & 0 & 0 & (C_{33} - C_{23})/2 & 0 & 0 \\ 0 & 0 & 0 & 0 & C_{55} & 0 \\ 0 & 0 & 0 & 0 & 0 & C_{55} \end{pmatrix}. \tag{3.9}$$

The most common fabric distributions in ice are cone (VTI), thick girdle (HTI) and partial girdle (orthorhombic) fabric. To be able to calculate seismic velocities and reflection coefficients for these fabrics orthorhombic medium needs to be considered.

3.2 Concept of Thomsen parameters

Thomsen (1986) derived a notation to further simplify the description of wave velocities in weakly anisotropic VTI media, the three so-called Thomsen parameters:

$$\varepsilon = \frac{C_{11} - C_{33}}{2C_{33}}, \tag{3.10}$$

$$\delta = \frac{(C_{13} + C_{55})^2 - (C_{33} - C_{55})^2}{2C_{33}(C_{33} - C_{55})}, \tag{3.11}$$

$$\gamma = \frac{(C_{66} - C_{44})}{2C_{44}}. \tag{3.12}$$

The Thomsen parameters are dimensionless and reduce to zero in case of isotropic material. They give a measure for the degree of existing anisotropy. The Thomsen parameter ε gives the difference between horizontal ($\sqrt{C_{11}/\rho}$) and vertical ($\sqrt{C_{33}/\rho}$) P-wave velocity. The same applies for γ as anisotropy parameter for the SH-wave. The parameter δ is the second derivation of the P-wave phase velocity with respect to the phase angle at vertical incidence. Thus, it describes the near vertical dependency of the P-wave velocity on the phase angle.

For the calculation of velocities with the Thomsen parameter the vertical P- and S-wave velocities are used. In VTI media vertical SH- and SV-velocities are equal. For the case of weak anisotropy an approximation of phase velocities in VTI media by means of the Thomsen parameters is given by

$$v_{\mathrm{p}}(\vartheta) = v_{\mathrm{p0}}(1 + \delta \sin^2\vartheta \cos^2\vartheta + \varepsilon \sin^4\vartheta), \tag{3.13}$$

$$v_{\mathrm{sv}}(\vartheta) = v_{\mathrm{s0}}\left(1 + v_{\mathrm{p0}}^2/v_{\mathrm{s0}}^2(\varepsilon - \delta)\sin^2\vartheta\cos^2\vartheta\right), \tag{3.14}$$

$$v_{\mathrm{sh}}(\vartheta) = v_{\mathrm{s0}}(1 + \gamma \sin^2\vartheta), \tag{3.15}$$

with the zero-offset velocities $v_{\mathrm{p0}} = v_{\mathrm{p}}(0^\circ)$ and $v_{\mathrm{s0}} = v_{\mathrm{sv}}(0^\circ) = v_{\mathrm{sh}}(0^\circ)$.

The description of Thomsen parameters has been extended to the symmetry planes of orthorhombic media by Tsvankin (1997) and is, thus, obviously also valid for HTI media. In the $[x_1, x_3]$-plane the Thomsen parameters stay the same as for the VTI media given by equations (3.10)–(3.12), and are normally denoted with the index (2). This is, however, only the case if the Thomsen parameters for VTI media are defined as in equations (3.10)–(3.12). If the component C_{44} is used instead of C_{55} (VTI media $C_{44} = C_{55}$) for the Thomsen parameter δ this is no longer valid. The Thomsen parameters for orthorhombic media in the $[x_2, x_3]$-plane, denoted with index (1), are then given by

$$\varepsilon^{(1)} = \frac{C_{22} - C_{33}}{2C_{33}}, \tag{3.16}$$

$$\delta^{(1)} = \frac{(C_{23}+C_{44})^2-(C_{33}-C_{44})^2}{2C_{33}(C_{33}-C_{44})}, \tag{3.17}$$

$$\gamma^{(1)} = \frac{(C_{66}-C_{55})}{2C_{55}}, \tag{3.18}$$

and for the $[x_1, x_2]$-plane, denoted with index (3),

$$\delta^{(3)} = \frac{(C_{12}+C_{66})^2-(C_{11}-C_{66})^2}{2C_{11}(C_{11}-C_{66})}. \tag{3.19}$$

This notation allows it to calculate seismic velocities for orthorhombic media within each symmetry plane.

When an ice core is drilled the information of the original orientation of the ice core within the borehole, the core azimuth, can normally not be gained. Thus, the orientation of the vertical girdle is unknown. Hereinafter, and if not stated differently, the used girdle is oriented in the $[x_2, x_3]$-plane, corresponding to HTI media. In this case the same Thomsen parameters apply for the HTI as for the VTI medium (eq. (3.10)–(3.12)). The Thomsen parameters ε, δ and γ without indices relate to $\varepsilon^{(2)}, \delta^{(2)}$ and $\gamma^{(2)}$ of equations (3.10)–(3.12). If velocities for other symmetry planes are calculated for the following analyses (Ch. 4 and 7–8) the elasticity tensor for the girdle fabric is rotated by 90° and the notation of the Thomsen parameters as given in equations (3.10)–(3.12) can be used again.

3.3 Seismic velocities

Many approximations as well as exact solutions of the Christoffel matrix exist for the calculation of velocities for the different anisotropic fabrics. Most studies have been done on VTI media (e.g., Daley and Heron, 1977) and are still valid within the symmetry planes of HTI media. To be able to calculate seismic velocities for the different fabrics in ice a calculation of velocities for orthorhombic media derived by Daley and Krebes (2004) is used here (sec. 3.3.1). For the special case of seismic waves in ice with c-axes orientations within a cone fabric velocities were derived by Bennett (1968) (sec. 3.3.2).

3.3.1 Velocities in orthorhombic media

Equations for P-wave velocities in anisotropic media were derived by Backus (1965) and for SH- and SV-wave velocities by Crampin (1977). To be able to calculate velocities for partial girdle fabric the calculation of phase velocity for orthorhombic media derived by Daley and Krebes (2004) is used. They rearrange linearized equations to obtain the velocity by an ellipsoidal part with anellipsoidal correction term:

$$v_{\mathrm{p}}(\vec{n}) = \sqrt{1/\rho(C_{11}n_1^2 + C_{22}n_2^2 + C_{33}n_3^2 + 2B_{12}n_1^2n_2^2 + 2B_{13}n_1^2n_3^2 + 2B_{23}n_2^2n_3^2)}, \tag{3.20}$$

$$v_{\mathrm{sv}}(\vec{n}) = \sqrt{1/\rho(C_{44}\sin^2\psi + C_{55}\cos^2\psi + 2B_{12}n_1^2n_3^2\sin^2\psi - 2B_{13}n_2^2n_3^2 - 2B_{23}n_1^2n_3^2)}, \tag{3.21}$$

$$v_{\mathrm{sh}}(\vec{n}) = \sqrt{1/\rho(C_{44}n_3^2\cos^2\psi + C_{55}n_3^2\sin^2\psi + C_{66}\sin^2\vartheta - 2B_{12}n_1^2\sin^2\psi)}, \tag{3.22}$$

with

$$B_{12} = (C_{13} + 2C_{66}) - (C_{11} + C_{22})/2, \tag{3.23}$$
$$B_{13} = (C_{12} + 2C_{55}) - (C_{11} + C_{33})/2, \tag{3.24}$$
$$B_{23} = (C_{23} + 2C_{44}) - (C_{22} + C_{33})/2, \tag{3.25}$$

and the unit phase normal vector

$$\vec{n} = (n_1, n_2, n_3) = (\sin\vartheta\cos\psi, \sin\vartheta\sin\psi, \cos\vartheta). \tag{3.26}$$

with the phase angle ϑ and the azimuth ψ, here the azimuth for the orientation of a girdle fabric (Figure 2.2).

From the linearized phase velocities v_{ph} (v_{p}, v_{sv}, v_{sh}; eq. (3.20)–(3.22)) the corresponding group velocity $\vec{v_{\mathrm{g}}}$ and group angle θ can then be calculated (e.g., Rommel and Tsvankin, 2000; Tsvankin, 2001). The components of the group velocity vector are given by

$$v_{\mathrm{g},x_1} = v\sin\vartheta + \left.\frac{\partial v_{\mathrm{ph}}}{\partial\vartheta}\right|_{\psi=const}\cos\vartheta, \tag{3.27}$$
$$v_{\mathrm{g},x_2} = \frac{1}{\sin\vartheta}\left.\frac{\partial v_{\mathrm{ph}}}{\partial\psi}\right|_{\vartheta=const}, \tag{3.28}$$
$$v_{\mathrm{g},x_3} = v_{\mathrm{ph}}\cos\vartheta + \left.\frac{\partial v_{\mathrm{ph}}}{\partial\vartheta}\right|_{\psi=const}\sin\vartheta. \tag{3.29}$$

Within the symmetry planes the group velocity can be calculated using v_{g,x_1} and v_{g,x_3} and rearranged to

$$v_{\mathrm{g}} = v_{\mathrm{ph}}\sqrt{1 + \left(\frac{1}{v_{\mathrm{ph}}}\frac{\partial v_{\mathrm{ph}}}{\partial\vartheta}\right)^2} \tag{3.30}$$

with the group angle in the symmetry plane defined by

$$\tan\theta = \frac{v_{\mathrm{g},x_1}}{v_{\mathrm{g},x_3}} = \frac{\tan\vartheta + \frac{1}{v_{\mathrm{ph}}}\frac{\partial v_{\mathrm{ph}}}{\partial\vartheta}}{1 - \frac{1}{v_{\mathrm{ph}}}\frac{\partial v_{\mathrm{ph}}}{\partial\vartheta}\tan\vartheta}. \tag{3.31}$$

Outside the symmetry planes of the HTI media the component v_{g,x_2} can not be neglected as the derivation $\frac{\partial v}{\partial\psi}$ is no longer zero. In this case v_{g} is the norm of the group velocity vector $\vec{v_{\mathrm{g}}}$ considering all three components v_{g,x_1}, v_{g,x_2} and v_{g,x_3}. Here, a second group angle exists for the direction outside the plane with

$$\tan\theta_{\mathrm{out}} = \frac{v_{\mathrm{g},x_2}}{\sqrt{v_{\mathrm{g},x_1}^2 + v_{\mathrm{g},x_3}^2}}. \tag{3.32}$$

Figure 3.2 shows the phase (dashed curves) and group velocities (solid curves) in dependency of the corresponding phase ϑ and group angle θ of P-, SV- and SH-wave for a VSM-fabric. The largest difference between phase and group velocity can be observed for the SV-wave (light blue curves) with a triplication in the group velocity for group angles of

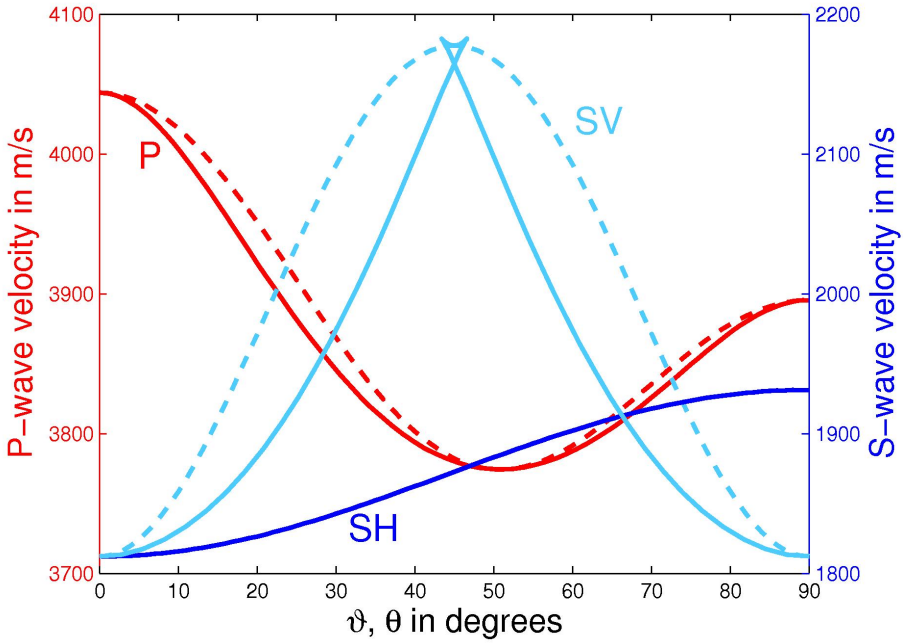

Figure 3.2: Phase (dashed lines) and group velocities (solid lines) over the corresponding phase ϑ and group angle θ for P- (red curves), SH- (blue curves) and SV-waves (light blue curves) of a VSM-fabric. The SV-wave group velocity shows a triplication. For group angles θ between 43° and 46° three different velocities are given for each angle.

43–47°. Here three different velocities are given for each angle. The SV-velocity is largest for 45° incoming angle (phase as well as group angle) with 2180 m/s decreasing for 0° and 90° to 1810 m/s. Variations for the SH-wave are rather small with velocities increasing between 0° and 90° from 1810 m/s to 1930 m/s. The P-wave velocity has a minimum at ∼51° incoming angle with 3770 m/s. The highest wave speed is observed for waves that parallel to the c-axis of an ice crystal (0° incoming angle) with 4040 m/s and 150 m/s slower perpendicular to it.

3.3.2 Velocity calculation for cone fabrics

For the special case of wave propagation in ice with a developed a cone fabric anisotropy Bennett (1968) derived equations of the slowness surface for P-, SV- and SH-waves. The phase velocities are given by the inverse of the slowness surface,

$$v_{\mathrm{p}}(\vartheta) = \frac{1}{(A_{\mathrm{v_p}} - B_{\mathrm{v_p}} \sin^2\vartheta + C_{\mathrm{v_p}} \sin^4\vartheta)}, \tag{3.33}$$

$$v_{\mathrm{sh}}(\vartheta) = \frac{1}{A_{\mathrm{v_s}} + B_{\mathrm{v_{sh}}} \sin^2\vartheta}, \tag{3.34}$$

$$v_{\mathrm{sv}}(\vartheta) = \frac{1}{A_{\mathrm{v_s}} + B_{\mathrm{v_{sv}}} \sin^2\vartheta \cos^2\vartheta}, \tag{3.35}$$

with the variables

$$A_{v_p} = a_1 + \frac{1}{15}b_1 + \frac{1}{3}c_1 + \frac{1}{15}(16b_1 - 10c_1)(\cos\varphi + \cos^2\varphi) - \frac{8}{5}b_1(\cos^3\phi + \cos^4\phi), \quad (3.36)$$

$$B_{v_p} = (4b_1 - c_1)(\cos\varphi + \cos^2\varphi) - 8b_1(\cos^3\varphi + \cos^4\varphi), \quad (3.37)$$

$$C_{v_p} = 3b_1(\cos\varphi + \cos^2\varphi) - 7b_1(\cos^3\varphi + \cos^4\varphi), \quad (3.38)$$

$$A_{v_s} = a_3 - \frac{1}{15}(8b_2 - 5b_3)(1 + \cos\varphi + \cos^2\varphi) + \frac{4}{5}b_2(\cos^3\varphi + \cos^4\varphi), \quad (3.39)$$

$$B_{v_{sh}} = (b_2 - b_3)(\cos\varphi + \cos^2\varphi) - b_2(\cos^3\varphi + \cos^4\varphi), \quad (3.40)$$

$$B_{v_{sv}} = 3b_2(\cos\varphi + \cos^2\varphi) - 7b_2(\cos^3\varphi + \cos^4\varphi), \quad (3.41)$$

and the parameters

- a_1 = 256.28 μm/s,
- b_1 = 5.92 μm/s,
- c_1 = 5.08 μm/s,
- a_2 = 501.97 μm/s,
- b_2 = 45.37 μm/s,
- a_3 = 531.40 μm/s,
- b_3 = 15.94 μm/s.

These equations were derived by an approximation of the slowness surface. To calculate the slowness surface over different angle Bennett (1968) first derived the elastic modules from single natural ice crystals by measurements of ultrasonic pulses with 600 kHz. The ice was stored at $-40°$C and measured at $-10°$C. Afterwards, the slowness surface of a single crystal could be calculated and curves fit to these slowness surfaces with constants a_1 to b_3. Thus, velocities for different incoming angles θ in dependence of the cone opening angle φ can be calculated. Bennett (1968) also derived velocities for what he calls a surface cone, which is referred to as small circle distribution by Wallbrecher (1986) (sec. 2.1). As small circle distributions are not considered in this work these derivations are not introduced here.

The problem of the Bennett (1968) equations is that the derived velocities do not consider girdle fabrics. Thus, the influence of girdle fabric on traveltimes can not be investigated. Further, they do not give the possibility to investigate reflection coefficients as the elasticity tensor is unknown.

3.4 Reflection coefficients

The calculation of reflection coefficients for different incoming angles is already rather complicated for layered isotropic media given by the Zoeppritz equations (e.g., Aki and Richards, 2002). In case of anisotropic media most of the studies have been done for VTI media (Keith and Crampin, 1977; Daley and Heron, 1977) and in terms of Thomsen parameters (Thomsen, 1993). An comprehensive overview of the different calculations of reflection coefficients for VTI and HTI media is given by Rüger (2002). Apart from cone

(VTI) and thick girdle (HTI) anisotropy, partial girdle (orthorhombic) fabric is considered here. Thus, a calculation of reflection coefficients for orthorhombic media is required.

A solution for general anisotropy was derived by Zillmer et al. (1997) by means of the perturbation theory. As a reference the isotropic medium is used. This yields a set of more complicated equations. In a second step these results were simplified by assuming an interface with a weak contrast (Zillmer et al., 1998). Thus, reflection coefficients for P-, SV- and SH-waves are obtained. The R_{shsh} and R_{svsv} reflection coefficients are restricted to a symmetry plane of the layered medium. The indices give the polarisation of the incoming and reflected wave, e.g., R_{shsh} is the reflection coefficient for an incoming SH-wave, reflected as SH-wave, equivalent for R_{pp} and R_{svsv}. The reflection coefficients are than given by

$$\begin{aligned} R_{\mathrm{pp}} &= \frac{1}{4}\left(\frac{\Delta C_{33}}{C_{44}^{(0)}+2C_{12}^{(0)}}+\frac{\Delta\rho}{\rho^{(0)}}\right)-\frac{1}{4}\frac{\Delta\rho}{\rho^{(0)}}\tan^2(\vartheta)+\frac{1}{4}\frac{2\Delta C_{13}-C_{33}-4\Delta C55}{C_{44}^{(0)}+2C_{12}^{(0)}}\sin^2\vartheta \\ &\quad +\frac{1}{4}\frac{\Delta C_{11}}{C_{44}^{(0)}+2C_{12}^{(0)}}\sin^2\vartheta\tan^2\vartheta, \end{aligned} \tag{3.42}$$

$$\begin{aligned} R_{\mathrm{svsv}} &= -\frac{1}{4}\left(\frac{\Delta C_{55}}{C_{12}^{(0)}}+\frac{\Delta\rho}{\rho^{(0)}}\right)-\frac{1}{4}\frac{\Delta\rho}{\rho^{(0)}}\tan^2(\vartheta)+\frac{1}{4}\frac{\Delta C_{11}-2\Delta C_{13}+C_{33}-3\Delta C55}{C_{12}^{(0)}}\sin^2\vartheta \\ &\quad -\frac{1}{4}\frac{\Delta C_{55}}{C_{12}^{(0)}}\sin^2\vartheta\tan^2\vartheta, \end{aligned} \tag{3.43}$$

$$R_{\mathrm{shsh}} = -\frac{1}{4}\left(\frac{\Delta C_{44}}{C_{12}^{(0)}}+\frac{\Delta\rho}{\rho^{(0)}}\right)+\frac{1}{4}\left(\frac{\Delta C_{66}}{C_{12}^{(0)}}+\frac{\Delta\rho}{\rho^{(0)}}\right)\tan^2\vartheta, \tag{3.44}$$

where Δ denotes the difference between the upper layer 1 and the lower layer 2, for example $\Delta C_{33} = C_{33}^{(2)} - C_{33}^{(1)}$. The superscript (0) gives the isotropic reference values. When reflection coefficients are calculated for different anisotropic ice fabrics, the density is constant, i.e., the $\Delta\rho$-terms can be neglected ($\rho^{(2)} - \rho^{(1)} = 0$).

This description is especially practical for the reflection coefficients in ice. For the isotropic reference values the elasticity tensor for isotropic ice can be used and no average needs to be taken over different materials as the different anisotropic fabrics are just variations of the same material. However, it is not practical for the calculation of the reflection coefficient for the ice-bed interface. For the calculation of the reflection coefficient between cone fabric (VTI) and the bed the derivation of Thomsen (1993), further developed by Rüger (1997), for the P-wave reflection coefficient can be used.

3.5 NMO and RMS velocity

One major step in the processing sequence of seismic data is the normal moveout (NMO) correction, to correct for the additional two-way traveltime (TWT) for increasing offset x. In section 3.5.1 the theoretical concept of NMO correction in anisotropic media will be explained. This problem is illustrated in section 3.5.2 on the example of a 50 m layer consisting of VSM-fabric.

3.5.1 Concept of anisotropic NMO and RMS velocities

During the NMO correction hyperbolas are fit to the moveout of reflections to determine the root mean square (RMS) velocity V_{RMS} over depth for multiple layers. The traveltime for increasing offset $T(x)$ for N layers is given by

$$T^2(x) = T_0^2(N) + \frac{x^2}{V_{\mathrm{NMO}}^2}, \tag{3.45}$$

with the TWT for the zero-offset case $T_0(N) = \sum_{i=1}^{N} t_0^{(i)}$, summed over the zero-offset TWT t_0 of the single layers (i). In the case of isotropic material and normal spread length (offset/depth-ratio $\leq$1) the NMO velocity V_{NMO} is identified as RMS velocity,

$$V_{\mathrm{RMS}}(N) = \sqrt{\frac{1}{T_0(N)} \sum_{i=1}^{N} [v^{(i)}]^2 t_0^{(i)}}, \tag{3.46}$$

with the interval velocity v for the layers (i). The approach is the same regardless if P- or S-wave data are analysed. Hereinafter, variables considering the effect of multiple layers are denoted by upper case letters (e.g., V_{NMO}), whereas lower case letters are variables of single layers (e.g., v_{p}).

In the anisotropic case the traveltime for different offsets now not only depends on the increasing travel way due to the increase in offset but also on the change in velocity, as the velocity depends on the incoming group angle. The NMO velocity $v_{\mathrm{nmo},\zeta}$ for a single layer (Thomsen, 1986) with normal spread length (offset/depth-ratio ≤ 1) is given by

$$v_{\mathrm{nmo},\zeta} = v_{\zeta 0} \sqrt{1 + 2\xi}, \tag{3.47}$$

where ζ represents either P- or SH-wave, so $v_{\zeta 0}$ is either $v_{\mathrm{p}0}$ or $v_{\mathrm{sh}0}$ and ξ the corresponding Thomsen parameter δ or γ, respectively. In VTI media $v_{\mathrm{sh}0}$ would just be equal to $v_{\mathrm{s}0}$. These equations were derived for VTI media but are as well valid for orthorhombic media with wave propagation in the symmetry planes (Tsvankin, 1997).

For the SV-data the NMO velocity for a single layer is calculated using

$$v_{\mathrm{nmo,sv}} = v_{\mathrm{s}0} \sqrt{1 + 2v_{\mathrm{p}0}^2 / v_{\mathrm{s}0}^2 (\varepsilon - \delta)}. \tag{3.48}$$

As SV-wave data are not analysed here, only P- and SH-waves are considered hereinafter.

For normal spread length the two-way traveltime can now be calculated (equivalent to eq. (3.45)) and the moveout for a single layer is then given by

$$t^2(x) = t_{\zeta 0}^2 + \frac{x^2}{v_{\mathrm{nmo},\zeta}^2}. \tag{3.49}$$

Here, the vertical TWT $t_{\zeta 0}$ is a function of the vertical P- or SH-wave velocity, respectively, and the thickness h of the layer, so that $t_{\zeta 0} = 2h/v_{\zeta 0}$. If not only one but multiple layers are considered the NMO velocity in the anisotropic case is as well a RMS velocity of the velocities of single layers. The anisotropic NMO velocity for multiple layers can then be

calculated from the NMO velocity of the single layers $v_{\mathrm{nmo},\zeta}$ (equivalent to eq. (3.46) for the isotropic case),

$$V_{\mathrm{NMO},\zeta}(N) = \sqrt{\frac{1}{T_{\zeta 0}} \sum_{i=1}^{N} [v_{\mathrm{nmo},\zeta}^{(i)}]^2 t_{\zeta 0}^{(i)}}. \tag{3.50}$$

This equation can be rewritten in the form of equation (3.47), here for the multi-layer case in dependency of the vertical RMS velocity $V_{\mathrm{RMS},\zeta 0}$

$$V_{\mathrm{NMO},\zeta}(N) = V_{\mathrm{RMS},\zeta 0}(N) \sqrt{1 + 2\xi_{\mathrm{eff}}}. \tag{3.51}$$

The parameter ξ_{eff} is the RMS value of ξ over depth (Tsvankin, 2001) and expressed by

$$\xi_{\mathrm{eff}} = \frac{1}{V_{\mathrm{RMS},\zeta 0}^2(N) T_{\zeta 0}(N)} \sum_{i=1}^{N} \left[v_{\zeta 0}^{(i)} \right]^2 \xi^{(i)} t_{\zeta 0}^{(i)}. \tag{3.52}$$

This description of the change in TWT with offset is no longer sufficient if the spread length of the seismic data is long (offset/depth-ratio > 1). Here, the non-hyperbolic part of the moveout becomes to large, so that the 2nd-order approximation (eq. (3.45)) of the traveltime is no longer valid. This is also the case for isotropic materials (Yilmaz, 2001). Thus, for long spread length a 4th-order term needs to be added to sufficiently describe the TWT depending on the offset. For P-waves in VTI media this x^4-term was derived by Alkhalifah and Tsvankin (1995). Therefore, they introduced the anellepticity parameter η, with

$$\eta = \frac{\varepsilon - \delta}{1 + 2\delta}. \tag{3.53}$$

For elliptical anisotropy, where $\varepsilon = \delta$, η is zero. The P-wave NMO velocity $v_{\mathrm{nmo,p}}$ can also be given by means of η and the horizontal P-wave velocity $v_{\mathrm{p}}(90^\circ)$,

$$v_{\mathrm{nmo,p}} = \frac{v_{\mathrm{p}}(90^\circ)}{\sqrt{1 + 2\eta}}. \tag{3.54}$$

The TWT with increasing offset for the 4th-order NMO correction in the anisotropic case (ηNMO correction) is then given by

$$\begin{aligned} T_{\mathrm{P}}^2(x) &= T_{\mathrm{P0}}^2(N) + \frac{x^2}{V_{\mathrm{NMO,P}}^2(N)} \\ &\quad - \frac{2\eta_{\mathrm{eff}}(N) x^4}{V_{\mathrm{NMO,P}}^2(N) [T_{\mathrm{P0}}^2(N) V_{\mathrm{NMO,P}}^2(N) + (1 + 2\eta_{\mathrm{eff}}(N)) x^2]}, \end{aligned} \tag{3.55}$$

with the RMS η-value η_{eff}

$$\eta_{\mathrm{eff}}(N) = \frac{1}{8} \left(\frac{1}{V_{\mathrm{NMO,P}}^4(N) T_{\mathrm{P0}}(N)} \left[\sum_{i=1}^{N} (v_{\mathrm{nmo,p}}^{(i)})^4 (1 + 8\eta^{(i)}) t_{\mathrm{p0}}^{(i)} \right] - 1 \right). \tag{3.56}$$

Thus, it is also possible to correct for the additional TWT with increasing offset in case of long spread length.

A problem of processing seismic data from anisotropic material exists in the conversion of TWT to depth after stacking the data. From the NMO correction the NMO velocity $V_{\mathrm{NMO},\zeta}$ is derived for normal-spread seismic data. However, for the depth conversion the zero-offset velocity $V_{\mathrm{RMS},\zeta 0}$ is needed. Thus, as long as the anisotropy is unknown it is not possible to derive the depth of the layers. Or in reverse, only when the depth of the layers is known, it is possible to derive information about the existing anisotropy. If long-spread seismic P-wave data are analysed $V_{\mathrm{NMO,P}}$ and η_{eff} are derived. This means, η_{eff} yields information about the existing anisotropy. However, the vertical P-wave velocity, needed for the depth conversion, cannot be derived only the horizontal P-wave velocity (eq. (3.54)).

I will apply the concepts introduced above to derive information about the COF in Chapter 9. A possibility to gain information about these different anisotropic fabrics over depth is by linking reflections from seismic data to those of other data sets, e.g., radar and ice core data. With information of the depth of reflections the RMS velocity can be derived for the zero-offset case $V_{\mathrm{RMS},\zeta 0}$. Together with the NMO velocities $V_{\mathrm{NMO},\zeta}$ derived during the stacking process the effective Thomsen parameters δ_{eff} and γ_{eff} can be derived from the P- and SH-wave by means of equation (3.51). For a multi-layer case the interval Thomsen parameter δ and γ can then be derived from equation (3.52). Those information about the anisotropy can be gained from seismic data sets.

3.5.2 Example: single anisotropic layer

As an example for the influence of anisotropy on seismic traveltimes a single layer of 50 m thickness, where all ice crystals are oriented vertically (VSM-fabric), is considered here. This is the most extreme form of anisotropy one can expect in a glacier or ice sheet.

With the equations (3.20), (3.22) and (3.30) the group velocities $v_{\mathrm{p}}(\theta)$ and $v_{\mathrm{sh}}(\theta)$ for the different incoming angles are calculated. From these velocities, the corresponding traveltimes for the different offsets can be derived for the P- and SH-wave, respectively. The red curves in Figure 3.3 show these traveltimes derived from the angle dependent velocities $v_{\mathrm{p}}(\theta)$ (Figure 3.3, a) and $v_{\mathrm{sh}}(\theta)$ (Figure 3.3, b) for an offset/depth-ratio$\leq$1. The corresponding anisotropic NMO velocities (eq. (3.47)) for a single layer are given by the dashed blue lines. They approximate the true moveout (red curves) very good. In case of the P-wave the difference in TWT calculated from the group velocity $v_{\mathrm{p}}(\theta)$ and the NMO velocity $v_{\mathrm{nmo,p}}$ for 50 m offset is only 1%.

In case of the P-wave the approximation of the TWT using the NMO velocity $v_{\mathrm{nmo,p}}$ becomes more inaccurate if the offset becomes larger than the depth (offset/depth-ratio$>$1; Figure 3.4). Here, the parameter δ that describes the variation for nearly vertical incidence of the P-wave is no longer sufficient to describe the velocity distribution. The green curves show the traveltimes for a wave traveling with the zero-offset velocities ($v_{\zeta 0}$). To be able to stack the data the NMO velocity ($v_{\mathrm{nmo},\zeta}$, blue dashed lines) is needed. For the depth conversion the zero-offset velocity ($v_{\zeta 0}$, green lines) has to be used, which is normally unknown. The difference between zero-offset ($v_{\zeta 0}$) and NMO velocity ($v_{\mathrm{nmo},\zeta}$) is 21% in case of the P-wave ($v_{\mathrm{nmo,p}} = 3207$ m/s, $v_{\mathrm{p0}} = 4043$ m/s) but only 6% for the SH-wave ($v_{\mathrm{nmo,sh}} = 1931$ m/s, $v_{\mathrm{sh0}} = 1812$ m/s) for this example of a 50 m layer of VSM-fabric. Thus, the mistake that is introduced by assuming isotropic material and using the NMO velocity ($v_{\mathrm{nmo},\zeta}$) as zero-offset velocity ($v_{\zeta 0}$) for the depth conversion is much smaller in case of the SH-wave than in

case of the P-wave.

If the offsets become larger (offset/depth-ratio>1) it is no longer sufficient to use the 2nd-order approximation of the traveltime (eq. (3.49)) for the P-wave moveout. The extension using a 4th-order term (eq. (3.55)) allows a sufficiently accurate approximation of P-wave traveltimes (Figure 3.4, a, dashed light blue line). Now the calculation of the traveltime depends on the NMO velocity ($v_{\mathrm{nmo,p}}$) and the anisotropic parameter η. For the SH-wave the 2nd-order approximation of the traveltime is still accurate for an offset/depth-ratio>1 (Figure 3.4, b).

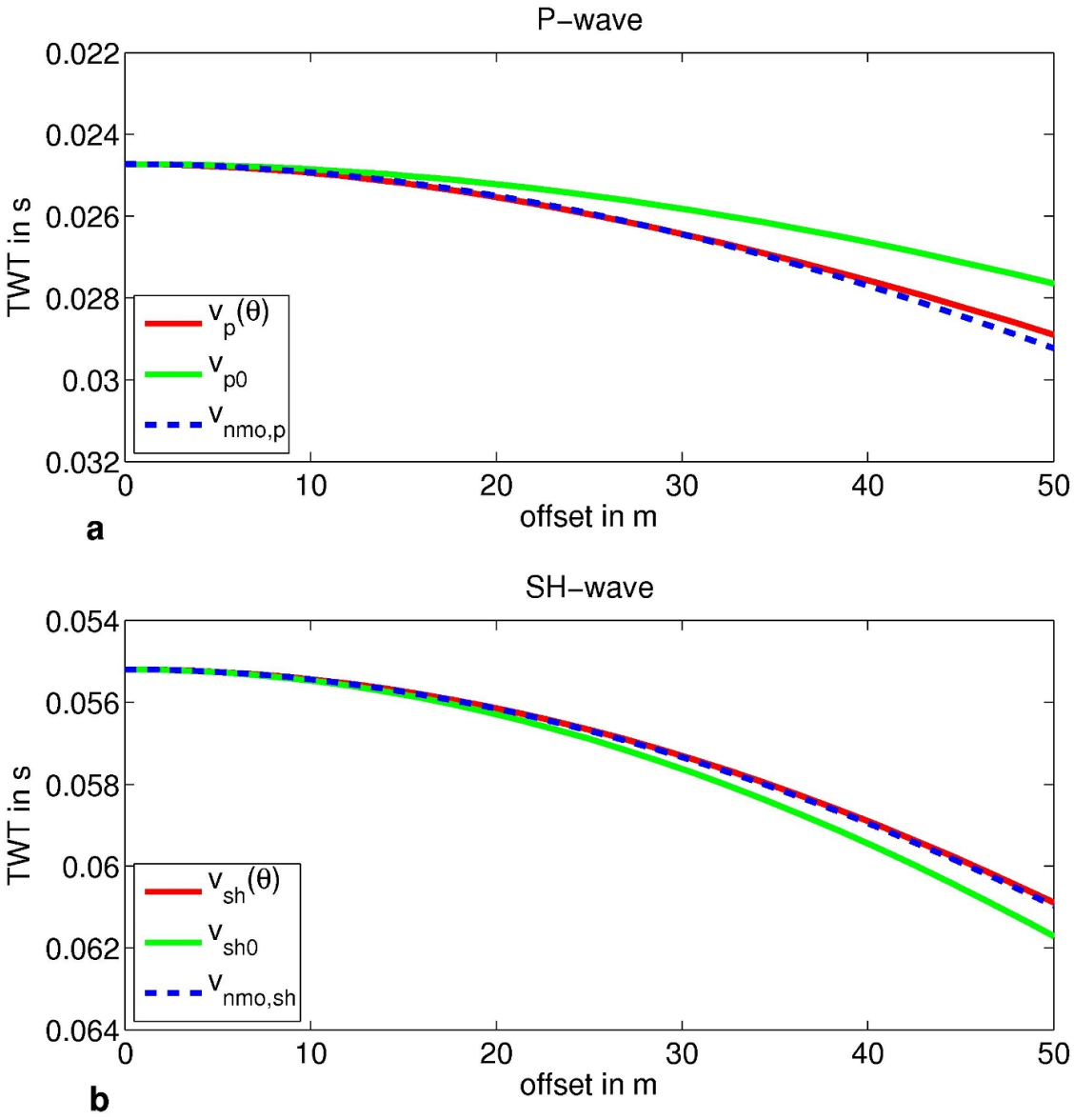

Figure 3.3: Moveout for P- (a) and SH-wave (b) for a VSM-fabric with 50 m thickness and an offset/depth-ratio$\leq$1. The red curves are traveltimes calculated from velocities given by equations (3.20), (3.22) and (3.30). The dashed blue curves show traveltimes calculated from the corresponding NMO velocities (eq. (3.47)), the green curves form the zero-offset velocities ($v_{\zeta 0}$, with $\zeta = \mathrm{p}, \mathrm{sh}$). The difference between NMO velocity $v_{\mathrm{nmo},\zeta}$ and zero-offset velocity $v_{\zeta 0}$ is 21% for the P-wave and 6% for the SH-wave.

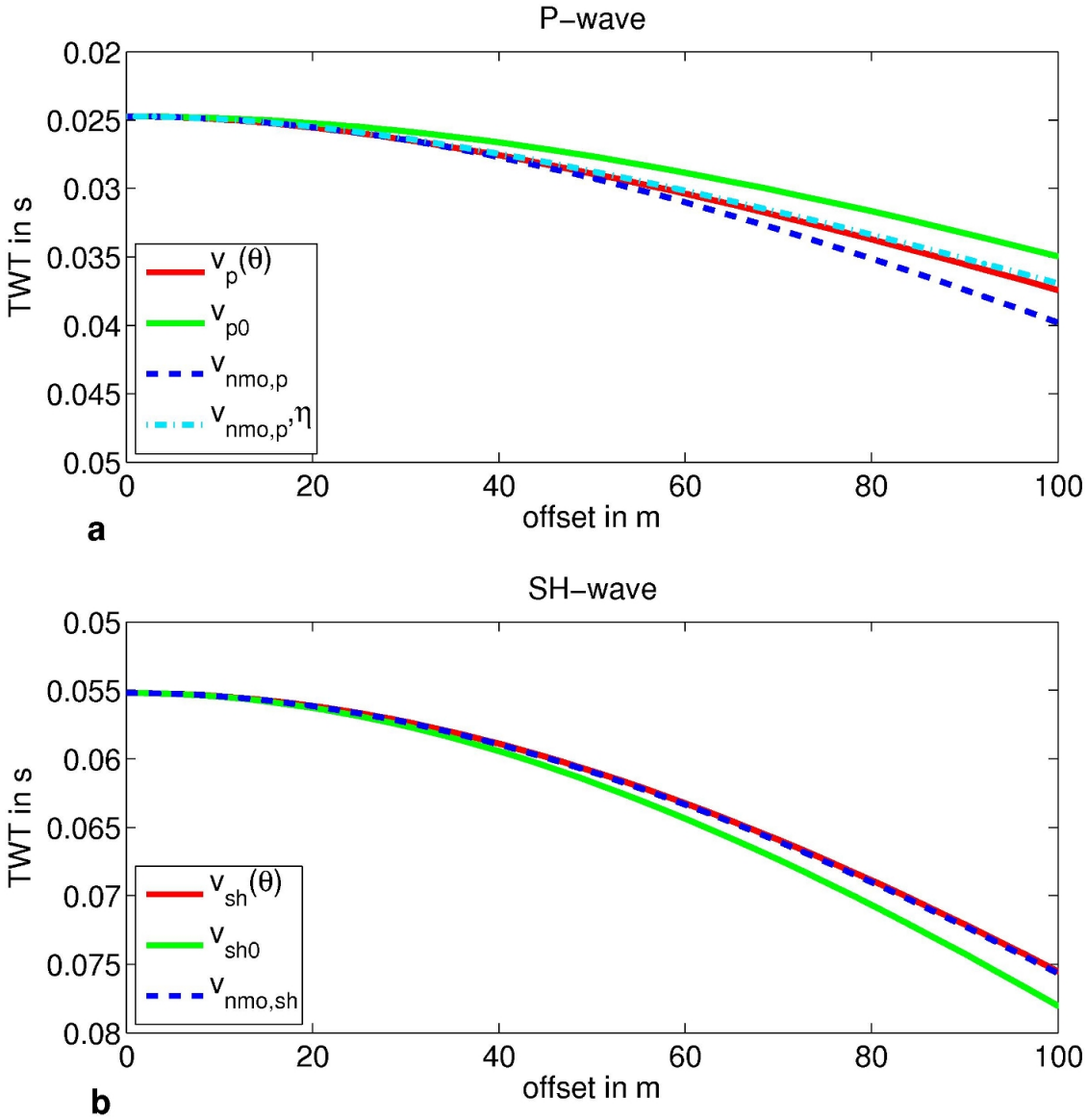

Figure 3.4: Moveout for P- (a) and SH-wave (b) for a VSM-fabric with 50 m thickness and an offset/depth-ratio>1. The red curves are traveltimes calculated from velocities given by equations (3.20), (3.22) and (3.30). The dashed blue curves show traveltimes calculated from the corresponding NMO velocities (eq. (3.47)), the green curves form the zero-offset velocities ($v_{\zeta 0}$, with $\zeta = \mathrm{p}, \mathrm{sh}$). This corresponds to results of Figure 3.3 for larger offsets. The dashed light blue curve shows traveltimes that were calculated using the 4th-order approximation for traveltimes (eq. (3.55)).

4 Combining seismic and ice core measurements

The seismic wave propagation in ice is influenced by different physical properties of ice, of which the main parameters are density, temperature and crystal orientation fabric. The first section (sec. 4.1) provides some insight into the development of the seismic measurements and their results on ice science 1926. The dependency of the seismic P-wave velocity on the density as well as the dependency of the seismic P- and S-wave velocity on the temperature have been studied by different authors. Their findings are introduced in section 4.3 and 4.4. A connection between seismic velocities and the crystal orientation fabric was introduced by Bennett (1968) (sec. 3.3.2) and also by Bentley (1972). In section 4.2 a new method is introduced to calculate the elasticity tensor from COF eigenvalue measurements, providing the possibility to calculate velocities, reflection angles and reflection coefficients for different cone and girdle fabrics.

4.1 History of seismic measurements on ice

First seismic measurements on ice were carried out on frozen lakes, with focus of exploring the ground below the lake. As test and preparation for the planed Greenland expedition of Alfred Wegener the first seismic measurement on a glacier was carried out by Hans Mothes. He successfully deployed explosive charges to determine the thickness of Hintereisferner, Austria (Mothes, 1926, 1927), validated with glaciological determinations of the ice thickness, and later as well of the Konkordiaplatz, Aletschgletscher, Switzerland (Mothes, 1929).

As the seismic method proofed to work well for the determination of the ice thickness, seismic measurements were carried out on the Greenland ice sheet on the pre-expedition in 1929 for the German Greenland Expedition Alfred Wegener and also during the main expedition in 1931. The main focus was to determine the ice thickness and the potential of seismics to determine temperatures in ice sheets (Brockamp, 1933, 1935). Further studies of Brockamp and Mothes (1930, 1931) at the Pasterz glacier (Austria) were used for a better understanding of the waveforms of P- and S-waves in ice as well as their reproducibility.

The first larger seismic measurement in Antarctica was carried out during the Norwegian-British-Swedish Antarctic Expedition, 1949–1952 (Robin, 1958) with a long traverse in Dronning Maud Land to determine the ice thickness. The results were used by Robin (1958) to derive information about density distribution, temperature and crystal anisotropy.

Until then, the main focus of seismic measurements was to derive information about the ice thickness. However, radar measurements soon proved to be much more efficient in answering this question for the large ice caps (Ch. 5) compared to the labour intensive seismic measurements. Nevertheless, seismic measurements were further used to investigate

physical properties of ice. To investigate the dependency of seismic waves on density, temperature and also anisotropy larger seismic studies have been carried out near Byrd station by Kohnen and Bentley (1973). The density-velocity relationship derived by Kohnen (1972), as well as derived temperature gradients (Kohnen, 1974) are still used for the analysis and interpretation of seismic data from glaciers and ice sheets. The most extensive study on the influence of anisotropy on seismic wave propagation and the calculation of seismic velocities for anisotropic ice, solid cone fabrics as well as small circle distributions, was done by Bennett (1968). He first measured the elasticity tensor of a single ice crystal and used these results to calculate the slowness surface of the above mentioned fabrics. The obtained equations were applied to seismic measurements from Dome C, Antarctica, by Blankenship and Bentley (1987). They already pointed out the importance of the crystalline fabric for modeling ice sheet dynamics and the potential of seismic measurements to obtain information about these anisotropic fabrics. Further studies on anisotropy were carried out by Bentley (1972) using ultrasonic sounding and averaging velocities for different incoming angle of a single ice crystal to determine velocities for other COF distributions.

Another large project in Antarctica was done on the Ross ice shelf (Ross Ice Shelf Geophysical and Glaciological Survey, RIGGS) between 1973 and 1978 with numerous glaciological and geophysical measurements including different seismic surveys (Robertson and Bentley, 1990; Albert and Bentley, 1990; Kirchner and Bentley, 1990). Since then, the main focus in deploying seismic measurements has been on the determination of basel processes (e.g., Blankenship et al., 1986; Nolan and Echelmeyer, 1999a,b; King et al., 2004; Smith and Murray, 2008). The big advantage of seismic over radar methods is that seismic signals below the ice-bed interface are still strong enough and can be interpreted, especially if thin water layers or lakes exist under the ice (e.g., Peters et al., 2008; Horgan et al., 2012). Further inside into the properties of the basel conditions can be gained by analysing the reflection coefficient over offset (amplitude versus offset, AVO, or amplitude versus angle, AVA, analysis) from the bed reflection (Smith, 1997; Anandakrishnan, 2003; Smith, 2007; Holland and Anandakrishnan, 2009; Booth et al., 2012)

Beside analysing the basal properties a lot of focus is still put into a better understanding of the physical properties that influence wave propagation and the possibility to determine these, such as the attenuation and the influence on the temperature (Peters et al., 2012; Gusmeroli et al., 2010) or the Poisson's ratio (King and Jarvis, 2007) as well as a better understanding of the anisotropic ice crystals on wave velocity (Anandakrishnan et al., 1994). Here, englacial seismic reflections were observed in seismic surveys from Antarctica (Horgan et al., 2012; Hofstede et al., 2013) and Greenland (Horgan et al., 2008) and have been interpreted as arising from abrupt changes in the orientation of the ice crystal fabric.

Explosive sources are still the most common source for seismic measurements on ice. This is, however, labour intensive as shot holes have to be drilled. Vibroseismic methods in combination with snow streamers show huge potential here (Hofstede et al., 2013; Diez et al., 2013; Polom et al., 2014) for efficient seismic surveys over larger areas on the ice sheets and shelves in the future, especially for the investigation of the ice-bed interface, the geological properties or the seafloor below ice shelves .

4.2 Calculation of elasticity tensor from eigenvalues

The state of the art to gain information about the orientation of ice crystal fabric is by analysing thin sections from ice cores. Thus, the orientations of the single crystals can be determined and the main direction of the momentum of inertia are calculated and expressed in form of the COF eigenvalues (Ch. 2). For the calculation of seismic velocities and reflection coefficients in anisotropic media the elasticity tensor is required (Ch. 3). To be able to compare results from seismic measurement to ice-core COF measurements or to derive information about the COF from seismic data, a relationship between the COF eigenvalues and the elasticity tensor is needed.

The components of the elasticity tensor have been measured by a number of authors for monocrystalline ice with different methods (Table 4.1). The used frequencies were mostly in the range of ultrasonic waves (>16 kHz). The derived elasticity tensors can be used to calculate velocities for a VSM-fabric. However, a possibility is needed to calculate velocities (sec. 3.3) and reflection coefficients (sec. 3.4) for different distributions of the ice crystal fabric as well.

The two most common fabrics are cone and girdle fabrics (Figure 2.2). I therefore develop a scheme to derive the elasticity tensor for these distributions from the elasticity tensor of a single ice crystal and the given eigenvalues of the fabric (Figure 4.1). Thus, a connection between the description of eigenvalues from ice core measurements and the elasticity tensor needed for the description of wave propagation in anisotropic material is provided. The classification for different fabrics (Wallbrecher, 1986) introduced in section 2.1 is used here. Thus, elasticity tensors are derived for uniform, cluster, thick girdle, and partial girdle distributions from the COF eigenvalues.

The first step is to decide on the kind of fabric from the eigenvalues. To differentiate between cone and girdle Woodcock (1977) suggests a logarithmic representation of the eigenvalues and classification by a slope

$$m = \frac{\ln(\lambda_3/\lambda_2)}{\ln(\lambda_2/\lambda_1)}. \tag{4.1}$$

The fabric is a cluster or cone fabric with $m > 1$ and a girdle fabric with $m < 1$. Thus, in the transition between girdle and cone fabric the fabric is mostly classified as girdle fabric. Girdle fabric, however, is seismically classified as HTI media. Due to the unknown orientation of the girdle azimuth ψ girdle fabric is more complicated to handle for the calculation of velocities and reflection coefficients than VTI media, i.e., cone fabric. To have a stronger tendency for cone fabrics a threshold is set to distinguish between cone and girdle fabric. If $\lambda_1 <= 0.1$ and $\lambda_2 >= 0.2$ the fabric is classified as girdle fabric, everything else is classified as cone fabric. The azimuth ψ of the girdle fabric cannot be determined from the eigenvalues. This is only possible if the eigenvector belonging to the eigenvalue λ_1, the normal to the plane of the girdle, is known in geolocated coordinates.

The next step is the calculation of the opening angles for the different fabrics. Therefore, the two angle χ and φ, giving the extend of the c-axes distribution in the x_1- and x_2-direction (Figure 2.2), are calculated. Wallbrecher (1986) gives equations for the connection of, e.g, the opening angle φ of a cone fabric and the eigenvalue $\lambda_3 = 1 - 2/3 \sin^2 \varphi$ (red curve, Figure 4.2). To verify this calculation the eigenvalues for cone angles between 0 and 90° were calculated. In total 10000 randomly distributed vectors were created, giving a random

	method	C_{11}	C_{33}	C_{55}	C_{12}	C_{13}
Bass et al. (1957)	artificial ice, -2–$-20°$C, here $-16°$C, 5–50 kHz, resonance frequency	13.3±0.8	14.2±0.7	3.06±0.015	6.3±0.8	4.6±0.9
Green and Mackinnen (1956)	artificial ice, $-16°$C, ultrasonic pulses, measured C_{33}, C_{55}, rest calculated following Penny (1948)	13.33±1.98	14.28±0.54	3.26±0.08	6.03±0.72	5.08±0.72
Dantl (1968)	artificial ice, 0–$-140°$C, here $-16°$C, 28–30 MHz, ultrasonic pulse	13.21±0.04	14.43±0.06	2.89±0.02	6.7±0.13	5.79±0.41
Brockamp and Querfurth (1964)	lake ice, 0–$-20°$C, here $-16°$C, 2 and 12 MHz, ultrasonic pulse	13.63	14.85	3.04	6.69	(5.19)
Gammon et al. (1983)	artificial & natural ice, $-16°$C, 10 GHz, Brillouin spectroscopy	13.93±0.04	15.01±0.05	3.01±0.01	7.08±0.04	5.77±0.02
Jona and Scherrer (1952)	artificial ice, $-20°$C, here $-16°$C, 15–18 Mhz, Schaefer-Bergman method	13.845±0.08	14.99±0.08	3.19±0.03	7.07±0.12	5.81±0.16
Bennett (1968)	glacier ice, $-10°$C, 600 kHz, ultrasonic pulse	14.06±0.08	15.24±0.12	3.06±0.03	7.15±0.15	5.88±0.25
Penny (1948)	theoretical derivation, temperature unknown	15.2	16.2	3.2	8	7

Table 4.1: Different elasticity tensors, measured and calculated. All values in 10^9 N/m^2. The order follows later calculations of the P-wave velocities (sec. 7.2) from lower to higher velocities using the given elasticity values.

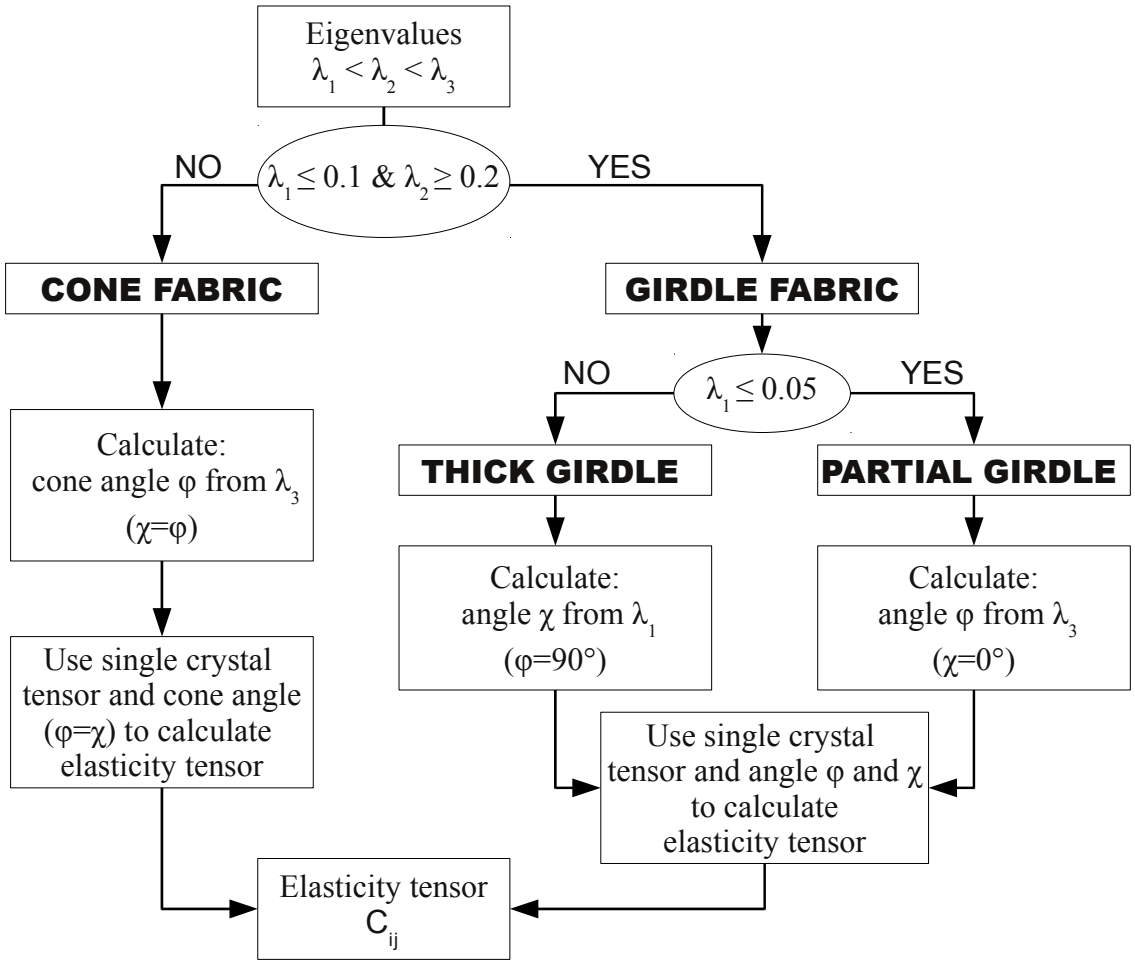

Figure 4.1: Workflow for calculation of elasticity tensor from COF eigenvalues (λ_1, λ_2, λ_3). The two angles determining the distribution of the fabric in x_1-direction χ and in x_2-direction φ are derived as intermediate step to calculate the elasticity tensor.

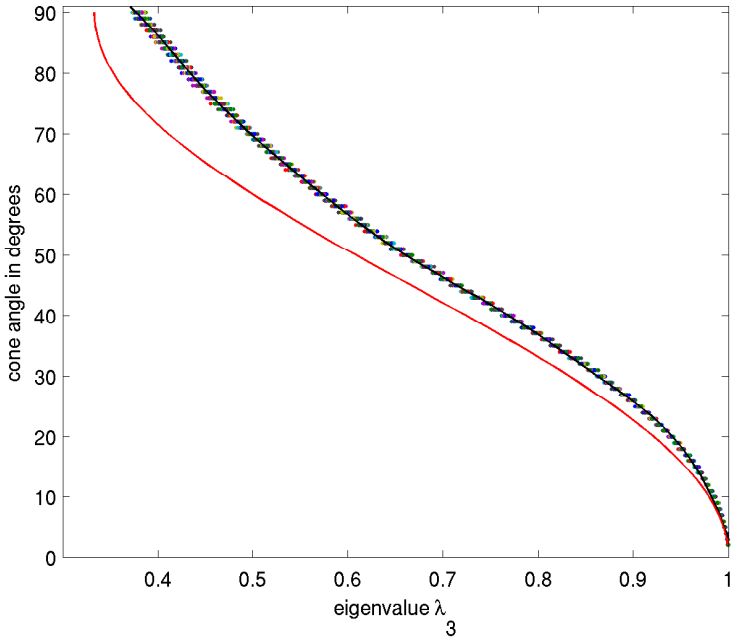

Figure 4.2: The dots in different colours show the eigenvalues λ_3 for the different cone angel φ with 100 calculation of random c-axes per cone angle. The black curve gives the 4th-order polynomial, that was fitted to calculated λ_3 and φ values. The red curve gives the connection between λ_3 and φ given by Wallbrecher (1986).

distribution of c-axes. For each cone angle the vectors within this cone angle were selected. The eigenvalues for this cone angle could then be calculated from these vectors. The process was repeated 100 times for each cone angle φ (dots, Figure 4.2). The calculated $\lambda_3(\varphi)$ values (red curve, Figure 4.2) from the equation given by Wallbrecher (1986) differ by up to 15° for φ. A 4th-order polynomial was fitted to the λ_3–φ values (black curve, Figure 4.2), to have a simpler connection for this relationship. The same was done for the calculation of χ from λ_1 for thick girdles, as well as for the calculation of φ from λ_3 for partial girdles (app. A.1).

In the next step the elasticity tensor can be derived with help of the measured elasticity tensor for a single ice crystal (Table 4.1) and the derived angles χ and φ. For the calculation of the elasticity tensor C_{ij} I follow the idea of Nanthikesan and Sunder (1994). They use the concept of the Voigt (1910) and Reuss (1929) bounds to calculate the elastic moduli of isotropic polycrystals. The concept is generalized to calculate the elasticity tensor for anisotropic fabrics.

The assumption of Voigt (1910) is, that the strain on the polycrystal introduces the same uniform strain in all monocrystals. To calculate the elasticity tensor of the polycrystal one has to average over the elastic tensor C_{ij} of the single crystals. The assumption of Reuss (1929) is that the stress on the polycrystal introduces the same uniform stress in all monocrystals. Here, the compliance tensor of the polycrystal is calculated by averaging over the compliance tensor S_{ij} of the single crystals. The compliance tensor of an crystal is the inverse of the elasticity tensor. In terms of Hook's law (eq. (3.1)) this gives

$$\tau_{mn} = s_{mnop}\sigma_{op}. \tag{4.2}$$

The equations to invert the compliance tensor to obtain the elasticity tensor as well as the equation to invert the elasticity tensor to obtain the compliance tensor are given in appendix A.2. The method of Voigt (1910) and Reuss (1929) is an approximation of the elasticity tensor due to violation of local equilibrium and compatibility conditions across grain boundaries, respectively. Hill (1952) showed that the concept of Voigt (1910) (elasticity tensor of polycrystal C^{V}_{ij}) and Reuss (1929) (elasticity tensor of polycrystal C^{R}_{ij}) give the

	step	rotation axis	angle
cone	1	x_1	$\varphi = \chi$
	2	x_3	90°
partial girdle	1	x_1	φ
thick girdle	1	x_1	90°
	2	x_2	χ

Table 4.2: Steps for calculation of elasticity tensor (eq. (A.20)–(A.22)) or compliance tensor (eq. (A.23)–(A.25)) for different fabrics (Figure 2.2).

upper and lower limit for the elastic moduli of the polycrystal C_{ij}, referred to as Voigt–Reuss bounds.

$$C_{ij}^{\mathrm{R}} \leq C_{ij} \leq C_{ij}^{\mathrm{V}}, \tag{4.3}$$

where the superscripts R and V denote Reuss and Voigt calculation, respectively.

To obtain the elasticity tensor of the anisotropic polycrystal C_{ij}^{p} from the elasticity tensor of the monocrystal C_{ij}^{m} with different orientations one has to integrate the elasticity tensor $C_{ij}^{\mathrm{m}}(\phi)$ with a probability density function $F(\phi)$ for the different c-axes orientations, where ϕ gives the minimum (ϕ_1) and maximum (ϕ_2) extent of the c-axes in the plane. For a uniform distribution

$$F(\phi) = \frac{1}{\phi_2 - \phi_1} \qquad \text{for} \quad \phi_1 \leq \phi \leq \phi_2 \tag{4.4}$$

$$= 0 \qquad \text{for} \quad \phi_2 \leq \phi \leq \pi; -\pi \leq \phi \leq \phi_1, \tag{4.5}$$

which is symmetric around the main orientation, so that $\phi_1 = -\phi_0$ and $\phi_2 = +\phi_0$, the elasticity tensor of the anisotropic polycrystal is calculated by

$$C_{ij}^{\mathrm{p}} = \frac{1}{2\phi_0} \int_{-\phi_0}^{+\phi_0} C_{ij}^{m}(\phi)\mathrm{d}\phi, \tag{4.6}$$

and the compliance tensor is calculated by

$$S_{ij}^{\mathrm{p}} = \frac{1}{2\phi_0} \int_{-\phi_0}^{+\phi_0} S_{ij}^{\mathrm{m}}(\phi)\mathrm{d}\phi. \tag{4.7}$$

The rotation matrices for the elasticity and compliance tensor are given in appendix A.3. Thus, the elasticity tensor and the compliance tensor of the polycrystal can be calculated. After considering the orthorhombic symmetry and some rearranging of the results of equations (4.6) and (4.7) the components of the elasticity tensor and compliance tensor of a polycrystal can be expressed in compact form (app. A.4). Here, a differentiation between the expansions with respect to the different spatial directions x_1, x_2 and x_3 needs to be done.

For the calculation of the elasticity tensor of a partial girdle (Figure 2.2) the elasticity tensor of

the monocrystal C_{ij}^{m} is rotated around the x_1-axis with the opening angle of the partial girdle in x_2-direction (φ). The polycrystal for a partial girdle is calculated using equations (A.20) with $\phi_0 = \varphi$. For a thick girdle φ is 90° to gain a full girdle in the [x_2,x_3]-plane in the first step. In a second step this elasticity tensor obtained for a full girdle is then rotated around the x_2-axis (eq. (A.21)) with $\phi_0 = \chi$. For cone fabrics with different opening angles the elasticity tensor of a monocrystal is rotated around the x_1-axis (eq. (A.20)) in a first step using the cone opening angle ($\phi_0 = \varphi = \chi$) and, afterwards, the obtained elasticity tensor is rotated around the x_3-axis with $\phi_0 = 90°$ (eq. (A.21)). For a better overview, the steps for the different fabrics are listed in Table 4.2. They are as well valid for the compliance tensor with equations (A.23)–(A.25).

Nanthikesan and Sunder (1994) developed the approach to calculate the elasticity tensors for, what they call, S1 (vertical single maximum), S2 (horizontal girdle) and S3 (horizontal partial girdle) ice. They found that the Voigt–Reuss bounds for these fabrics are within 4.2% of each other and concluded from this that either calculation, by means of the elasticity tensor (eq. (4.6)) or compliance tensor (eq. (4.7)), can be used to calculate the elasticity tensor of the polycrystal. Here, this approach is also used for the calculation of thick girdles and cone fabrics. By comparing the individual components of the elasticity tensor with those of the compliance tensor the largest difference of 4.2% can be found for the components C_{44} (S_{44}) of a partial girdle with an opening angle of 50 and 90°. Thus, for all fabrics in this study, the Voigt–Reuss bounds are within 4.2% of each other and I follow Nanthikesan and Sunder (1994) in their argumentation that either calculation can be used. Using the Voigt (1910) calculation no extra step in the calculation is needed to invert the compliance tensor. Thus, for all further calculations the approach by Voigt (1910) is used (eq. (4.6)).

For the calculation of the anisotropic polycrystal from the monocrystal neither grain size nor grain boundaries are considered. Elvin (1996) investigated the number of grains that are necessary to homogenize the elastic properties of the polycrystalline ice and found, that at least 230 grains are needed for S2 ice (girdle). This number of ice crystals should be reached with seismic waves in ice of around 300 Hz, i.e., a wavelength of more than 10 m and ice crystals with $\leq$0.1 m diameter in average. Additionally, Elvin (1996) considered two cases, with and without grain boundary sliding. In absence of grain-boundary sliding the anisotropy mainly defines the elastic behaviour. Otherwise, grain shape and grain-boundary sliding become important as well. A certain mistake is, thus, made for the calculation of the polycrystal by only considering anisotropy.

4.2.1 Velocities for anisotropic ice

By deriving the elasticity tensor for different fabrics the group and phase velocities of P-, SH- and SV-wave for these fabrics can now be calculated. Figures 4.3 and 4.4 show the P- and SH-wave phase velocity, respectively, for different cone and girdle fabrics calculated with the equations given in section 3.3.1 and the equations derived by Bennett (1968) for a solid cone (sec. 3.3.2). The phase velocity for the SV-wave as well as the corresponding group velocities are displayed in appendix A.5.

The subfigure (d) in Figure 4.3 and 4.4 shows the velocities calculated from the equations derived by Bennett (1968) for a solid cone from the elasticity tensor he measured at −10°C corrected to −16°C (sec. 4.4). The other subfigures are phase velocities calculated with the

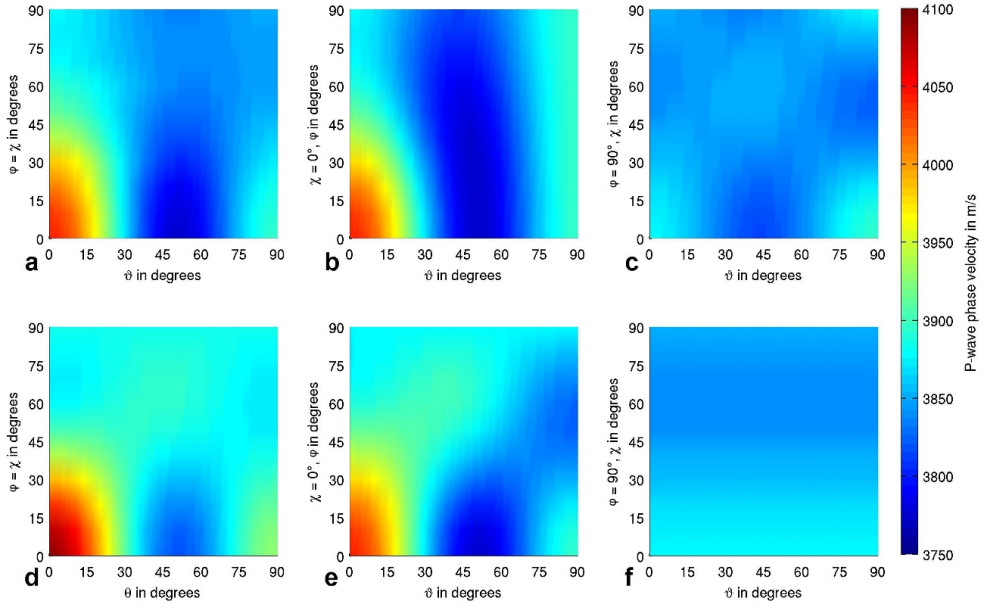

Figure 4.3: P-wave phase velocities over phase angle ϑ for different fabrics. P-wave velocity for (a) different cone opening angles ($\varphi = \chi$), (b) partial girdle ($\chi = 0°$) and (c) thick girdle ($\varphi = 90°$) within the [x2,x3]-plane, (e) partial girdle ($\chi = 0°$) and (f) thick girdle ($\varphi = 90°$) within the [x1,x3]-plane calculated with equation (3.20) given by Daley and Krebes (2004). (d) shows the P-wave velocity for different cone opening angles ($\varphi = \chi$) calculated with equation (3.33) given by Bennett (1968).

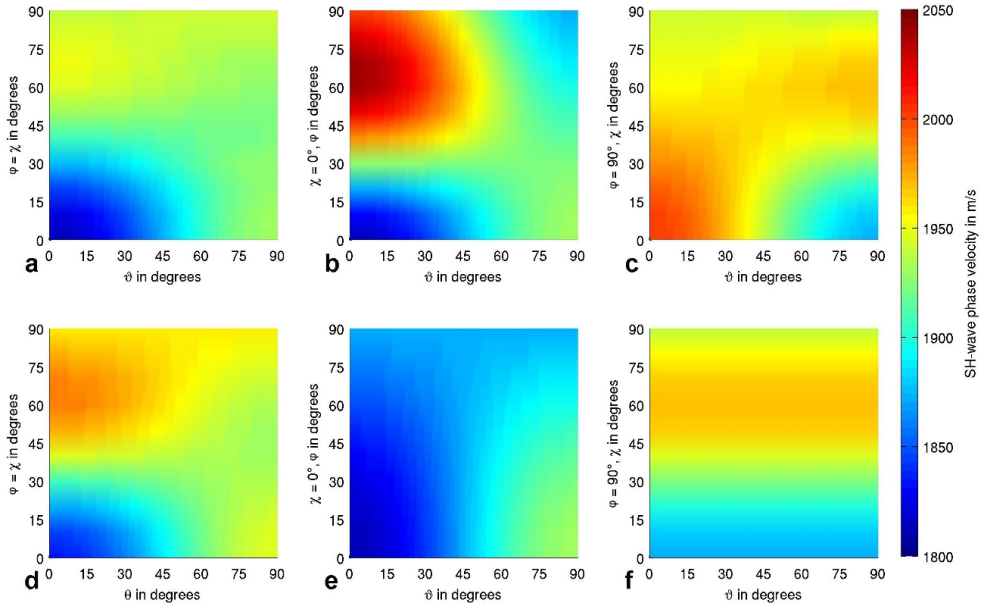

Figure 4.4: SH-wave phase velocities over phase angle ϑ for different fabrics. SH-wave velocity for (a) different cone opening angles ($\varphi = \chi$), (b) partial girdle ($\chi = 0°$) and (c) thick girdle ($\varphi = 90°$) within the [x2,x3]-plane, (e) partial girdle ($\chi = 0°$) and (f) thick girdle ($\varphi = 90°$) within the [x1,x3]-plane calculated with equation (3.22) given by Daley and Krebes (2004). (d) shows the SH-wave velocity for different cone opening angles ($\varphi = \chi$) calculated with equation (3.34) given by Bennett (1968).

equations given in section 3.3.1 from an elasticity tensor derived following the steps in Table 4.2 with the elasticity tensor measured by Gammon et al. (1983) at −16°C. The top rows (Figure 4.3 and 4.4) show velocities for cone fabric (a, VTI) as well as partial girdle fabric (b, HTI, [$x2$,$x3$]-plane) and thick girdle fabric (c, HTI, [$x2$,$x3$]-plane) in the [$x2$,$x3$]-plane, while the bottom rows show velocities for cone fabric calculated following Bennett (1968) (d, VTI, Bennett (1968)) as well as partial girdle fabric (f, $\psi = 90°$, [$x1$,$x3$]-plane) and thick girdle fabric (e, $\psi = 90°$, [$x1$,$x3$]-plane) in the [$x1$,$x3$]-plane.

The partial girdle (b, e) with $\varphi = 90°$ displays the same fabric as the thick girdle (c, f) with $\chi = 0°$. The cone fabric with an opening angle of 90° (a, d) as well as the thick girdle with $\chi = 90°$ (c, f) show the isotropic state. Apart from the Bennett (1968) velocities, these velocities for the isotropic state (a, c, f) are obviously not isotropic. Slight variations still exist for these velocity with increasing incoming angle. This is due to artifacts that appear due to the derivation of the elasticity tensor for the isotropic state using the single crystal elasticity tensor.

It should also be noted, that for a thick girdle with $\varphi = \chi = 90°$ the variations over the incoming angle are just reversed to that of the cone fabric with opening angle $\varphi = \chi = 90°$. This reflects the difference in the calculation of the elasticity tensor from cone fabric and girdle fabric. While a girdle with $\varphi = 90°$ ($\chi = 0°$) is calculated in the first step for both fabrics (Table 4.2) by integration with rotation around the x_1-axis, the second step is an integration with rotation around the x_3-axis for the cone fabric and around the x_2-axis for the thick girdle fabric.

The higher velocities calculated with the equations of Bennett (1968) (subfigure d) are due to the difference in the elasticity tensor as the elasticity tensor derived by Gammon et al. (1983) was used for the other subfigures (a–c, e, f). The Bennett (1968) calculation exhibits isotropic state for $\varphi = \chi = 90°$. However, this is only possible due to the fitting of curves Bennett (1968) used for the derivation of the slowness surface.

An often used concept for the investigation of earth mantle anisotropy in seismology is that of S-wave splitting. If an S-wave in isotropic material reaches a boundary towards anisotropic material it is split into to perpendicularly polarized S-waves (Yilmaz, 2001). Due to the different polarisation directions these two S-waves travel with different speed in anisotropic media. Thus, their traveltimes can give information about the existing anisotropy. In the case of cone fabric the zero-offset velocities of SH- and SV-wave ($v_{\mathrm{sh0}} = v_{\mathrm{sv0}} = v_{\mathrm{s0}}$) are the same. Here, the difference in traveltime is only observable for increasing offset. In case of a full girdle ($\varphi = 90°$, $\chi = 0°$, HTI) the difference in the zero-offset velocity between SV-wave (2003 m/s) and SH-wave (1873 m/s) is 7%. However, in our data sets neither converted S-waves, nor S-wave splitting could be observed.

4.2.2 Differences in calculation of δ

In the case of weak anisotropy ($\delta \ll 1$) the Thomsen parameter δ can be calculated from the P-wave velocity instead of the elasticity tensor (eq. (3.11))

$$\delta_{\mathrm{vel}} = 4\left[\frac{v_{\mathrm{p}}(45°)}{v_{\mathrm{p0}}} - 1\right] - \left[\frac{v_{\mathrm{p}}(90°)}{v_{\mathrm{p0}}} - 1\right]. \tag{4.8}$$

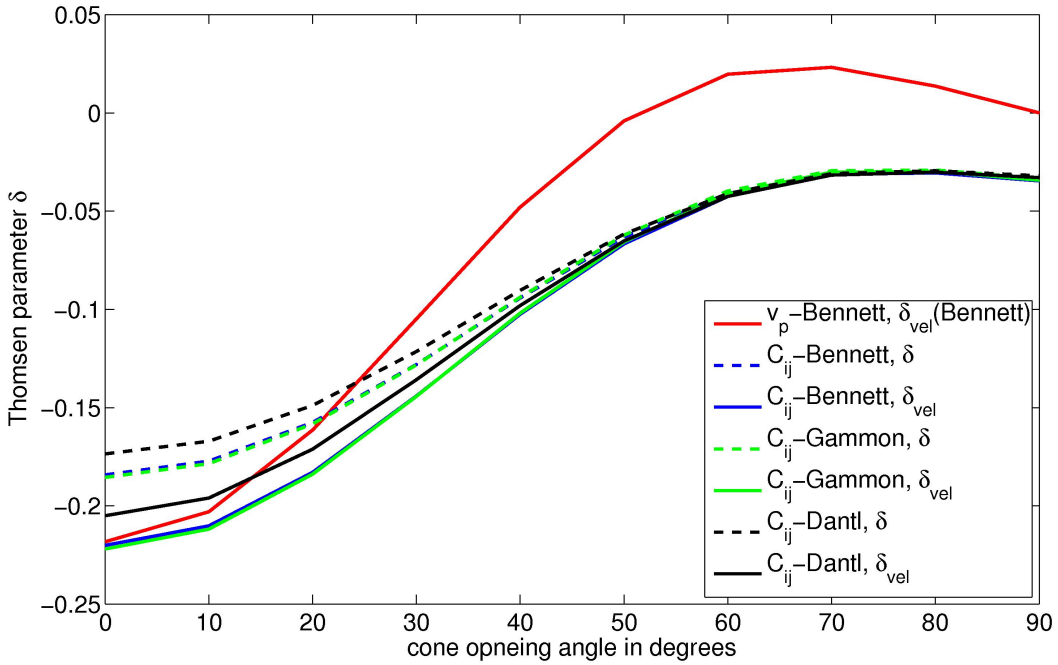

Figure 4.5: Calculation of the Thomsen parameter δ for different cone opening angles ($\varphi = \chi$) and elasticity tensors (Bennett, 1968; Gammon et al., 1983; Dantl, 1968, blue, green, black, respectively), either directly from the elasticity tensor (dashed lines) or from the derived velocities (eq. (4.8), solid lines). The red curve gives the Thomsen parameter δ_{vel} calculated from the Bennett (1968) velocity (eq. (3.33)).

This approach was used to calculate δ_{vel}-values from the velocities derived by Bennett (1968) (eq. (3.33)) for different cone opening angles. For comparison, δ_{vel}-values from P-wave velocities (eq. (3.20)) calculated from the derived polycrystal elasticity tensor for these cone fabrics using the monocrystal elasticity tensors of Bennett (1968); Gammon et al. (1983) and Dantl (1968) are shown in Figure 4.5 (solid lines). Additionally, δ-values that were directly calculated from the polycrystal elasticity tensors are plotted (eq. (3.11)) in Figure 4.5 (dashed lines).

The parameter δ depends, of course, on the monocrystal elasticity tensor (Bennett, 1968; Gammon et al., 1983; Dantl, 1968) used for the calculations of the elasticity tensor for the different cone opening angles. The elasticity tensors of Bennett (1968) and Gammon et al. (1983) both show similar results for the calculation of the parameter δ, whereas the elasticity tensor of Dantl (1968) yields weaker anisotropy for VSM-fabric of about 8%. The difference between the dashed and solid lines with the same color shows the error made by calculating δ_{vel} using the P-wave velocities (eq. (4.8)) instead of the more exact equation of δ using the elasticity tensor (eq. (3.11)). For cone opening angle $\geq 50^\circ$ the calculations using the velocities are still exact. Towards stronger anisotropy the differences between δ_{vel} and δ increases to a difference of 16% for a VSM-fabric ($\varphi = \chi = 0^\circ$). For large opening angles φ, i.e. isotropy, δ should converge to zero. Obviously, this is not the case. This is related to the calculation of the elasticity tensor for a cone opening angle of $\varphi = \chi = 90^\circ$ from the single crystal.

The difference between the red solid line and the blue solid line (Figure 4.5) shows the difference in calculation of the velocity following Bennett (1968) and the calculation with

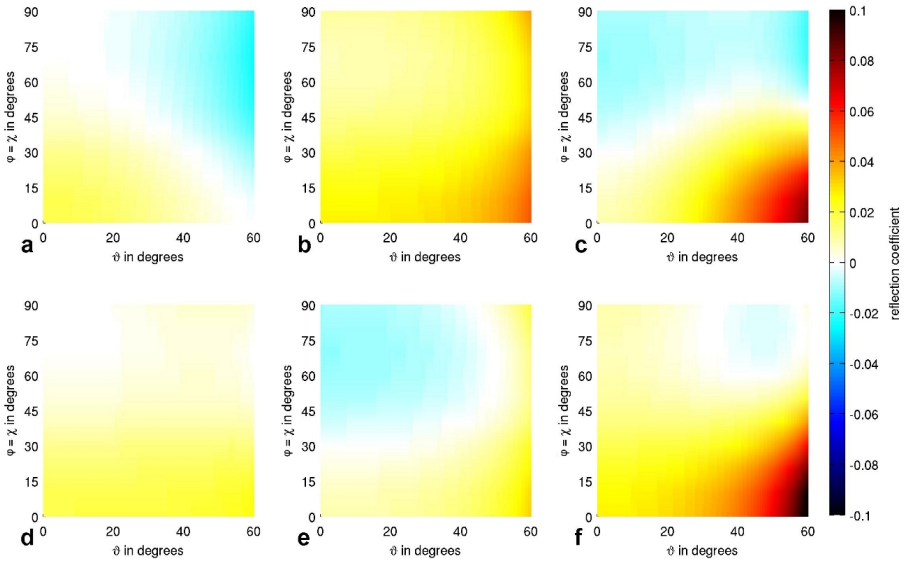

Figure 4.6: Reflection coefficients for the boundary between an isotropic (upper) layer and a partial girdle fabric (lower) layer with different opening angles φ ($\chi = 0°$) of the girdle. The reflection coefficients are calculated with equations given in section 3.4 for different incoming angles ϑ. The subfigures (a), (b) and (c) show the reflection coefficients for a girdle orientation (lower layer) perpendicular to the travelpath of the wave (HTI media) for PP-, SHSH- and SVSV-reflection, respectively. The subfigures (d), (e) and (f) show the reflection coefficients for a girdle orientation parallel to the travelpath of the wave (azimuth $\psi = 90°$) for PP-, SHSH- and SVSV-reflection, respectively.

help of the elasticity tensor introduced in this work. For a VSM-fabric the δ-value is nearly the same, whereas they differ strongly for larger cone opening angles. Using the Bennett (1968)-velocities δ becomes zero for a cone opening angle of 52°, positive for cone opening angles of $\geq 52°$ and zero again for isotropic material. In contrast, the δ-values calculated from the derived polycrystal elasticity tensor does not reach isotropic state for a cone opening angle of 90°.

4.2.3 Reflection coefficients for anisotropic ice

The main focus of this work is on the influence of anisotropy on the traveltime. Nevertheless, this section touches on the possibility to calculate the reflection coefficient by gaining the elasticity tensor for the different anisotropic fabrics. With the equations given in section 3.4 reflection coefficients can be calculated for different fabric transitions. A large amount of fabric combinations is possible here. Figure 4.6 and 4.7 show two examples: first the transition at a layer interface from isotropic state to a partial girdle fabric with different opening angles φ and second for the transition at a layer interface from a full girdle to a cone fabric, both for HTI media ($\psi = 0°$) and with an azimuth of $\psi = 90°$.

The reflection coefficients are given for angles of incidence between 0° and 60°. This has two reasons. Firstly, most seismic surveys do not exceed an incoming angle of 60° as this already corresponds to a large offset. Secondly and more important, the calculation of the reflection coefficients using equations (3.43)–(3.44) is not exact. Thus, the error increases

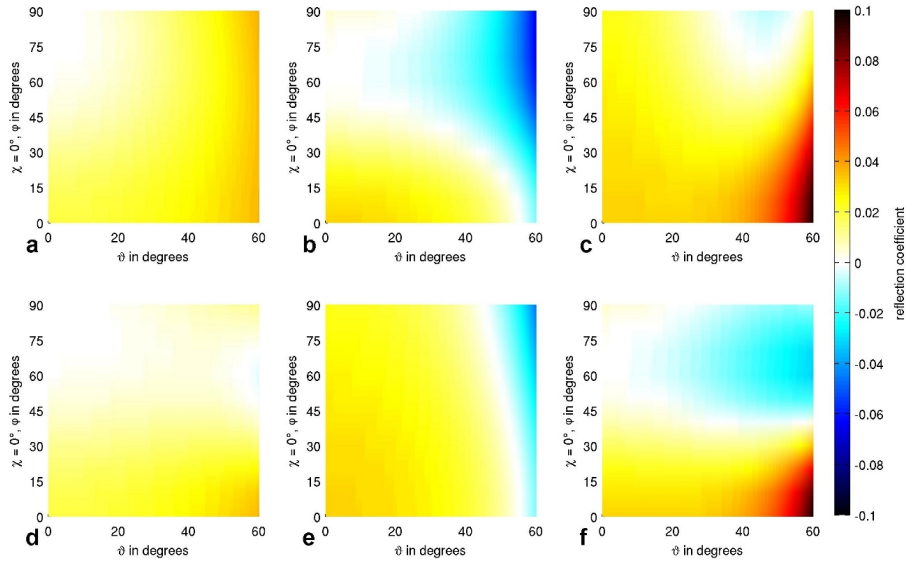

Figure 4.7: Reflection coefficient for the boundary between a girdle fabric (upper) layer and a cone fabric (lower) layer with different opening angles $\varphi = \chi$. The reflection coefficients are calculated with equations given in section 3.4 for different incoming angles ϑ. The subfigures (a), (b) and (c) show the reflection coefficients for a girdle orientation (upper layer) perpendicular to the travelpath of the wave (HTI media) for PP-, SHSH- and SVSV-reflection, respectively. The subfigures (d), (e) and (f) show the reflection coefficients for a girdle orientation parallel to the travelpath of the wave (azimuth $\psi = 90°$) for PP-, SHSH- and SVSV-reflection, respectively.

with increasing incoming angle.

The transition from isotropic state to VSM-fabric is shown in Figure 4.6 with $\varphi = 0°$ (ordinate). The largest reflection coefficients can be observed for the SVSV-reflection. However, the reflection coefficients is $\leq$0.1 for all fabric combinations shown here. Especially for the PP-reflection the reflection coefficients between different anisotropic fabrics are small. The PP-reflection between isotropic and VSM-fabric ice for normal incident is $<$0.02. For comparison the reflection coefficient between isotropic and lithified sediments (Figure 4.8) is $\sim$0.4. Hence, reflection coefficients at the ice-bed interface are an order of magnitude larger than reflection coefficients for the transition between different anisotropic fabrics. To be able to observe englacial seismic reflections abrupt changes (i.e., within a wavelength) with significant variations in the orientation of the ice crystals are needed.

Of special interest in glaciology is the ice-bed interface. It is possible to determine the bed properties below an ice sheet or glacier by analysing the normal incident reflection coefficient (e.g. Smith, 2007) or the AVO variations (Anandakrishnan, 2003; Peters et al., 2008). Figure 4.8 shows reflection coefficients for the transition from isotropic and anisotropic (VSM-fabric) ice to different possible bed properties. The properties, P-wave, S-wave velocity and density, for the different bed scenarios and the isotropic ice are taken from Peters et al. (2008). For the anisotropic VSM-fabric the elasticity tensor of Gammon et al. (1983) is used.

Exact solutions are calculated using the equations given by Graebner (1992), with corrections by Rüger (2002). Their equations were used to calculate the exact reflection coefficients for the isotropic ice above the bed (solid lines red, black, blue and light green) and for the anisotropic ice above the bed (dashed lines red, black, blue and light green). The

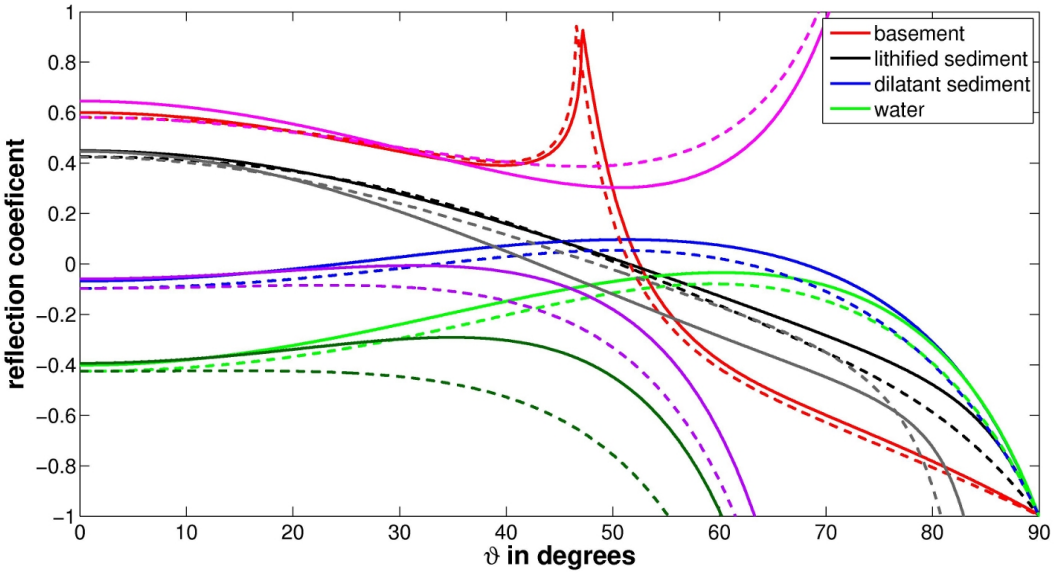

Figure 4.8: Reflection coefficients for ice-bed interface with different bed properties: basement (red, magenta), lithified sediments (black, grey), dilatant sediments (blue, purple) and water (light, dark green). The solid lines are the reflection coefficients for an isotropic ice overburden, the dashed lines for the anisotropic overburden. The red, black, blue and light green lines are the reflection coefficients calculated with exact equations in VTI media given by Graebner (1992) and Rüger (2002). The magenta, gray, purple and dark green lines are approximate calculations following the approach by Aki and Richards (2002) for the isotropic and that of Rüger (1997) for the anisotropic case. Bed property values for bed and isotropic ice are taken from Peters et al. (2008), for the anisotropic ice the elasticity tensor given by Gammon et al. (1983) is used.

material	v_p in m/s	v_s in m/s	ρ in kg/cm^3
ice	3810	1860	920
basement	5200	2800	2700
lithfied sediment	3750	2450	2450
dilatant sediment	1700	200	1800
water	1498	0	1000

Table 4.3: P- and S-wave velocity as well as density for different bed scenarios and isotropic is as given in Peters et al. (2008).

approximate reflection coefficients for the isotropic ice above the bed (solid lines magenta, gray, purple and dark green) are calculated using equations given in Aki and Richards (2002). The approximate reflection coefficients for the VSM-fabric above the bed (dashed lines magenta, gray, purple and dark green) are calculated using equations given in Rüger (1997).

The differences between the isotropic (solid lines) and anisotropic reflection coefficients (dashed lines) are small ($\leq$0.04) for the exact solutions. The approximate calculations fit well up to a group angle of about 30°, with differences in the same order as isotropic to anisotropic variations. However, differences between exact and approximate reflection coefficients become large for increasing group angle ($\geq$30°). Thus, errors introduced by using approximate calculations for the reflection coefficients are larger than the effect of anisotropic ice fabric above the bed.

Peters et al. (2008) analysed the reflection amplitude from a survey near the South Pole. For the reflection coefficients they derive from the seismic data they give error bars $\geq \pm 0.04$, with increasing error bars for decreasing incoming angels, up to $\pm$0.2. However, the variation observable for reflection coefficients between an isotropic and a VSM-fabric overburden are $\leq$0.04. The VSM-fabric is the strongest anisotropy expectable in ice. If an anisotropic layer exist above the bed, it influences the reflection coefficient compared to the isotropic ice overburden. However, the difference between the isotropic overburden reflection coefficient and the anisotropic overburden reflection coefficient is within the range of the error bars given by Peters et al. (2008). Thus, the anisotropic fabric will not have an influence on the analysis of the bed properties.

For englacial reflections caused by changing COF the variations in the reflection coefficient with offset are very small. The variation of the PP-reflection coefficient for the transition from isotropic to VSM-fabric ($\varphi = 0°$, Figure 4.6) from 0° to 60° is only between 0.019 and 0.036. It cannot be expected that error bars determining the reflection coefficient of englacial reflections would be smaller than those given for the bed reflection coefficients ($\geq \pm 0.04$; Peters et al., 2008). However, the change in the reflection coefficient with offset for englacial reflection is smaller than the given error bars. Thus, it is very unlikely that it is possible to derive information about the anisotropic fabric from englacial reflections using AVO analysis. To be able to derive fabric information from AVO analysis the error in determining the reflection coefficient from seismic data needs to be reduced. This would be possible by, e.g., better shooting techniques to reduce the signal-to-noise ratio (SNR) in the data or a better understanding of the source amplitude as well as the damping of seismic waves in ice.

4.3 Influence of density on seismic wave propagation

The strongest influence on the wave velocity of seismic waves in ice is caused by the density gradient within the firn column. P-wave velocities for the upper layers are around 800 to 1000 m/s. Due to the density gradient seismic waves in firn are continuously refracted. Thus, these so-called diving waves dive through the firn pack. The dependency of seismic P-waves on density in firn was investigated by Robin (1958) and Kohnen (1972). Robin (1958) gives a linear relationship between P-wave velocity and firn density. The equation derived by Kohnen (1972) is more exact for densities towards the ice density and is widely

used in seismic studies on ice. The density ρ in kg/m^3 is then given by

$$\rho = \frac{\rho_{\text{ice}}}{1 + \left[(v_{\text{p,ice}} - v_{\text{p}})/2250\right]^{1.22}} \tag{4.9}$$

with the velocity $v_{\text{p,ice}}$ of isotropic ice in m/s. Kohnen (1972) gives a value of $\rho_{\text{ice}} = 915$ kg/m^2. The increasing velocity is given in relation to the increasing density. This means, that the elastic moduli in firn increase even stronger than the density.

Analysing compressional diving waves the Herglotz-Wiechert inversion can be used to derive a velocity–depth profile of the firn column (Kirchner and Bentley, 1990; King et al., 2004; Diez et al., 2013). It can then be used with help of the formula given by Kohnen (1972) to derive a density–depth profile of the firn column.

For forward calculation of seismic velocities in an ice sheet or glacier the firn part needs to be taken into account. For the analysis of seismic data form Antarctica and the Swiss Alps in Chapters 8 and 9 not only P-waves but also SH-waves are considered. Thus, an equation was required for the relationship between S-wave velocity and density. Such a relationship was derived from SH-wave data of a survey carried out on Colle Gnifetti in 2010 (Diez et al., submitted). The analysis of the diving waves and the derivation of the S-wave–density relationship as well as the discussion of this result can be found in Chapter 8.1.1. I provide the result here already in the context of velocities. The density can be calculated from the S-wave velocity by

$$\rho = \frac{\rho_{\text{ice}}}{1 + [(v_{\text{s,ice}} - v_{\text{s}})/950]^{1.17}} \tag{4.10}$$

with the S-wave velocity of ice $v_{\text{s,ice}}$ in m/s.

4.4 Influence of temperature on seismic wave propagation

The seismic wave velocity is not only influenced by the density and anisotropic fabric but also by the temperature gradient in the ice sheet. Most of the elasticity tensors were measured at -16°C (Table 4.1). To be able to compare calculated velocities with measured seismic data the velocities need to be corrected for the existing temperatures within the glacier or ice sheet.

Different measurements were carried out to investigate the dependence of seismic wave velocities on temperature. Most studies determine a gradient Δv_ζ to correct P- and S-wave velocity measured at temperature $\mathfrak{T}_{\text{m}}$ for the temperature $\mathfrak{T}$.

$$v_\zeta(\mathfrak{T}) = v_\zeta(\mathfrak{T}_{\text{m}}) + \Delta v_\zeta(\mathfrak{T} - \mathfrak{T}_{\text{m}}). \tag{4.11}$$

Here, laboratory measurements (Bass et al., 1957; Robin, 1958; Brockamp and Querfurth, 1964; Vogt et al., 2008; Helgerud et al., 1968), with gradients of -2.2 to -3.4 m s^{-1}K^{-1} for the P-wave and -1.1 to -1.43 m s^{-1}K^{-1} for the S-wave, show slightly lower values than in-situ measurements (Thiel and Ostenso, 1961; Brockamp and Kohnen, 1965; Thyssen, 1966; Kohnen, 1974), with gradients of -3.4 to -7.4 m s^{-1}K^{-1} for the P-wave and -1.2 to -3.6 m s^{-1}K^{-1} for the S-wave (Table 4.4).

	Δv_p	Δv_s		Δv_p	Δv_s
Thiel and Ostenso (1961)	-7.4	-3.4	Bass et al. (1957)	-3.4	-1.4
Brockamp and Kohnen (1965)	-5.5	-3.6	Robin (1958)	-2.3	
Thyssen (1966)	-4.5		Brockamp and Querfurth (1964)	-2.2	-1.1
Kohnen (1974)	-2.3 ± 0.17	-1.20 ± 0.03	Vogt et al. (2008)	-2.81 ± 0.01	-1.43 ± 0.03
			Helgerud et al. (1968)	-2.67 ± 0.05	-1.24 ± 0.01

Table 4.4: Gradients derived in different studies for the dependency of P-and S-wave to the temperature with $[\Delta v_\zeta]$= m s^{-1}K^{-1}.

Of special interest are the works of Dantl (1968) and Gammon et al. (1983) that give dependencies for the components of the elasticity tensor on the temperature. Dantl (1968) derived quadratic equations for the components of the elasticity and compliance tensor in dependence of the temperature from measurements between -0.7 and -140°C. A linearized version of these equations for the elasticity tensor is given by Gammon et al. (1983),

$$C_{ij}(\mathfrak{T}) = C_{ij}(\mathfrak{T}_m)\frac{1 - a\mathfrak{T}}{1 - a\mathfrak{T}_m}. \tag{4.12}$$

From their measurements of the elasticity tensor between -3°C and -16°C they derive $a = 1.418 \cdot 10^{-3}$ K^{-1} while Dantl (1968) derives $a = 1.427 \cdot 10^{-3}$ K^{-1} from his measurements. Gammon et al. (1983) additionally derive a similar expression for the P-wave velocity

$$v_p(\mathfrak{T}) = v_p(\mathfrak{T}_m)\frac{1 - b\mathfrak{T}}{1 - b\mathfrak{T}_m}, \tag{4.13}$$

with $b = 6.196 \cdot 10^{-4}$ K^{-1}. By algebraic manipulations this equation can be transformed into the gradient form of equation (4.11):

$$v_p(\mathfrak{T}) = v_p(\mathfrak{T}_m) + b \cdot v_p(0°C)(\mathfrak{T}_m - \mathfrak{T}), \tag{4.14}$$

so that the velocity gradient is given by $\Delta v_p = b \cdot v_p(0°C)$. In other words, the gradient Δv_p depends on the 0°C-velocity, which is different for the different anisotropic fabrics. Thus, gradients between 2.48 m s^{-1}K^{-1}, with the upper boundary of a 0°C-velocity for a VSM-fabric with 0° incoming angle, and 2.31 m s^{-1}K^{-1}, with the lower boundary of a 0°C-velocity for a VSM-fabric with 51° incoming angle can be derived from the Gammon et al. (1983) values.

Furthermore, Petrenko and Withworth (1998) altered the equation of Gammon et al. (1983) to

$$C_{ij}(\mathfrak{T}) = C_{ij}\mathfrak{T}_m(1 - a(\mathfrak{T} - \mathfrak{T}_m)). \tag{4.15}$$

Equations (4.12) and (4.15) are not exactly the same but results are within 0.5%. Thus, the differences are negligible.

In the analyses of seismic data from Antarctica and the Swiss Alps (Ch. 7, 8 and 9) the temperature correction is always done on the elasticity tensor using equation (4.12) if possible. Otherwise, the gradients given by Kohnen (1974) are used.

5 Radar

Radar measurements are extensively used to study ice sheets by analysing coherent reflections and incoherent backscatter of electromagnetic waves. This chapter gives a brief introduction to the propagation of radar waves in ice, with special focus on the influence of the anisotropic COF on the radar waves. For an introduction of radar wave propagation see the works of, e.g., Telford et al. (1990); Knödel et al. (2005); Reynolds (2011) and with special respect to radar application on glaciers and ice sheets see, e.g., Plewes and Hubbard (2001); Dowdeswell and Evans (2004); Bingham and Siegert (2007); Navarro and Eisen (2009).

The radio-echo sounding (RES) or ground penetrating radar (GPR) method has primarily been used to investigate the thickness of glaciers and ice sheets for mass balance studies. The usefulness of radar for the investigation of the ice thickness and bed topography was discovered when air planes flying over Antarctica and Greenland observed problems with their radar altimeters as the cold ice was largely transparent for the high frequency electromagnetic waves. It was discovered that, beside the reflection from the ice-bed interface, englacial reflectors could be observed, caused by changes in density, impurities (salt and acids) or changes in COF. A lot of these layers, caused by variations of impurities during the deposition of the snow, are isochronous layers, i.e., layers of equal age. Thus, these signals can be used to track layers over large distances and retrieve information about accumulation patterns. In the following, I will refer to GPR measurements as those carried out with a sled on the ground, and RES measurements as those done from an airplane.

To map the basal typography and internal reflection horizons (IRH) with a radar system one transmitter and only one receiver are used, in contrast to seismic measurements were mostly one source and numerous receivers are deployed. Transmitter and receiver are then moved over the surface with a fixed distance (common offset), either directly on the snow surface behind, e.g., a snowmobile or on a plane for efficient surveying of larger areas. Other applications like borehole radar and common midpoint (CMP) surveys are also carried out, but not used here and, thus, not discussed further. From the transmitter an electromagnetic pulse is emitted, attenuated during propagation in the ice, partially reflected at layer boundaries and afterwards recorded at the receiver antenna. In case of an impulse radar the pulse contains about one to three cycles of a center frequency determined by the characteristics of the special radar system with a certain bandwidth (Plewes and Hubbard, 2001; Navarro and Eisen, 2009). Theoretically, the vertical resolution of the radar system is then determined by a quarter wavelength ($\lambda/4$) of the emitted pulse for radar systems where no phase information is recorded. However, in reality the resolution is rather half of a wavelength (Sheriff and Geldart, 1995). Hence, the resolution increases with smaller wavelength but at the same time the penetration depth decreases due to stronger attenuation for the signals with smaller wavelength. The distance between transmitter and receiver is normally small, $<$1 m for GPR and $\sim$10 m for RES measurements (for common offset surveys). Hence, the traces are regarded as being zero-offset.

From the recorded electromagnetic waves information can be gained about the subsurface. The velocity and reflection coefficient of the electromagnetic wave are determined by the complex relative permittivity ϵ

$$\epsilon = \epsilon' - i\epsilon'', \tag{5.1}$$

which depends on the real part, the relative permittivity (ϵ') and the imaginary part, the relative dielectric loss factor (ϵ'') (e.g., Knödel et al., 2005). Note that ϵ is the complex relative permittivity here and not the complex effective permittivity, i.e., the complex effective permittivity would be given by $\epsilon \cdot \epsilon_0$ (ϵ_0 vacuum permittivity). For a low-loss medium ($\epsilon''/\epsilon' \ll 1$) like ice the propagation velocity can be approximated as

$$v_\mathrm{r} \approx \frac{c_0}{\sqrt{\epsilon'}} \tag{5.2}$$

with c_0 the wave speed in vacuum and values for ϵ' in ice between 3.1–3.2 (Bohleber et al., 2012). To account for the density variation within the firn a relation was derived by Kovacs et al. (1995) relating the relative permittivity in snow and firn to the density ρ (in kg/m^3)

$$\epsilon' = (1 + 0.000845\rho)^2. \tag{5.3}$$

The amplitude reflection coefficient for vertical incidence between two media (upper and lower media, 1 and 2, respectively) with the relative permittivities ϵ_1 and ϵ_2 can be calculated from

$$R = \frac{\sqrt{\epsilon_1} - \sqrt{\epsilon_2}}{\sqrt{\epsilon_1} + \sqrt{\epsilon_2}}. \tag{5.4}$$

If the velocity is known (in ice ≈167 m μs^{-1}, Plewes and Hubbard (2001)) the depth of the reflections can be calculated. If the penetration depth is large enough to reach the ice–bed interface the thickness of the glacier and ice sheet can, thus, be calculated. Additionally, the depth of isochronous layers can be determined over large areas. When the age of the layer is known the accumulation rate and the density distribution can be determined or equal layers from different ice cores can be linked by following these isochronous signals.

5.1 Radar in anisotropic ice

Similar to seismic waves the reflection coefficient and the velocity of radar waves are influenced by an aligned orientation of the anisotropic ice crystals. Often it is difficult to distinguish reflections caused by changing COF from the large amount of reflections caused by conductivity contrasts due to changing impurities.

Fujita et al. (2000) derived, for the relative permittivity, a difference between waves travelling parallel ($\parallel$) and perpendicular ($\perp$) to the ice crystal c-axis of $\Delta\epsilon'_{\parallel,\perp} = \epsilon'_\parallel - \epsilon'_\perp \approx 0.035$. Using equation (5.2) this gives a difference in velocity for waves travelling parallel and perpendicular to the ice crystal c-axis of ∼0.001 m μs^{-1}. Hence, the change in radar wave velocity caused by changing COF is smaller than 1%. These COF induced variations of the velocity depend slightly on the temperature.

The influence on the power reflection coefficient of changing COF can be calculated with

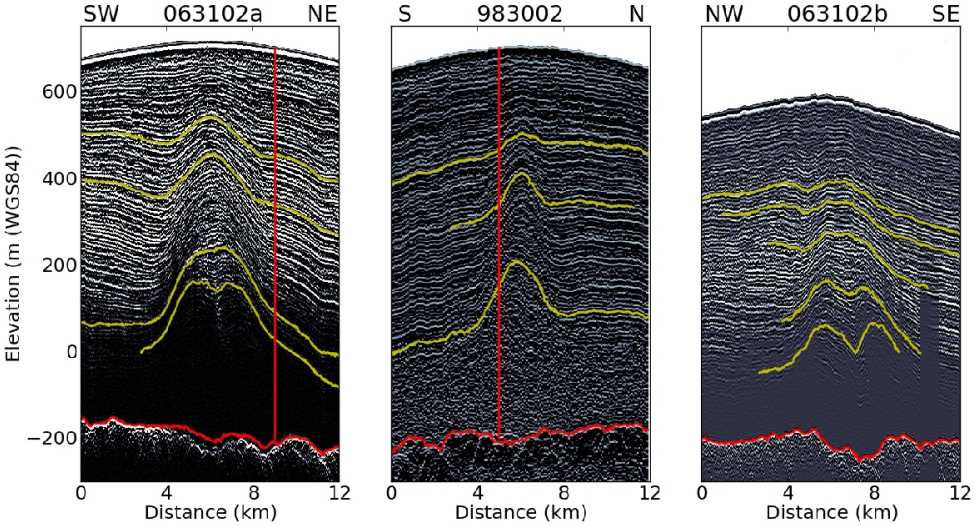

Figure 5.1: RES profiles from Halvfarryggen ice dome, Dronning Maud Land, Antarctica (sec. 6.2). Figure from Drews et al. (2013), with the two profiles 063102a and 983002 crossing each other at the vertical red lines and 063102b about 15 km south-west of these profiles along the ice divide. The yellow lines indicate picked horizons, the red lines the ice-bed interface. Line 063102 a and b show a double bump developed at a depth of ∼510 m and 370 m, respectively.

the approximation derived by Paren (1981)

$$|R_\mathrm{r}| = \left(\frac{\Delta\epsilon'}{4\epsilon'}\right)^2, \tag{5.5}$$

with $\Delta\epsilon' = \epsilon'_1 - \epsilon'_2$ the difference of the relative permittivity between the upper (ϵ'_1) and lower (ϵ'_2) layer. To calculate the velocity and reflection coefficient of the radar wave for anisotropic material the relative permittivity ϵ' can be calculated from the COF eigenvalues λ_i with $\epsilon' = \epsilon'_\perp + \Delta\epsilon'\lambda_i$ (Eisen et al., 2007). Hence, the strongest possible reflection would be between a VSM-medium and a medium with all c-axes in the horizontal plane, corresponding to a power reflection coefficient of −51 dB. For comparison, an ice-water interface would cause a power reflection coefficient of −3.5 dB ($\epsilon'_{water} \approx 82$).

A direct evidence of developed anisotropic ice fabric in radar data are the anisotropic features at a Raymond bump, like double bump and synclines at the flanks (Figure 5.1). Modeling these features was possible by including anisotropic ice fabric into a full-Stocks model (Martin et al., 2009; Drews et al., 2013). The isochronous layers in the radargram clearly show the double bump features and synclines. However, this does not give information about the kind of existing anisotropy. It only indicates that some kind of developed anisotropic ice fabric exists.

To be able to identify COF reflectors in radar sections multi-frequency and multi-polarisation studies are used. Eisen et al. (2007) were able to link a single radar reflector to changing COF by multi-polarisation measurements at Kohnen station, Dronning Maud Land, Antarctica. The same data were used by Drews et al. (2012) to investigate a change in backscatter over depth and the different polarisations for changes in anisotropic bubble orientation and

changes in COF. Multi-polarisation measurements were also done by Matsuoka et al. (2012) in the area of the West Antarctic Ice Sheet (WAIS) divide, finding a shift in the girdle azimuth over depth indicating a non-stable ice divide. Further investigation of radar data for the influences of anisotropy include the analyses of the effect of birefringence caused by the anisotropic ice crystal (Matsuoka et al., 2009).

Whether radar reflectors due to changing COF are isochronous layers is not yet clear. A study by Kennedy et al. (2013) investigated whether variations in COF induced by climate variations within the snow and firn could be preserved over time. They model the evolution of the fabric over time and find that signals induced by climate variations at the surface may very well be preserved. In this case, the radar reflector caused by changing COF would be an isochronous layer.

5.2 Potential to combine seismics and radar

Seismic, i.e., elastic waves as well as electromagnetic waves are influenced by an aligned orientation of the anisotropic ice crystals. However, the influence on the wave propagation and, thus, velocity and reflection coefficients, is quite different as well as the cause of further coherent signals in the data sets. Thus, seismic and radar data yield the potential to complement each other in the analysis of COF distribution.

In both cases, to be able to analyse the changes of the properties over depth, abrupt changes in the properties are needed to cause distinct reflections. The largest influence on seismic waves in ice is from

- density,
- COF, and
- temperature,

while radar waves are mainly influenced by

- density,
- conductivity,
- COF, and
- temperature (by influencing the liquid water content).

For the upper 100 m, depending on the location and the thickness of the firn pack, variations in the density have the largest influence on seismic and radar waves. In both cases, the wave velocities are strongly influenced by the low densities of the snow. Ice lenses and layers caused by summer melt events can cause clear reflections. For both, seismics and radar, empirical equations exist for the connection of density and wave velocity, equations (4.9) and (5.3), respectively.

In case of the elastic waves the velocity is further influenced by the temperature of the ice with velocity increasing with decreasing temperature (sec. 4.4). However, seismic reflections caused by changes in temperature are not very likely, as a sudden change in temperature should be present for this. Temperature dependency for radar wave propagation speed is

only small (Matsuoka et al., 1997). The largest amount of englacial reflections in radar data below the firn ice transition zone is caused by changes in conductivity. However, they do not cause reflections in the seismic data.

The common cause for reflections below the firn-ice transition in seismic and radar data are, thus, reflections due to changing COF. While the influence of the anisotropic COF is small (<1%) in case of the radar wave velocity (sec. 5), the seismic wave velocity is clearly more influenced by the COF distribution (sec. 4.2.1). Especially the influence on the NMO velocity is noticeable in the anisotropic case for seismic data (sec. 3.5). Using the more precise conversion from TWT in depth from the radar data the depth of COF reflections can be determined. The information of the NMO velocities from the seismic data then yields the possibility, in combination with the information of the reflector depth from the radar data, to derive information about the existing anisotropy.

To be able to analyse the existing anisotropy by combination of seismic and radar data equal reflections need to be identified. The challenge of course remains to distinguish COF reflectors from conductivity reflectors in the radar data. If a good velocity–depth profile already exists here for the seismic data, distinct reflections in the seismic data can help to identify COF reflectors in the radar data. Still, for both, seismic and radar waves abrupt changes in the COF distribution causing clear reflections are needed to resolve changes in COF over depth.

A further common reflector for seismic and radar data is the reflection from the ice–bed interface, if the radar wave frequency is low enough, so that the damping is not too large and radar waves reach the ice–bed interface. Especially in case of a thin water layer the radar wave is limited to this depth, as most of the power is reflected by this very strong change in permittivity between ice and water. The seismic waves penetrate further through the water and into the rock. Thus, the bed properties can still be analysed in case of a thin water layer with seismic measurements. This is also valid for the bed properties of lakes below the ice sheet or the investigation of the seafloor below ice shelves, which is not possible with radar measurements.

Part 2:

Data analysis

6 Field sites and seismic surveys

The seismic, radar and ice core data used in this study were obtained at three different locations. At Colle Gnifetti (sec. 6.1), in the Monte Rosa, on the Swiss-Italian border, we carried out a seismic survey with a small light-weight electrodynamic vibrator. The other two field sites are in Dronning Maud Land, Antarctica. One survey was carried out at Halvfarryggen (sec. 6.2) close to the German overwintering station Neumayer III and a second survey on the Antarctic plateau next to the Kohnen station (sec. 6.3). All seismic data were collected within the LIMPICS project by the Alfred Wegener Institute (AWI). The processing of the seismic data sets was done using the commercial software Paradigm Echos.

For the three different locations not only data from seismic measurments exists but also from ice cores, firn cores and radar surveys. The relevant data sets, that will be used in Chapters 7, 8 and 9 for comparisons and the anlysis of the seismic data sets, will be introduced first. The processed seismic data are presented here. The discussion follows in these Chapters (Ch. 7, 8, 9) with respect to the different problems.

6.1 Colle Gnifetti

Colle Gnifetti is a glacier saddle at an elevation of 4500 m a.s.l, situated next to the highest mountain of the Monte Rosa range, the Dufourspitze (Figure 6.1, a). It has been studied intensively during the past decades. Falling into the recrystallisation-infiltration zone (Schumskii, 1964) it is an excellent, near-by field site to study of climate records from Europe and test new methods and techniques for investigations in polar regions. Only some thin melt layers and ice lenses can be found. The overall net snow accumulation at Colle Gnifetti is quite low with strong interannual variations between 15 and 50 cm water equivalent per year, caused by strong wind erosion (Alean et al., 1983). One of the numerous ice cores, the ice-core KCI, was drilled on Colle Gnifetti in 2005 in an area of especially low accumulation (Bohleber, 2011). Beside the study of the glaciological features of Colle Gnifetti (Haeberli and Alean, 1985; Schwerzmann, 2006) ice thickness and stratigraphy were investigated using ground penetrating radar (GPR) methods (Haeberli et al., 1988; Wagner, 1996; Lüthi, 2000; Eisen et al., 2003; Konrad et al., 2013).

The available ice-core and borehole data will be introduced in section 6.1.1. Here, velocities are calculated from the measured COF eigenvalues. The seismic data is introduced in 6.1.2. The seismic, radar and ice-core data sets are later used for a comparison in section 8.1 as well as to derive information about the existing anisotropy at Colle Gnifetti in section 9.1.

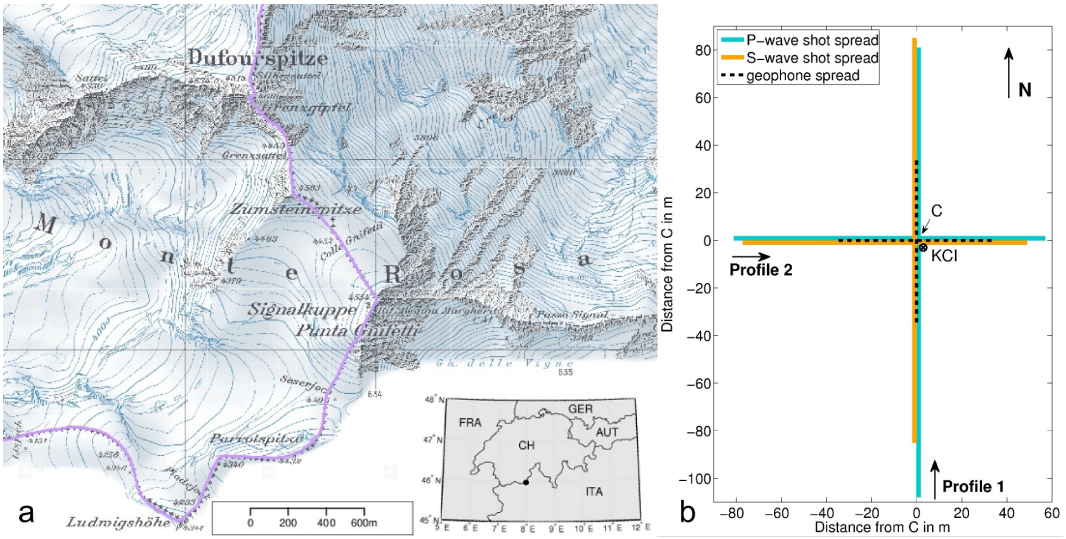

Figure 6.1: (a) Colle Gnifetti, located between Zumsteinspitze and Signalkuppe on the Swiss-Italian border, scale 1:20000 (www.schweizmobil.ch, Geodata ©swisstopo, Swiss Grid). The inset shows the location of Colle Gnifetti (black dot) on the Swiss-Italian border (WGS84).
(b) Geometry of seismic surveys. The green lines denote the shot spread of the P-wave, the orange lines the shot spread for the SH-wave survey. The dashed black lines show the geophone spread, geophones placed in 3 m intervals for the P-wave and 1.5 m intervals for the SH-wave survey. Crossing of the lines is at the center point C, close to the ice core KCI.

6.1.1 Ice-core and borehole data

The ice core KCI was drilled near the Swiss-Italian border. Drilling nearly reached the glacier bed at a depth of 62 m. However, drilling was stopped when first dirt intrusions occurred, so that the bed is probably around 1 m deeper (Bohleber, 2011). Seismic surveys carried out in 2008 and 2010 were centered around the borehole location (45.92972°N, 7.87692°E, WGS84, measured in 2008) of the KCI ice core (Figure 6.1, b). Thus, ice core measurements can be used for comparison with the seismic data sets.

Density measurements (Jahn, 2006) on the ice core using γ-attenuation profiling (GAP) (Wilhelms, 1996) on a sub-centimeter resolution revealed some melt layers in the upper 15 m and the firn-ice transition zone in about 30 m depth. Temperatures measured on numerous borehole sites on the plateau were analysed by Hölzle et al. (2011), finding an increase in firn temperature since 1991 presently being around 0.16°C per year. Temperature measurements in the KCI borehole in 2007 revealed temperatures of -11 to -13°C. A strong negative temperature signal of -15°C in 7 m depth was observed by measurements in 2008 (http://cryomap.cryosphere.ch, B05-1).

After storing the KCI ice core between 2005–2012 at -30°C c-axes orientation fabrics were measured on the ice below the firn-ice transition zone ($\sim$30m depth) in approximately 5 m intervals (12 samples used for this study) down to the ice-bed interface and in high resolution (0.1 m intervals) between 54 m and 54.5 m. Measurements have been carried out on thin sections (about 50 x 100 x 0.3 mm^3) using the classical polarisation microscopy method applying an automatic fabric analyser (e.g., Wilson et al., 2003; Peternell et al.,

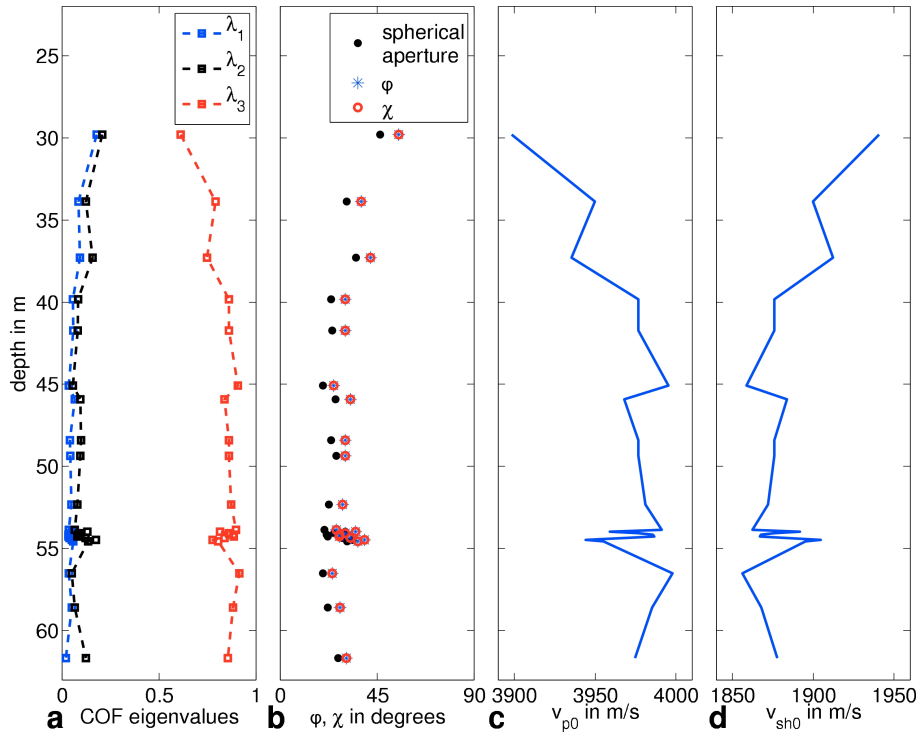

Figure 6.2: (a) Eigenvalues derived from measured c-axis orientation of thin sections of the KCI ice core (I. Weikusat and J. Eichler, pers. comm.). (b) Spherical aperture (Wallbrecher, 1986) black dots calculated from the orientation tensors and opening angles φ (red circles) and χ (blue stars) derived from the eigenvalues (sec. 4.2). The corresponding zero-offset P- wave and SH-wave velocities calculated from the derived elasticity tensors with equations (3.20) and (3.22) are given in (c) and (d), respectively.

2010). The measured cross-sectional area of the crystallites is used as the statistical weight of the polycrystal (Gagliardini et al., 2004). This resembles very well the conditions for the seismic waves, as grain size is implicitly included in this information. Additionally to the eigenvalues, the spherical aperture (Wallbrecher, 1986) has been calculated, describing the opening angle of a cone, the distribution of c-axes (Figure 6.2, a and b). This COF data was kindly provided by I. Weikusat and J. Eichler (AWI).

Velocities from COF eigenvlaues

Form the COF eigenvalues the opening angles and the elasticity tensors are calculated as descibed in section 4.2. Further, P- and SH-wave velocities are calcualted that can be used in section 9.1 for comparison with the velocities derived from the seismic measurments.

The spherical aperture directly calculated from the orientation tensor can be compared to the opening angles φ and χ derived from the COF eigenvalues (Figure 6.2, b). The orientation tensor as well as the eigenvalues were derived below the firn-ice transition. A cone fabric (φ=χ) was derived from the eigenvalues with opening angles ranging between 24° and 55°. The spherical apertures derived from the orientation tensor show slightly smaller values between 22° and 47°.

From the opening angles the corresponding elasticity tensors (sec. 4.2) were calculated using

	P-wave survey		S-wave survey	
	Profile 1	Profile 2	Profile 1	Profile 2
sweep frequency (Hz)	30–240	20–160	60–360	30–240
geophone spacing (m)	3	3	1.5	1.5
shot spacing (m)	3	3	1.5	1.5
shot spread (m)	−108–81	−81–57	−85–85	−77–49
depth shift (m)	6	8	-	-

Table 6.1: Geometry for P and SH-wave survey of Profile 1 and Profile 2 at Colle Gnifetti.

the values of the elasticity tensor derived by Gammon et al. (1983). The elasticity tensors are then used to calculate seismic velocities or reflection coefficients. Figure 6.2, c and d, show as an example the zero-offset P-wave (v_{p0}) and SH-wave (v_{sh0}) velocities, respectively. These velcoities will be compared to velocities derived from the seismic data in section 9.1.1.

6.1.2 Seismic measurements at Colle Gnifetti

A first seismic survey was carried out on Colle Gnifetti in August 2008. As source the Seismic Impulse Source System (SISSY) was used. The strong surface and diving waves made it difficult to process and analyse the data (Diez et al., 2013). In August 2010 the survey at Colle Gnifetti was repeated (Polom et al., 2014). We shot two profiles perpendicular to each other (Figure 6.1, b). As source we used the light-weight micro-vibrator ElViS (Electrodynamic-Vibrator System; Druivenga et al., 2011), which we operated in P-wave, as well as in SH-wave mode on both profiles. The difference for the geometry settings on both profiles and for both wave types are listed in Table 6.1 (Polom et al., 2014; Diez et al., 2013) .

The raw data were correlated with the corresponding measured pilot sweep, afterwards amplitude scaling, bandpass filter, and frequency wavenumber (*fk*)-filters were applied. The data were then used to pick RMS velocities for the different wave types and profiles independently. These RMS stacking velocities were used for the NMO correction and afterwards in a smoothed form for the conversion of TWT to depth (Polom et al., 2014).

Processed data

The stacked data clearly show the bed reflection for the P-wave as well as for the SH-wave and a few internal reflections above (Polom et al., 2014; Diez et al., 2013). The thickness of about 62 m of the glacier at our survey location is known from the length of the ice core KCI. The depth of the bed reflection of the SH-wave data, after depth conversion, fitted to this length. The depth of the bed reflection of the P-wave data was about 6 m (Profile 1) and 8 m (Profile 2) too shallow.

Diving waves observed in the SH-wave data sets are used in section 8.1.1 to derive the S-wave–density realtionship given in equation (4.10). The discussion of the englacial reflections and the bed reflection of these seismic data sets follows in section 8.1.2. The error in

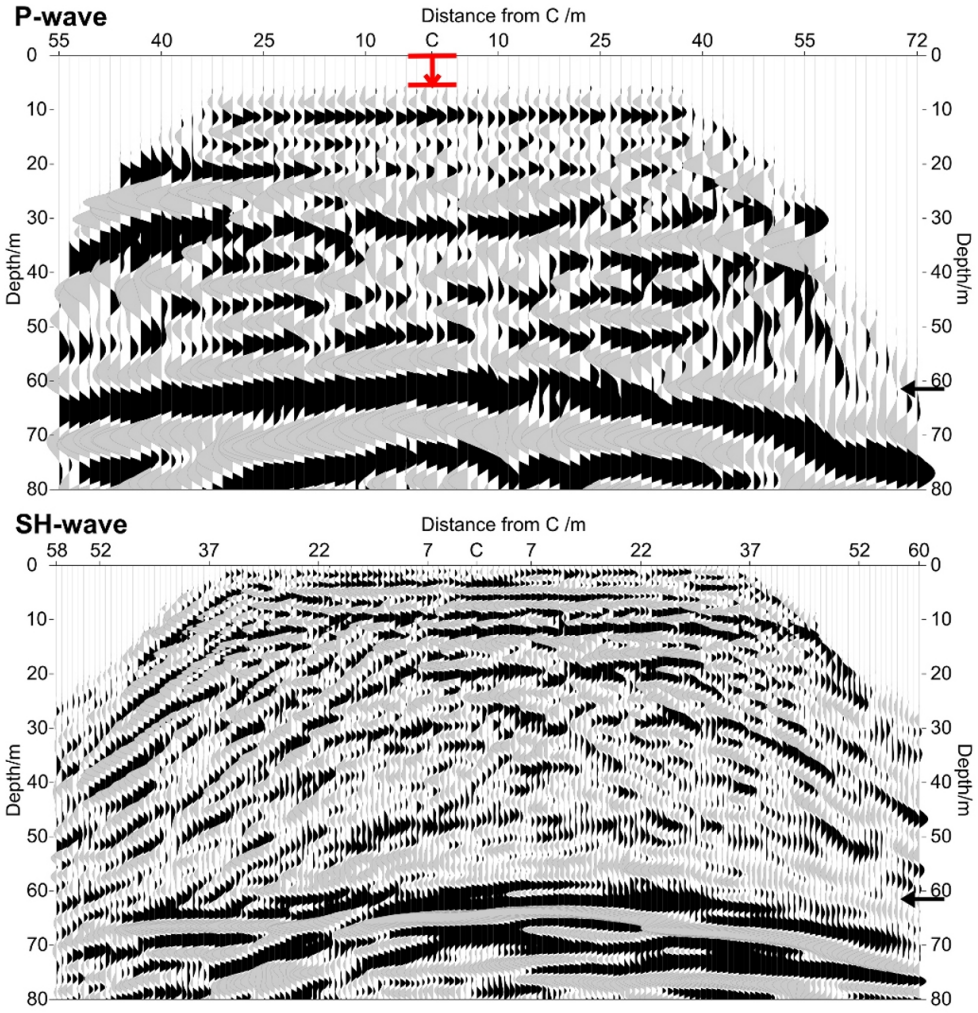

Figure 6.3: Stacked data from the survey using the micro-vibrator ElViS as source on Profile 1 (North–South) in P-wave and SH-wave mode. Distances are shown from the center point C, close to the ice core KCI. The bed reflector can clearly be seen at around 60 m depth (marked with arrow), with coherent englacial reflections visible above. The P-wave stack was shifted down 6 m (marked with red arrow).

the depth of the bed reflection can be explained with the existing anisotropy (sec. 9.1.1). Finally, the seismic data is combined with radar data to derive information about the existing anisotropy in section 9.1.2.

6.2 Halvfarryggen

Halvfarryggen is a local dome in Dronning Maud Land, Antarctica (71°10'S, 6°45'E, WGS84), about 80 km south-east of the overwintering station Neumayer III (Figure 6.4). It is part of the catchment area of the Ekström ice shelf on which the Neumayer Station is located. Halvfarryggen has three ice divides, so the dome consists of a triple point (Drews et al., 2013), with an ice thickness of about 910 m. This corresponds to an elevation of ∼700 m a.s.l. (Wesche et al., 2009).

Halvfarryggen is a possible drill location for a new intermediat deep ice core (sec. 6.2.2). This included some presurveys collecting RES and GPR data and the drilling of a firn core.The seismic data is introduced in section 6.2.2. Englacial reflections and the bed reflection as well as a critically refracted wave in the seismic data will later be used to derive velocities of the ice and the bed (sec. 9.2).

6.2.1 Pre-surveys for ice core drilling at Halvfarryggen

Within the IPICS 2K/40k project (IPICS - International Partnerships in Ice Core Sciences) locations for a new ice core were investigated around Halvfarryggen and the neighbouring dome Sørasen. The aim of the project is to drill intermediate deep ice cores with the possibility to resolve annual layers with high resolution to increase temporal and spatial resolution provided from ice core records (Brook et al., 2006). For the drill site selection an 80 m deep firn core was drilled at Halvfarryggen (Fernandoy et al., 2010) providing a density profile for the firn part. By now it has been decided, that the new intermediate deep ice core of the IPICS 2K/40k project is going to be drilled on the dome of Halvfarryggen.

In the region around Halvfarryggen RES as well as GPR measurements were carried out (Drews et al., 2013). The RES data showed an upwarping of the isochronous, a Raymond bump (Figure, 5.1), indicating a stable position of the ice divide for the last 2700–4500 years. Next to a common Raymond bump a double bump could be observed in some of the RES profiles indicating a developed anisotropic ice fabric. Thus, an existing anisotropy was expeted within the ice here and the location was selected for seismic measurements.

6.2.2 Seismic measurements at Halvfarryggen

Seismic profiling and wideangle data sets were collected at Halvfarryggen (Figure 6.4) within the Antarctic field seasons 2009/10 and 2010/11 using explosives as well as vibroseismics as source. The profiling that was carried out with explosives as source revealed at least eleven englacial reflections, that were interpreted as arising from sudden changes in COF (Hofstede et al., 2013). The vibroseis data were used to investigate the ice–bed interface at

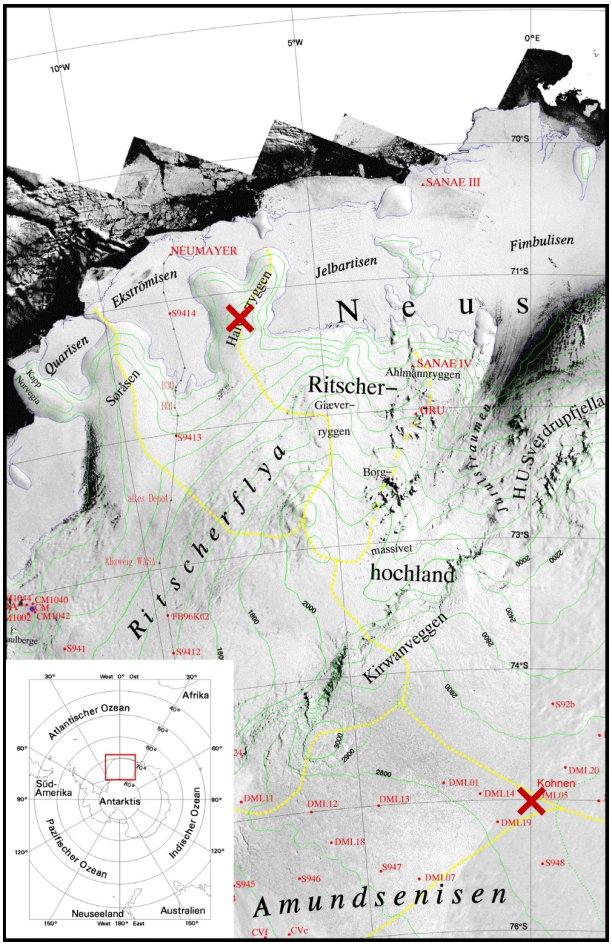

Figure 6.4: Field sites of Halvfarryggen and Kohnen station (marked with red crosses) in Dronning Maud Land, Antarctica. (Extract from the Satellite Image Map 1:2000000 Dronning Maud Land, Draft Version 4.2, Bundesamt für Kartographie und Geodäsie (BKG), Nov. 1998, http://www.stagn.de/antarktis/aaaa_karten_einleitung.htm.)

Halvfarryggen (Hofstede et al., 2013) as well as geological settings below the Ekströmisen on a longer survey between Halvfarryggen and Neumayer III (Kristoffersen et al., in prep.).

For the recording of our measurements we used a 1.5 km long snow streamer with 60 channels, hence, a channel spacing of 25 m. Each channel consists of 8 gimballed SM-4 geophones from SENSOR, with an eigenfrequency of 14 Hz and a geophone spacing of 3.125 m. As the main focus of our surveys were the physical properties of the ice column as well as the ice bed interface at a depth of about 910 m we tied the streamer in a loop (Figure 6.5). Thus, the channel spacing was decreased to 12.5 m increasing the spatial resolution.

The explosive profile analysed by Hofstede et al. (2013) is used in section 9.2.1 to investigate the bed topography. The shot increment for this survey was 125 m resulting in 3-fold data. Thus, the bed topographie in the region of the wideangle survey could be maped.

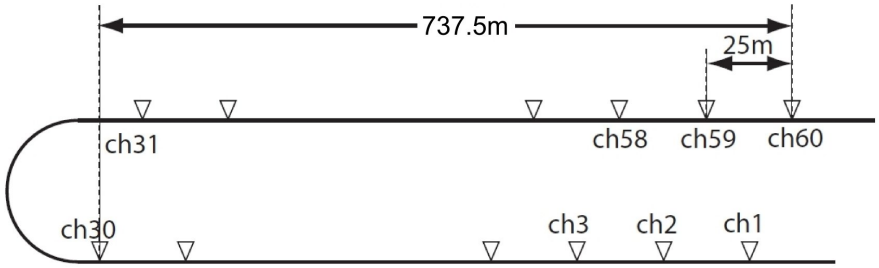

Figure 6.5: To increase the resolution for the target depth of the bed reflection at Halvfarryggen (∼900 m) the streamer was used in a loop. Thus, the channel spacing was reduced to 12.5 m. Two shots were carried out per shot location with a shift of 6.25 m to increase the spatial distribution of the CMPs. Figure adapted from Hofstede et al. (2013).

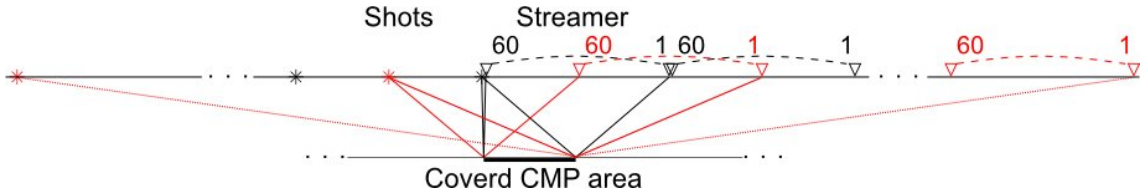

Figure 6.6: Wideangle survey, where streamer and shot positions move away from each other, covering a wide range of incoming angles. The streamer was used in a loop for the Halvfarryggen survey (Figure 6.5). Channel 60 in this case denotes the channel closest to each shot position, not the actual channel 60. Shot and streamer were moved by 325 m between shot locations.

Wideangle data

Beside the different profiles we also shot a wideangle survey. While source and receivers move apart from each other, a wide range of incoming angles can be covered. Normally several geophones and one source are used per shot. Hence, the same CMPs are mapped over and over again (Figure 6.6). Afterwards, it is assumed that the physical properties do not change over the small range of covered CMPs so that all source-receiver combinations can be assigned to one CMP.

For the wideangle survey at Halvfarryggen the streamer moved towards the South in increments of 325 m and the shot position moved towards the North in increments of 325 m. To increase the spatial resolution further at each shot location, two shots were carried out while the streamer moved forward by 6.25 m, thus, decreasing the CMP increment to 3.125 m. Hence, 9 shot positions were used covering offsets up to 6795 m and, theoretically, incoming angles up to 75°. For the recording of the data we used a Strataview R60. The record length was set to 11 s with a sample interval of 0.5 ms.

As source we deployed explosive charges (pentolite, PETN/TNT mixture) in holes between 10 and 30 m depth, increasing with increasing offset. The holes were drilled with an air-pressure drill (RAMdrill; deloped by the Physical Sciences Lab of the University of Wisconsin-Madison). As the energy decreases for larger offsets due to geometrical spreading and damping the charge size was gradually increased (Table 6.2).

As streamer and source move away from each other the trigger signal was sent by radio.

Shot position	1	2	3	4	5	6	7	8	9
Offset to center in m	0	375	750	1125	1500	1875	2250	2625	3000
Charge in g									
first shot	400	650	800	1600	2400	3200	4000	4800	5600
second shot	400	650	1200	1600	2400	3200	4000	4800	5600

Table 6.2: Geometry of seismic survey at Halvfarryggen. Offset is given with respect to the center of the survey, so that the offset to the first geophone is twice this length plus 50 m initial offset. The offset to the center for the second shot is always plus 6.25 m.

This caused some problems during the measurements. Hence, triggering was finally done manually by radio command of the detonator and for larger offsets via satellite telephone. Thus, the different shots had to be aligned later by fitting the diving waves to each other, which of course includes the possibility of traveltime errors. Processing for this data set mainly includes careful frequency and *fk*-filtering to reduce signals from surface and diving waves.

Processed seismic wideangle data

The bed reflection is clearly visible over the complete range of offsets up to 6795 m (Figure 6.7). At an offset of $\sim$2080 m the refracted wave emerging from the reflection at the ice-bed interface can be seen. Additionally, a number of englacial reflectors is visible for the first 325 m offset (Figure 6.8). A really strong englacial reflection can be followed to larger offset, approximately up to 1.3 km just above the ice-bed interface. The reflections of the wideangle survey are analysed and discussed in section 9.2.1. The critically refracted wave is used in section 9.2.2 to derive information about the bed properties.

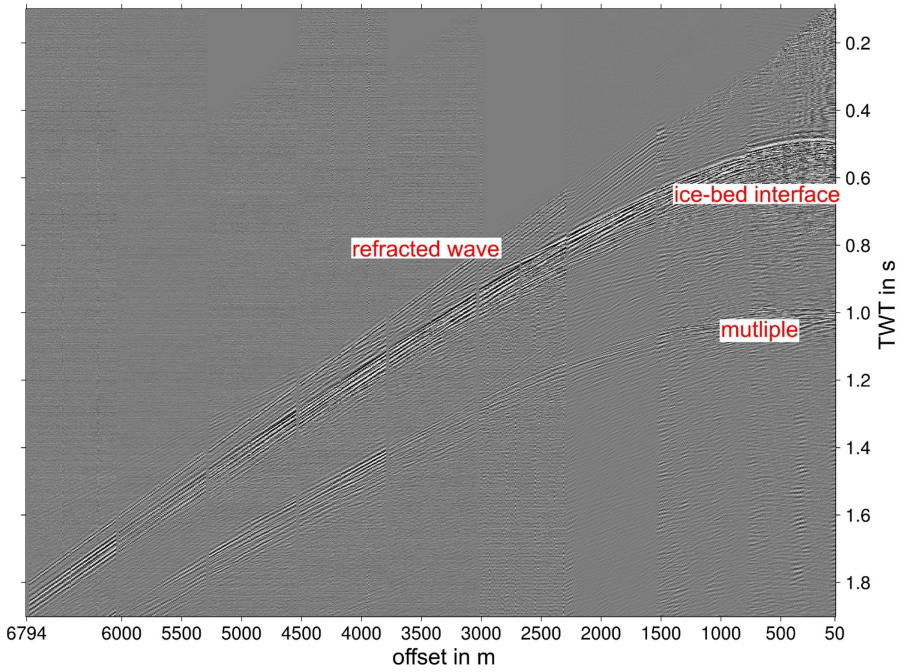

Figure 6.7: Processed wideangle data set from Halvfarryggen consisting of 18 shots sorted by offset. The streamer moved towards the South, while the shot position moved towards the North. The ice-bed interface is clearly visible for all offsets. A citically refracted wave can be observed emerging from the ice-bed reflector at an offset of ∼2080 m. The data sets were frequency and *fk*-filtered, the top part was muted.

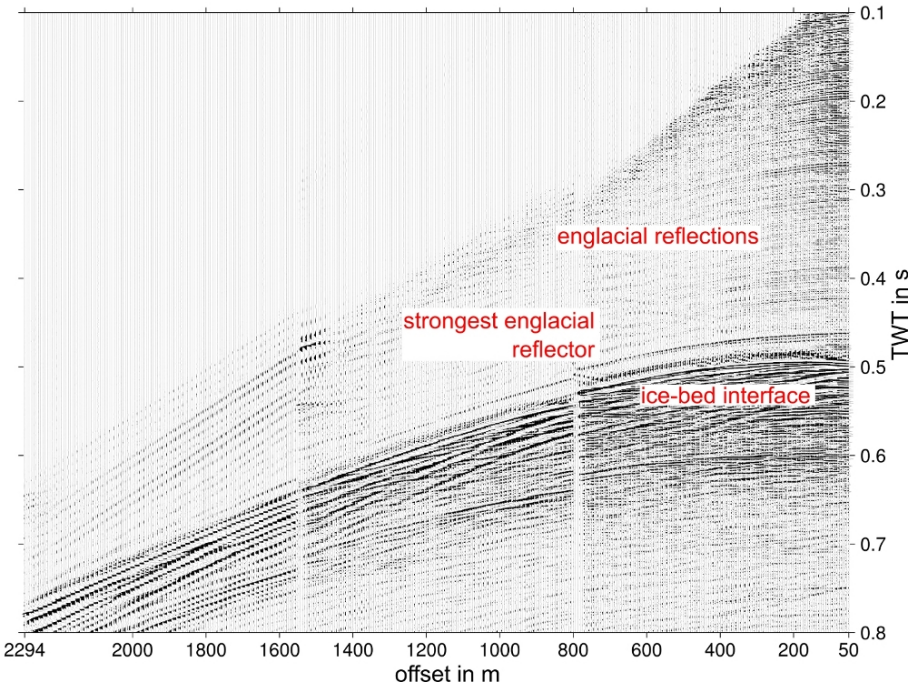

Figure 6.8: Zoom of the first 6 shots from the wideangle survey at Halvfarryggen (Figure 6.7). The streamer moved towards the South, while the shot position moved towards the North. The bed reflection is clearly visible as well as a strong englacial reflection just above the bed and further englacial reflections between 0.1 and 0.45 s TWT.

6.3 Kohnen

Kohnen station is located on the Antarctic plateau at an elevation of 2900 m a.s.l. about 750 km south of Neumayer III (75°00'S, 0°04'E, WGS84). Within the EPICA Project (European Project for Ice Coring in Antarctica) an ice core, EDML (EPICA Dronning Maud Land) has been drilled during 2001 and 2006, down to a depth of 2774 m (Oerter et al., 2009). The over all thickness of the ice was estimated from RES data to be 2782±5 m (Wesche et al., 2007). We carried out seismic profile and wideangle measurements with explosives and vibroseis in January 2012 and 2013 in the vicinity of Kohnen station.

In section 6.3.1 the ice-core and radar data is introduced. This inculdes the calculation of seismic velocities from the COF data and results from radar studies that derive information about the existing anisotropy. The different seismic wideangle data sets are introduced in section 6.3.2. Addtitionaly, a vertical seismic profiling (VSP) survey was carried out in the EDML borhole. This data is as well introduced in section 6.3.2 and will be analysed in Chapter 7. Seismic, radar and ice core data sets will be compared to each other in section 8.3 and velocities derived from the wideangle data set will be used in section 9.3 to derive information about the existing anisotropy.

6.3.1 Ice core and radar data Kohnen

On the ice-core EDML measurements of the density and dielectric properties were carried out by means of GAP and dielectrical profiling (DEP), down to a depth of 448 m and 2565 m, respectively (Eisen et al., 2006) (Figure 6.9, a). During the field season 2011/12 a new temperature measurement was carried out logging temperatures in the undisturbed borehole between 80.05–2591.44 m depth revealing temperatures of $-44°$ to $-7°$C (Figure 6.9, b; H. Miller, pers. comm.).

COF measurements were also carried out on the EDML ice core between 104–2563 m depth (Eisen et al., 2007) (Figure 6.10, a). After the ice core was stored at $-30°$C c-axes distribution was determined on horizontal (0.5 x 50 x 50 mm^3) and vertical (0.5 x 50 x 100 mm^3) thin sections using an automatic fabric analyzer in 2005. The derived eigenvalues from the horizontal and vertical sections show some variations within ±0.1 which is attributed to the cutting of the samples and, thus, exclusion of certain grains (Eisen et al., 2007; Drews et al., 2013). Statistical weighting was done per grain for the calculation of the COF eigenvalues.

Velocities from COF eigenvalues

From the measured eigenvalues (Figure 6.10, a) the opening angles (Figure 6.10, b) and elasticity tensors can be calculated (sec. 4.2). Down to a depth of 450 m a cone fabric with large opening angels ($\varphi = \chi \geq 70°$) is derived from the eigenvalues, so a fabric close to isotropic. At this depth the eigenvalues show a distinct jump to a more anisotropic fabric. Here, a cone fabric with opening angels between 55° and 80° is derived. At the depth of 800 m a changeto a thick girdle fabric follows. The eigenvalues show larger variations for the eigenvalues λ_2 and λ_3 for this depth downward. Nevertheless, this change in the eigenvalues of λ_2 and λ_3 is a gradual change, not a distinct jump. Below 1150 m a partial girdle fabric can be observed with decreasing opening angle φ over depth and the onset of a

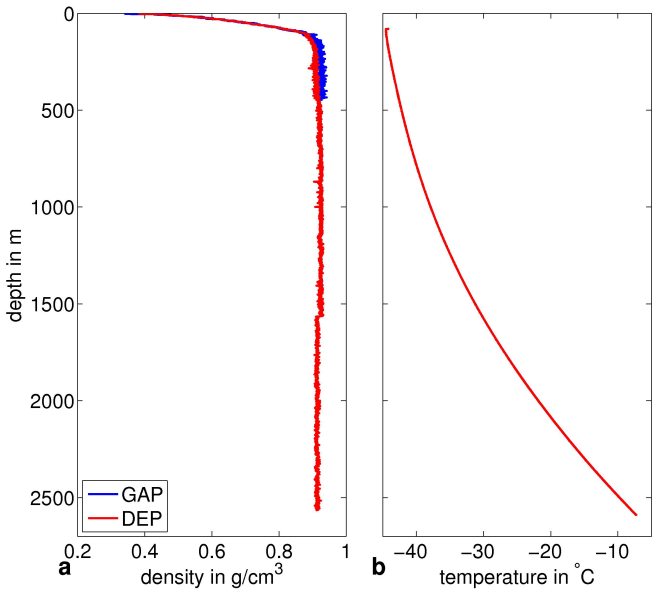

Figure 6.9: (a) Density distribution measured along the EDML ice core with GAP and DEP. From the DEP measurements the densities were calculated using the equation given by Kovacs et al. (1995). (b) Temperature profile measured within the undisturbed borehole of the EDML ice core, measured in January 2012.

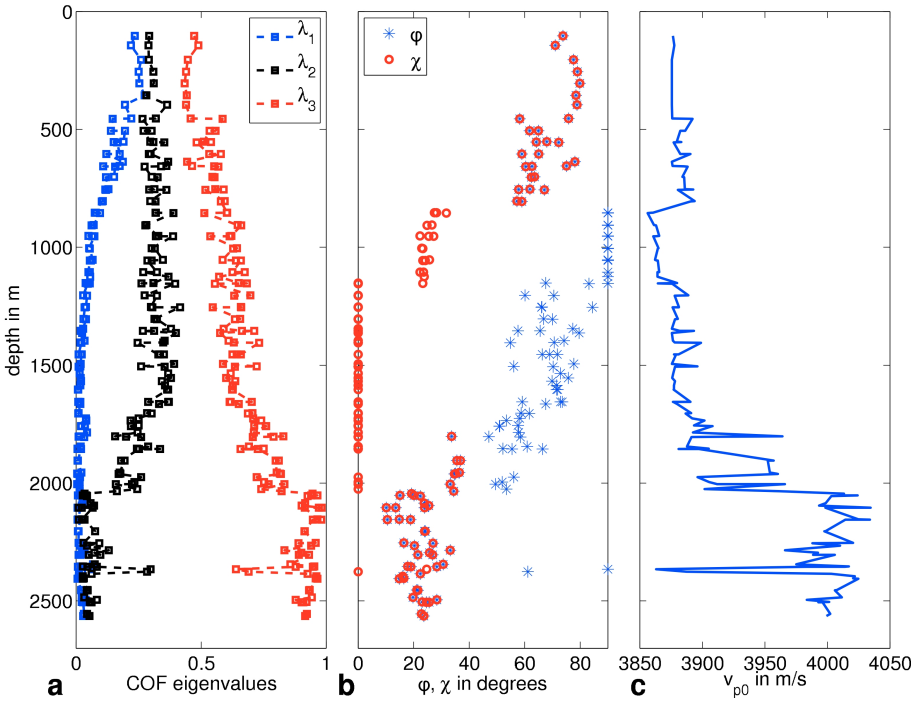

Figure 6.10: (a) COF eigenvalues derived from the orientation tensor measured on thin section of the ice core EDML. (b) Opening angels derived from the eigenvalues in (a). Regions with φ=χ contain cone fabrics, regions with $\varphi = 90°$ contain thick girdle fabrics and regions with $\chi = 0°$ contain partial girdles. (c) Zero-offset P-wave velocity v_{p0} calculated from the elasticity tensors derived from the opening angles in (b).

cone fabric with opening angles around 35° at 1800 m depth, interrupted by thin regions of partial girdle fabric. Below 2040 m a strong cone fabric is developed with opening angles between 10° and 33° interrupted by a very narrow (30 m) layer of girdle fabric.

From the elasticity tensor derived from the opening angels φ and χ the velocities over depth and for different incoming angles can be calculated. Figure 6.10, c shows as an example the zero-offset P-wave velocity calculated from the elasticity tensors. This velocity profile will be used in section 7 in comparison to a velocity profile derived from the VSP data set. Furher the calculated velociteis are compared to velocities picked from the wideangle data in section 9.3.

Girdle orientation from radar data

Radar data sets from the region (Figure 6.11) include RES profiles with 60 ns (Profile 023150) and 600 ns pulse (Profile 022150) recorded during flight with the AWI-airplane Polar 2. Additionally, a survey was carried out with a plane sliding on the ground in a circle with a radius of about 50 m and 6 legs crossing the circle in different directions using a 60 ns pulse (Profile 033042, Figure 6.11, inset). The radar measurements, in combination with the COF measurements were used in a study by Eisen et al. (2007) to reveal a strong radar reflector at 2035 m depth caused by a transition of girdle fabric distribution to a narrow cone fabric distribution. Further the change in COF was attributed to a change in the azimuthal backscatter of the radar signals over depth by Drews et al. (2013). Both, Eisen et al. (2007) and Drews et al. (2013), conclude from the observed reflection pattern an orientation of the girdle fabric parallel to the ice divide.

6.3.2 Seismic measurements Kohnen

Seismic measurements near the Kohnen station, close to the drill site of the EDML ice core were carried out in January 2012 and 2013. The measurements included profiling, wideangle and VSP surveys. For the recording 3-component (3C) geophones as well as a streamer and a borehole geophone were used. We carried out explosive and vibroseis surveys using boosters as well as denotation cord for the explosive surveys and the small vibrator ElViS as well as a new low impact vibrator system (EnviroVibe) with a peak force of 66000 N. The charges used showed large differences in the resolution and the possibility to efficiently process the data. Appendix B.1 gives some results about the different sources. Here, I concentrate on the wideangle surveys done with explosives and the EnviroVibe and the VSP measurements carried out with explosives. Seismograms of the wideangle survey can be found in the appendix B.2.

Wideangle data

The wideangle survey was carried out twice on two cross lines, centered close to the drill location of the ice core EDML one parallel (WNW–ESE) and one perpendicular (NNE–SSW) to the ice divide (Figure 6.11). The streamer in a straight line, i.e., 1.5 km long, moved forward in steps of 750 m for all measurements. The source moved in the opposite direction as well in steps of 750 m. The streamer moved towards the WNW on the parallel line and

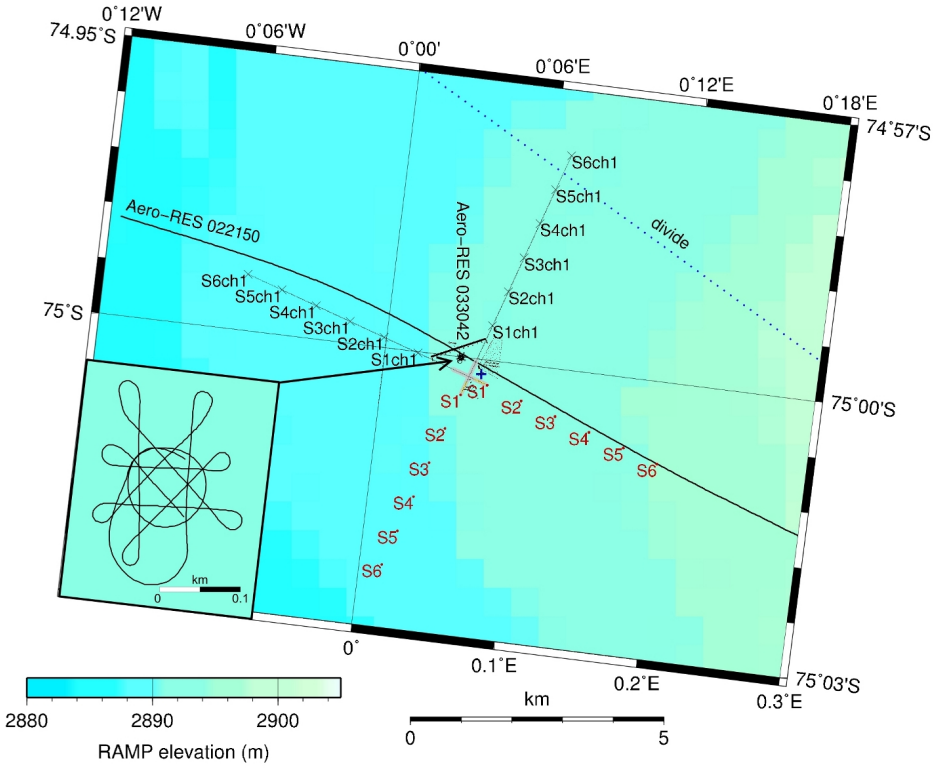

Figure 6.11: Geometry of wideangle survey carried out at Kohnen in January 2012 and 2013. Two lines were shot, one parallel and one perpendicular to the ice divide. The red dotes with S1–S6 give the shot locations, the black crosses with S1ch1–S6ch1 the location of channel number 1, channel number 60 is then 1.5 km closer to the shot location. The blue cross marks the drill location of the EDML ice core. Additionally, the flight line of the radar survey 022150 is plotted. The radar profile 023150 is on the same line. The inset shows the survey 033042 done with the air plane driving on the ground. (Figure adapted from O. Eisen, pers. comm.)

Survey	Source	Recording
para-exp-12m	explosive, 12 m, 5.6 kg	Strataview R60, 10 s/0.25 ms
perp-exp-12m	explosive, 12 m, 5.6 kg	Strataview R60, 10 s/0.25 ms
perp-exp-30m	explosive, 30 m, 5.6 kg	Strataview R60, 10 s/0.25 ms
para-vib	EnviroVibe, 10 s, 10–220 Hz	Geode, 16 s/0.25 ms
perp-vib	EnviroVibe, 10 s, 10–220 Hz	Geode, 16 s/0.25 ms

Table 6.3: Seismic wideangle profiles carried out at Kohnen. The survey name gives the direction of the survey parallel (para) or perpendicular (perp) to the ice divide and the source type, explosive (exp) or EnviroVibe (vib). For the explosives the borehole depth and charge size are given, for the EnviroVibe the sweep length and the sweep frequency, followed by the recording device, record length and sample interval.

towards the NNE on the perpendicular line, while the source moved towards the ESE and SSW, respectively. In 2012 explosives (pentolite, PETN/TNT mixture) were used as source deployed in holes of 12 m depth, drilled with a auger hand drill. Additionally, 3 shots (S 1, 2 and 3) were carried out on the perpendicular line in boreholes of 30 m depth drilled with the RAM drill, which broke down afterwards. The wideangle survey was repeated in 2013 with the EnviroVibe as source on the same shot locations as in 2012. For the recording a 10 s sweep of 10–220 Hz and a 500 ms ramp was used. On the parallel line the For the explosive as well as the vibroseis survey Specifications of the source, and receiver settings are given in Table 6.3.

Processed wideangle data

Before starting the standard processing the vibroseis data first need to be cross correlated with the initial sweep, to reduce the source signal to a Klauder wavelet. Afterwards, the processing of both data sets, explosive and vibroseis, was quite similar, mainly including editing of traces that were not recorded correctly, muting of the onset of the shots, frequency and *fk*-filtering. In contrast to the Halvfarryggen wideangle data englacial reflections could not clearly be observed, neither in the explosive nor in the EnviroVibe data sets. Nevertheless, the bed reflection will be used to carry out a ηNMO correction to derive information about the orienation of the girdle fabric observed in the ice core data (sec. 9.3).

VSP survey geometry

Another survey carried out was a VSP measurement. Here, a borehole geophone was lowered to a depth of 2580 m within the borehole of the EDML ice core. Shooting the VSP data set was done in two steps. First 1 m detonation cord (100 g pentolite) was used as source curled up, always at the same location. The borehole geophone was pulled up from the depth of 2580 m to 60 m depth in 40 m steps. The last geophone position was, however, outside of the borehole fluid so that proper coupling of the borehole geophone was not obtained any longer. A day later the same measurement was repeated with 150 g-boosters as source on the same location as the detonation cord in a depth interval between 2560 m and 1600 m, again in 40 m steps. By combining both measurements the depth intervals below 1600 m were effectively reduced to 20 m intervals. The depth provided here is always given

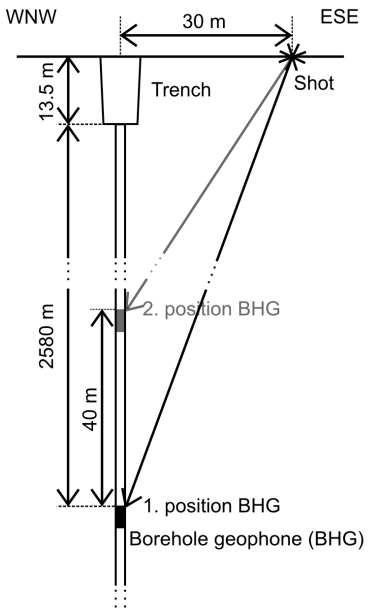

Figure 6.12: Geometry setup for shooting of VSP survey. The shot location with detonation cord was 30 m away from the borehole location. The borehole geophone was pulled up in intervals of 40 m from a depth of 2580 m to 6 m depth. The survey was complemented between 2560 m and 1600 m with boosters as source and locations of the borehole geophone (BHG) shifted by 20 m to the previeous survey. The depth is given to the top of the borehole casing, measured to be 13.5 m below the surface (January 2012).

with respect to the top of the borehole casing, which was 13.5 m below the surface. The shot location at the surface was 30 m away from the borehole (Figure 6.12). The recording was done with Geodes, where the sample interval was set to 0.25 ms with a record length of 5 s. During the recording the generator of the close-by Kohnen station was always disconnected from the Kohnen power supply system. This was an important step during the survey as the generator otherwise produced a strong 50 Hz signal, picked up by the borehole cable of the geophone, making it impossible to clearly detect the first arrivals of the seismic waves.

Parallel to the recording of the borehole geophone a line of 24 3C-geophones was placed about 100 m South from the shot location. The 3C-geophones were placed in intervals of 5 m coveringt a spread of 115 m This yields the possibility of comparing the reproducibility of the different shots and compare the quality of the detonation cord and booster shots. Here, the recording was done together with the borehole geophone, i.e., on the Geodes with a sample interval of 0.25 ms and a record length of 5 s. The results of the VSP measurement are discussed in detail in Chapter 7 and used to evaluate the approach of calculation of polycrystal elasticity tensors from the measured monocrystal elasticity tensor (sec. 4.2).

7 Vertical seismic profiling (VSP)

In this section velocities from the VSP survey at Kohnen station, Antarctica, are compared to velocities calculated from the COF eigenvalues of the EDML ice core. The big advantage of the VSP survey is, that the velocities can be calculated directly from the traveltimes due to the known travelpath in contrast to reflection seismic profiles where the depth of the layer is often unknown. The goal of this comparison of velocities determined from the VSP survey and the EDML eigenvalues is to find out if variations in the VSP velocities can be observed that fit to velocity variations expected from the COF variations and if the velocities calculated from the COF eigenvalues (sec. 4.2) fit to the observed velocities from the VSP survey.

The shot-receiver geometry of the VSP survey is described above (sec. 6.3.2). First, the traveltimes of the direct travelpath from the shot location on the surface to the geophone within the borehole are picked and corrections are discussed (sec. 7.1). Second, the obtained interval velocities are compared to velocities calculated from the COF eigenvalues of the EDML ice core (sec. 7.1). The elasticity tensors of ice measured by different authors (Table 4.1) are compared (sec. 7.2) and the temperature dependency (sec. 7.3) is analysed.

7.1 Evaluation of traveltimes

The recorded seismic data of the VSP survey show clear signals from the direct wave (Figure 7.1) travelling from the shot at the surface to the geophone within the borehole (Figure 6.12). For the detonation cord survey (Figure 7.1, a) the onset of the first break is well defined. Some more variations can be observed in the data with the boosters as source (Figure 7.1, b). Strong noise is visible in most of these shots for traveltimes $\leq$0.2 s. For Shot 11 the trigger did obviously not work correctly and in case of shot 14 strong noise throughout the record is visible, making it difficult to pick the signal of the direct wave.

The shots were also recorded on 3C-geophones placed $\sim$100 m away from the shot location. These data show the variability of repeated explosive shots, with the same charge size on the same location (Figure 7.2). For the detonation cord survey (Figure 7.2, a) the first 9 shots are very similar, afterwards the shape of the wavelets become significantly more variable and the arrival times have variations of up to 1 ms. In case of the boosters as source variations are all together larger with differences in arrival time of up to 2 ms (Figure 7.2, b). A reason for these variations for both source types might be the detonation at the same point over and over again, producing a hole of $\sim$1 m depth over time.

To derive information about the change of seismic velocity over depth the traveltime from the VSP survey with the detonation cord and boosters were picked. The data were resampled from 0.25 ms recording interval to 0.125 ms for a more precise picking of the first arrivals, as picks are only possible on samples. Resampling was done with the software ECHOS by a

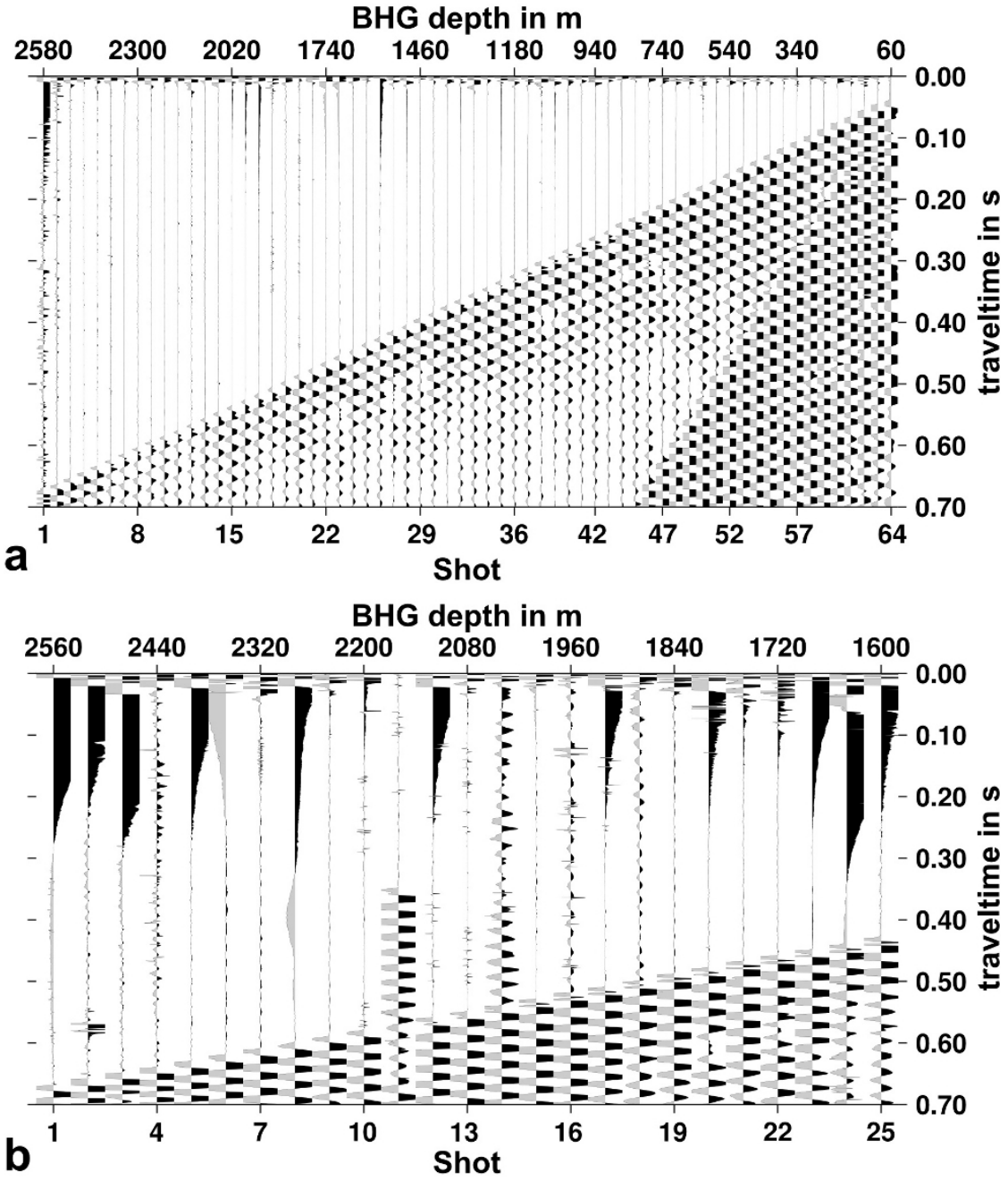

Figure 7.1: Recorded first arrivals from the VSP surveys with detonation cord (a) and booster (b) as source. The top ordinate gives the location, hence, the depth of the borehole geophone (BHG), the bottom ordinate shows the shot number for comparison with Figure 7.2. In (a) not only the direct P-wave arrival is visible but also a borehole guided wave traveling with a velocity of 1150 m/s. Depth here is to top of casing.

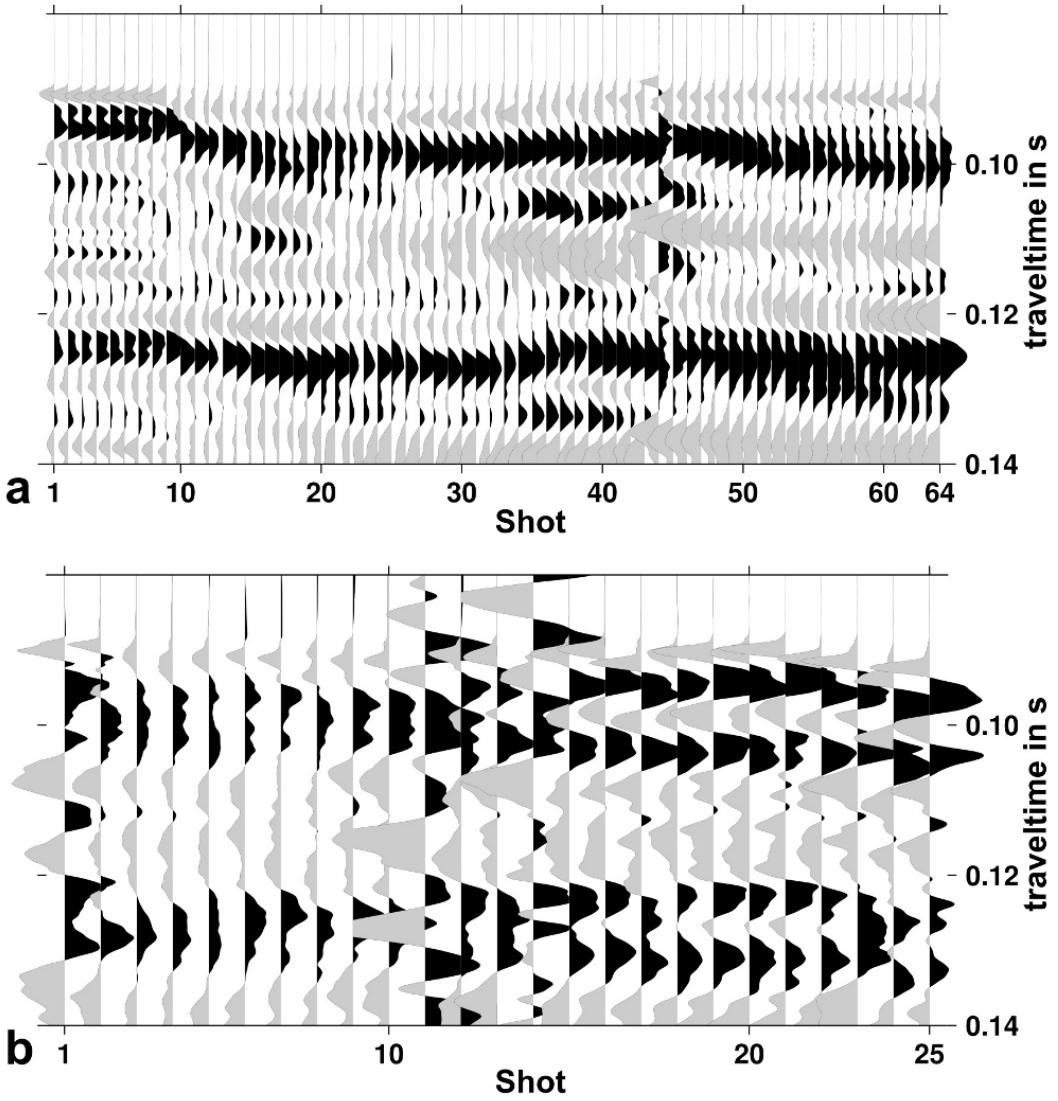

Figure 7.2: Traces of the vertical component of the 3C-geophone on the surface, closest to the shot location (∼100 m) during the VSP survey with the detonation cord (a) and booster (b) as source.

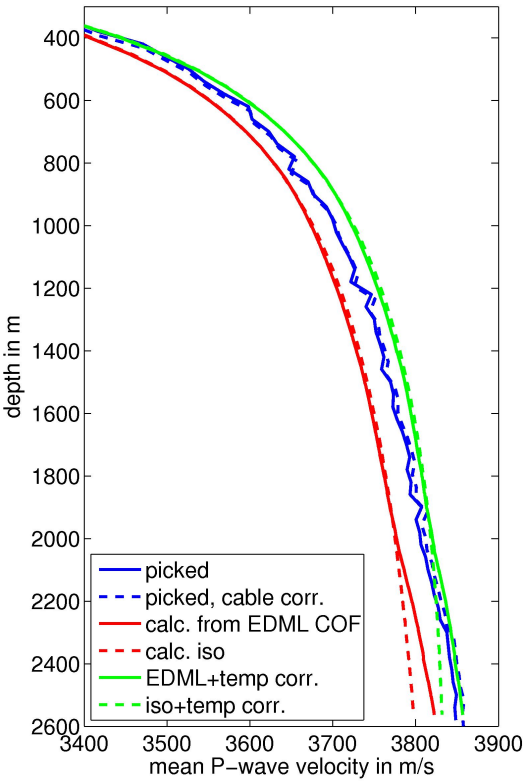

Figure 7.3: Mean velocities for picked traveltimes from VSP survey (solid blue line), corrected for the cable elongation (dashed blue line), compared to mean velocities calculated from the COF eigenvalues of the EDML ice core (red solid line) with temperature correction (green solid line). For comparison the mean velocities for an isotropic case with a P-wave velocity of 3880 m/s (dashed red line) are given, as well with temperature correction (dashed green line). The temperature correction is done using equation (4.13).

four-point interpolation filter. Some of the picks were corrected due to distinct changes in the traveltime observed in the data of the 3C-geophones like, for example, visible for shot 44 of the detonation cord survey (Figure 7.2, a). To reduce the picking error, the first break, the first maximum and the first zero crossing of the direct arrival were picked from two different persons.

Mean velocities with temperature and elongation correction

In a first step mean velocities are calculated from the picked traveltimes of the first break (Figure 7.3, blue, solid line). Due to the VSP shooting geometry (Figure 6.12) the travelpath is just divided by the picked traveltime. Thus, the velocity is really a mean and not a RMS velocity. Additionally, mean velocities and traveltimes for the same travelpath as for the picked VSP velocities can be calculated using the zero-offset P-wave interval velocities (Figure 6.10, c) derived form the EDML eigenvalues (Figure 7.3, red solid line). This yields the opportunity of comparison between calculated and derived mean velocities.

For the calculation of the velocities from the EDML eigenvalues the elasticity tensor derived by Gammon et al. (1983) was used (Figure 7.3, solid red line). The velocities are afterwards corrected for the existing temperatures in the ice (Figure 6.10, a) with equation (4.13) (Figure 7.3, solid green line). For comparison mean velocities for isotropic ice (v_p=3880 m/s) are plotted in Figure 7.3, dashed lines (red and green, without and with temperature correction, respectively). They show strong deviations from the anisotropic velocities, especially below 2000 m depth.

Additionally, the depth of the borehole geophone was corrected for the elongation of the cable used to lower the borehole geophone into the EDML borehole. Due to the weight

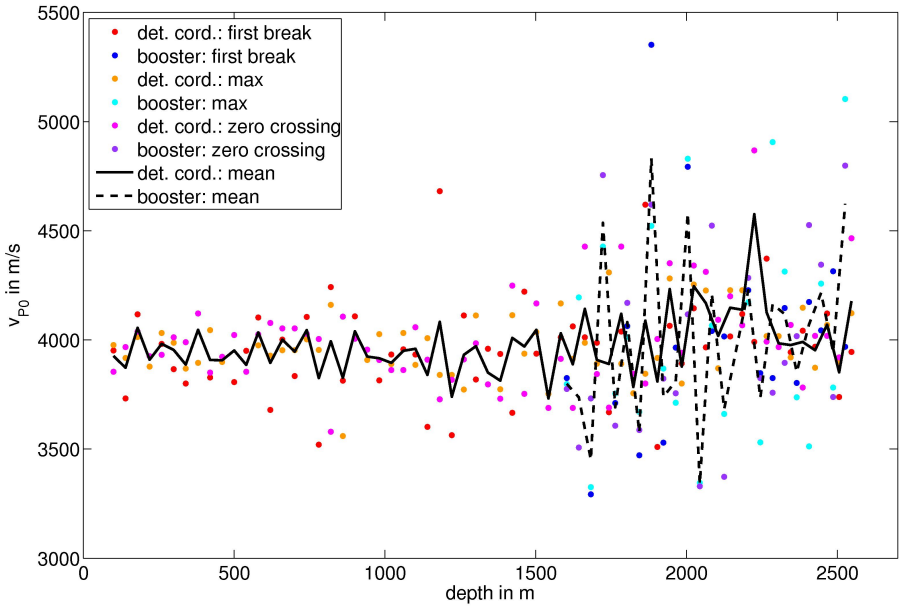

Figure 7.4: Interval velocities calculated from the picked traveltimes and the difference in the travelpaths, considering the VSP shooting geometry (Figure 6.12). The picks of the first break (fb), the maximum (max) and the zero crossing (zc) for the survey with detonation cord and booster are used here. The mean over the different picks (fb, max, zc) of the detonation cord and booster interval velocities is given by the black solid and dashed line, respectively. Plotted depth is to top of casing for comparison with Figures 7.1 and 7.2.

of the borehole geophone (25 kg) and more importantly the weight of the cable itself the cable stretches with increasing depth. The borehole is filled with a borehole fluid with a density of about the ice density. With the weight of the cable in a material with a density like ice of 212 kg/km the elongation of the cable, 0.44 m $km^{-1}kN^{-1}$, and the weight of the borehole geophone, 25 kg, the elongation can be calculated. Thus, the elongation is 6.3 m for the deepest measured depth at 2580 m. This effect was correct on the mean velocities (Figure 7.3, dashed blue line) as it has an effect on the total depth. However, for interval velocities this elongation effect becomes negligible ($\leq$20 cm).

Interval velocities

A better comparison of velocities determined from the VSP measurement and velocities derived from the EDML eigenvalues is the comparison of the interval velocities for the 40 m depth intervals between shots. Here, the traveltimes of the detonation cord and booster survey were analysed separately (Figure 7.4). Due to the shooting geometry (Figure 6.12) the difference in travelpath from one shot to the next is $\leq$40 m. For the calculation of the interval velocities the difference in the travelpath was used. Of course, small picking errors become more significant for interval velocities compared to the contemplation of the mean velocities. The idea was to reduce picking errors by combining the interval velocities derived from the different picks of the wavelet, i.e., first break (fb), maximum (max) and zero crossing (zc), of the direct wave. This is only valid if the wavelet does not change over depth due to, e.g., dispersion or frequency-dependent damping.

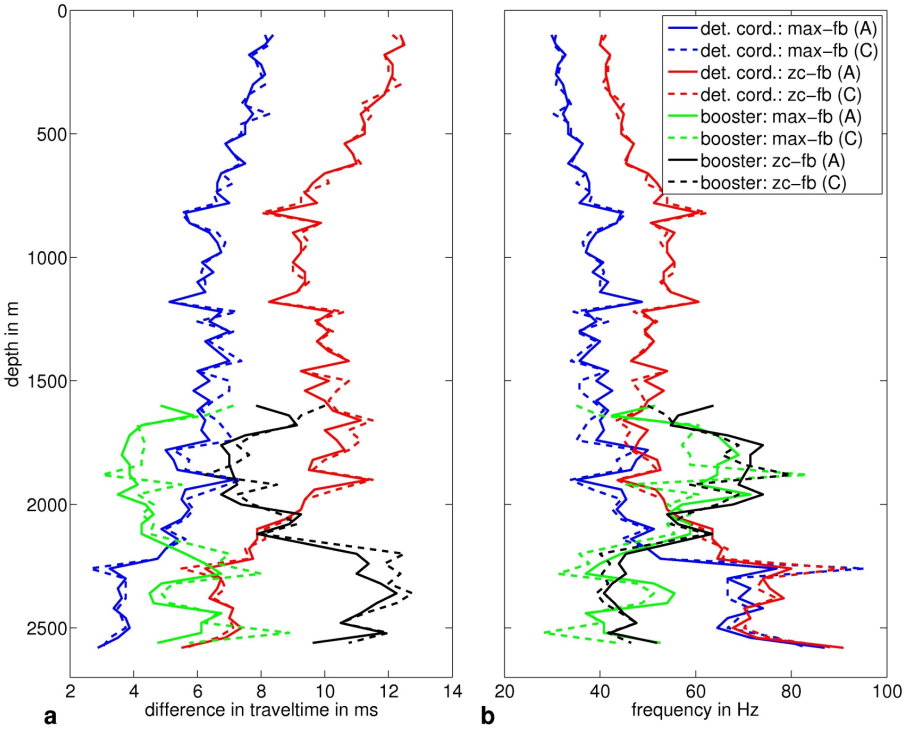

Figure 7.5: (a) Differences in picked traveltimes between first break (fb) and maximum (max), as well as first break and zero crossing (zc) of the direct wave, separate for detonation cord and booster picked from two different persons ((A), solid lines and (C), dashed lines. (b) Frequencies calculated from the differences in traveltime (a) for the different source types and picks with a constant velocity of 3880 m/s. Plotted depth is to top of casing for comparison with Figures 7.1 and 7.2.

Wavelet shape

For an unchanged wavelet shape over depth the traveltime difference between the picked maximum and the first break [max−fb], as well as the zero crossing and the first break [zc−fb] should be constant. Figure 7.5, a, shows these traveltime differences ([max−fb]-, [zc−fb]-traveltime difference) calculated separately for the detonation cord and booster source, as well as the picks of person A and C. The picks of person A (solid lines) and C (dashed lines) show very similar results. However, the traveltime differences are not constant over depth, hence, not independent of dispersion or frequency-dependent damping.

A change to larger traveltime differences calculated from the detonation cord survey ([max−fb] and [zc−fb], blue and red, respectively) can be observed from a depth of 2260 m towards shallower depth of 2220 m (depth to top of casing). This corresponds to the the transition from shot 9 (2260 m depth) to 10 (2220 m depth). The seismic traces of the 3C-survey in Figure 7.2, a show that Shot 10 is the first shot in this survey where the wavelet changes significantly. This change in wavelet shape is reflected, as well, in the interval velocities (Figure 7.4). The interval velocity calculated from the first break at 2260 m depth fits well into the neighbouring velocities (Figure 7.4, red dot) whereas the velocities calculated from the picked maxima and zero crossing stand out with 4848 m/s (Figure 7.4, orange and magenta dot). This indicates, that the velocity change at 2260 m depth is introduced by a

change in the excitation of the elastic waves rather than a change of velocity in depth.

The traveltime differences for the booster data ([max−fb] and [zc−fb]), green and black, respectively) show an increase between 2200 m and 2120 m depth, similar in strength as the traveltime differences of the detonation cord. However, this increase is opposite to the traveltime decrease in the detonation cord survey around 2200 m depth (Figure 7.5, a).

In case of the detonation cord the change in traveltime difference is definitely a feature of a changing wavelet due to a change in the excitation of the seismic waves , e.g., a change in the surface due to multiple shooting at this location. In case of the booster shots a lot of variations in the wavelet are observable for shots 10, 11 and 12 (Figure 7.2, b; shot 11 was not picked). The wavelets seem to be quite similar for shots 2 to 10 and then again for shots 15 to 25. The surveys with the detonation cord and the boosters were shot on two following days, so that the snow surface had time to settle again. Hence, these changes in the traveltime differences, in the detonation cord survey as well as in the booster survey, appear to be a feature from the changing surface during repeated shooting at the same location, rather than a change in the physical ice properties at depth.

Frequency of the wavelet

Taking the inverse of the traveltime difference frequencies (f) of the wavelet can be calculated (Figure 7.5, b). The [max−fb]- and [zc−fb]-traveltime differences of the booster survey as well as for the first 9 shots of the detonation cord survey yield the same frequencies. Hence, the [zc−fb]-traveltime difference is twice as large as the [max−fb]-traveltime difference. This means, that the maximum of the wavelet is centered between first break and zero crossing and the wavelet is symmetric. However, the frequencies calculated from [max−fb]- and [zc−fb]-traveltime differences of the detonation cord survey are not equal for shots 10–64 which corresponds to a depth $\leq$2260 m. Thus, the wavelet is asymmetric for these shots. This can as well be observed in the seismic traces of the 3C-geophones (Figure 7.2, a) where shot 10 is the first shot with a clear change in the wavelet shape.

The overall frequency trend is a slight increase in frequency with depth for the first 800 m. Normally, it is expected that the frequencies decrease with depth as the high frequencies are attenuated stronger. Hence, it is suggested that this increase in frequency with depth is an effect of the repeated shooting at one location. After repeated shooting at one location with alteration of the surface, coupling during the shot might become weaker. A possibility for the opposite trend in frequency for the detonation cord survey and the booster survey might be a different coupling behaviour for these two sources. While coupling decreases after repeated shooting in case of the detonation cord as source leading to lower excited frequencies, coupling increases in case of the booster as source leading to higher excited frequencies.

Altogether the derived interval velocities show larger variations for the boosters than for the detonation cord source (Figure 7.4, mean values, black lines, dashed and solid, respectively). The velocity determined from the picked maximum and zero crossing traveltime at 2260 m depth is significantly larger than the normal variations (about $\pm$200 m/s) around the mean velocity and can clearly by attributed to the change in wavelet shape. Therefore, these velocities are not considered for further calculations. In case of the booster survey variations around the mean velocity are altogether larger (about $\pm$800 m/s) and no strong velocity

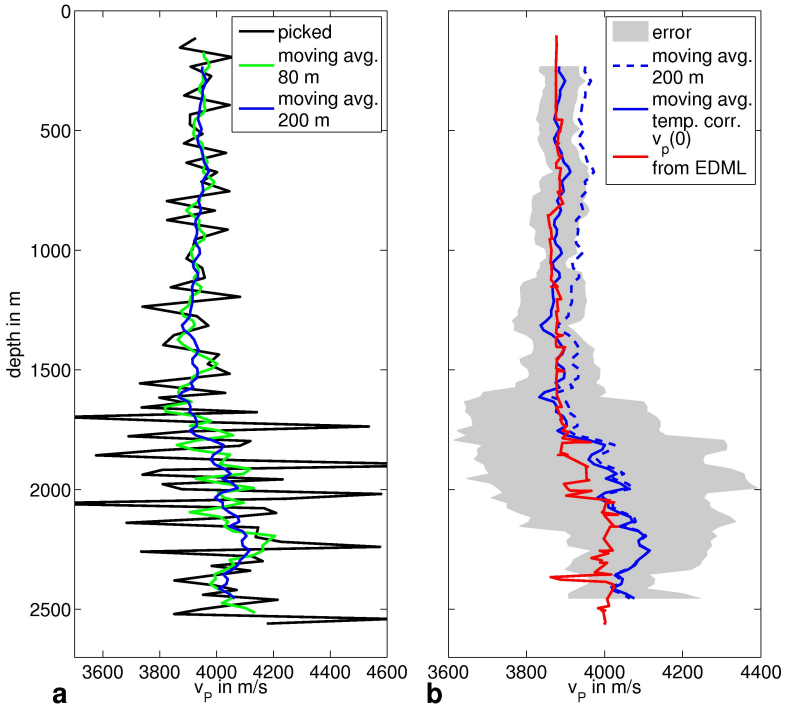

Figure 7.6: (a) Average interval velocity from the detonation cord and booster survey for the three different picks (first break, maximum, zero crossing) (black line) and its moving average with a sliding window of 80 m (green line) and 200 m (blue line). (b) Comparison between vertical P-wave velocity calculated from EDML COF values with the VSP interval velocity, 200 m moving average (dashed blue line) and temperature correction (solid blue line). The gray area gives the RMS error.

variations can clearly be attributed to changes in the wavelet. Thus, no corrections are done on these values.

Comparison VSP and EDML interval velocities

Figure 7.6, a, black curve, shows the mean interval velocities taking all derived interval velocities of the different sources (booster, detonation cord) and picks from different wavelet regions (first break, maximum, zero crossing) into account. To be able to compare these VSP interval velocities with the interval velocities calculated from the EDML COF eigenvalues (Figure 6.10, c) a 200 m moving average of the VSP interval velocities is used. This gives the possibility to compare the overall trend of the VSP and EDML velocity profiles (Figure 7.6, b, blue and red lines, respectively). Of course RMS errors of the VSP interval velocities are rather large (Figure 7.6, b, gray area), especially in the region between 1600 m depth and 2200 m depth. The large error in this region is attributed to incoherent excitation of elastic waves from the booster survey for shots 10 to 25.

The comparison of the EDML interval velocity (solid red line) and the VSP interval velocity (dashed blue line) in Figure 7.6 shows a difference of about 75 m/s at 200 m depth. This is an effect of the temperature gradient within the ice sheet and the influence of the temperature on the seismic wave velocity (sec. 4.4). Temperatures vary between $-44°C$ and $-7°C$ at

Kohnen station (Figure 6.9, b). The elasticity tensor used for the calculation of the EDML interval velocities is given for $-16°C$. Thus, the VSP interval velocities are corrected to $-16°C$ with equation (4.13) for the temperature distribution measured in the borehole of the EDML ice core (Figure 6.9, b). This improves the agreement between VSP and EDML velocities significantly above 1500 m depth (Figure 7.6, b, blue and red line, respectively).

The vertical EDML and VSP interval velocities show good agreement above 1800 m depth with a velocity around 3870 m/s. This is the region of cone fabric with large opening angles ($\leq$450 m depth) and girdle structures below (Figure 6.10, c). The VSP interval velocities show an abrupt change to larger velocities ($\geq$4020 m/s) at 1800 m depth. This is the region where the narrow cone fabric slowly starts to develop from the girdle fabric. The fine structured velocity variations observable in the interval velocities calculated from the EDML COF eigenvalues are not reflected in the VSP interval velocities. However, these structures are anyway a feature of the classification of cone and girdle fabric in the calculation of the opening angles. For the strong developed cone fabric with small opening angles below 2030 m depth the VSP and EDML interval velocities agree well again with an average velocity of $\sim$4040 m/s for the VSP velocities and $\sim$30 m/s slower for the EDML velocities.

For this comparison between EDML and VSP interval velocities an average of all interval velocities (picks from detonation cord, booster and first break, maximum, zero crossing and two different person) was calculated. However, to avoid including the effect of dispersion, hereinafter, the interval velocities of the first break, the maximum and the zero crossing are considered separately.

7.2 Different elasticity tensors

In section 4.2 the different elasticity tensors, calculated and measured, were introduced (Table 4.1). For the calculation of velocities in section 7.1 only the elasticity tensor derived by Gammon et al. (1983) was used. The vertical P-wave velocities calculated with the different elasticity tensors are plotted together with the VSP interval velocities from the first break, the maximum and the zero crossing in Figure 7.7. Thus, the influence of the different elasticity tensors on the results can be compared to each other,

The VSP interval velocities are corrected for the temperature distribution (Figure 6.9, b) within the ice sheet with equation (4.13) to $-16°C$. The only elasticity tensor that is not given for a temperature of $-16°C$ is the one of Bennett (1968) which is given for $-10°C$. Therefore, the P-wave velocity calculated using the elasticity tensor of Bennett (1968) is as well corrected with equation (4.13) to $-16°C$.

The different vertical P-wave velocities calculated from the different elasticity tensors all follow the same velocity trend over depth, as this is determined by the COF eigenvalues. The highest P-wave velocities are calculated from the theoretically derived elasticity tensor of Penny (1948), the lowest derived P-wave velocities from the elasticity tensor of Bass et al. (1957), who used the resonance frequencies to derive the components of the elasticity tensor. The velocities derived from the elasticity tensors of Gammon et al. (1983), Jona and Scherrer (1952) and Bennett (1968) all show good agreement with the VSP velocities. While the velocities derived by the Jona and Scherrer (1952) and Gammon et al. (1983) elasticity tensor fit well to the VSP velocities above 1800 m, hence, for lower velocities of $\sim$3870 m/s

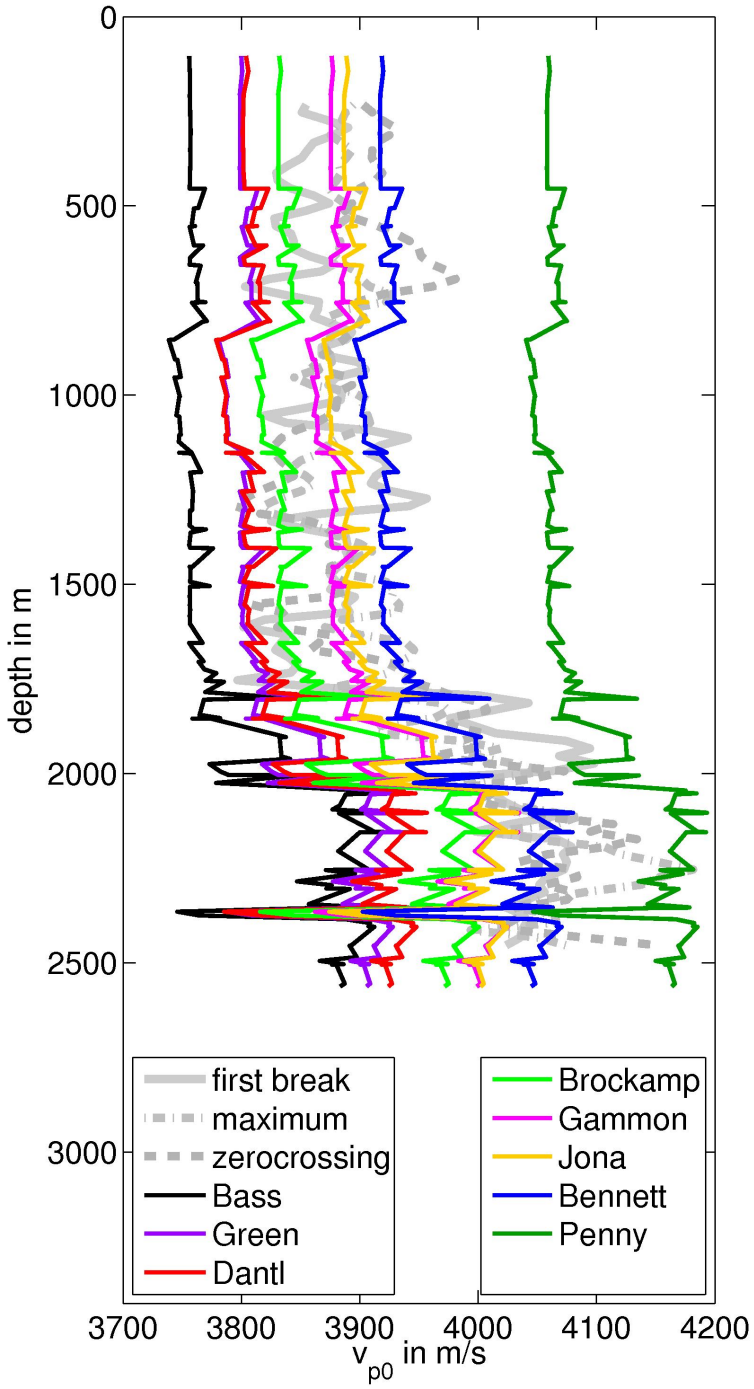

Figure 7.7: Comparison of vertical P-wave velocities calculated from the EDML eigenvalues with different elasticity tenors (Table 4.1) with the interval velocities derived from the VSP data sets for the first break, the maximum and the zero crossing (gray lines)

	first break	maximum	zero crossing
Bass et al. (1957)	147	160	155
Green and Mackinnen (1956)	115	125	121
Dantl (1968)	106	117	112
Brockamp and Querfurth (1964)	79	87	83
Gammon et al. (1983)	**59**	**61**	**57**
Jona and Scherrer (1952)	**58**	**57**	**54**
Bennett (1968)	**62**	**53**	**52**
Penny (1948)	171	155	159

Table 7.1: RMS difference in m/s between the vertical P-wave velocities calculated with the different elasticity tensors (Table 4.1) and the VSP interval velocities for first break, maximum and zero crossing picks.

depth, the ones derived from the Bennett (1968) elasticity tensor fit better below for the higher velocities ∼4040 m/s.

To find the elasticity tensor which describes our VSP interval velocities best the RMS difference between the VSP interval velocities from first break, maximum and zero crossing picks and the EDML interval velocities derived with the different elasticity tensors were calculated (Table 7.1). The elasticity tensors given by Jona and Scherrer (1952) shows the smallest difference to the VSP velocities. However, keeping the error bars in mind (up to ±350 m/s; Figure 7.6, b) the velocities derived from the elasticity tensors of Gammon et al. (1983), Jona and Scherrer (1952) and Bennett (1968) are all capable of explaining the velocity profile derived from the VSP survey by using the EDML COF values. Neither elasticity tensor reaches the complete range of minimum and maximum interval velocities (3870–4040 m/s) of the VSP results between the more isotropic velocities towards the surface and velocities of the strongly developed cone fabric below 2030 m depth. The Gammon et al. (1983) and Jona and Scherrer (1952) RMS differences are smaller than the Bennett (1968) RMS differences. This is because the EDML interval velocities derived from the Gammon et al. (1983) and Jona and Scherrer (1952) elasticity tensor fit well with the VSP velocities above 1800 m depth, while the EDML interval velocities derived from the Bennett (1968) elasticity tensor fit well with the velocities below 1800 m (Figure 7.7). Due to the larger depth interval and, thus, greater weight of the region between 200 m and 1800 m depth, with lower velocities, compared to the region between 1800 m and 2600 m depth, with higher velocities, EDML interval velocities derived from the Gammon et al. (1983) and Jona and Scherrer (1952) elasticity tensor give the smaller RMS differences.

7.3 Temperature

Next to identifying the elasticity tensor that fits the data best I investigate the temperature correction that is necessary to correct for the difference between the temperature at which the elasticity tensor was measured and the temperatures within the ice sheet (Figure 6.9) to be

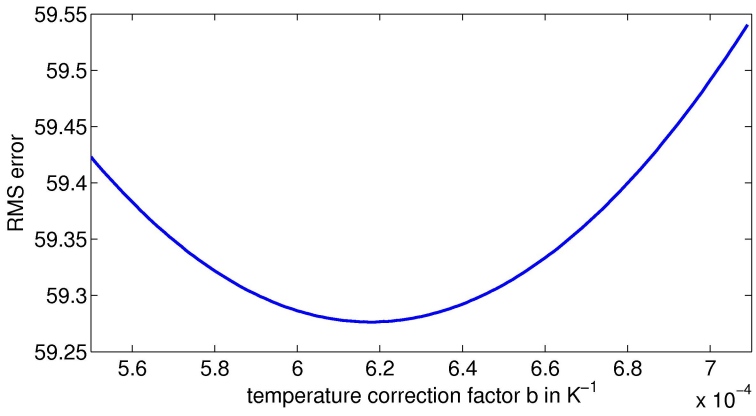

Figure 7.8: RMS error between VSP and EDML interval velocities for different temperature corrections of the VSP interval velocities to -16°C. The EDML interval velocities are calculated using the the elasticity tensor of Gammon et al. (1983), for the temperature correction equation (4.13) is used. The minimum can be found for $b = 6.18 \cdot 10^{-4}$ K^{-1}

able to compare VSP and EDML interval velocities. For this investigation of the temperature correction the mean velocities (Figure 7.3) could be used as well. However, to avoid dealing with the influence of the velocity variations due to the density gradient within the firn pack the interval velocities are used again.

The VSP interval velocities (first break pick) are corrected with equation (4.13) to -16°C and compared to the EDML interval velocities calculated using the elasticity tensor of Gammon et al. (1983). The temperature correction factor b in equation (4.13) is varied between $5.5 \cdot 10^{-4}$ and $7.1 \cdot 10^{-4}$ K^{-1}. To find the best fit between temperature corrected VSP and the EDML interval velocities the RMS error is calculated (Figure 7.8). The best agreement is found for $b = 6.18 \cdot 10^{-4}$ K^{-1}. This corresponds to a velocity gradient $\Delta v_\mathrm{p} = b v_\mathrm{p}(0°\mathrm{C})$ between 2.5 m s^{-1}K^{-1} ($v_\mathrm{p}(0°\mathrm{C})$=4040 m/s) and 2.3 m s^{-1}K^{-1} ($v_\mathrm{p}(0°\mathrm{C})$=3780 m/s; sec. 4.4), depending on the 0°C P-wave velocity $v_\mathrm{p}(0°\mathrm{C})$. The difference between the value derived here ($b = 6.18 \cdot 10^{-4}$ K^{-1}) and the value for the temperature correction factor given by Gammon et al. (1983) ($6.196 \cdot 10^{-4}$ K^{-1}) is negligible.

Most of the values given by other authors (Table 4.4) for the temperature gradient Δv_p are around 2.4 m s^{-1}K^{-1}. The larger values (3.4–7.4 m s^{-1}K^{-1}) given for the temperature gradient as derived by, e.g., Thiel and Ostenso (1961); Brockamp and Kohnen (1965); Thyssen (1966); Bass et al. (1957), are too large for the temperature correction in case of our picked VSP velocities compared to the EDML velocities.

7.4 Discussion of VSP survey

Interval velocities derived from a VSP survey within the borehole of the EDML ice core at Kohnen station were compared to interval velocities derived from the COF eigenvalues of the EDML ice core (sec. 7.1). The comparison shows good agreement between the VSP and EDML interval velocities. The main trend of the VSP velocity profile, velocities ∼3870 m/s above 1800 m depth, an increase in velocity between 1800–2030 m depth and velocities ∼4040 m/s below 2030 m, can be reproduced with the calculations of velocities from the COF eigenvalue data.

The interval velocities derived from VSP are compared to the zero-offset velocities calculated

from the eigenvalues. As the shots during the survey were carried out on the surface 30 m away from the drill location of the EDML ice core (Figure 6.12) the travelpath of the seismic wave is not zero-offset. The first measurement was done at a depth of 100 m. This corresponds to an angle between borehole and travelpath of 14.8°, neglecting effects of refraction within the firn. In the anisotropic case the velocity for an incoming angle θ of 14.8° differs of course from the zero-offset velocity. For the existing anisotropy in this depth region, with a cone opening angel $\varphi = \chi \approx 75°$, the difference between the zero-offset velocity and the $v_p(\theta = 14.8°)$ is <5 m/s. At the depth of 450 m where a stronger girdle anisotropy develops the angle between borehole and wave propagation θ is already only 3.7°. Thus, the error that is introduced by using the zero-offset EDML interval velocities for the comparison to the VSP interval velocities instead of the velocities corresponding to the actual angle between borehole and travelpath during the VSP survey is found to be negligible.

For the calculation of the VSP interval velocities the traveltime differences between the 40 m shot intervals are used. Another effect of the VSP shooting geometry (Figure 6.12) is that the used intervals determine the investigated layer thickness. The boundaries between thus layers are tilted as the layer boundary is normal to the travelpath of the wave. Thus, the actual depth difference between shots is not 40 m but depends on the difference in the length of the travelpaths ($\leq$40 m). For the calculation of the interval velocities the difference between the travelpaths is used, so this is taken into account. Another effect is that due to the titled layer boundaries the derived velocity is assigned to a wrong depth interval. However, this makes a difference of 2 m at 100 m depth, i.e., the derived interval velocity at 100 m depth is actually at 102 m depth, approaching to zero for increasing depth. Thus, this effect is regarded as negligible as well.

The comparison of VSP velocities to velocities derived form the EDML COF eigenvalues using different elasticity tensors showed best agreement for the elasticity tensors of Gammon et al. (1983), Jona and Scherrer (1952) and Bennett (1968). A recent study that investigates the influence of COF on elastic waves was done by Gusmeroli et al. (2012). They carried out an ultrasonic sounding experiment within the deep borehole at Dome C, East Antarctica exciting P- and SV-waves with frequencies of 28 kHz. They compared their picked velocities from the ultrasonic sounding with velocities calculated by averaging the VSM-fabric velocity for different incoming angles as introduced by Bentley (1972). They found best agreement between their picked velocities and velocities calculated based on the elasticity tensor derived by Dantl (1968). This is in strong contrast with the results here, where the velocities derived with the elasticity tensor from Dantl (1968) (Figure 7.7, red line) show a poorer fit to the VSP interval velocities (Table 7.1). Possible reasons for the different results include the difference in calculation of the velocities or the fact that the samples in this VSP study are over significantly larger depth intervals from shot to shot than for the ultrasonic sounding. However, more likely is that the different result reflects the difference in the used frequencies. While Gusmeroli et al. (2012) use frequencies in the kHz range the seismic waves of the VSP Kohnen survey are around 100 Hz (Figure 7.5, b). The dependency of seismic wave velocities on the frequency is not yet understood.

7.5 Conclusions of VSP survey

The comparison of VSP and EDML velocities shows that the velocities calculated form the COF eigenvalues show the same trend in the velocity profile as the VSP velocities. The small-scale variations in the EDML interval velocities reflect the increments of the COF eigenvalues and the classification of these eigenvalues in the different fabrics for the calculation of opening angles. This is especially obvious for the increase in velocity in the region between 1800 and 2030 m depth where the narrow cone fabric develops from the girdle fabric. Here, eigenvalues are classified as cone and girdle fabric alternately. These variations in velocity are, thus, an effect of this classification and can not be expected to appear in the VSP velocity profile.

At 2345 m depth a thin layer, with a thickness of 40 m, consisting of girdle fabric exists. It is unlikely to detect such a signal with the VSP interval velocities. One point is, that the frequencies for the detonation cord survey at this depth are between 70–80 Hz, for the booster survey between 40–50 Hz. With a velocity of ∼4040 m/s, like present at this depth, the wavelength can be calculated to be ∼50 m and ∼70 m, respectively. Additionally, depth intervals between the shots are 40 m and shifted compared to the depth interval of the girdle fabric. Finally, for the comparison of VSP and EDML velocities a 200 m moving average of the VSP interval velocities is used to compare the main trend of the velocity profile. All this leads to an averaging over larger areas with different velocities so that such short pulse signals, although strong in their velocity change, are not detectable.

For the comparison of the EDML interval velocities in Figure 7.7 the VSP interval velocities are plotted separately for the picked traveltimes of first break, maximum and zero crossing. They show very similar velocities below 1800 m depth, towards the surface variation becomes larger with the lowest velocities calculated from the picks of the first break and the highest velocities from the picks of the zero crossing. This effect is attributed to the changing wavelet form due to repeated shooting at the same location (Figure 7.2). Both VSP surveys show a change in the form of the wavelet after 9 shots and while frequencies decrease for later shots using detonation cord, they increase using boosters as source. Thus, care has to be taken when data are analysed with numerous shots at the same location. In case of detonation cord this should be avoided, while in case of boosters the repeated shooting at the shot location seem to help to increase the coupling.

The comparison of the EDML interval velocities (Figure 7.7) calculated from different elasticity tensors (Table 4.1) with the VSP interval velocities showed best agreement using the elasticity tensor of Gammon et al. (1983); Jona and Scherrer (1952) and Bennett (1968), respectively. However, for all three cases it is either the low velocities above 1800 m depth or the high velocities below 2030 m depth that fit well. With none of the elasticity tensors the full range between low and high velocities (3870–4040 m/s) can be obtained. Two effects are likely responsible for this: (i) the actual values of the monocrystal elasticity tensor and (ii) the calculation of the polycrystal elasticity tensor. The components of the elasticity tensor determine the velocity, e.g., the component C_{33} determines the zero-offset velocity v_{p0} while the component C_{11} determines the horizontal velocity $v_{\mathrm{p}}(90^\circ)$. If the difference between these two values is small, the velocity difference is small and also the range of velocities that can be calculated for different anisotropic fabrics from these values. The same applies for the other components of the elasticity tensor. The other reason for the limited range of velocities might be in the calculation of the polycrystal elasticity tensor by integration

over the monocrystal elasticity tensor (sec. 4.2). The velocities calculated for an isotropic ice crystal (sec. 4.2.1) derived from the monocrystal elasticity tensor are not isotropic. This could also be observed on the corresponding Thomsen parameter δ (sec. 4.2.2) that is not zero for the isotropic ice crystal. Thus, the calculation of the elasticity components become more inaccurate with larger cone opening angels. As the calculated 'isotropic elasticity' is, thus, still slightly anisotropic the velocities for large cone opening angels might be overestimated.

The result, that the elasticity tenors of Gammon et al. (1983); Jona and Scherrer (1952) and Bennett (1968) gain equally good results by explaining the VSP interval velocities stands in contrast to the findings of the ultrasonic logging experiment of Gusmeroli et al. (2012). They concluded that the elasticity tensor given by Dantl (1968) explains their determined velocities best. These different results and the difference in the used frequencies of the experiments indicate a frequency dependency of seismic waves in ice that is, so far, not understood.

For the following analysis of seismic data in Chapter 8 and 9 the elasticity tensor given by Gammon et al. (1983) will be used. Gammon et al. (1983) did the most comprehensive measurements on artificial and natural ice from different locations. Additionally, he investigated the temperature dependency and gives equations for the temperature corrections on the elasticity tensor itself.

8 Improved interpretation of combined seismic, radar and ice-core data

It is often difficult to clearly identify the origin of reflections especially in radar data. A comparison between different data sets can help here, for a better understanding of the reflection origin. In the following ice core, seismic and radar data sets are compared to each other from Colle Gnifetti (sec. 8.1) and Kohnen station (sec. 8.2) to identify, in particular, COF-induced reflections. The results are discussed in section 8.3.

8.1 Comparison of data sets from Colle Gnifetti

Diving waves from the SH-wave survey at Colle Gnifetti are used to determine a velocity profile over depth for the firn region. By combining these velocities with density measurements from the ice core KCI a new S-wave velocity–density relationship is derived (sec. 8.1.1) (Diez et al., submitted) that was already introduced in section 4.3. The P- and SH-wave seismic data are combined with the measurements of physical properties of the ice-core KCI, density and COF, as well as radar data to identify the origin of seismic reflections (sec. 8.1.2, 8.1.3) (Diez et al., 2013).

8.1.1 New S-wave–density relationship from diving waves

At Colle Gnifetti the vibroseis source ElViS was used to excite P- and also SH-waves. Kohnen (1972) derived a relationship between P-wave velocity and density, equation (4.9). King and Jarvis (2007) derived the Poisson's ratio in polar firn, from velocity-depth functions of P- and S- waves derived from diving waves. However, no relationship exists connecting S-wave velocity and density. To compare SH-wave velocities derived from the seismic reflection data (sec. 6.1.2) with velocities calculated from the KCI ice core data (sec. 6.1.1) I derive a relationship here that connects the S-wave velocity with the density.

The diving waves of the Colle Gnifetti SH-wave survey are analysed using the Herglotz-Wiechert inversion (Slichter, 1932) to derive a velocity-depth profile for the S-wave within the firn. As the diving waves are continuously refracted waves, the ray parameter p at the deepest point (Z) that is reached by the diving wave is equal to the inverse of the velocity. Hence, for the S-wave

$$p = \frac{1}{v_\mathrm{s}(Z)}. \tag{8.1}$$

The goal is to derive the depth z for the velocity v_s from traveltime–offset pairs (Aki and

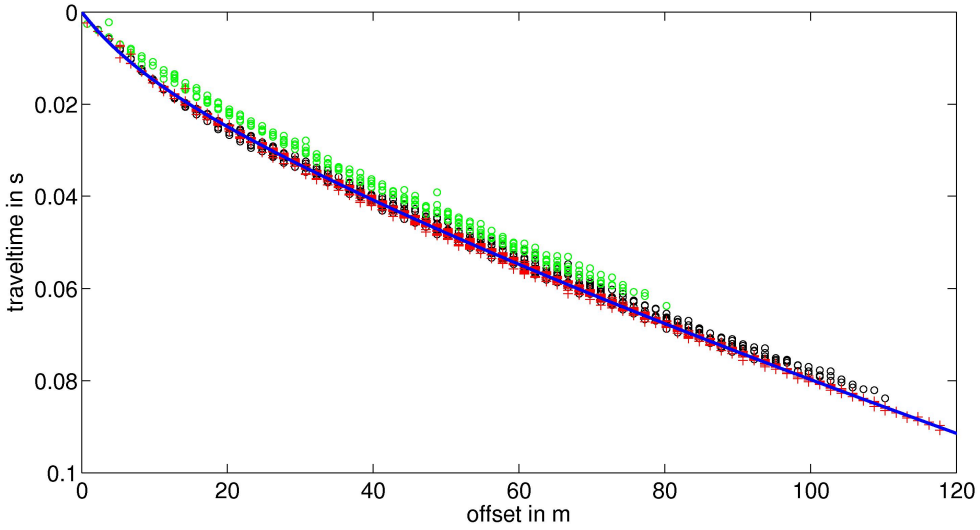

Figure 8.1: Red crosses: picked traveltimes of shots outside of the geophone line of Profile 1; black circles: picked traveltimes of shots outside of the geophone line of Profile 2, west of KCI; green circles: picked traveltimes of shots outside of the geophone line of Profile 2, east of KCI with fitted curve in blue.

Richards, 2002; Kirchner and Bentley, 1990), with

$$z(v_{\mathrm{D}}) = -\frac{1}{\pi}\int_{x=0}^{x=D}\left[cosh^{-1}\left(\frac{v_{\mathrm{D}}}{v_{\mathrm{A}}(x)}\right)\right]^{-1} dx. \tag{8.2}$$

The velocity $v_{\mathrm{D}} = (\partial x/\partial t)_D$ is the gradient of the traveltime t at the greatest source-to-receiver offset D, whereas v_{A} is the apparent velocity given by $v_{\mathrm{A}}(x) = x/t$.

To derive the velocity v_{D} traveltimes of approximately every 3 shot outside of the geophone line from both SH-wave profiles were piked (Figure 6.1, b and Figure 8.1). The shots outside the geophone line, so shots with large offset (up to 120 m), are important to get information of deeper layers within the firn. Figure 8.1 shows the picks of Profile 1 in north and south direction (red crosses) and of Profile 2, towards the west (black circles) and towards the east (green circles). While the picked traveltimes of Profile 1 for the same offset vary only little ($\sim$0.003 s), the variations for Profile 2 are significantly larger ($\sim$0.006 s), especially the difference between the east and west side of the profile can clearly be seen. This reflects the high variability of the accumulation pattern found at Colle Gnifetti (Alean et al., 1983). The traveltimes of Profile 1 are clearly more homogeneous. To be able to compare these velocities derived from the seismic traveltimes with results obtained from the ice core, so a point measurement, only the traveltimes of Profile 1 are used for the following analysis.

To fit a curve to the picked offset-traveltime pairs I follow the approach by Kirchner and Bentley (1990) and fit a curve of the form

$$t = a(1 - \mathrm{e}^{-bx}) + c(1 - \mathrm{e}^{-dx}) + ex, \tag{8.3}$$

with the variables a, b, c, d and e offset x and traveltime t (Figure 8.1, blue line). With this traveltime-offset relationship the velocity v_{D} can be calculated. Thus, a S-wave velocity–

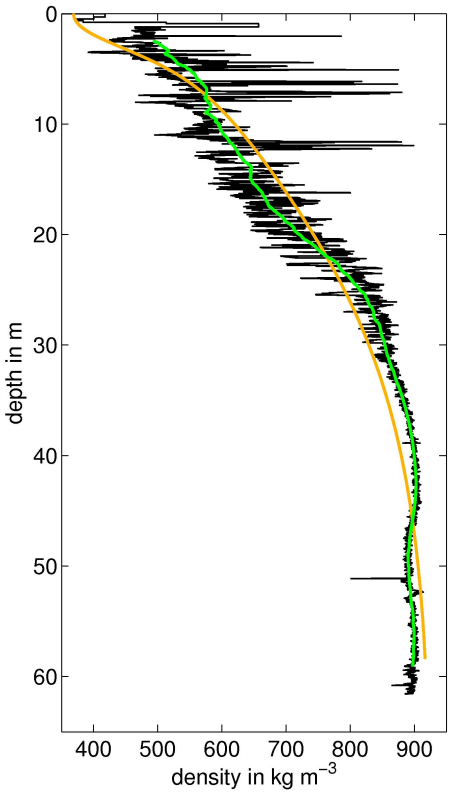

Figure 8.2: Densities from the KCI ice-core in black with 0.5 m moving average in green. Orange gives the best fit between the moving average of the KCI densities and densities calculated from the S-wave velocities of the diving waves (Profile 1). This yields the new S-wave velocity–depth function (eq. (4.10)).

depth relationship is derived from the SH-wave data from Colle Gnifetti. This velocity-depth function is then used to find the best fit to a moving average (Figure 8.2, green line) of the KCI densities (black line) for a velocity-density function of the form given by Kohnen (1972) for the P-wave. This yields the S-wave velocity–density function given in equation (4.10), section 4.3. The orange line in Figure 8.2 shows the corresponding densities over depth. The RMS deviation of densities calculated from the S-wave velocities derived from the diving waves of Profile 1 (orange line) to a moving average of the KCI densities (green line) is ± 25 kg/m^3. This deviation is small, especially above the firn-ice transition, compared to the variations of the measured KCI densities (black line) to its moving average (green line) with ± 48 kg/m^3 above and ± 5 kg/m^3 below 30 m depth.

8.1.2 Englacial seismic reflections

For the different lines and wave types of the ElViS-survey at Colle Gnifetti, different frequency ranges for the sweeps were chosen (Table 6.1). The maximum resolution (quarter wavelength) can be calculated from the center frequency of the sweeps and the P- and S-wave velocity in ice, with 3900 m/s and 2100 m/s, respectively. Thus, for the P-wave surveys, a theoretical resolution of 7 m (frequency 30–240 Hz) for Profile 1 and 11 m (frequency 20–160 Hz) for Profile 2 is obtained; for the SH-wave surveys 2.5 m (frequency 60–360 Hz) for Profile 1 and 4 m (frequency 30–240 Hz) for Profile 2. Hence, the SH-wave has a more than twice as good resolution than the P-wave with the same maximum frequency content (240 Hz), which is due to the slower velocity of the S-wave in comparison to the P-wave. The resolution is of course better within the firn column, where velocities are slower. The smallest wavelength starts with about 2 m for the SH-wave and 6 m for the P-wave. The resolution then decreases over depth with increasing seismic velocities due to increasing

densities. Since the ElViS sweeps for Profile 1 contained higher frequencies resulting in higher resolution data for both the P-wave and SH-wave surveys of Profile 1 in respect to Profile 2, only results of Profile 1 are used to investigate the origin of the englacial reflections and comparison to radar and ice-core data.

P-wave data from Profile 1 (Figure 6.3) show a first strong reflection at 10 m depth, followed by two weaker reflections. A strong englacial reflector at 30 m depth can be observed, followed by a quiet zone. The strongest reflection in the section is the bed reflector at around 60 m depth, with another strong englacial reflection just above the bed at around 50 m depth.

In the SH-wave section of Profile 1 (Figure 6.3) some obliquely incident signals are seen towards the north side of the profile, where the ice drops towards the Monte Rosa east face. A couple of reflections are observed between the surface and around 10 m depth and a strong reflection is visible around 20 m depth. Further down the reflections are less pronounced, with some laterally coherent signals around 30, 40 and 50 m depth, followed by the strong bed reflection at around 60 m depth.

8.1.3 Comparison with ice-core and GPR data (Colle Gnifetti)

An improved understanding of the physical ice properties that produce the englacial seismic reflections observed in the ElViS P-wave and SH-wave surveys can be gained by comparing the seismic data with GPR and ice-core data. In Figure 8.3, a GPR profile (a) and a single GPR trace (b) are plotted together with the ice-core density (c) and COF data (d), as well as part of the SH-wave (e) and P-wave section (f) of Profile 1. The differences in resolution for these measurements range from sub-centimeter scale for the ice-core densities, to around 16 cm resolution for the GPR data in ice, $\leq$7 m for the P-wave data, and $\leq$2.5 m for the SH-wave data as well as 5 m for the COF data. Different events are marked with A to F. A comparison of the GPR and the ice-core data was performed by Eisen et al. (2003) and Bohleber (2011) to clarify the origin of reflection horizons in the GPR data. The comparison of seismic, density and radar data was discussed in Diez et al. (2013) before the COF data were available.

Prior to comparison, the P- and SH-wave sections have to be shifted in depth to obtain a consistent lower boundary of the seismic sections with the ice-core data and GPR sections. The ElViS survey (2010) was conducted 5 years after the drilling of the ice core KCI (2005). During these 5 years, about 1.75 m of snow were accumulated at the surface, measured at the borehole casing. This causes an analogous shift in the depth of some physical properties like ice layers and impurities, i.e., they are advected downwards. The GPR data were also corrected for the additional accumulation between 2005 (ice-core drilling) and 2008 (GPR measurement) (Bohleber, 2011). To achieve a consistent lower boundary, the seismic data are shifted down for 3 m, so the bed reflections of the seismic sections fit with the 62 m ($\pm$1 m accuracy) of the ice-core and the GPR data. This shift is feasible, as the TWT-to-depth conversion is within an accuracy of 10–15%. Thus, it is possible to compare the seismic signals to the GPR and ice-core data (Figure 8.3).

The depth of event A at around 10 m denotes the first clear reflection of the seismic SH-wave data. Strong peaks are visible in this region in the density data. The second event, B, shows a prominent peak in the density data and is the onset of a series of englacial-reflection

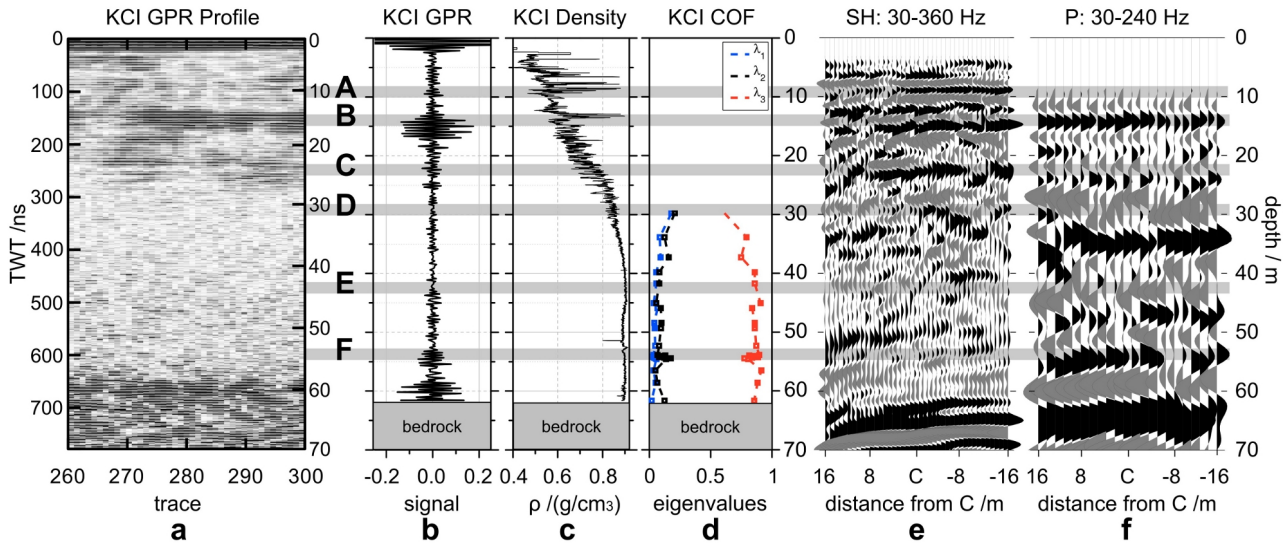

Figure 8.3: Comparison of radar (a–b), ice-core (c) and seismic (c–d) date from Colle Gnifetti. Signals marked with A–F are discussed in the text.

horizons in the GPR data. At this depth the first strong reflection in the P-wave data is also visible. Reflections near event B exist in both the P-wave and SH-wave data, but in case of the SH-wave data they are not clearly separated from the reflections of event A.

The region between events C and D contains the firn–ice transition zone with the pore close-off. The density data show no strong peaks in this depth range, but a decrease in density variability. At event C the deepest continuous englacial reflection horizon in the GPR data can be observed. In the seismic data, a strong reflection is present in the SH-wave profile, that also appears to be subdued, though visible, within the P-wave profile. At event D, just below the firn–ice transition, a distinct reflection is visible in the P-wave profile, but is unclear in the SH-wave profile. No corresponding signal can be found in the GPR data. Below event D, COF measurements exist for further comparison. In the depth range 40–50 m, around event E, a rather quiet zone can be observed in the seismic data as well as in the ice-core density and COF data. Some strong signals are visible in the single trace plot of the GPR data. However, a coherent continuous GPR reflection horizon is missing. Below, near event F, a strong reflector in the P-wave data can be seen, though no distinct reflection is observable in the SH-wave data. The depth of event F corresponds to a region of variations in the COF. The GPR data show a rather blurred subglacial bed reflection. However, the bed is clearly visible in both the SH- and P-wave data (Figure 8.3).

8.1.4 Interpretation of englacial reflections (Colle Gnifetti)

The reflections in the P-wave data, as well as in the SH-wave data, in the region of A and B, seem to be caused by peaks in the density distribution from melt layers and ice lenses within the firn pack. The region between events C and D does not correspond to strong changes in ice-core densities over short depth scales, in contrast to the reflections due to density inhomogeneities near events A and B. These observed reflections, events A and B, are caused by changes in seismic velocities within the ice, which suggest a change in

COF or some change in seismic velocities due to pore close-off in the firn-ice transition zone. As COF measurements only exist below the firn–ice transition, i.e., below event D, a change can neither be confirmed nor excluded as reason for this reflection. Polom et al. (2014) could derive a change in the Poisson ratio from P- and S-wave velocities for the depth between events C and D, where the strong englacial seismic reflection in the P-wave data is observed. Reflections from the firn–ice transition zone have also been observed in ElViS data from Antarctica by Eisen et al. (2012). The reason of low GPR reflectivity below the firn–ice transition zone is still unclear. It can currently only be speculated that signal reduction is because clutter is involved (Konrad et al., 2013).

For the split reflector about 2 m above the bed of the SH-survey, I suspect that the upper signal is due to some layered dirt intrusion which was found when drilling was stopped at 62 m depth. The second reflection then belongs to the actual bed. The reflection 5 m above the bed in the P-wave data (event F) is more difficult to interpret, especially as there is no counterpart in the SH-section. No clear signal can be seen in the radar section, Nevertheless, an increase in reflection power can be observed in the single radar trace. The density minimum at around 51 m is probably an artifact, due to an unnoticed crack in the ice core. The small positive inhomogeneity in the density profile at around 52 m seems to be real and would cause a reflection coefficient of $\sim$0.009. However, this density jump should also cause a reflection in the SH-wave data as strong as in the P-wave data. As there is no reflection in the SH-data at that depth, it is not likely that the P-wave reflection is due to the density anomaly. Another possibility for englacial reflections at this depth are again changes in seismic velocity due to changes in the orientation of the anisotropic ice crystals, i.e., changes in COF over depth. Measurements with a borehole radar carried out during the field season 2010 tentatively indicate that anisotropic ice fabric might exist in the lowest part of the ice column (Bohleber, 2011). The COF measurements reveal variations in the orientation of the ice crystals at this depth, that might be responsible for the reflection in the P-wave data.

8.2 Kohnen wideangle data

At Kohnen station COF measurements as well as radar data exist next to the seismic data sets. These three data sets are compared to each other for a better understanding of the origin of englacial seismic and radar reflectors with a focus on changing COF. Unfortunately it was not possible to unambiguously identify englacial reflections in the seismic shot records after processing. Therefore, 60 traces of one shot were stacked. This enhances the SNR (sec. 8.2.1) and it was possible to identify distinct englacial reflections. Thus, a comparison of seismic, radar and ice-core data is possible (sec. 8.2.2, 8.2.3).

8.2.1 Stacked seismic traces

After processing the different wideangle data sets from Kohnen station it was not possible to follow englacial reflection moveouts in these shot gathers (app. B.1). The data was, therefore, NMO corrected using the velocities derived during the VSP-survey (sec. 7.1). Afterwards, the first 60 traces of each shot where stacked to enhance the SNR.

To stack 60 traces of one shot is, of course, only valid for flat layers. Figure 8.4 shows the

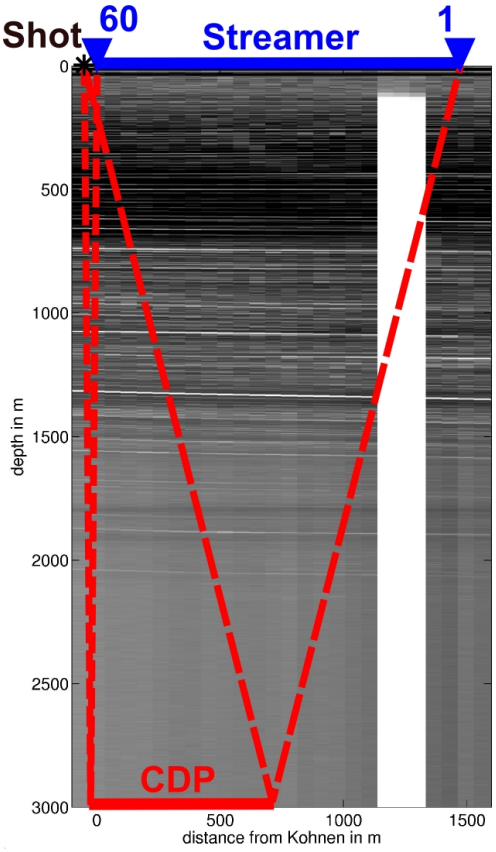

Figure 8.4: Travelpath of seismic wave from shot to receiver reflected at the ice-bed interface for the first channel and last channel (channel 60) of the 1.5 km long streamer on a radar sections (60 ns pulse, 023150) close to the seismic survey to illustrate the flatness of the englacial layers for the used shot–geophone spread (to scale).

direct travelpath from the seismic source at the surface down to the ice-bed interface and back to the streamer. The travelpath is plotted onto a radar section at Kohnen parallel to the ice divide to illustrate the curvature of the layers. The englacial reflections in the radar data are not completely flat. As the dip is only in the range of 1° they can be considered to be flat for the following analysis.

Unfiltered stacked seismic traces from the different explosive and vibroseis shots carried out at Kohnen in the seasons 2012 and 2013 are compared in Figure 8.5. The compared traces include data from the parallel and perpendicular lines of the wideangle surveys with vibroseis (para-vib, g; perp-vib, h) and explosives in 12 m (para-exp-12m (5.6 kg), b; perp-exp-12m (5.6 kg), d) and 30 m boreholes (perp-exp-30m (5.6 kg), e) with 5.6 kg charge size (Table 6.3). Additionally, data from profiles with explosives in 12 m boreholes and 0.4 kg charge size (para-exp-12m (0.4 kg), a; perp-exp-12m (0.4 kg), c) and a shot of a detonation cord survey (det. cord. (1.8 kg)) is used. The traces stacked from filtered data can be found in the appendix B.3. Frequency and *fk*-filters reduce surface, diving and air wave signals. However, *fk*-filtering normally induces strong noise as well, with a dip close to that of the edge of the filter. By stacking filtered data sets filter induced noise might interfere constructively. Thus, noise might by interpreted. By stacking the traces after NMO correction diving and surface waves interfere destructively and the signals are weakened. Therefore, the stacked raw data are used for the interpretation.

The bed reflection is visible at ∼1.44 s TWT in all shots of Figure 8.5. Traces are individually scaled. For the vibroseis shots the signals seem to arrive earlier. This is due to the fact, that the vibroseis wavelet is not a minimum phase wavelet in contrast to the wavelet of explosive shots. The vibroseis data (Figure 8.5, g–h) show some englacial signals, for example at ∼0.85 s or ∼0.95 s.

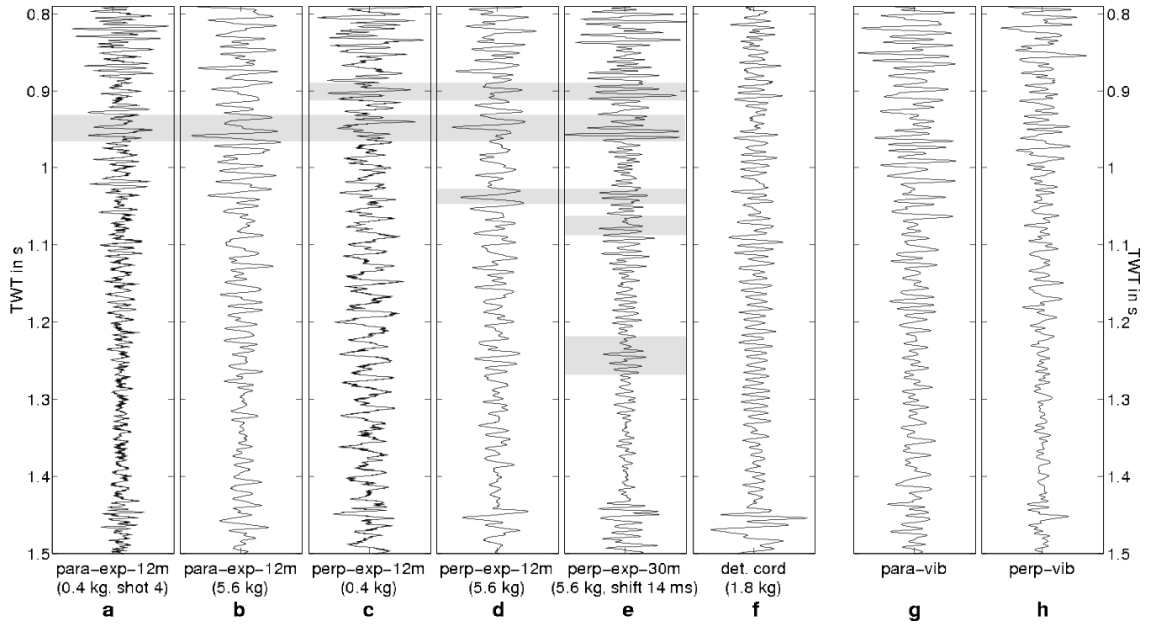

Figure 8.5: Stacked traces from different shots with different sources. The source settings for the wideangle surveys (b, d, e, g, h) are listed in Table 6.3. The shot para-exp-12m (0.4 kg; a) and perp-exp-12m (0.4 kg; c) are part of the profiles shot parallel and perpendicular to the ice divide, respectively, with 0.4 kg charge size in 12 m deep boreholes. The first shot of the profile survey parallel to the ice divide (a) has very strong noise. Thus, it is not representative for this line and Shot 4 (2250 m SSE of the center) was used instead. In (f) the stacked trace of a shot with detonation cord as source is displayed. Nine parallel lines of 10 m detonation cord were placed 1 m apart from each other (comp-shaped) and connected with detonation cord as lead in to one detonator. This shot is about 9 km ESE of the Kohnen station. The vibroseis data were correlated before stacking, with additional stacking of two shots for para-vib (g) and three shots for perp-vib (h) from the same location. Scaling is individual for each trace. The signals highlighted with gray are interpreted with the radar and ice core data (sec. 8.1.3)

All shots within 12 m deep boreholes (a–d) contain significantly stronger noise compared to the shot within the 30 m deep borehole (e). This is due to the much stronger surface and diving waves excited from the shots within the shallower boreholes (app. B.1). Some high frequency noise can be observed for the explosive shots with 0.4 kg charge size (a, c). Nevertheless, englacial signals can still by seen in the raw data, especially above 1.1 s.

The detonation cord shot shows a strong bed reflection and englacial signals around 0.9 s, 0.95 s and 1.05 s. The clearest englacial signals can be observed in the perp-exp-30m shot (Figure 8.5, (e)) around 0.82, 0.9, 0.95, 1.05, 1.08 and 1.25 s. The significantly better SNR of the perp-exp-30m shot compared to the other shots is explainable with the raw shots of the different surveys (app. B.1). The strongest, coherent noise within the shots is from the diving and surface waves. They are really weak in case of the perp-exp-30m (e) shot. Surface and diving waves are, of course, weakened during the stacking. Nevertheless, amplitudes of especially the surface waves are large and still visible in the stacked para-exp-12m and perp-exp-12m (0.4 kg) traces. Due to the better SNR and the number of clear signals the perp-exp-30m shot is used for the comparison with ice core and radar data.

The events interpreted in the following with the radar and ice core data (sec. 8.2.2) are highlighted in gray within the explosive shots close to each other. However, these events are also visible in the stacked traces of the vibroseis and detonation cord survey. The signal at 0.95 s can, for example, be observed in all shots and the signal at 0.9 s in most shots. Signals from deeper layers with longer traveltimes are no longer visible in all stacked traces. The SNR becomes weaker with increasing traveltime especially in case of shots with strong surface waves. This is due to the difference in geometrical spreading between surface and body waves. Thus, the deeper englacial reflectors can primarily be observed in the perp-exp-30m (5.6 kg) shot.

Further, it would be interesting to compare differences in traveltime and reflection strength for shots parallel and perpendicular to the ice divide. However, the SNR of the shots from 12 m deep boreholes is not sufficient for such a comparison. A shot parallel to the ice divide in a 30 m deep borehole and, thus, better SNR is needed here. Due to a breakdown of the drilling system in the season 2011/12 it was not possible to drill 30 m deep holes on the parallel line. Thus, no comparison is done on signals from shots parallel and perpendicular to the ice divide.

8.2.2 Comparison with ice-core and GPR data (Kohnen)

To compare the different data sets form Kohnen station the ice core COF data (a) is plotted together with a seismic stacked trace (b) of the perp-exp-30m survey (Figure 8.5, e), radar data (c–d) and modeled radar traces (e) in Figure 8.6 for a depth range of 1500–2500 m. The radar traces displayed in (c) show trace 4205 of the survey 022150 (600 ns pulse) in blue and 023150 (60 ns pulse) in red (survey map, Figure 6.11). A stack of all traces of the 033042 survey (60 ns pulse) is shown in black . In (d) stacked radar traces of the different legs with different air plane headings of the survey 033042 (inset, Figure 6.11) are plotted. The last subfigure (e) shows a radar trace for a 60 ns pulse (Eisen et al., 2007) modeled from DEP data with and without conductivity peaks removed from the DEP data, in black and blue, respectively. As the modeled trace does not include information about the COF distribution, signals that are interpreted as arising from changing COF should not have

a corresponding signal within the modeled trace (e). Five regions are marked A–E with signals corresponding in at least two of the measurements.

The radar reflection in D was already connected to a change in COF (a) from girdle to cone fabric between 2025–2045 m depth by Eisen et al. (2007). A strong signal can be seen in the 600 ns pulse radar trace (c, blue) as well as in the 60 ns pulse trace (c, red). Additionally, no corresponding signal can be found in the modeled radar trace (e). The periodic pattern of the traces with different air plane headings (d) indicates an orientation of girdle above cone fabric vertical and parallel to the ice divide (Eisen et al., 2007). This COF-induced radar reflection corresponds to a rather quite zone within the seismic trace (b), followed by a distinct peak.

Further distinct signals marked A and B in the seismic trace correspond to clear signals in the radar data. The strongest seismic reflector is signal B. Signal A is slightly weaker. For both events strong reflections are visible within the 600 ns radar pulse (a, blue) and a clear signal in the 60 ns radar pulse (a, red) as well with a weaker reflection at event A than event B. Additionally, no signal can be observed in the modeled traces based on DEP measurements (e). If the radar signal differs for different air plane headings (d) is difficult to judge for event A due to strong noise. Nevertheless, the stacked trace of the same survey (c, black) with increased SNR shows a weak reflection for event A. In case of event B the reflection is also clearly visible on the radar traces for the different air plane headings (d). Clear signals can be observed for headings in E, SE, W and NW directions. The signals are very weak for headings in N and NE directions, and weak for headings in S and SW directions. However, these are slightly shifted in traveltime compared to the signals from the E, SE, W and NE directions. There seems to be a pattern in this reflection behaviour for different air plane headings but not as clear as the pattern of event D. A jump in the COF eigenvalues (a) λ_2 and λ_3 can be observed over a very short depth interval at event B. In contrast, no variation in the COF eigenvalues can be observed in the region of event A.

Event C shows a clear signal in the seismic trace, in strength similar to that of event D, the signal that was already linked to changing COF. However, at event C no clear signal can be observed in the radar data, but therefore an extremely quite zone within the trace of the 600 ns pulse (c, blue).

The deepest marked reflection is event E at a depth of $\sim$2350 m corresponding to a 50 m layer of girdle fabric within a region of strong developed cone fabric visible in the COF eigenvalues (a). A very small increase in reflection power seems to be observable on the 600 ns pulse (c, blue). However, no clear signals are visible within the radar data for this depth anymore. In the seismic data a quite zone is followed by a signal at the depth of $\sim$2350 m, the transition of the girdle fabric back to the cone fabric.

To investigate the coherency of the lateral extend of COF-induced reflections Figure 8.7 shows parts of the radar surveys 023150 (60 ns pulse; b and d) and 022150 (600 ns pulse; c and e). Marked are the two COF reflectors of Figure 8.6, event B ($\sim$1800 m) and event D ($\sim$2035 m) with light blue triangles and a light blue line. The yellow triangles and yellow line mark a conductivity-induced reflection (Eisen et al., 2006) caused by the 71$\pm$5 kyr Toba volcanic eruption (Svensson et al., 2013). Subfigure (b) and subfigure (d) show the same data (023150) as variable density and variable amplitude wiggle plot, respectively. The same applies to subfigures (c) and (e) of the 022150 data. Subfigure (a) is the same as subfigure (c) of Figure 8.6, repeated here for better comparison.

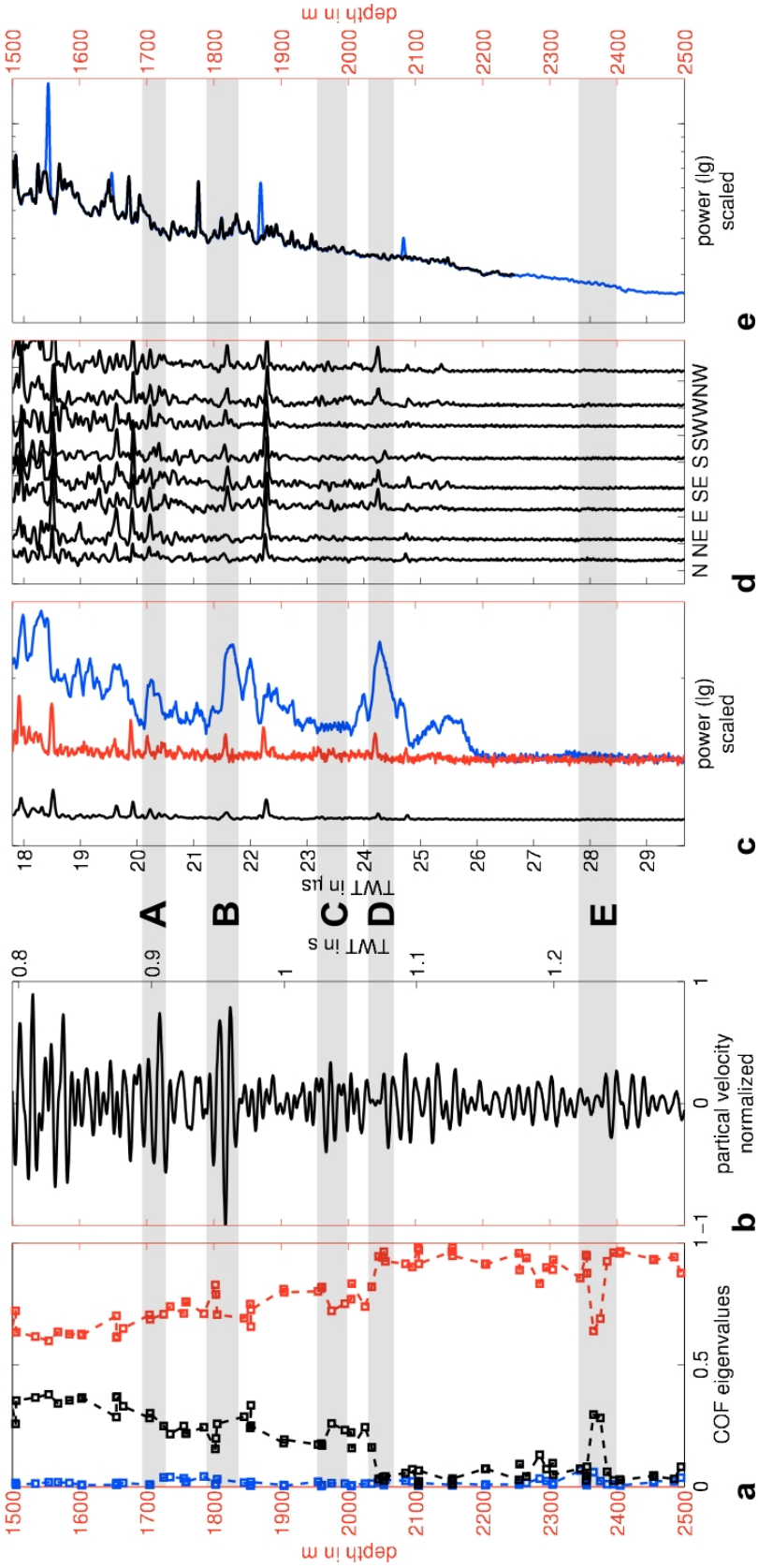

Figure 8.6: Comparison of ice-core COF eigenvalues (a), with a stacked seismic trace (b), radar data (c, d) and modeled radar data (e). The seismic trace is a stack of 60 channels, unfiltered data of the perp-exp-30m survey (Table 6.3). The NMO correction was done with the velocities derived from the VSP survey (sec. 7.1). (c) shows radar traces from the survey 022150 (600 ns pulse) in blue and 023150 (60 ns pulse) in red, together with a stack of all traces of the survey 033042 (60 ns pulse). (d) shows stacked traces of the survey 033042 with different polarisations. (e) is a forward modeled radar trace from DEP measurements with (blue) and without (black) conductivity peaks (Eisen et al., 2007). All figures are plotted over depth (red axis), with additionally marking the TWT on the seismic and radar traces (black axis). The calculation of depth from TWT was done with the VS velocities in case of the seismic data and with a constant velocity of 0.168 m/s, with a firn correction of 13 m in case of the radar data. The marked events A–E are discussed in the text.

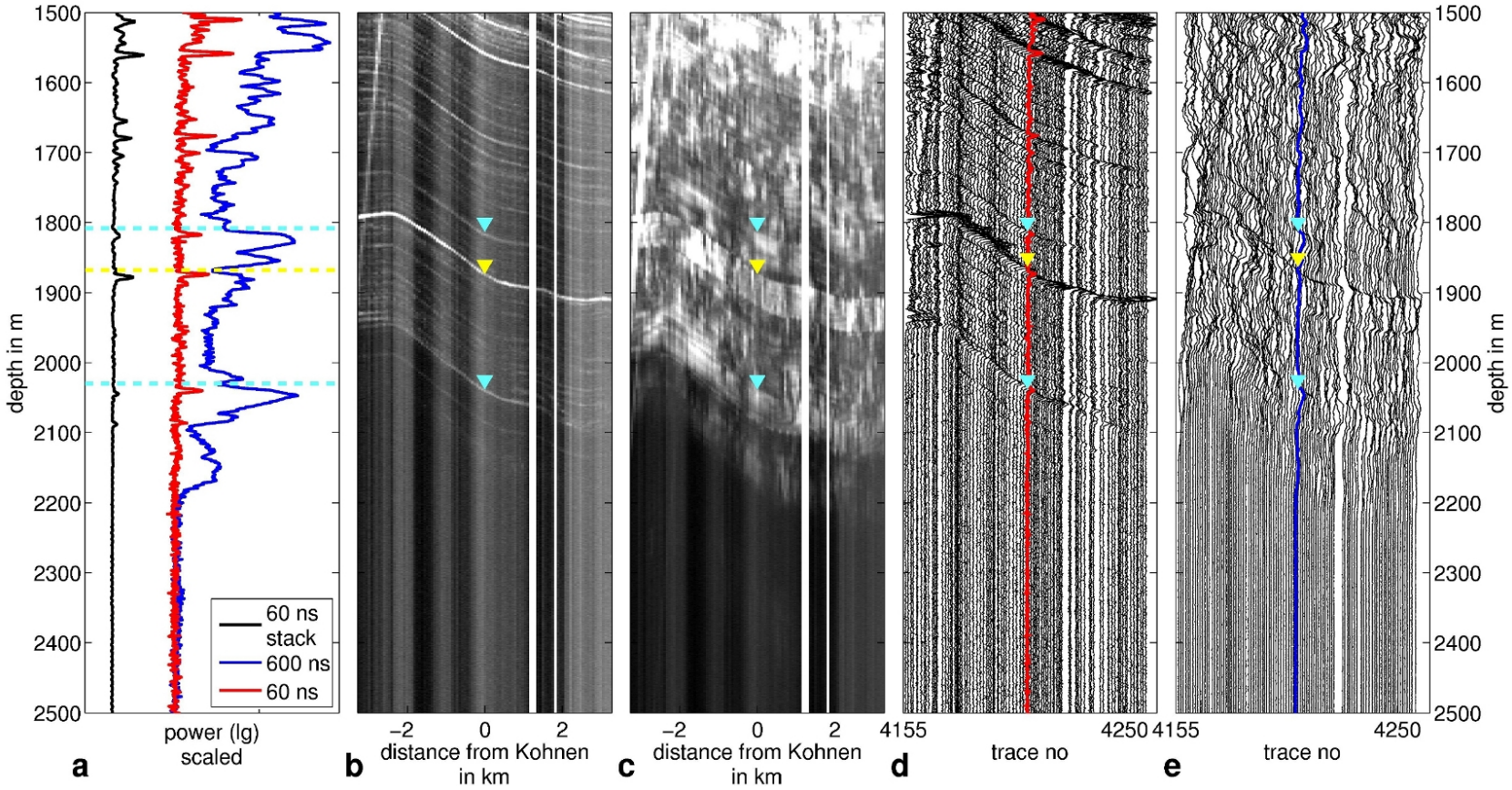

Figure 8.7: Radar data from Kohnen station from the 60 ns pulse survey (023150) and 600 ns survey (022150) as density plot (b and c, respectively) and wiggle plot (d and e, respectively). Subfigure (a) shows the trace 4205 of the 60 ns pulse (red) and 600 ns pulse (blue) survey, as well as the stack of all traces of survey 033042. The light blue triangle and lines indicate COF-induced reflections whereas the yellow triangles and line show a conductivity-induced reflection for comparison.

The COF-induced reflections (light blue line) in the 600 ns trace (Figure 8.7, a, blue) are stronger than the conductivity-induced reflection (yellow line). In the 60 ns trace the COF-induced reflections (a, red) are slightly weaker than the conductivity-induced reflector. However, the most coherent signal in the horizontal direction, for both the 60 ns (b, d) and 600 ns pulse (c, e), is the conductivity signal. This is most obvious within the two wiggle plots (d, e). While the COF reflections in the 60 ns pulse can be followed quite well the signal of the 600 ns pulse is more incomplete.

8.2.3 Interpretation of englacial reflections (Kohnen)

By comparing the seismic and radar reflectors with the COF measurements of the EDML ice core a better understanding of the origin of the reflections can be gained (Figure 8.6). Beside the radar reflector at 2035 m depth (event D) that was already linked to changing COF (Eisen et al., 2007) I also interpret the reflectors in the radar data at 1690 m (event A) and 1810 m depth (event B) as being induced by changing COF.

Both, event A and B have no corresponding signal in the modeled radar trace. This meets the expectation as no information about anisotropy were included in the modeled radar traces. The measured COF eigenvalues do not show a jump within the region of event A and only a small jump in the eigenvalues λ_2 and λ_3 in the region of event B. However, clear signals can be observed within the seismic trace for both events. The COF eigenvalues in this region were measured with a resolution of $\sim$50 m. This resolution is not high enough to show distinct jumps over short depth scales that can cause reflections in the seismic and radar data.

The change in the COF eigenvalues at event B corresponds to a reflection coefficient of 0.009 (zero-offset). In comparison, the jump in the eigenvalues at event C corresponds to a reflection coefficient of -0.006 (zero-offset). The reflection coefficient for both signals are two orders of magnitude smaller than those of bed reflections (sec. 4.2.3). However, compared to the strong seismic reflection observable at event B the seismic reflection amplitude that can be observed at event C is significantly weaker. It seems that the difference in the calculated reflection coefficients is not large enough to explain the difference in reflection strength between event B and C. Event C is, of course, $\sim$150 m deeper than event B. Even if geometrical spreading and damping are considered it is still difficult to explain the difference in reflection strength between event B and C. An explanation might by, that the true change in anisotropy is not resolved with the eigenvalue measurements for event B. Thus, I assume that event B as well as event A are COF-induced reflections in the seismic and radar data even though the changes in anisotropy are not resolved in the COF eigenvalue data.

The strongest COF-induced reflector in the radar data with a clear azimuth dependent pattern is event D with the transition from girdle to cone fabric Eisen et al. (2007). The eigenvalues for this clear jump from girdle (2025 m depth) to cone fabric (2045 m depth) would correspond to P-wave reflection coefficient of 0.014 (zero-offset). However, in the seismic trace a quite zone is followed by a reflection about the same strength as that of event C (reflection coefficient -0.006). The COF changes over a depth interval of 20 m. With frequencies around 200 Hz in the seismic data a maximal resolution of $\sim$10 m ($\lambda_w/2$) is reached. Thus, the transition from girdle to cone fabric over 20 m depth might be too gradual and not sudden enough to cause such a reflection. A similar effect can be observed

at event E. The 50 m layer of developed girdle fabric is visible in the COF eigenvalue data. This corresponds to a quite zone followed by a clear reflection in the seismic data. The depth of this reflection fits to the transition back from girdle to cone fabric. However, no clear signal can be observed for the transition from cone to girdle fabric 20 m above. This is explainable if the transition from cone to girdle is more a gradual change while the transition from girdle to cone is really a sharp boundary.

The lateral coherency of COF reflectors and conductivity-induced reflectors can be observed in the radar profiles of Figure 8.7. In the 60 ns pulse data, i.e., the radar data with higher resolution, is the conductivity-induced reflection clearly the strongest signal. The COF reflections are stronger than the the conductivity-induced reflection in the 600 ns pulse data. However, this is mainly true for the trace 4205 closest to EDML. Following the COF reflections in the wiggle plot of the 600 ns pulse it becomes clear that the COF reflections are not as coherent as the conductivity reflection. Here, it is easier to follow the lateral extend of the COF reflections in the 60 ns pulse data. From the Kohnen radar data I would conclude that COF-induced reflections are more inhomogeneous than conductivity-induced reflections. It is easier to follow COF reflections in the 60 ns pulse data than in the 600 ns pulse data. The COF-induced reflections are partly stronger for the 600 ns pulse than the conductivity-induced reflections. Additionally, the strong conductivity peak visible in the radar data (Figure 8.7) at a depth of $\sim$1865 m shows no corresponding signal in the seismic trace.

8.3 Conclusions of data set comparison (Colle Gnifetti and Kohnen)

Different physical data sets from Colle Gnifetti and Kohnen station were compared. The different sensitivities of theses data sets yield the potential to distinguish between different reflection mechanisms. The main reason for englacial reflections in seismic data below the firn-ice transition is a change in the anisotropic ice fabric. However, these reflections might be weak and it is not easy to distinguish them from the surrounding noise. The radar data show a lot of englacial reflections and it is difficult to distinguish between conductivity-induced and COF-induced signals. In the data sets introduced here measurements from ice cores were available for the comparison with the seismic and radar data sets. In the largest part of the ice sheet these information are not available so that conclusions about the COF need to be drawn from seismic and radar data alone.

The comparison of the Kohnen data sets show, that the combination of seismic and radar data has a great potential for identifying COF-induced reflections. With clear signals in both radar and seismic data sets the reflections at 1690 m and 1810 m depth are interpreted as arising from COF changes. Here, the seismic data help to distinguish between COF- and conductivity-induced reflections. The seismic data shows, for example, no signal at the depth ($\sim$1865 m) of the strong conductivity peak in the radar data. This insensitivity of the seismic data to changes in conductivity supports the idea to use seismic data to identify COF-induced reflections in the radar data. At the same time, the coincident occurrence of reflectors in both data sets strengthens the conclusion that these reflections are due to a change in COF, the common reflection mechanism for seismic and radar data in ice. Further, seismic signals can be observed in regions with low radar backscatter. This is, e.g, the case

for the echo-free zone at Kohnen where a reflection for the transition from girdle to cone fabric can be observed at ∼2350 m in the seismic data. It can also be observed in the region below the firn-ice transition at Colle Gnifetti where clear signals are missing in the radar data but a strong englacial reflection can be observed in the P-wave data.

At Colle Gnifetti the seismic P-wave and SH-wave data do also complement. Beside the different resolution, the P- and SH-wave stacks show a different reflection pattern. The sensitivity of the SH-wave seems to be stronger for variations in density. Theses density variations cannot be resolved in this clarity with the P-wave data. Therefore, reflections from the ice column, probably caused by changing COF, can be observed in the P-wave data. They show no counterpart in the SH-wave data.

The big advantage of the Colle Gnifetti data set is that englacial reflections could be observed in the CMP sorted data and used to derive the velocity profile. At Kohnen these reflections are only visible after stacking a shot gather. Of course, the distance to the ice-bed interface is only 62 m at Colle Gnifetti compared to the 2782 m at Kohnen station. Thus, it is more difficult to get enough high frequency energy in the ground and especially back to clearly resolve the englacial reflections at Kohnen. Additionally, the ratio of energy between the surface and body waves has an influence on the stacked seismic trace from Kohnen. For increasing traveltime the amplitudes of the body wave decay faster compared to those of the surface waves due to the difference in geometrical spreading (3D and 2D propagation of the wave, respectively). Hence, in the stacked trace the strong surface waves are superimposed on the reflection signals of the body waves for increasing traveltimes. The weakest surface waves could be observed from an explosive shot carried out in a 30 m deep borehole at Kohnen (perp-exp-30m (5.6 kg); app. B.1). Here, the shot is placed at a depth in the firn with a density of ∼600 kg/m^3, i.e., below the pore-close. Thus, the energy goes into the excitation of elastic waves and to less extent into the densification of the snow around the shot location. Additionally, it could be observed that higher frequencies were excited from shots with 0.4 kg charge size than shots with 5.6 kg charge size in the same borehole. To be able to detect clear englacial reflections in seismic data high frequency data with as little as possible disturbing noise of diving and surface waves is needed. Thus, a possibility to increase the resolution of the shots at Kohnen station would be to carry out shots in 30 m deep boreholes with 0.4 kg charge size to combine the advantages of weak surface waves and exited high frequencies.

Some reflections that are visible in both radar and seismic data from Kohnen do not show a counterpart in the COF eigenvalues. No or no significantly large jump in the COF eigenvalues can be observed for these reflections. Nevertheless, they are interpreted as COF-induced reflections. This seems reasonable as the COF eigenvalue sampling resolution for the EDML ice core is partly only 50 m. Thus, changes in the fabric over short depth scales that can cause seismic and radar reflections might not be resolved in the COF eigenvalue measurements. Here is a need for a really high resolution measurement of COF or ultrasonic logging on ice cores to be able to learn about the small scale variations of changing COF over depth.

9 Normal moveout correction in anisotropic ice

To derive information about the anisotropic ice fabric it is possible to analyse the hyperbolic and non-hyperbolic moveout of seismic reflections. The theoretical basis was introduced in section 3.5, with the anisotropic NMO velocity $V_{\mathrm{NMO},\zeta}$ and the difference to the zero-offset RMS velocity $V_{\mathrm{RMS},\zeta 0}$. To gain information about the variations of the anisotropic ice fabric over depth englacial reflections over increasing offset need to be visible, strong enough to be able to analyse the traveltimes.

Reflection seismic data and wideangle data of P- and SH-wave surveys are analysed in the following. The Colle Gnifetti, Switzerland, reflection seismic data yield the possibility to analyse P- and SH-wave englacial reflections (sec. 9.1). In the wideangle data set from Halvfarryggen, Antarctica, englacial reflections over depth can be observed as well as a clear bed reflection. The analysis of the reflections here is problematic due to a dipping bed reflector. A critically refracted wave, emerging from the ice-bed interface, can be used to derive bed properties (section 9.2). The two wideangle data sets perpendicular to each other from Kohnen station yield the opportunity to derive information about the COF distribution parallel and perpendicular to the ice divide and the orientation of the girdle fabric measured on the EDML ice core (sec. 9.3).

9.1 Colle Gnifetti velocity analysis

The processed data from Colle Gnifetti were depth converted using the RMS velocities derived during the stacking process (sec. 6.1.2). While the depth of the bed reflector of the SH-wave survey aligned well with the length of the KCI ice-core and, thus, the known depth of the ice-bed interface, the depth of the P-wave bed reflection was too shallow (6 m for Profile 1, 8 m for Profile 2, Figure 6.3). The influence of the anisotropy on the traveltime analysis (sec. 9.1.1) and the possibility to use the seismic data in combination with the radar data to derive information about the COF (sec. 9.1.2) is investigated in the following.

9.1.1 Colle Gnifetti velocity profiles from COF data

For the analysis of the influence of anisotropy on the traveltimes and, thus, the differences between stacking velocity and depth-conversion velocity, the KCI ice-core data are used for the calculation of anisotropic velocities. Three KCI data sets are important here for the calculation of velocities: the density (Figure 8.2), the temperature profile and the COF measurements in form of the opening angle (Figure 6.2).

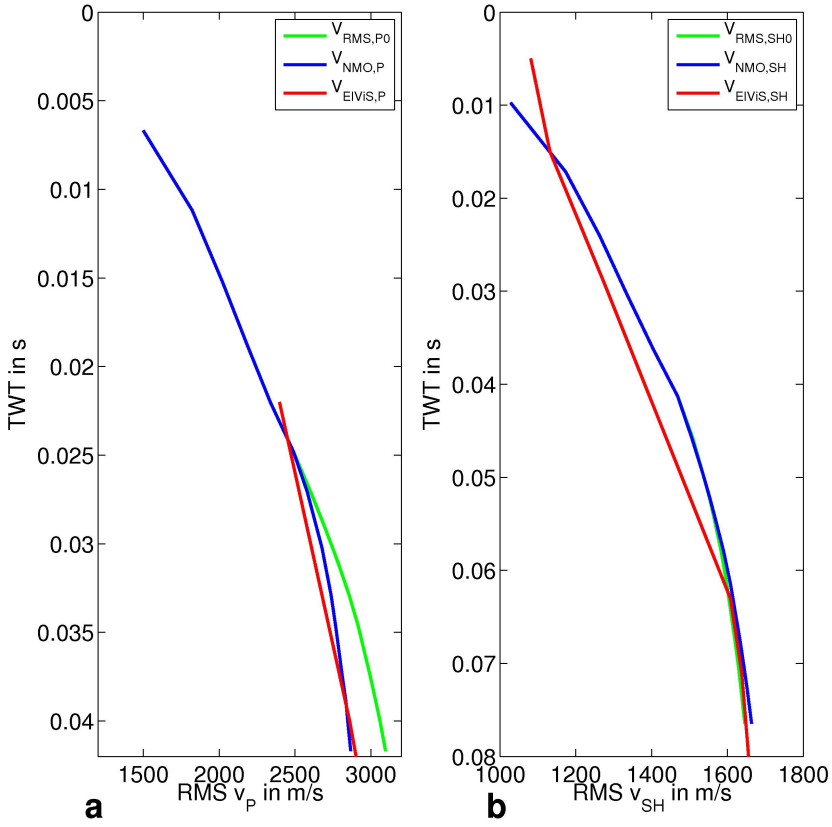

Figure 9.1: Picked and calculated (a) P- and (b) SH-wave velocities for the investigation of the influence of anisotropy on the seismic velocities. The red lines show the velocities $V_{\mathrm{ElViS},\zeta}$ picked from the NMO analysis of the ElViS data sets of Profile 1. With help of the KCI measurements of density, temperature and COF the anisotropic NMO velocities $V_{\mathrm{NMO},\zeta}$ (blue lines) and the zero-offset RMS velocities $V_{\mathrm{RMS},\zeta 0}$ (green lines) are calculated.

For the calculation of velocities the elasticity tensor by Gammon et al. (1983) is used ($\mathfrak{T}_{\mathrm{m}} = -16°\mathrm{C}$). The derived velocities are corrected for the existing temperatures measured in the borehole of the KCI ice core by Hölzle et al. (2011) ($\mathfrak{T} = -11$ to $-13°\mathrm{C}$; sec. 6.1.1). As variations are only moderate over the whole depth I correct the velocities to a constant temperature of $\mathfrak{T} = -12°\mathrm{C}$. The correction is done on the elasticity tensor using equation (4.12) and the temperature correction value $a = 1.418^{-3}\ \mathrm{K}^{-1}$ derived by Gammon et al. (1983) (sec. 4.4).

At Colle Gnifetti a strong density gradient exists for the firn pack of about 30 m thickness (Figure 8.2). For the calculation of the P-wave velocity depending on the density in firn I use equation (4.9) derived by Kohnen (1972) and equation (4.10) for the SH-wave velocity, that was derived from the diving wave of the Colle Gnifetti SH-wave survey (sec. 8.1.1).

Thus, taking the temperature and the measured COF eigenvalues into account the elasticity tensors for the single layers and the corresponding Thomsen parameter can be calculated. Between 0 and 30 m depth, where no COF measurements were carried out, the ice is assumed to be isotropic. With corrections for the density gradient first interval velocities ($v_{\mathrm{nmo},\zeta}$ and $v_{\zeta 0}$) and then the NMO velocities ($V_{\mathrm{NMO},\zeta}$) and zero-offset RMS velocities ($V_{\mathrm{RMS},\zeta 0}$) are determined.

Figure 9.1 shows the anisotropic NMO velocity (blue line) and zero-offset RMS velocity (green line) for P- (a) and SH-wave (b). For comparison the stacking velocities picked during the ElViS processing of Profile 1 are plotted in red. The ElViS stacking velocities are derived from the hyperbolic moveout of the englacial reflection and bed reflection. Thus, they should be equal to the calculated anisotropic NMO velocities ($V_{\mathrm{NMO},\zeta}$; blue line). For both, the P- and SH-wave the calculated NMO velocities $V_{\mathrm{NMO},\zeta}$ are within 3% of the stacking velocities $V_{\mathrm{ElViS},\zeta}$ picked by Polom et al. (2014). The difference is slightly larger (5%) in regions without picks. This is especially the case for SH-wave ElViS stacking velocities where englacial velocities were picked within the firn an then again at the bed. For the depth conversion of the ElViS seismic data the stacking velocities $V_{\mathrm{ElViS},\zeta}$ were used. However, needed for the depth conversion are the zero-offset RMS velocities $V_{\mathrm{RMS},\zeta 0}$. The difference between anisotropic NMO velocity $V_{\mathrm{NMO},\zeta}$ and zero-offset RMS velocity $V_{\mathrm{RMS},\zeta 0}$ is 229 m/s for the P-wave and 18 m/s, for the SH-wave, corresponding to 8% and 1%, respectively. Hence, it is possible to explain why the conventional depth conversion based on stacking velocities worked so well for the SH-wave but caused a considerable difference in case of the P-wave. By assuming isotropic state and using stacking velocities for the depth conversion the mistake made for the bed reflector at Colle Gnifetti is only 1% for the SH-wave, but 8% for the P-wave stacked data.

Instead of using the ElViS stacking velocities $V_{\mathrm{ElViS,P}}$ for the depth conversion the calculated P-wave zero-offset RMS velocities $V_{\mathrm{RMS,P0}}$ can be used. Thus, the bed reflector of the P-wave stack of Profile 1 is shifted down for 4 m. However, to align the P-wave bed reflection and the KCI ice-core length (sec. 6.1.2) the P-wave stack was shifted down for 6 m. The calculated discrepancies between $V_{\mathrm{NMO,P}}$ and $V_{\mathrm{RMS,P0}}$ of 8% can, thus, not explain the complete depth difference between the derived depth of the ElViS P-wave bed reflection and the ice-core length of 62 m. This depth difference is 10% for Profile 1 and 13% for Profile 2. However, information about the COF fabric are only available below 30 m depth, so about 50% of the total depth. For the calculation of anisotropic velocities it was assumed that the region above 30 m is isotropic. At this depth, already a strong developed cone fabric ($\varphi = \chi \approx 55^{\circ}$) can be observed. Thus, it is very likely that a developed anisotropy exists above 30 m depth within the firn region, that leads to a larger difference between anisotropic NMO ($V_{\mathrm{NMO,P}}$) and zero-offset RMS velocity ($V_{\mathrm{RMS,P0}}$) of the P-wave.

9.1.2 Deriving δ as a proxy for anisotropy

The sensitivity of the P-wave traveltime to the existing anisotropic fabric enables us to derive information on the anisotropy from the seismic P-wave data. The NMO velocities $V_{\mathrm{NMO,P}}$ are derived during the stacking from the hyperbolic moveout of layer interfaces. To be able to derive the anisotropic Thomsen parameter δ the zero-offset RMS velocity $V_{\mathrm{RMS,P0}}$ needs to be known as well. $V_{\mathrm{RMS,P0}}$ can be derived from the depth of the layers, which in the anisotropic case can not be derived from the P-wave data. In order to obtain the depth of the layer interfaces I combine the seismic data with radar data at Colle Gnifetti. Therefore, I have to be able to identify identical layer interfaces in the seismic and radar data set from Colle Gnifetti. Care has to be taken here if only a few out of many existing layers can be identified. In this case calculating the velocity from depth gives a mean velocity and would underestimate the zero-offset RMS velocity ($V_{\mathrm{RMS,P0}}$) and, thereby, also the anisotropy.

By combining the information of the seismic P-wave and radar data sets it is possible to

derive δ_{eff}, an RMS δ-value, i.e., an average δ over the depth of the identified layers (eq. (3.51) and (3.52), for the P-wave $\xi = \delta$). When more than one layer is identified the interval delta values $\delta^{(i)}$ for the different intervals can be calculated with equation (3.52) from the derived δ_{eff}-values. Compared to the resolution of the COF eigenvalue measurements these layers are still averaged layers, as it is only possible to derive anisotropy parameters for identified layers where reflections from the layer interfaces are visible. Nevertheless, information about the changes in anisotropy over depth can be gained from the seismic–radar data combination.

I link the bed reflection of the P-wave seismic data from Colle Gnifetti to that of the radar data (Figure 8.3). Additionally, the strong reflection around the firn-ice transition zone in case of the ElViS P-wave data is linked with a vanishing of internal reflection horizons that was observed in the radar data around the firn-ice transition zone (Konrad et al., 2013). Thus, using equation (3.52) it is possible to derive information about the existing anisotropy for a two-layer case.

Figure 9.2 shows the result of the derived δ-values for the 2-layer case (b, black lines) in comparison to a 1-layer case (b, dashed lines) and the δ-values (b, green dots) calculated from the COF eigenvalue data (a). From the derived δ-value the cone opening angle of about 77° for the first 27 m depth and a cone opening angle of 36° for the lower ice column (Figure 9.2, c) is estimated. The derived δ-value and cone opening angel (36°) between the englacial reflector (27 m depth) and the glacier bed fit quite well to the values calculated from the COF eigenvalues, with opening angles in the range of 24° to 55°. If only 1 layer is considered the δ_{eff}-value (green dashed line, b) and the effective cone opening angle (red dashed line, c) can be calculated from the COF eigenvalues assuming isotropy above 30 m depth. They are in good agreement with the values derived from the seismic data (black dashed lines). The COF derived values are 6% larger than the seismic derived values. Assuming, that the developed anisotropic fabric already exists above 30 m depth the true δ_{eff}-value and the effective cone opening angle for the 1-layer case should be smaller, this means more anisotropic than the values derived from the COF eigenvalues.

At Colle Gnifetti analysing the anisotropy from the combination of seismic and radar data is extremely sensitive to the chosen depth of the reflection. The problem is, that 62 m thickness is a rather shallow case where a shift of a layer by 1 m up or down already introduces a rather big change in the resulting anisotropy. Shifting the two-layer boundary down by 1 m would result in opening angles of 54° for the upper 28 m and 40° below. However, if it is possible to apply this method to reflection signatures in ice sheets where the overall thickness is much larger, the sensitivity towards small shifts in depth will decrease.

The δ-values derived from the seismic-radar combination for the firn column show an anisotropic ice fabric. This supports the idea that the still existing depth discrepancies of 2 m between the P-wave bed reflection, depth converted using the calculated zero-offset RMS velocity $V_{\text{RMS,P0}}$, and the KCI ice-core length (sec. 9.1.1) can be attributed to an existing anisotropic ice fabric within the firn.

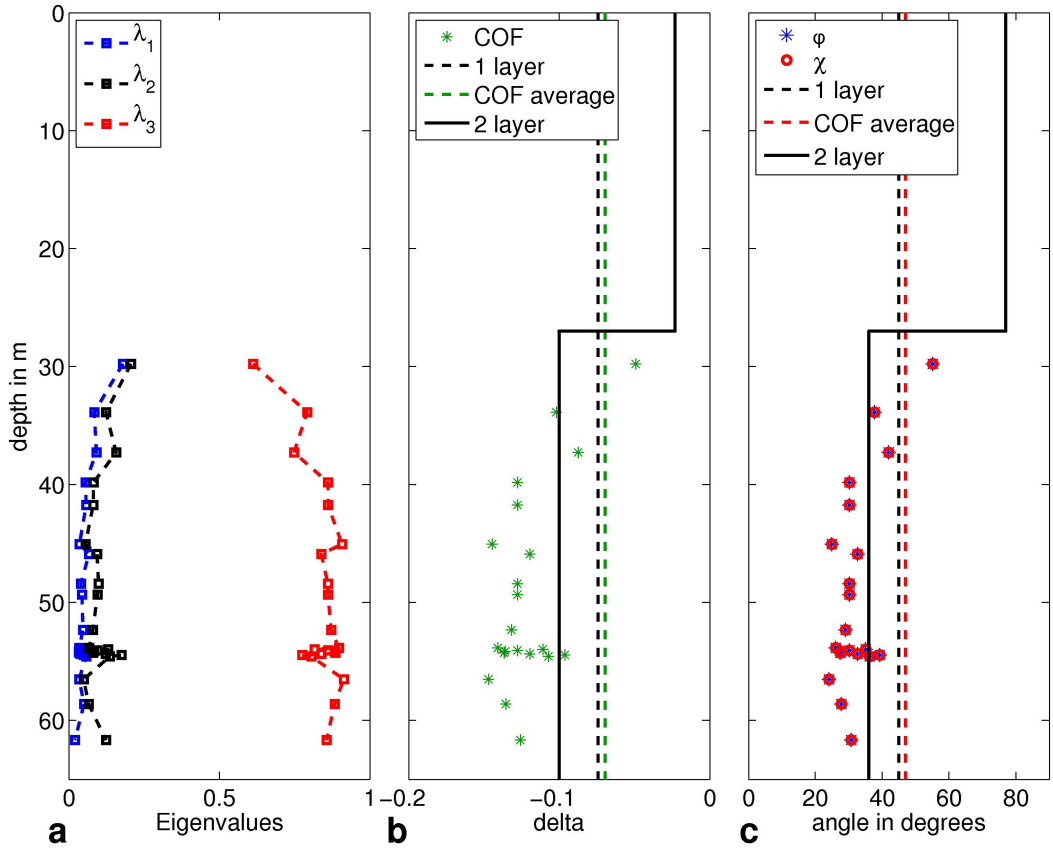

Figure 9.2: (a) COF eigenvalues measured below a depth of 30 m with the corresponding δ-values in (b), green dots and the corresponding cone opening angels ($\varphi = \chi$) in (c), red circles and blue dots. (Eigenvalue plot (a) is equivalent to Figure 6.2, a, here again for better comparison). The green dashed line (b) gives the δ_{eff}-value calculated form the COF eigenvalues over the complete depth, the dashed red line (c) the corresponding effective opening angle. The black dashed lines in (b) and (c) give the δ_{eff}-value and the corresponding average cone opening angel ($\varphi = \chi$), respectively, for a 1 layer case derived by combing seismic and radar bed reflection. The solid black lines in (b) and (c) give the δ-value and the corresponding cone opening angel ($\varphi = \chi$), respectively, for a 2 layer case.

9.2 Halvfarryggen velocity analysis

At Halvfarryggen the wideangle data set was shot and the velocities of the layers were picked using the englacial reflection and the bed reflection. However, it can be seen in the profile data from Halvfarryggen (Hofstede et al., 2013) that the bed at the location of our wideangle survey is slightly tilted. The problems that are introduced due to the tilted bed at Halvfarryggen are discussed in section 9.2.1. Due to the large offsets of the wideangle survey a critically refracted wave can be observed for offsets larger than 2000 m. A refraction seismic analysis is used to derive information about the bed properties (sec. 9.2.2). The source at Halvfarryggen were explosives. Thus, the following discussion is limited to P-waves.

9.2.1 Tilted layers

When wideangle data are shot the same area of CMPs is covered over and over again (Figure 6.6). It is then assumed that all shots belong to one CMP which is reasonable if the layers are flat and it can be expected that the properties do not change over the lateral extent of the CMP area. If it is considered that the reflections of different offsets arise from one point in depth (common depth point, CDP) NMO and ηNMO corrections can be carried out.

The shots of the Halvfarryggen wideangle survey were adjusted in depth to correct for the missing automatic trigger using the diving waves (sec. 6.2). However, jumps can be observed in the traveltime of the bed reflection between the shots of the different positions. This is particularly visible between the shots of position 1 and 2 at an offset of 800 m in Figure 6.8. Here, an increase in traveltime can be observed in the bed reflection from 787.5 m offset to 800 m offset. This jump in the traveltime can be explained with the tilted bed at Halvfarryggen (Figure 9.3).

Hofstede et al. (2013) discuss explosive and wideangle data from Halvfarryggen. The bed reflection in the processed data is mainly flat but shows a dip in the region of the wideangle survey. Figure 9.3 is adapted from Hofstede et al. (2013) and shows the bed reflection in the region of the wideangle survey. The red solid line marks the CMP area that was mapped during the wideangle survey. The location of the shot corresponds to CMP 259 with the geophones located towards the south from this location. For the covered CMP area (CMP 263–204) the depth of the bed reflector (red dashed line) decreases towards the geophones furthest away from the shot. The difference between the traveltime at CMP 263 and CMP 204 is 0.015 s TWT. Assuming an ice velocity of 3900 m/s this corresponds to a depth difference of $\sim$30 m and a dip of $\sim 5^\circ$.

Effect of a titled layer on TWT

Figure 9.4 shows a sketch of the situation with the tilted bed for the travelpath of the waves. In the zero-offset case the wave travels all the way to the bed and back. However, the travelpath is normal to the reflector in the zero-offset case (dotted gray line, Figure 9.4). Thus, the traveled depth is not equal to the depth d below the shot position. For increasing offset the depth is reduced due to the dipping reflector. The change in depth depends on the dip α of the reflector. In the following a positive dip α will indicate a decrease in depth with increasing geophone or streamer offset like observable in the Halvfarryggen

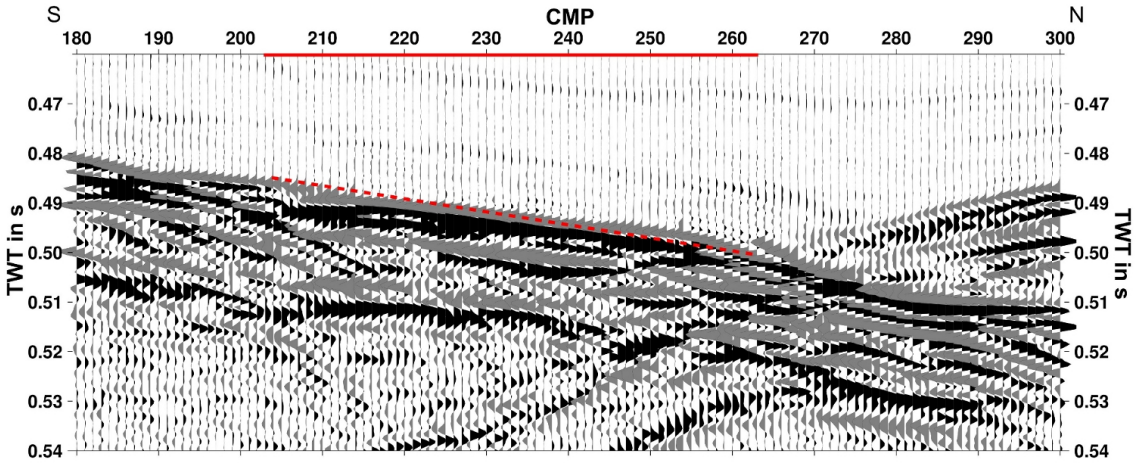

Figure 9.3: Part of the seismic profile shot at Halvfarryggen adapted from Hofstede et al. (2013). The profile was shot on the same line as the wideangle survey. The red line marks the CMP area of the wideangle survey, the red dashed line the corresponding area in depth. Due to the tilted layer this does not correspond to the CDP (common depth point) area. The shots of the wideangle survey move towards the North (CMP 300), the streamer moves towards the South (CMP 180).

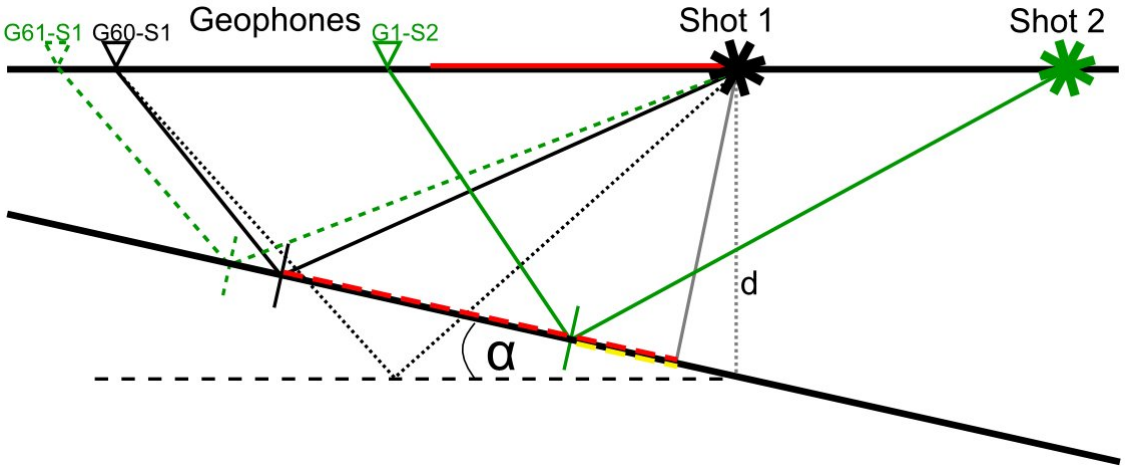

Figure 9.4: Sketch to illustrate the difference in travelpath for a flat and a tilted layer in case of a wideangle survey. The dip α is the angle between horizontal and the tilted layer for the direction from the shot to the geophone. Thus, a decrease in depth towards the geophone is a positive angle $\alpha > 0°$, an increase in depth towards the geophone is a negative angle $\alpha < 0°$. The gray lines show the zero-offset travelpaths, the black lines the travelpath for an offset>0 in case of a flat reflector ($\alpha = 0°$, dotted lines) and a tilted reflector ($\alpha > 0°$, solid lines). Assuming numerous geophones starting with geophone 1 at shot position 1 to the last geophone (G60-S1) a CMP area indicated by the red solid line would be covered. The corresponding CDP area is shown by the red dashed line. For the same offset range in case of a true CMP survey the corresponding CDP area indicated in yellow would be covered. For increasing offset shot and geophones are moved in opposite direction for a wideangle survey. Thus, instead of the travelpath between shot 1 and G61-S1 (dashed green line) the travelpath from shot 2 to G1-S1 is covered (solid green line).

data (Figure 9.3). The reflection point on the dipping reflector for increasing offset is at the point where angle of incidence and angle of reflection are equal to the normal on the dipping reflector. This assumption is no longer valid in the anisotropic case as velocities for incoming and outgoing ray are no longer the same. The travelpath (solid black line, Figure 9.4) between shot an receiver for a dipping reflector with $\alpha > 0^\circ$ is reduced compared to the travelpath for a flat reflector (dotted black line, Figure 9.4). Thus, the traveltime is reduced. This means, that the velocity of the layer will appear to be larger than the true velocity for a tilted reflector with $\alpha > 0^\circ$ and under the assumption of a flat reflector.

The strong influence of the dipping reflector on the traveltime has to do with the shooting geometry of the wideangle survey and the assumption of lateral homogeneity. For a true CMP survey each geophone position corresponds to one shot position with shot and geophone moving away from the center point in equal steps. This survey has one CMP that belongs to all shot–geophone combinations whereas the wideangle survey with one shot and numerous geophones has one CMP for each shot–geophone combination. In case of the true CMP survey the depth of the reflection point changes with increasing offset to fulfill the condition of equal angle of incident and reflection. Hence, no common depth point (CDP) exists anymore for the dipping reflector. The CDP area that would be covered with a true CMP survey is indicated with the dashed yellow line in Figure 9.4. In case of the wideangle survey the CMP position moves. Thus, the depth below the CMP changes as well with increasing offset. The CDP area covered with a wideangle survey for the same offset range than the true CMP survey is shown by the red dashed line in Figure 9.4. For the wideangle survey it is just assumed afterwards that all shot–geophone combinations belong to one CMP. However, the covered CDP area is much larger and consequently also the change in depth over this area for the wideangle survey compared to the true CMP survey. Thus, the influence on the traveltime compared to a flat reflector is larger in case of the wideangle survey than for the true CMP survey.

The influence of the dipping reflector on the moveout can be illustrated using the example of the 50 m layer with VSM-fabric introduced in section 3.5.2 (Figure 9.5). Here, the traveltimes are calculated for one shot and numerous geophones with different offsets. The shot is always at the same location so that the depth below the shot does not change. This corresponds to the shooting geometry during a wideangle survey. The traveltimes calculated from the group velocities (red curve), the NMO velocity (dark blue curve), the NMO velocity with anisotropy parameter η (light blue curve) and the zero-offset velocity (green curve) in Figure 9.5 are the same as given in Figure 3.4 for the flat reflector ($\alpha = 0^\circ$). The dashed black lines show the moveout for reflections at an interface with a dip α between -5° and 5°. For simplification I assume for the calculation that the phase angels of the angle of incident and angle of reflection are equal. However, the group velocities used for incoming and outgoing ray are calculated separate for the corresponding phase angles.

The moveout in case of the dipping reflector is no longer hyperbolic. Additionally, the zero-offset traveltimes are different for the different dips. This is due to the changing length of the zero-offset travelpath as the zero-offset travelpath is normal to the reflector. It can be observed, that the traveltime decreases with increasing dip α and the velocity appears to be faster. The strong changes in traveltime due to the dipping reflector can be attributed to the shooting geometry of the wideangle survey as discussed before. When carrying out a NMO correction and estimating the velocity of the layer a hyperbola is fit to the moveout of the dipping reflector under the assumption of a flat layer. For the dipping reflector with

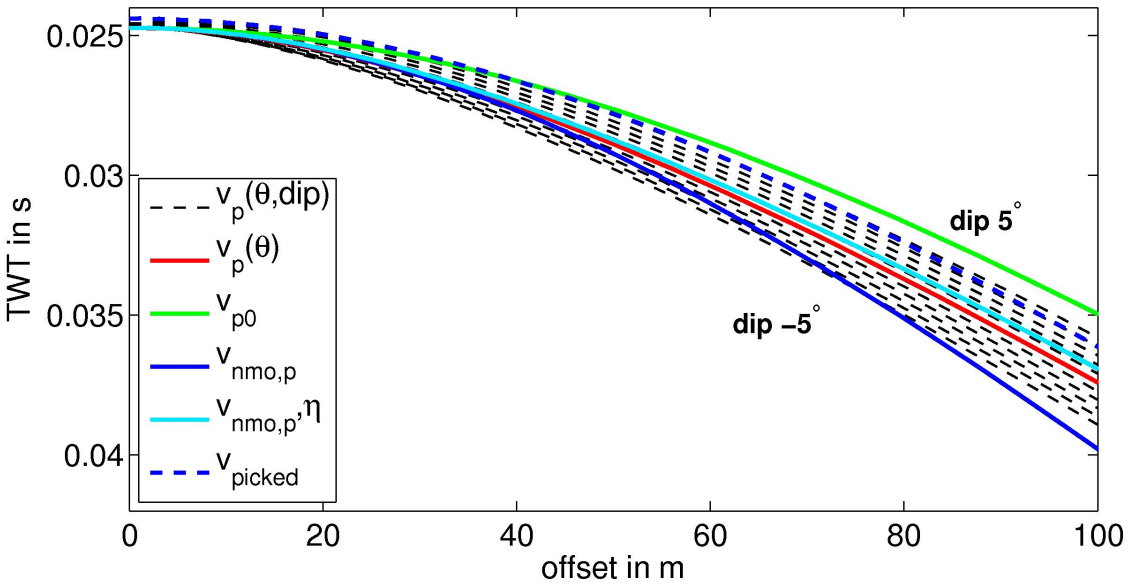

Figure 9.5: Moveout for the example of a 50 m layer VSM-fabric and an offset/depth-ratio>1. The red curve gives the moveout calculated from the group velocity given by equations (3.20) and (3.30). The dark blue curve shows traveltimes calculated from the corresponding NMO velocity (eq. (3.47)), the green curve form the zero-offset velocity (v_{p0}) and the light blue curve gives the moveout derived from the 4th-order approximation for traveltimes (ηNMO correction, eq. (3.55)). These traveltimes were calculated for a flat reflector. The dashed black lines give the moveout calculated from the group velocity given by equations (3.20) and (3.30) for a dipping reflector. The depth under the shot is 50 m. A positive angle corresponds to an decrease in depth towards the geophone a negative angle to an increase in depth towards the geophone. The traveltimes for the dipping reflectors are given for reflector dips α between -5° and 5° in steps of 1°.

$\alpha = 5^\circ$ and normal-spread length (offset up to 50 m) for the example of a 50 m layer with VSM-fabric (Figure 9.5) I would determine a TWT of 0.0244 s and a velocity of 3750 m/s (blue dashed line). The picked velocity here is ∼550 m/s faster and the TWT 0.003 s less compared to the velocity and TWT of the flat reflector. Hence, a significant difference of 17% can be observed between picked NMO velocities in case of a flat reflector and a dipping reflector with $\alpha = 5^\circ$. Using these picked values and the knowledge of the depth of the reflector (50 m) the zero-offset RMS velocity and further the δ-value and the cone opening angle φ can be derived. Here, a cone opening angle of 42° is calculated instead of the true value for the VSM-fabric (0°). Hence, due to the topography of reflections large errors can be introduced in the analysis of anisotropy.

Another effect of a dipping reflector in case of a wideangle survey is a jump in traveltime between shot locations. With the first shot the whole CMP area is covered (Figure 6.6). For the second shot geophone and shot positions are moved away from each other for one CMP length to cover the next range of incoming angles on the same CMP area. The CMP area covered with shot 1 and 2 is plotted as red solid line in the sketch, Figure 9.4. At Halvfarryggen we used a streamer with 60 geophones. Thus, the CMP area (Figure 9.4) corresponds to the area from the first geophone (zero-offset case at shot position 1) up to geophone 60 (G60-S1). The next larger offset would correspond to a combination of shot 1 and geophone 61 (G61-S1). This geophone does not exist. For a wideangle survey streamer and shot position are now moved for one CMP length. Thus, the offset between shot 2 and geophone 1 (G1-S2) is equal to the offset between shot 1 and the imaginary geophone 61 (S1-61). For a flat reflector the travelpath would be equal as well. However, for a tilted reflector ($\alpha > 0^\circ$) the travelpath between shot 2 and geophone 1 (G1-S1, green solid line) is longer than the travlepath between shot 1 and the imaginary geophone 61 (S1-61, green dashed line). Additionally, the reflection point of the travelpath between shot 2 and geophone 1 (G1-S2) does not correspond to the same reflection point as the zero-offset trace of shot 1. This is again due to the increased offset and the fact that angle of incident and reflection need to be equal. Thus, the CDP area will be shifted for shot 2 and the corresponding geophones 1 to 60 compared to the CDP area of shot 1. If all traces are now sorted with offset and the assumption is made that they all belong to one CMP, a jump in traveltime can be observed between the seismic trace of shot 1 with geophone 60 and the trace of shot 2 with geophone 1. This traveltime jump depends on the dip α of the reflector and the total offset. For increasing offset, the traveltime jump between shot positions will become weaker as the ratio between total length of the travelpath and the change due to the depth jump becomes smaller. This effect causes the jump in the traveltime we can observe for the bed reflection at an offset of 800 m in the Halvfarryggen wideangle data in Figure 3.4.

Halvfarryggen wideangle data

The traveltime difference (TWT) between shot position 1 and 2 of the Halvfarryggen wideangle data is ∼0.014 s. This corresponds to a travelpath difference of ∼54 m by assuming a P-wave velocity in ice of 3900 m/s and, thus, approximately a depth difference of 27 m. This fits quite well to the depth difference of ∼30 m derived from the dip of the bed reflector between CMP 263 and CMP 204 (Figure 9.3). The NMO velocity for three englacial reflectors, including the strong englacial reflector above the bed, and the ice-bed interface from the first shot position of the Halvfarryggen wideangle data set were picked (Figure 3.4). Thus, an interval velocity of 4700 m/s was derived for the layer above the

strong englacial reflection and a velocity of 4250 m/s for the layer between the strongest englacial reflector and the bed reflection. These velocities are really high for P-waves in ice, even under the assumption of a tilted reflector with a dip of $\alpha = 5^\circ$. Due to the dipping reflectors no attempt will be made here to determine the anisotropy exactly from the seismic wideangle data of Halvfarryggen. However, the dip of the englacial reflector is slightly weaker but follows the trend of the bed reflection. Hence, the velocity decrease from above to below the strong englacial reflector of -450 m/s indicates an anisotropic fabric. Due to the decrease in velocity it can be suggested that the ice crystal c-axis cluster more towards the vertical with depth. This indicates a decrease in the opening angle φ with depth at Halvfarryggen.

Hofstede et al. (2013) discuss the englacial reflections observed in the seismic data from Halvfarryggen and interpret the strong englacial reflection above the ice-bed interface as arising from changing COF. Thus, it would be very interesting to analyse seismic traveltimes in combination with radar data from this location to actually derive information about the change in COF. With the now available profile data a position for the survey could be chosen where the bed is flat. Additionally, with the now available, efficient, vibration seismic method a true CMP survey or a profile with a really high fold could be shot to decrease the effect of dipping reflectors on the traveltime. For true CMP surveys concepts exist to handle dipping layers in anisotropic medium (Alkhalifah and Tsvankin, 1995; Tsvankin, 1997). Whether a true CMP survey or a wideangle data set with a dipping reflector is analysed the possibility of 3D effects has to be taken into account. If the reflector is not only titled in the plane but also perpendicular to the plane of the seismic profile the observed reflection pattern might not map the topography of the reflector below the profile. To handle such 3D effects high resolution seismic or radar data from the analysed region are needed to get a reliable picture of the subsurface.

9.2.2 Bed properties from refracted wave

The dynamics of ice sheets and glaciers are strongly influenced by the sliding and deformation processes at the glacier bed. Thus, to determine the properties of the glacier bed is of great interest. At Halvfarryggen a refracted wave from the ice-bed interface could be observed. The velocity of the bed is calculated using the traveltimes and the offset of the emerging refracted wave.

For the analyses of the refracted wave the filtered data were used (sec. 6.2). Due to the triggering by hand no absolute time was recorded. This was corrected with help of the diving waves. After muting of the diving waves all shots were merged together sorted by offset (Figure 6.7 and 6.8). The refracted wave can be observed from a TWT of $\sim$0.7 s and an offset of $\sim$2080 m.

As discussed in section 9.2.2 a titled bed can be observed in the processed data from Halvfarryggen (Hofstede et al., 2013) at the location of the wideangle survey with a dip of about 5°. For the analysis of refracted waves in case of a tilted layer a forward and revere traveltime profile is normally analysed (e.g., Reynolds, 2011). However, no reverse direction was shot at Halvfarryggen, so that the analysis needs to be carried out using the forward direction alone. Thus, the estimate of the dip angle of 5° is used for the derivation of the bed velocity.

	Shot 8	Shot 10	Shot 14	mean
apparent velocity in m/s	5898	5686	5727	5771
random error	±30	±79	±47	±52
velocity in m/s	5429	5234	5271	5312

Table 9.1: Apparent velocities derived from fitting regression lines to the picked TWT-offset data of the refracted wave visible in Shot 8, 10 and 14 of the wideangle survey at Halvfarryggen. From the apparent velocities the velocity of the bed is calculated using equation (9.1).

In a first step the apparent velocity is derived from the TWT of the refracted wave. For this analysis the TWT of 3 shots in an offset range of 2556–3006 m (Shot 8), 2081–3307 m (Shot 10) and 4556–4844 m (Shot 14) are picked. Here, the refracted wave is clearly visible. As the absolute time was not recorded during the survey the TWTs from one shot to the next are not comparable. By fitting a regression line to the TWT-offset pairs for each shot the apparent velocity of the bed is derived from the gradient of the line (Table 9.1). There are slight differences in the calculated apparent velocities between the shots as shown in Table 9.1. The mean value of all shots would give an apparent velocity of 5771 m/s. In addition to the random error stated in Table 9.1 I estimate an systematic error of 50 m/s due to the stacking of 8 geophones distributed over 25 m per channel and variations in the bed topography in addition to the dip of the reflector.

In a second step the critical angle β is determined. The refracted wave emerges from the bed reflection at an offset of 2080±12.5 m. With the thickness of the ice of 900±20 m the critical angle in case of a tilted layer with a dip $\alpha = 5 \pm 1^\circ$ can be calculated. Thus, a critical angle of 49±2° is derived. The velocity of the bed v can be calculated using the information of the critical angle β, the dip of the reflector α and the picked apparent velocity v_A to be

$$v = v_\mathrm{A} \frac{\sin(\beta - \alpha)}{\sin(\beta)}. \tag{9.1}$$

Thus, velocities for the bed between 5230–5430 m/s (Table 9.1) are derived with an error of ∼200 m/s.

Reynolds (2011) and Telford et al. (1990), among others, give velocities for different rock and sediment types with velocities between 5000–5800 m/s for igneous rock. Taking these information into account and the derived velocity of around 5300 m/s the basement of Halvfarryggen is interpreted as igneous rock. Layering that could be observed in the vibroseis data was interpreted by Hofstede et al. (2013) as some sediment layers. Thus, it is assumed that some sediment layers overlay a basement consisting of igneous rock at the local dome Halvfarryggen.

9.3 Kohnen velocity analysis

Clear englacial reflections to pick traveltimes and determine the change in velocity over depth are missing in the Kohnen wideangle data sets. A clear signal is, however, visible from the ice-bed interface in the wideangle data sets from the explosive and vibroseis surveys, both parallel and perpendicular to the ice divide. This is exploited to determine the anisotropic NMO velocity ($V_{\mathrm{NMO,P}}$) and η_{eff}-value from the bed reflection of the P-wave data (sec. 9.3.1) and derive the major orientation of the girdle fabric (sec. 9.3.2).

9.3.1 ηNMO correction of bed reflection

Carrying out an ηNMO correction is done in two steps. In the first step the anisotropic NMO velocity ($V_{\mathrm{NMO,P}}$) is determined from the normal spread seismic data (offset/depth-ratio$\leq$1). Afterwards, the η_{eff}-value is determined from the long spread seismic data (offset/depth-ratio>1) using the derived anisotropic NMO velocity.

Figure 9.6 and 9.7 show the NMO (a) and ηNMO corrected data (b) for the vibroseis wideangle survey parallel and perpendicular to the ice divide, respectively. The corresponding values are given in the first part of Table 9.2. The vibroseis data are used here as it shows clear and strong bed reflections, also for larger offsets (app. B.2). The explosive data sets, para-exp-12m and perp-exp-12m, however, give similar anisotropic NMO velocities and η-values.

During the 2nd-order NMO correction the data are corrected for the hyperbolic moveout of the TWT due to increasing offset. Thus, reflections become flat. This hyperbolic approximation works quite well in case of both the para-vib and perp-vib data set for an offset up to 3 km. With the 2nd-order NMO correction the offsets with an offset/depth-ratio>1 are bended up. It is possible to correct the bed reflection for both data sets, para-vib and perp-vib. However, for an offset/depth-ratio$\leq$1 the analysis yields different anisotropic NMO velocities ($V_{\mathrm{NMO,P}}$) of about 100–150 m/s.

Afterwards, the ηNMO correction is applied. Therefore, the anisotropic NMO velocities derived during the 2nd-order NMO correction are used to derive the η_{eff}-value. With the ηNMO correction the reflection moveout become flat as well for offsets up to 6 km (Figure 9.6 and 9.7, b). The η_{eff}-value directly gives information about the existing anisotropy without the problem that the depth of the layer needs to be known to derive δ_{eff} from the anisotropic NMO velocities. Nevertheless, δ_{eff} can of course be calculated with the information about the thickness of the ice (2782$\pm$5 m) given by Wesche et al. (2007) (Table 9.2).

9.3.2 Girdle azimuth

The difference in anisotropic NMO velocity ($V_{\mathrm{NMO,P}}$) as well as η_{eff}- and δ_{eff}-values for the survey parallel and perpendicular to the ice divide can give a hint to derive the orientation (azimuth ψ) of the girdle fabric. Using the density, the temperature and the COF eigenvalue information of the ice core EDML the anisotropic NMO velocities $V_{\mathrm{NMO},\zeta}$ and the anisotropy parameter η_{eff} and δ_{eff} can be calculated for comparison with the values derived from the bed reflection of the seismic data (Table 9.2).

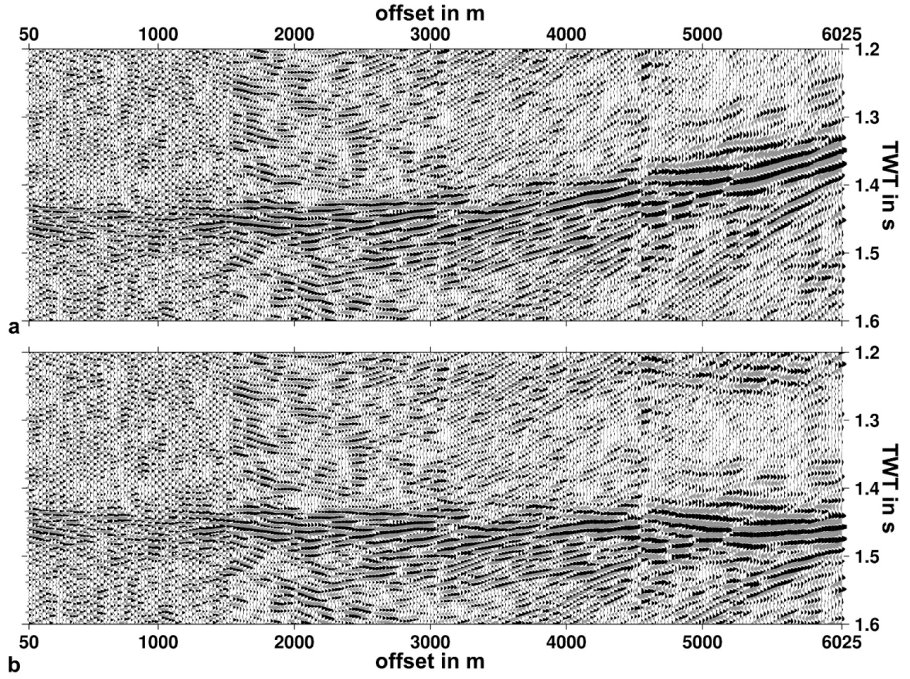

Figure 9.6: ηNMO corrected data for the survey para-vib, parallel to the ice divide: (a) is the 2nd-order NMO correction (eq. (3.45)) with the picked velocity for the bed reflection of 3563 m/s and (b) is the ηNMO correction (eq. (3.55)) with the determined η_{eff}-value 0.08842.

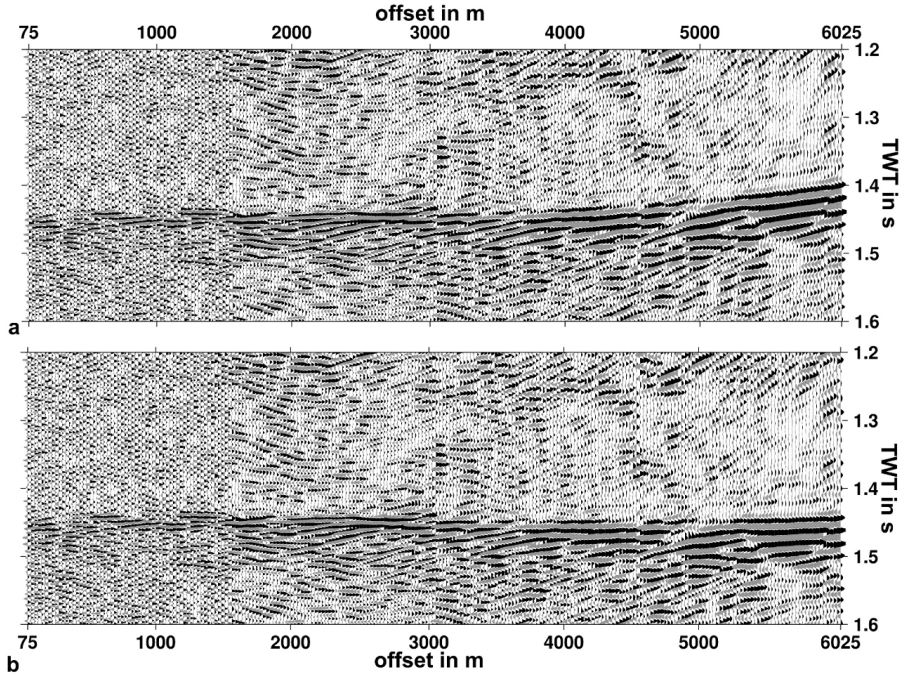

Figure 9.7: ηNMO corrected data for the survey perp-vib, perpendicular to the ice divide: (a) is the 2nd-order NMO correction (eq. (3.45)) with the picked velocity for the bed reflection of 3656 m/s and (b) is the ηNMO correction (eq. (3.55)) with the determined η_{eff}-value 0.04306.

Derived from seismic data				
Survey	TWT in s	$V_{\mathrm{NMO,P}}$ in m/s	η_{eff}	δ_{eff}
para-vib	1.432	3563	0.08842 (45°)	-0.08009 (42°)
perp-vib	1.442	3656	0.04306 (60°)	-0.05099 (58°)
Calculated from ice-core data				
Seismic anisotropy	TWT in s	$V_{\mathrm{NMO,P}}$ in m/s	η_{eff}	δ_{eff}
HTI $\psi = 0°$	1.436	3552	0.0861 (45°)	-0.0817 (42°)
$\psi = 90°$	1.436	3699	0.0310 (67°)	-0.0463 (61°)
Difference in %				
	TWT in s	$V_{\mathrm{NMO,P}}$ in m/s	η_{eff}	δ_{eff}
HTI $\psi = 0°$ & para-vib	0.3	0.3	3 (0)	2 (0)
$\psi = 90°$ & perp-vib	0.4	1	39 (10)	10 (5)

Table 9.2: The first part of the table gives the results from ηNMO correction of the seismic wideangle data from survey parallel and perpendicular to the ice divide at Kohnen station. The given TWT is the zero-offset TWT of the bed reflection. The δ_{eff}-values derived from seismic data were calculated using the derived NMO velocities and the thickness of the ice given by Wesche et al. (2007) to be 2782 m. The values in brackets give the corresponding cone opening angle derived from η_{eff} and δ_{eff} (app. A.6). The second part of the table gives the anisotropic NMO velocities, the η_{eff}- and δ_{eff}-values calculated from the EDML ice core data. The azimuth $\psi = 0°$ for an orientation of the girdle perpendicular to the seismic profile (HTI media) and parallel to the seismic profile for $\psi = 0°$. The last part gives the differences between the values derived from the seismic data and the values calculated from the EDML ice-core data.

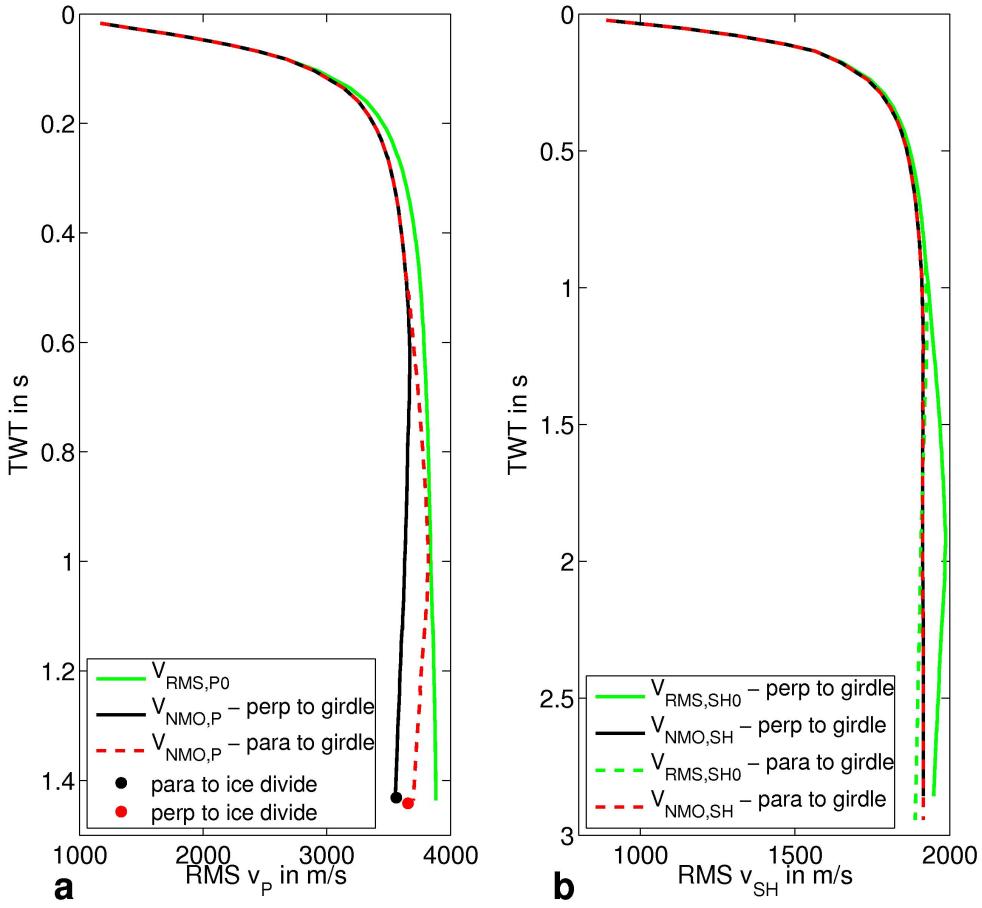

Figure 9.8: Anisotropic NMO velocities $V_{\mathrm{NMO},\zeta}$ and zero-offset RMS velocities $V_{\mathrm{RMS},\zeta 0}$ calculated for P- (a) and SH-wave (b) propagation from the EDML eigenvalues. The solid lines give the velocities calculated for a wave propagation perpendicular to a girdle fabric (HTI media, $\psi = 0°$), the solid lines give the velocities calculated for a wave propagation parallel to a girdle fabric ($\psi = 90°$). The green lines give $V_{\mathrm{RMS},\zeta 0}$, the black line $V_{\mathrm{NMO},\zeta}$ for $\psi = 0°$, the dashed red line the $V_{\mathrm{NMO},\zeta}$ for $\psi = 90°$. The dots blotted for the P-wave data (a) give the anisotropic NMO velocity $V_{\mathrm{NMO,P}}$ for the bed reflection determined from the survey parallel (para-vib, black) and perpendicular (perp-vib, red) to the ice divide. The thickness of the dots corresponds roughly to the estimated error of ± 20 m/s.

Figure 9.8 shows anisotropic NMO velocities $V_{\mathrm{NMO},\zeta}$ and zero-offset RMS velocities $V_{\mathrm{RMS},\zeta 0}$ for P- and SH-waves calculated for a girdle orientation perpendicular (HTI media, azimuth ψ=0°) and parallel to the direction of shooting (azimuth ψ=90°). No SH-wave surveys from Kohnen station are analysed here. Nevertheless, the influence of the anisotropic fabric, especially of the girdle fabric, on SH-wave propagation is discussed here for completeness. The velocities and anisotropic values calculated for the P-wave bed reflection ($V_{\mathrm{NMO,P}}$, η_{eff} and δ_{eff}) are given in the second part of Table 9.2.

The P-wave zero-offset RMS velocity is independent of the orientation of the girdle fabric (Figure 9.8, a). The anisotropic NMO velocity $V_{\mathrm{NMO,P}}$ is slower than the zero-offset RMS velocity $V_{\mathrm{RMS,P0}}$. Here, the anisotropic NMO velocity $V_{\mathrm{NMO,P}}$ for a propagation of the wave perpendicular to the orientation of the girdle (HTI media, $\psi = 0°$) is even slower than for a wave with a propagation parallel to the girdle orientation ($\psi = 90°$), i.e., in the isotropy plane. For the bed reflection the calculated zero-offset RMS velocity is 3884 m/s. Thus, the anisotropic NMO velocity for a propagation of the wave perpendicular to the ice divide is 5% (3699 m/s) slower than the zero-offset RMS velocity and for a propagation of the wave parallel to the ice divide 9% slower (3552 m/s).

In case of the SH-wave the anisotropic NMO velocity $V_{\mathrm{NMO,SH}}$ is nearly the same for the propagation of the wave perpendicular or parallel to the girdle fabric (Figure 9.8, b). This is an effect of the polarisation perpendicular to the propagation direction in the horizontal plane. If the propagation of the wave is perpendicular to the girdle orientation the polarisation is within the isotropy plane ($\psi = 0°$). If the propagation of the wave is in the isotropy plane the polarisation is in the symmetry plane perpendicular to the girdle orientation ($\psi = 90°$). Thus, either the propagation direction or the polarisation is in the slower symmetry plane. However, zero-offset RMS velocity $V_{\mathrm{RMS,S0}}$ and, thus, also TWTs are different for the SH-wave propagation parallel and perpendicular to the orientation of the girdle fabric. The zero-offset RMS velocity is faster than the anisotropic NMO velocity for the propagation perpendicular to the girdle orientation ($\psi = 0°$). This difference is 2% for the bed reflection ($V_{\mathrm{RMS,SH0}} = 1984$ m/s, $V_{\mathrm{NMO,SH}} = 1915$ m/s). Here, the polarisation is within the isotropy plane of the girdle. For the propagation parallel to the girdle orientation ($\psi = 90°$) the zero-offset RMS velocity is slower than the anisotropic NMO velocity below ~1.5 ms TWT. This difference is 1% for the bed reflection ($V_{\mathrm{RMS,SH0}} = 1889$ m/s, $V_{\mathrm{NMO,SH}} = 1915$ m/s). The polarisation is, here, within the symmetry plane perpendicular to the girdle. Hence, the TWT for the propagation perpendicular to the girdle orientation is smaller than that parallel to the girdle orientation. This makes a difference of 0.087 s or 3% in the TWT for the S-wave bed reflector at Kohnen. Thus, in case of SH-waves the influence of the girdle azimuth can be seen in the difference of the TWT but not really in the values derived for the anisotropic NMO velocity. The anisotropic NMO velocity is slower than the zero-offset RMS velocity for the propagation of the SH-wave perpendicular to the girdle fabric and faster for the propagation of the SH-wave parallel to the girdle fabric.

For the P-wave bed reflection the anisotropic NMO velocities were picked using the para-vib and perp-vib data. The values given in Table 9.2 are as well plotted in Figure 9.8, a (dots). For the determined NMO velocities, 3563 m/s and 3656 m/s on the parallel and perpendicular line, respectively, an error of ±20 m/s is estimated. These velocities for the bed reflection can be compared to the velocities calculated from the EDML ice-core data (Table 9.2 and Figure 9.8, a). The determined NMO velocity from the survey parallel to the ice divide (para-vib, black dot) fits to the velocity calculated for a girdle orientation perpendicular to the

wave propagation (HTI media, $\psi = 0°$, solid black line). The determined NMO velocity from the survey perpendicular to the ice divide (perp-vib, red dot) fits to the velocity calculated for a girdle orientation parallel to the wave propagation ($\psi = 90°$, dashed red line). The differences between picked and calculated velocities for these combinations are 0.3% and 1%, respectively (Table 9.2). This connection of picked and calculated seismic velocities would indicate that the majority of girdle fabric at Kohnen station is oriented perpendicular to the ice divide.

A slight difference in the picked zero-offset TWT between the line parallel and perpendicular to the ice divide can be observed. A zero-offset TWT of 1.442 s is picked in the perp-vib survey and 1.432 s in the para-vib survey. Hence, a difference of 0.01 s TWT ($\sim$0.7%) is observed, which corresponds roughly to one wave length or 20 m depth. This raises of course the question, if the bed at Kohnen is tilted and if our picked anisotropic NMO velocities are influenced by a dipping bed reflector as seen in the Halvfarryggen data set (sec. 9.2.2).

An indication for a tilted bed would be a jump in the traveltimes of the bed reflection for offset sorted wideangle data between neighbouring traces of different shot positions. In case of a positive dip (decrease in depth from shot to receiver) a jump in traveltime between the trace of the last geophone of the first shot and the first trace of the second shot to larger traveltimes should be observed (Figure 9.4). In case of a negative dip (increase in depth from shot to receiver) a jump in traveltime between the trace of the last geophone of the first shot and the first trace of the second shot to smaller traveltimes should be observed.

It is very difficult to judge here if a jump between shot 1 and 2 for the para-vib and perp-vib line exists due to filtering artifacts and small variations in the bed reflector (seismograms in app. B.4). However, in the para-vib survey a tendency to smaller traveltimes can be observed, in the perp-vib survey a tendency to larger traveltimes. This would indicate a negative dip in case of the para-vib survey and a positive dip in case of the perp-vib survey. Additionally, due to the difference in zero-offset TWT the depth down to the bed, below the shot of the para-vib survey needs to be more shallow than the depth below the perp-vib survey. This can be compared to a map of the bed topography around Kohnen station interpolated from radar measurements (Steinhage et al., 1999). The tendency here is that the bed below the first shot of the para-vib survey is higher than for the perp-vib survey. Further the bed topography map would indicate a weak negative dip for the para-vib survey and a weak positive dip for the perp-vib survey. Hence, the topography of the bed map would fit to a possible tilt direction derived from the seismic data. However, the resolution of the bed topography is very low compared to the covered CMP area of the seismic survey. For a reliably map of the bed topography a high resolution, migrated, 3D seismic or radar survey is needed. As a tilted bed can not be ruled out it might influence the interpretation of the determined anisotropic NMO velocities.

For a girdle orientation parallel to the ice divide the picked velocity of the para-vib survey would have to fit to the to the velocity calculated for a girdle orientation parallel to the wave propagation ($\psi = 90°$) and the picked velocity of the perp-vib survey would have to fit to the to the velocity calculated for a girdle orientation perpendicular to the wave propagation (HTI media, $\psi = 0°$). Thus, the tilt of the layer would have to be such that corresponding anisotropic NMO velocity would by $\sim$140 m/s faster (3563 (picked)$\rightarrow$3699 (calculated, $\psi = 90°$) in case of the para-vib survey and $\sim$100 m/s slower (3656 (picked)$\rightarrow$3552 (calculated, $\psi = 0°$)) in case of the perp-vib survey. For such a variation in the NMO velocity due to a

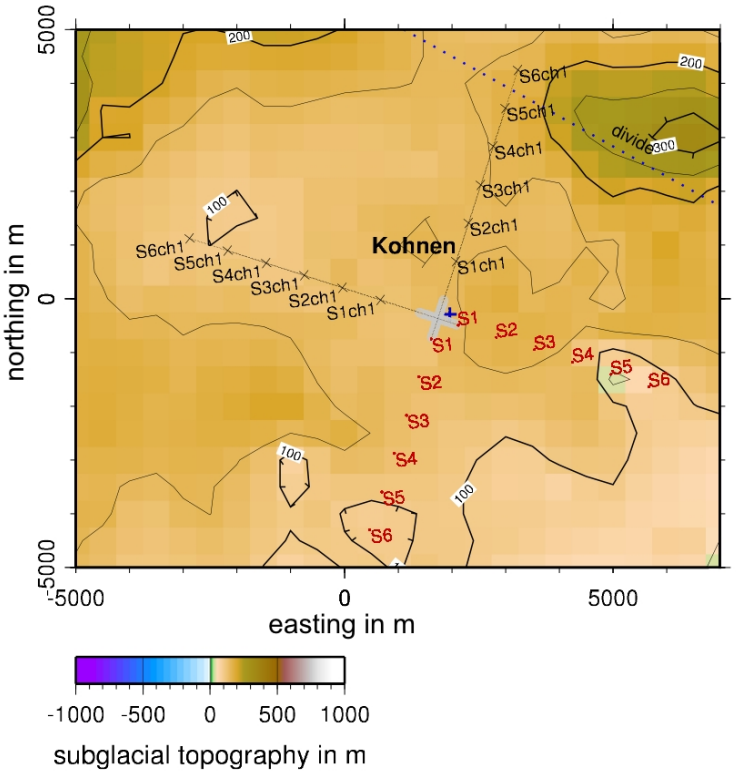

Figure 9.9: Bed topography interpolated from radar data (Steinhage et al., 1999), with the seismic wideangle survey shot at Kohnen station. The red dots give the location of the shots, the black crosses the corresponding position of the first channel of the streamer. The gray area indicates the CMP area that was covered over and over again during the wideangle survey. (Figure adapted from O. Eisen, pers. comm.)

tilted bed the dip needs to be negative in case of the para-vib survey and positive in case of the perp-vib survey. This, however, fits to the conclusion drawn from the seismic wideangle data and the bed topography map, i.e., that a tilted layer with a negative dip might exist on the para-vib line and a layer with positive dip might exist on the perp-vib line.

Assuming the bed reflector is flat and the picked anisotropic NMO velocity and the η_{eff}-value reflect the existing anisotropy the cone opening angle can be derived. Therefore the δ_{eff} value is derived fist (eq. (3.47)) using the depth of the bed (2782 m) given in Wesche et al. (2007). Afterwards, the cone opening angle for the different directions are calculates using the equations given in appendix A.6 for the η_{eff}- and δ_{eff}-values derived from the seismic data and for comparison from the η_{eff}- and δ_{eff}-values calculated from the EDML ice-core data. Thus, I would derive an opening angle of $\sim 43^\circ$ for the survey parallel to the ice divide and an opening angle of $\sim 59^\circ$ for the survey perpendicular to the ice divide as an average over the whole ice column at Kohnen. Hence, like a flattened cone fabric with the main orientation vertical and perpendicular to the ice divide, as a result of the main girdle orientation perpendicular to the ice divide.

9.3.3 The girdle orientation in the light of recent publications

A few paper exist that discuss the orientation of the girdle fabric at Kohnen station. Works by Eisen et al. (2007) and Drews et al. (2012) analyse reflections and backscatter from radar data of the radar survey 033042. Seddik et al. (2008) and Bargmann et al. (2012) model the development of the anisotropic ice fabric at Kohnen station. The study by Bargmann et al. (2012) is a further development of the work by Seddik et al. (2008). Eisen et al. (2007); Drews et al. (2012) and Bargmann et al. (2012), all find the orientation of the girdle fabric to be parallel to the ice divide.

In theory the ice crystal c-axis will orient perpendicular to the main direction of dilatation and parallel to the axis of main compression (Cuffey and Paterson, 2010). Wesche et al. (2007) give surface velocities in the vicinity of Kohnen station. The main velocity direction is WSW (273°N). These velocity measurements are used for the calculation of strain rates and the determination of a strain ellipsoid. This strain ellipsoid shows the main axis of dilatation perpendicular (NNE, 24°N) and the main axis of compression parallel (ESE, 114°N) to the ice divide (angles of strain ellipsoid given in Drews et al. (2012)). With an orientation of the c-axes perpendicular to the dilatation axis an orientation of the girdle parallel to the ice divide can be expected.

Changes in the reflection and the backscatter of radar data with changing polarisation direction were interpreted as an orientation of the girdle fabric parallel to the ice divide by Eisen et al. (2007). This includes the interpretation of the strong radar reflector at 2035 m depth and the reflection pattern that is observable in the different polarisation directions of profile 033042 (Figure 6.11). Due to the stronger reflection on the E (W) and SE (NW) directions the reflection is interpreted to be caused by a change from girdle fabric parallel to the ice divide to a narrow cone fabric. Further, they infer from integrated internal reflection power over a depth interval of ∼850–2530 m and the observed azimuthal reflection pattern that the major orientation of the girdle fabric is parallel to the ice divide. This conclusion is drawn from the assumption, that the backscatter due to statistical variations around the mean orientation is larger in the plane of the girdle than perpendicular to it.

The azimuthal backscatter of this data was as well analysed by Drews et al. (2012) over a depth interval of 200–1400 m. Here, they observe a change in the internal reflection power over depth with the main backscatter in the NNE (SSW) direction above 900 m depth and in the ESE (WNW) direction below 900 m depth. In terms of the COF variation, they also discuss bubble elongation. This is interpreted as arising from transition from isotropic fabric to girdle fabric above 900 m depth and a transition from girdle to VSM-fabric below. The backscatter pattern is connected with the variation of the eigenvalues λ_1 and λ_2 for measured intervals of 0.9 m. Here, variations are observed in λ_1, i.e., perpendicular to the plane of the girdle above 900 m depth and in λ_2, i.e., in the girdle plane below 900 m depth. This correlates with the backscatter pattern of the radar signal for an orientation of the girdle fabric parallel to the ice divide. Thus, it confirms the findings of Eisen et al. (2007) that the statistical variations in the plane of the girdle below ∼900 m depth at Kohnen are larger than perpendicular to it.

The modelling studies on the fabric development over depth at the EDML bore location by Seddik et al. (2008) and Bargmann et al. (2012) show good agreement with the fabric evolution down to a depth of 2100 m. However, the girdle fabric modeled by Seddik et al. (2008) show an orientation perpendicular to the flow direction, so an angle of 56° between ice divide and the girdle orientation. The model by Bargmann et al. (2012) is developed from the study by Seddik et al. (2008) and, additionally, includes rotation recrystallization, grain boundary migration and an horizontal extension ratio derived from observations. This yields an orientation of the girdle fabric parallel to the flow direction, i.e., an angle of 34° between ice divide and the girdle orientation. Nevertheless, the result is interpreted as fitting to the results from the radar measurements with an orientation of the girdle parallel to the ice divide.

Thus, all studies done so far on the orientation of the girdle fabric indicate an orientation of the the girdle vertical and parallel to the ice divide. This is in contrast to the seismic

measurements, that would indicate an orientation of the girdle perpendicular to the ice divide. The studies so far show two independent results. The first study is on the measured strain ellipsoid under the assumption that the measured stress field on the surface reflects the conditions over depth. This also includes the modeling studies. However, due to the calculation of the girdle orientation in the main flow direction and perpendicular to it some uncertainties exist here with respect to the interpretation of the girdle orientation perpendicular to the ice divide. The second study is on the analysis of the backscatter of the radar data. To explain that the seismic based conclusions of a girdle parallel to the ice divide are wrong the assumptions in both independent studies would have to be wrong. This would mean, that the assumption that the measured strain ellipsoid is representative for the strain field over depth at the EDML bore location is wrong. For the radar data study it would imply that the variation in the measured eigenvalues are an artifact of the measurement instead of being statistical variations around the mean orientation and that these statistical variations occur outside of the girdle plane during the transition to VSM-fabric.

With these theoretical considerations for the girdle fabric orientation of radar and modeling studies it seems unlikely that the derived orientation of the seismic data are unambiguously correct. Although picked velocities fit extremely well to the calculated velocities, the influence of a possible bed topography could not be determined conclusively. The bed topography map indicates a slightly tilted bed for both seismic lines that could explain the differences in the seismic velocities. The question remains if the picked anisotropic NMO velocities reflect the anisotropy present at the EDML drill site or if a stronger dependency on topography is superimposed on this result. To be able to finally answer this question the seismic profile data from the parallel and perpendicular lines need to be processed to get a reliable picture of the bed topography at exactly the location of the wideangle survey.

9.4 Conclusions from anisotropic NMO analysis

The traveltimes of reflections from three different sites were analysed to derive information on the anisotropic ice fabric. For the analysis of the velocities from the Antarctic sites, Halvfarryggen and Kohnen, the data from wideangle surveys were used. In principal such an approach is feasible but it introduces some problems and uncertainties in the traveltime analysis due to topography effects. More reliable results could be gained from the Colle Gnifetti survey where the existing anisotropy explains the differences between depth converted P-wave and SH-wave stacks.

The velocity analysis in case of the Colle Gnifetti data set was done after the data were CMP sorted and in case of the Halvfarryggen and Kohnen data set using the wideangle data. In both latter cases the assumption of a stack of flat layers was made. The Halvfarryggen data set showed a tilted reflector that introduced large errors on the velocity analysis due to the shooting geometry of the wideangle survey and the change in depth of the reflector over the survey area. The possibility of a tilted bed at Kohnen did introduce uncertainties in the derivation of the girdle orientation. It can only be suggested here, that locations for wideangle surveys should be chosen carrying out and processing seismic profile data first. Thus, a region of sufficiently flat layers can be chosen for the wideangle survey. Another possibility is to measure high fold seismic profile data. Hence, the data can be CMP sorted afterwards and with sufficiently large offsets a traveltime analysis can be carried out. The

influence of a dipping layer would be less pronounced. Furthermore, concepts exist for the analysis of such seismic data with tilted layers as well for anisotropic media (e.g., Alkhalifah and Tsvankin, 1995; Tsvankin, 2001). Thus, it might be worth while to carry out high fold data surveys with large offsets for a reliable analysis of the velocity profile. With the new vibrator technique allowing for more efficient surveying this will be readily feasible.

The dipping bed reflector at Halvfarryggen caused some additional uncertainties in the analysis of the velocities within the ice. However, the velocity decrease from the layer above to the layer below the strong englacial reflector indicates an anisotropic fabric with an increase of the c-axes orientation towards the vertical. Further, an observed critically refracted wave gave the possibility to analyse the bed properties and a bed velocity of 5300 ± 200 m/s was derived. In combination with the interpretation of sediment layers from vibroseis data (Hofstede et al., 2013) it can be concluded, that sediments overlay a basement of igneous rock. This result fits to passive geophysical measurements, gravimetry and magnetics (Riedel et al., 2012, 2013), from the region that find a positive magnetic anomaly at Halvfarryggen.

In the stacked and depth converted data from Colle Gnifetti a difference for the depth could be observed between P- and SH-wave stack. Using the measured density and temperature as well as measured COF data, that show a developed cone fabric, anisotropic NMO velocities and zero-offset RMS velocities could be calculated. Here, a difference between the anisotropic NMO velocities, derived during the stacking process, and the zero-offset RMS velocities, needed for the depth conversion, can be observed. For the P-wave this difference is 8%, for the SH-wave only 1%. Thus, the difference in the derived depth for the P-wave could be explained, as well as the good result in the depth conversion of the SH-wave data.

In contrast to the developed cone fabric at Colle Gnifetti girdle fabric exists over large parts in the ice at Kohnen. Thus, an azimuthal dependency for the anisotropic NMO velocity is observed. Using the EDML data the influence of this girdle fabric on the anisotropic NMO velocity and zero-offset RMS velocity could be investigated for P- as well as SH-waves. The anisotropic NMO velocities show observable differences between propagation parallel and perpendicular to the girdle fabric in case of the P-wave with differences to the zero-offset RMS velocities of 5% and 9%, respectively. For the SH-wave variations would theoretically only be observable in the zero-offset RMS velocity. The azimuthal variation of the anisotropic P-wave NMO velocity could be analysed on two different lines shot parallel and perpendicular to the ice divide. However, this traveltime analysis was carried out on the wideangle data introducing some uncertainties due to possible topography effects. Assuming that the layers are flat, an ηNMO correction was carried out so that anisotropic NMO velocities and η_{eff}-values were derived for the survey parallel and perpendicular to the ice divide on long-spread seismic data (offset/depth-ratio$>$1). From these values the conclusion could be drawn that the majority of the girdle fabric is oriented vertical and perpendicular to the ice divide. Furthermore, mean opening angles over the complete depth were derived with $\sim43^\circ$ within the plane of the ice divide and $\sim59^\circ$ perpendicular to it. This result is in contrast to the analysis of radar data and modeling studies that find the majority of the girdle fabric orientated parallel to the ice divide. However, all these results of the seismic, radar and modeling studies are based on different assumptions. To verify the result of the seismic wideangle data, the profile seismic data from Kohnen on the parallel and perpendicular line needs to be processed. Thus, it would be possible to finally conclude on the topography of the bed and, consequently, possible effects for the velocity analysis.

A possibility to derive information about the COF was given by the combination of seismic and radar data from Colle Gnifetti. The anisotropic NMO velocities were derived from normal-spread seismic data (offset/depth-ratio$\leq$1). These values were combined with zero-offset RMS velocities derived from the depth of reflections observed in the radar data. Thus, the Thomsen parameter δ_{eff} was derived for a two layer case. The cone opening angle derived from δ_{eff} for the lower layer ($\geq$28 m depth) fits quite well to the cone opening angle calculated from the COF eigenvalue data. Above the firn-ice transition ($\leq$28 m depth) an anisotropic fabric was derived with an cone opening angle of $\sim$77°. Thus, it is concluded that a developed anisotropic ice fabric exists already within the firn region at Colle Gnifetti.

Hence, two different possibilities exist to derive information about anisotropic ice fabric. In case of normal-spread seismic data the anisotropic NMO velocity is derived. The reflector depth needs to be derived from other data sets like radar or ice core data to obtain the Thomsen parameter δ. For long-spread seismic data the anisotropy parameter η can be determined, next to the anisotropic NMO velocity. This gives the possibility to directly conclude on the anisotropic fabric from the seismic data alone. Thus, the possibility is also given to include the information about the existing anisotropy in the derivation of the depth of layers from seismic data.

Of course, to be able to derive information about existing COF over depth englacial reflections need to be observable in the seismic data. This was possible at Colle Gnifetti for the shallow case. The Halvfarryggen data show that multiple englacial reflections can be observed in seismic data from Antarctica as well. The possibility to handle the influence of topography of the analysed layers and improved seismic shooting to gain high frequency data with low coherent noise also for thicker ice bodies like present at Kohnen is needed. Thus, the potential exists to resolve COF variations over depth from seismic data.

10 Conclusion and Outlook

The main focus of this work was to investigate the influence of the anisotropic ice fabric on seismic data and the possibility to use these seismic data sets to derive information about the distribution of COF. The advantage of seismic as well as radar data is that information about the distribution of COF can be gained over larger areas of glaciers and ice sheets with reasonably low effort. Thus, information about the COF distributions can be obtained away from the limited positions of ice cores. This gives the possibility to investigate the anisotropic ice fabric in flank-flow regimes but also on and in the vicinity of ice domes and divides in more detail.

To be able to observe COF-induced reflections in seismic and radar data abrupt changes in the COF distribution are needed. It is still difficult for models to reproduce these abrupt changes of the strain-induced anisotropy over depth. However, clear englacial and bed reflections were observable in the seismic data sets. The analysis of the traveltimes of these reflections showed great potential to derive information about the existing anisotropy in ice and, thus, about the elastic properties of anisotropic ice.

An improved understanding of the COF distribution might help to improve ice-flow models with anisotropic rheology. These models are needed for reliable age-depth scales of englacial layers and, thus, for a better understanding of the paleoclimate. It is still under discussion if COF does not only reflect existing stress regimes but is also influenced by the climate and is, thus, a climate proxy like results of Kennedy et al. (2013) suggest. COF as climate proxy and not only important for the flow behaviour would increase the importance to derive the COF distribution over larger parts in ice sheets.

The main results and conclusions gained from the seismic data and the combination of seismic and radar data are summarised below. The last part of this chapter will give an outlook about successful seismic surveys to detect COF and how to improve the understanding of seismic velocities in ice and the derivation of the velocities from COF eigenvalues further.

Conclusion

The elasticity tensor for different ice fabrics was derived from COF eigenvalues. Velocities and reflection coefficients calculated using these elasticity tensors were used to analyse seismic data from Antarctica and the Swiss Alps. It was found, that the influence of the anisotropy on the reflection coefficient is to weak for reliable analysis. Therefore, the focus was set on the analysis of the anisotropic ice fabric using the traveltimes. Two approaches were applied here: (i) the analysis of anisotropic NMO velocities from normal-spread seismic data in combination with other data sets determining the depth of reflectors and (ii) the analysis of the anisotropy parameter η determined from long-spread seismic data.

Calculation of elasticity tensor from COF eigenvalues (Ch. 4)

In a first step, a method was derived to calculate the elasticity tensor form the COF eigenvalue data for cone, thick girdle and partial girdle fabric. Using these polycrystal elasticity tensors the velocities, i.e., phase and group velocities, for P-, SH- and SV-waves in orthorhombic media were calculated. Thus, the velocity pattern of the anisotropic ice fabric could be investigated and the angle dependency of the velocity for these different fabrics. The velocities calculated by deriving the polycrystal elasticity tensor show good agreement with the velocities derived from Bennett (1968) for small cone opening angles. In both methods weaknesses can be observed for opening angels in the limit of isotropic state ($\varphi = \chi \rightarrow 90°$). The introduced framework to calculate elasticity tensors from COF eigenvalues extends the possibilities such that velocities of girdle fabrics can be investigated as well as reflection coefficients for the developed anisotropy within the ice.

Weak influence of anisotropy on reflection coefficients (sec. 4.2.3)

Using the derived elasticity tensors reflection coefficients were calculated for the transition between different anisotropic ice fabrics. It was found that the reflection coefficients and the variations of the reflection coefficients with increasing offset are weak for the transition between different COF distributions. They are at least an order of magnitude smaller than reflections from the ice-bed interface. Thus, significant changes in the COF distribution are needed to cause observable englacial reflections. The influence of anisotropic ice fabric compared to the isotropic case for the reflection at the ice-bed interface is so small that it is within the measurement inaccuracy of seismic AVO analysis. Here, the difference between exact and approximate calculations of reflection coefficients for the ice-bed interface is larger than the influence of an anisotropic ice fabric above the bed. Due to this weak influence of the anisotropic ice fabric on the reflection coefficient the focus was set on the derivation of the anisotropy using NMO and ηNMO correction.

Choice of elasticity tensor (Ch. 7)

The velocities derived from the VSP measurement at Kohnen show a clear transition from slower velocities above $\sim$1800 m depth to faster velocities below $\sim$2030 m depth. The same velocity trend could be derived from the COF eigenvalues of the EDML ice core with the transition form girdle to cone fabric between 1800 m to 2030 m depth. For a good correlation of the absolute velocity values, not only the trend, the choice of the monocrystal elasticity tensor is important for the calculation of the polycrystal elasticity tensor. It turned out that the best fit between calculated and derived velocities can be found using the monocrystal elasticity tensor given by Jona and Scherrer (1952), Gammon et al. (1983) or Bennett (1968). However, the calculated velocities using these elasticity tensors never reach the full range between the observed slowest and fastest velocities. Combining this result with the result of Gusmeroli et al. (2012) who found best agreement with velocities from ultrasonic sounding measurements using the elasticity tensor of Dantl (1968), the question on the frequency dependency of seismic wave velocities in ice remains.

New S-wave–density relationship (eq. (4.10); sec. 8.1.1)

The SH-wave data set from Colle Gnifetti was used to derive a new S-wave–density relationship. By applying the Herglotz-Wiechert inversion to traveltimes of diving waves from the SH-wave survey at Colle Gnifetti a S-wave velocity profile was derived. Combining this S-wave velocity profile with the densities measured at the KCI ice core the S-wave–density relationship given in equation (4.10) was obtained.

Identifying COF-induced reflections in seismic and radar data (Ch. 8)

The comparison of seismic, radar and ice-core data helped to identify COF-induced reflections in these data sets. The common reason for englacial reflections below the firn-ice transition in seismic and radar data is a sudden change in the COF. By detecting reflections of the same origin in seismic and radar data these reflectors can be identified as COF induced. This works best if a reliable depth conversion for the seismic and radar data exists. Especially, in case of the seismic data this might not by the case. At Kohnen the VSP velocities could be used for the depth conversion of the seismic data. Thus, it was possible to identify three reflections in the seismic and radar data as COF induced. For a clear reflection in the seismic data a sudden change in the COF distribution is required. At the same time a problem occurs if changes in COF occur at frequent intervals. If the depth intervals are too short it is not possible to resolve these layers. This depends, of course on the seismic wavelength. The identification of the COF-induced reflections at Kohnen also shows that the measurements of the COF eigenvalues from ice cores with 50 m resolution, as present for the EDML ice core, might miss sudden but strong variations in the COF distribution. But exactly those abrupt changes over short depth scales cause reflections in seismic and radar data.

Different influence of anisotropy on P- and SH-wave data (sec. 8.1 & Ch. 9)

Differences in the reflection behaviour of P- and SH-waves could be observed in the data from Colle Gnifetti. The resolution of P- and SH-waves is, of course, different. Nevertheless, the SH-wave seems to be more sensitive for density variations while the P-wave seem to be more sensitive to changes in anisotropy.

Using the eigenvalues of the EDML and KCI ice core anisotropic NMO velocities and zero-offset RMS velocities could be calculated. While a difference in the anisotropic NMO and zero-offset RMS velocities for the bed reflection at Colle Gnifetti and Kohnen could be observed of 1-2% for the SH-wave, a difference of up to 9% was derived for the P-wave. Hence, in case of the P-wave the velocities derived from the NMO correction, i.e., the anisotropic NMO velocities, should not be used for the depth conversion. In case of the SH-wave the error is small $\leq$2%. However, in case of the P-wave errors up to 9% can not be neglected. Additionally, a difference in the effect of azimuthal dependent anisotropy, i.e., of the orientation of girdle fabric, can be observed between anisotropic P- and SH-wave NMO velocities calculated from EDML eigenvalues. The girdle fabric, parallel and perpendicular to the direction of shooting introduces a difference of $\sim$4% in the anisotropic NMO velocity at Kohnen. For the anisotropic SH-wave NMO velocity this effect is negligible. However, the zero-offset RMS velocity differs by $\sim$5% and, thus, also the zero-offset TWT by $\sim$3%.

Hence, the orientation of girdle fabric can either be determined from the difference in the anisotropic P-wave NMO-velocity or the difference in the SH-wave zero-offset TWT.

NMO velocities to determine COF (Ch. 3 & Ch. 9)

The anisotropic NMO velocities are derived during the NMO correction. Thus, they are a result of the seismic data processing. The zero-offset RMS velocities are needed for the depth conversion. The difference between anisotropic NMO velocities and zero-offset RMS velocities depends on the existing anisotropy, the thickness over which this anisotropy occurs and the wave polarisation. Due to this difference of anisotropic NMO velocity and zero-offset RMS velocity of P-wave data information about the existing COF in glaciers and ice sheets can be gained from these data sets.

With additional information about the depth of the analysed reflector from, e.g., radar or ice-core data the zero-offset RMS velocity can be determined. This was applied to data from Colle Gnifetti where P-wave reflections were linked to radar reflectors. Thus, the cone opening angel for a two layer case could be derived. It could be concluded that anisotropy exists with an anisotropic cone opening angel of 77° in the firn and a stronger anisotropy with a cone opening angle of 36° below the firn-ice transition.

Anisotropic NMO velocities picked for the bed reflection at Kohnen station could be connected with anisotropic NMO velocities calculated for a girdle orientation parallel and perpendicular to the ice divide. This leads to the conclusion that the majority of the girdle fabric at Kohnen is oriented perpendicular to the ice divide. However, this is in contrast with results from radar data studies that conclude on an orientation of the girdle fabric parallel to the ice divide. The different result is explainable with a tilted bed. The strong influence of a tilted bed on the velocity analysis of seismic wideangle data could be observed on the Halvfarryggen wideangle data. To be able to definitely decide on the dominating effect, anisotropy or topography, for the analysis of the Kohnen wideangle data the seismic profile data needs to be processed.

η-value as proxy for COF distribution (Ch. 3 & Ch. 9)

If long-spread data (offset/depth-ratio$>$1) is available information about the anisotropy can be gained from the η-value determined during the ηNMO correction. Thus, it is possible to derive information about the existing anisotropy from seismic data alone. With the assumption of flat layers at Kohnen the ηNMO correction was used to derive a mean opening angle of 42° parallel and 58° perpendicular to the ice divide.

Outlook

To gain better and more reliable information about COF distributions in the future from seismic data the seismic surveys need to be improved on the one hand and on the other hand the understanding of the seismic velocities in ice and the derivation of these velocities from seismic data needs to be improved further. To be able to analyse the COF distribution over

depth from seismic data COF reflections need to be detectable. Therefore, high frequency data ($\geq$400 Hz) with only weak coherent noise from surface and diving waves are needed to resolve englacial reflections. This can possibly be achieved through explosive sources in boreholes with a depth around the pore-close off. Thus, less surface and diving waves are exited. High frequencies can be excited better with smaller charge sizes. At Kohnen, for example, higher frequencies could be excited with the 0.4 kg charge size compared to the 5.6 kg charge size. The charge size depends, of course, on target depth and offset. A further consideration should be to shoot high fold profile data. The CMP sorted data could be analysed to derive velocities from the traveltimes instead of wideangle data. Thus, effects of topography on the velocity analysis could be reduced. Beside the reduction of the influence of topography in the data it should be an aim for future analysis to be able to include dipping reflectors in the analysis of the velocity profile from glaciers and ice sheets.

Some limitations due to the calculation of the elasticity tensor from the eigenvalues and the monocrystal elasticity tenors exist. All monocrystal elasticity tensors used for the calculation of the polycrystal elasticity tensor were measured in the kHz to GHz range. The results of the VSP survey in combination with the results of the study by Gusmeroli et al. (2012) do, however, suggest a frequency dependency of the seismic wave velocity. This implies a frequency dependency for the components of the elasticity tensor. Dantl (1968) could not find such a frequency dependency of the elastic moduli in the range of 5–190 MHz. However, this is orders of magnitude different from the seismic frequencies that are normally in the range of $\sim$50–400 Hz. Here, the frequency dependency of seismic waves should be investigated further.

Another limitation in the calculation of the elasticity tensors was that the opening angles had to be derived from the COF eigenvalues of the momentum of inertia. To do so the fabric was divided in cone, thick and partial girdle fabric. Thus, artificial jumps in the calculated velocity profile were introduced. Here, it would be better to provide information about the COF distribution directly in form of two opening angels calculated from the c-axes orientations instead of the eigenvalues. Hence, the calculation of the elasticity tensor would no longer be limited to cone, thick and partial girdle fabric and their rigid classification.

Finally, the analysis and comparison of seismic velocities and the expectation of the occurrence of seismic reflections is based on the COF eigenvalue data. It showed that reflections in the seismic and radar data occur at a depth where they would not be expected from the COF measurements. Here, high resolution measurement of COF are needed. This is on the one hand important to see small scale variations of COF and on the other hand to evaluate on how representative COF measurements over depth intervals of several meters are. A better understanding, here, could help to increase the efficiency of seismic and radar methods in detecting the COF distribution by analysing COF-induced reflections and COF-influenced traveltimes.

Bibliography

Aki, K. and Richards, P. G. (2002). *Quantitative Seismology*. University Science Books Sausalito, California.

Albert, D. G. and Bentley, C. R. (1990). Seismic Studies on the Grid Eastern Half of the Ross Ice Shelf: RIGGS III and RIGGS IV. In *The Ross Ice Shelf: Glaciology and Geophysics*, pages 87–108. American Geophysical Union.

Alean, J., Haeberli, W., and Schädler, B. (1983). Snow accumulation, firn temperature and solar radiation in the area of the Colle Gnifetti core drilling site (Monte Rosa, Swiss Alps): Distribution patterns and interrelationship. *Zeit. Gletsch. Glaz.*, 19(2):131–147.

Alkhalifah, T. and Tsvankin, I. (1995). Velocity analysis for transversely isotropic media. *Geophysics*, 60(5):1550–1566.

Alley, R. B. (1992). Flow-law hypotheses for ice-sheet modeling. *J. Glaciol.*, 38(129):245–256.

Anandakrishnan, S. (2003). Dilatant till layer near the onset of streaming flow of Ice StreamC, West Antarctica, determined by AVO (amplitude vs offset) analysis. *Ann. Glaciol.*, 36:283–286.

Anandakrishnan, S., Fitzpatrick, J. J., Alley, R. B., Gow, A. J., and Meese, D. A. (1994). Shear-wave detection of asymmetric c-axis fabrics in the GISP2 ice core. *J. Glaciol.*, 40(136):491–496.

Ashby, M. F. and Duval, P. (1985). The creep of polycrystalline ice. *Cold Reg. Sci. Technol.*, 11:285–300.

Backus, G. E. (1965). Possible forms of seismic anisotropy of the uppermost mantle under oceans. *J. Geophys. Res.*, 70(14):4329–3439.

Bargmann, S., Seddik, H., and Greve, R. (2012). Computational modeling of flow-induced anisotropy of polar ice for the EDML deep drilling site, Antarctica: The effect of rotation recrystallization and grain boundary migration. *Int. J. Numer. Anal. Meth. Geomech.*, 36(7):892–917.

Bass, R., Rossberg, D., and Ziegler, G. (1957). Die elastischen konstanten des Eises. *Zeitschr. f. Physik*, 149:199–203.

Bennett, H. F. (1968). *An investigation into velocity anisotropy through measurements of ultrasonic wave velocities in snow and ice cores from Greenland and Antarctica*. PhD thesis, University of Wisconsin-Madison.

Bentley, C. R. (1972). Seismic-wave velocities in anisotropic ice: A comparison of measured and calculated values in and around the deep drill hole at Byrd Station, Antarctica. *J. Geophys. Res.*, 77(23):4406–4420.

Bingham, R. G. and Siegert, M. J. (2007). Radio-Echo Sounding over polar ice masses. *J. Environ. Eng. Geophys.*, 12(1):47–62.

Blankenship, D. D. and Bentley, C. R. (1987). The crystalline fabric of polar ice sheets inferred from seismic anisotropy. *The Physical Basis of Ice Sheet Modelling (Proceedings of the Vancouver Symposium) IAHS Publ.*, (170):54–57.

Blankenship, D. D., Bentley, C. R., Rooney, S. T., and Alley, R. B. (1986). Seismic measurements reveal a saturated porous layer beneath an active Antarctic ice stream. *Nature*, 322(6074):54–57.

Bohleber, P. (2011). *Ground-penetrating radar assisted ice core research: The challenge of Alpine glaciers and dielectric ice properties*. PhD thesis, Ruperto-Carola University Heidelberg, Germany.

Bohleber, P., Wagner, N., and Eisen, O. (2012). Permittivity of ice at radio frequencies: Part II. Artificial and natural polycrystalline ice. *Cold Reg. Sci. Technol.*, 83â84:13 – 19.

Booth, A. D., Clark, R. A., Kulessa, B., Murray, T., Carter, J., Doyle, S., and Hubbard, A. (2012). Thin-layer effects in glaciological seismic amplitude-versus-angle (AVA) analysis: implications for characterising a subglacial till unit, Russell Glacier, West Greenland. *The Cryosphere*, 6(4):909–922.

Bower, A. F. (2010). *Applied mechanics of solids*. CRC Press, Boca Raton, Fla.

Brockamp, B. (1933). *Deutsche Grönland-Expedition Alfred Wegener ... 1929 und 1930/1931*, volume 2: Seismik. Brockhaus, Leipzig.

Brockamp, B. (1935). *Deutsche Grönland-Expedition Alfred Wegener ... 1929 und 1930/1931*, volume 3: Glaziologie. Brockhaus, Leipzig.

Brockamp, B. and Kohnen, H. (1965). Ein Beitrag zu den seismischen Untersuchungen auf dem Grönländischen Inlandeis. *Polarfoschung*, 35(1/2):2–12.

Brockamp, B. and Mothes, H. (1930). Seismische Untersuchungen auf dem Paterzegletscher I. *Zeischr. f. Geophysik*, 6:482–501.

Brockamp, B. and Mothes, H. (1931). Seismische Untersuchungen auf dem Paterzegletscher II. *Zeischr. f. Geophysik*, 7:232–240.

Brockamp, B. and Querfurth, H. (1964). Untersuchungen über die Elastizitätskonstanten von See- und Kunsteis. *Polarfoschung*, 34(1/2):253–262.

Brook, E. J., Wolf, E., Dahl-Jensen, D., Fischer, H., and Steig, E. J. (2006). The future of ice coring: International Partnerships in Ice Core Siences (IPICS). *PAGES News*, 14(1):6–10.

Crampin, S. (1977). A review of the effects of anisotropic layering on the propagation of seismic waves. *Geophys. J. R. astr. Soc.*, 49:9–27.

Cuffey, K. M. and Paterson, W. S. B. (2010). *The Physics of Glaciers*. Elsevier.

Daley, P. and Heron, F. (1977). Reflection and transmission coefficients for transversely isotropic media. *Bulletin of the Seismological Society America*, 67(3):661–675.

Daley, P. F. and Krebes, E. S. (2004). Alternative linearized exoressions for qP, qS1 and qS2 phase velocities in a weakly anisotropic orthorombic medium. *CREWES Research Report*, 16:1–19.

Dantl, G. (1968). Die elastischen Moduln von Eis-Einkristallen. *Phys. kondens. Materie*, 7:390–397.

Diez, A., Eisen, O., Hofstede, C., Bohleber, P., and Polom, U. (2013). Joint interpretation of explosive and vibroseismic surveys on cold firn for the investigation of ice properties. *Ann. Glaciol.*, 54(64):201–210.

Diez, A., Eisen, O., Weikusat, I., Eichler, J., Hofstede, C., Bohlen, T., and Polom, U. (submitted). Influence of crystal anisotropy on seismic velocity analysis. *Ann. Glaciol.*

Diprinzio, C. L., Wilen, L. A., Alley, R. B., Fitzpatrick, J. J., Spencer, M. K., and Gow, A. J. (2005). Fabric and texture at Simple Dome, Antarctica. *J. Glaciol.*, 51(173):281–290.

Dowdeswell, J. A. and Evans, S. (2004). Investigations of the form and flow of ice sheets and glaciers using radio-echo sounding. *Rep. Prog. Phys.*, 67(10):1821–1861.

Drews, R., Eisen, O., Steinhage, D., Weikusat, I., Kipfstuhl, S., and Wilhelms, F. (2012). Potential mechanisms for anisotropy in ice-penetrating radar data. *J. Glaciol.*, 58(209):613–624.

Drews, R., Martin, C., Steinhage, D., and Eisen, O. (2013). Characterizing the glaciological conditions at Halvfarryggen ice dome, Dronning Maud Land, Antarctica. *J. Glaciol.*, 59(213):9–20.

Druivenga, G., Grossmann, E., Grüneberg, S., Polom, U., and Rode, W. (2011). Transportabler Scherwellenvibrator. *Deutsches Patent- und Markenamt*, (DE10327757A1).

Eisen, O., Diez, A., Hofsetde, C., Lambrecht, A., Mayer, C., and Miller, H. (2012). Performance of light vibroseismic sources on polar firn. *Geophysical Research Abstracts*, 14:EGU2012–1383.

Eisen, O., Hamann, I., Kipfstuhl, S., Steinhage, D., and Wilhelms, F. (2007). Direct evidence for continuous radar reflector originating from changes in crystal-orientation fabric. *The Cryosphere*, 1(1):1–10.

Eisen, O., Nixdorf, U., Keck, L., and Wagenbach, D. (2003). Alpine ice cores and ground penetrating radar: combined investigations for glaciological and climatic interpretations of a cold Alpine ice body. *Tellus*, 55B(5):1007–1017.

Eisen, O., Wilhelms, F., Steinhage, D., and Schwander, J. (2006). Instruments and Methods: Improved methode to determine radio-echo sonding reflector depth from ice-core profiles of permittivity and conductivity. *J. Glaciol.*, 52(177):299–310.

Elvin, A. A. (1996). Number of grains required to homogenize elastic properties of polycrystalline ice. *Mechanics of Materials*, 22:51–64.

Fernandoy, F., Meyer, H., Oerter, H., Wilhelms, F., Graf, W., and Schwander, J. (2010). Temporal and spatial variation of stable-isotope ratios and accumulation rates in the hinterland of Neumayer station, East Antarctica. *J. Glaciol.*, 56(198):673–687.

Fujita, S., Maeno, H., and Matsuoka, K. (2006). Radio-wave depolarization and scattering within ice sheets: a matrix-based model to link radar and ice-core measurements and its application. *J. Glaciol.*, 52(178):407–424.

Fujita, S., Matsuoka, T., Ishida, T., Matsuoka, K., and Mae, S. (2000). A summary of the complex dielectric permittivity of ice in the megahertz range and its application for radar sounding of polar ice sheets. In Hondoh, T., editor, *The physics of ice core records*, pages 185–212. Hokkaido University Press.

Gagliardini, O., Durand, G., and Wang, Y. (2004). Grain area as a statistical weight for polycrystal constituents. *J. Glaciol.*, 50(168):87–95.

Gammon, P. H., Kiefte, H., Clouter, M. J., and Denner, W. W. (1983). Elastic constant of artificial and natural ice samples by brillouin spectroscopy. *J. Glaciol.*, 29(103):433–460.

Gow, A. J. and Williamson, T. (1976). Rheological implications of the internal structure and crystal fabrics of the West Antarctic ice sheet as revealed by deep core drilling at Byrd Station. *Geol. Soc. Am. Bull.*, 87(12):1665–1677.

Graebner, M. (1992). Plane-wave reflection and transmission coefficients for a transversely isotropic solid. *Geophysics*, 57(11):1512–1519.

Green, R. E. and Mackinnen, L. (1956). Determination of the Elastic Contants of ice single crystaly by ultrasonic pulse method. *J. Acoust. Soc. Am.*, 28(6):1292.

Gusmeroli, A., Clark, R. A., Murray, T., Booth, A. D., Kulessa, B., and Barrett, B. E. (2010). Seismic wave attenuation in the uppermost glacier ice of Storglaciaren, Sweden. *J. Glaciol.*, 56(196):249–256.

Gusmeroli, A., Pettit, E. C., Kennedy, J. H., and Ritz, C. (2012). The crystal fabric of ice from full-waveform borehole sonic logging. *J. Geophys. Res.*, 117:F03021.

Haeberli, W. and Alean, J. (1985). Temperature and accumulation of high altitude firn in the Alps. *Ann. Glaciol.*, 6:161–163.

Haeberli, W., Schmid, W., and Wagenbach, D. (1988). On the Geometry, flow and age of firn and ice at the Colle Gnifetti core drilling site (Monte Rosa, Swiss Alps). *Zeit. Gletsch. Glaz.*, 24(1):1–19.

Helgerud, M. B., Waite, W. F., Kirby, S. H., and Nur, A. (1968). Elastic wave speeds and moduli in polycrystalline ice Ih,sI methane hydrate and sII methane-ethane hydrate. *Phys. kondens. Materie*, 7:390–397.

Hill, R. (1952). The elastic behaviour of a crystalline aggregate. *Proc. Phys. Soc. A*, 65:349–354.

Hofstede, C., Eisen, O., Diez, A., Jansen, D., Kristoffersen, Y., Lambrecht, A., and Mayer, C. (2013). Investigating englacial reflections with vibro- and explosive-seismic surveys at Halvfarryggen ice dome, Antarctica. *Ann. Glaciol.*, 54(64):189–200.

Holland, C. W. and Anandakrishnan, S. (2009). Subglacial seismic reflection strategies when source amplitude and medium attenuation are poorly known. *J. Glaciol.*, 55(193):931–937.

Hölzle, M., Darms, G., Lüthi, M. P., and Suter, S. (2011). Evidence of accelerated englacial warming in the Monte Rosa area, Switzerland/Italy. *The Cryosphere*, 5:231–243.

Horgan, H. J., Anandakrishnan, S., Alley, R. B., Peters, L. E., Tsoflias, G. P., Voigt, D. E., and Winberry, J. P. (2008). Complex fabric development revealed by englacial seismic reflectivity: Jakobshavn Isbræ, Greenland. *Geophys. Res. Letters*, 35(10):L10501+.

Horgan, H. J., Anandakrishnan, S., Jacobel, R. W., Christianson, K., Alley, R. B., Heeszel, D. S., Picotti, S., and Walter, J. I. (2012). Subglacial Lake Whillans–Seismic observations of a shallow active reservoir beneath a West Antarctic ice stream. *E. Plan Sci. Let.*, 331-332:201–209.

Horgan, H. J., Christianson, K., Jacobel, R. W., Anandakrishnan, S., and Alley, R. B. (2013). Sediment deposition at the modern grounding zone of Whillans Ice Stream, West Antarctica. *Geophys. Res. Letters*, 40(15):3934–3939.

Jahn, F. (2006). Einsatz der Continuous Flow Analysis zur vorläufigen Datierung eines alpinen Eiskerns. Master's thesis, Universität Heidelberg.

Jona, F. and Scherrer, P. (1952). Die elastischen Konstanten von Eis-Einkristallen. *Helvetica Physica Acta*, 25(1–2):35–54.

Keith, C. M. and Crampin, S. (1977). Seismic body waves in anisotropic media: reflection and refraction at a plane interface. *Geophys. J. R. astr. Soc.*, 49:181–208.

Kennedy, J. H., Pettit, E. C., and di Prinzio, C. L. (2013). The evolution of crystal fabric in ice sheets and its link to climate history. *J. Glaciol.*, 59(214):357–373.

King, E., Woodward, J., and Smith, A. (2004). Seismic evidence for a water-filled canal in defoming till beneath Rutford Ice Stream, West Antarctica. *Geophys. Res. Letters*, 31:61–76.

King, E. C. and Jarvis, E. P. (2007). Use of Shear Waves to Measure Poissons Ratio in Polar Firn. *J. Environ. Eng. Geophys.*, 12(1):15–21.

Kirchner, J. F. and Bentley, C. R. (1990). RIGGS III: Seismic Short-Refraction Studies Using an Analytical Curve-Fitting Technique. In *The Ross Ice Shelf: Glaciology and Geophysics*, pages 109–126. American Geophysical Union.

Knödel, K., Krummel, H., and Lange, G. (2005). *Geophysik*. Handbuch zur Erkundung des Untergrundes von Deponien und Altlasten. Springer Verlag.

Kohnen, H. (1972). Über die Beziehung zwischen Geschwindigkeiten und der Dichte in Firn und Eis. *Zeitschr. f. Geophysik*, 38:925–935.

Kohnen, H. (1974). The temperature dependence of seismic waves in ice. *J. Glaciol.*, 13(67):144–147.

Kohnen, H. and Bentley, C. R. (1973). Seismoglaziologische Untersuchungen nahe Byrd Station, Antarktis. *Meteorology and Atmospheric Physics*, 22(2):311–324. 10.1007/BF02247550.

Konrad, H., Bohleber, P., Wagenbach, D., Vincent, C., and Eisen, O. (2013). Determining the age distribution of Colle Gnifetti, Monte Rosa, Swiss Alps, by combining ice cores, ground-penetrating radar and a simple flow model. *J. Glaciol.*, 59(213):179–189.

Kovacs, A., Gow, A. J., and Morey, R. M. (1995). The in-situ dielectric constant of polar firn revisited. *Cold Reg. Sci. Technol.*, 23:245–256.

Lüthi, M. (2000). *Rheology of cold firn and dynamics of a polythermal ice stream*. PhD thesis, Versuchsanstalt für Wasserbau, Hydrologie und Glaziologie der ETH Zürich.

Martin, C., Gudmundsson, G. H., Pritchard, H. D., and Gagliardini, O. (2009). On the effects of anisotropic rheology on ice flow, internal structure, and the age-depth relationship at ice devides. *J. Geophys. Res.*, 114:1–18.

Matsuoka, K., Furukawa, T., Fujita, S., Maeno, H., Urantsuka, S., Naruse, R., and Watanabe, O. (2003). Crystal orientation fabrics within the Antarcitc ice sheet revealed by a mutlipolarization plane and dual-frequency radar survey. *J. Geophys. Res.*, 108(B10).

Matsuoka, K., Power, D., Fujita, S., and Raymond, C. F. (2012). Rapid development of anisotropic ice-crystal-alingment fabrics inferred from englacial radar polarimetry, central West Antarctica. *J. Geophys. Res.*, 117:F03029.

Matsuoka, K., Wilen, L., Huerly, S. P., and Raymond, C. F. (2009). Effects of birefingence within ice sheets on obliquely propagating radio waves. *IEEE Transactions on geoscience and remote sensing*, 47(5):1429–1443.

Matsuoka, T., Fujita, S., Morishima, S., and Mae, S. (1997). Precise measurement of dielectric anisotropy in ice Ih at 39 GHz. *Journal of Applied Physics*, 81(5):2344–2348.

Motagnat, M., Buiron, D., Arnaud, L., Broquet, A., Schlitz, P., Jacob, R., and Kipfstuhl, S. (2012). Measurements and numerical simulation of fabric evolution along the Talos Dome ice core, Antarctica. *E. Plan Sci. Let.*, 357–358:168–178.

Mothes, H. (1926). Dickenmessungen von Gletschern mit seismischen Methoden. *Geologische Rundschau*, 17(6):397–400.

Mothes, H. (1927). Seismische Dickenmessung von Gletschereis. *Zeischr. f. Geophysik*, 3:121–135.

Mothes, H. (1929). Neue Ergebnisse der Eisseismik. *Zeischr. f. Geophysik*, 5:120–144.

Nanthikesan, S. and Sunder, S. S. (1994). Anisotropic elasticity of polycrystalline ice Ih. *Cold Reg. Sci. Technol.*, 22:149–169.

Navarro, F. and Eisen, O. (2009). Ground-penetrating radar. In Pellika, P., editor, *Remote sensing of glaciers*, pages 195–229. W. Gareth Rees London: Taylor & Francis.

Nolan, M. and Echelmeyer, K. (1999a). Seismic detection of transient changes beneath Black Rapids Glacier, Alaska, U.S.A. : I. Techniques and observations. *J. Glaciol.*, 45(149):119–131.

Nolan, M. and Echelmeyer, K. (1999b). Seismic detection of transient changes beneath Black Rapids Glacier, Alaska, U.S.A. : II. Basal morphology and processes. *J. Glaciol.*, 45(149):132–146.

Oerter, H., Drücker, C., Kipfstuhl, S., and Wilhelms, F. (2009). Kohnen Station–the Drilling Camp for the EPICA Deep Ice Core in Dronning Maud Land. *Polarforschung*, 78(1–2):1–23.

Paren, J. G. (1981). Reflection coefficent at a dielectric interface. *J. Glaciol.*, 27(95):203–204.

Penny, A. H. A. (1948). A theoretical determination of the elastic constants of ice. *Mathematical Proceedings of the Cambridge Philosophical Society*, 44(3):423–439.

Peternell, M., Hasalova, P., Wilson, C. J. L., Piazolo, S., and Schulmann, K. (2010). Evaluating quartz crystallographic preferred orientations and the role of deformation partitioning using EBSD and fabric analyser techniques. *Journal of Structural Geology*, 32:803–817.

Peters, L. E., Anandakrishnan, S., Alley, R. B., and Voigt, D. E. (2012). Seismic attenuation in glacial ice: A proxy for englacial temperature. *J. Geophys. Res.*, 117:F02008.

Peters, L. E., Anandakrishnan, S., Holland, C. W., Horgan, H. J., Blankenship, D. D., and Voigt, D. E. (2008). Seismic detection of a subglacial lake near the South Pole, Antarctica. *Geophys. Res. Letters*, 35:L23501.

Petrenko, V. F. and Withworth, R. W. (1998). *Physics of ice*. Oxford University Press, New York.

Plewes, L. A. and Hubbard, B. (2001). A review of the use of radio-echo sounding in glaciology. *Progress in Physical Geography*, 25(2):203–236.

Polom, U., Hofstede, C., Diez, A., and Eisen, O. (2014). First glacier-vibroseismic experiment-results from the cold firn of Colle Gnieftti. *Near Surface Geophysics*, in press (doi:10.3997/1873-0604.2013040).

Raymond, C. F. (1983). Deformation in the vicinity of ice divides. *J. Glaciol.*, 29(103):357–373.

Reuss, A. (1929). Berechnung der Fliessgrenzen von Mischkristallen auf Grund der Platizitätsbedingung für Einkristalle. *Zeitschr. f. angew. Math. und Mech.*, 9(1):49–58.

Reynolds, J. M. (2011). *An introduction to applied and environmental geophysics*. Wiley-Blackwell, Oxford, 2. ed. edition.

Riedel, S., Jacobs, J., and Jokat, W. (2013). Interpretation of new regional aeromagnetic data over Dronning Maud Land (East Antarctica). *Tectonophysics*, 585(0):161–171.

Riedel, S., Jokat, W., and Steinhage, D. (2012). Mapping tectonic provinces with airborne gravity and radar data in Dronning Maud Land, East Antarctica. *Geophys. J. Int.*, 189(1):414–427.

Robertson, J. D. and Bentley, C. R. (1990). Seismic Studies on the Grid Western Half of the Ross Ice Shelf: RIGGS I and RIGGS II. In *The Ross Ice Shelf: Glaciology and Geophysics*, pages 55–86. American Geophysical Union.

Robin, G. D. Q. (1958). Glaciology III, Seismic shooting and related investigations. *Norwegian-British-Swedish Antarctic Expedition, 1949-52, Scientific Results, Norsk Polainstitutt, Oslo*, 5.

Rommel, B. E. and Tsvankin, I. (2000). Analytic description of P-wave ray direction and polarization in orthorombic media. In Ilkelle, L. T., editor, *Anisotropy 2000 : fractures, converted waves, and case studies*, pages 1–19. Society of Exploration Geophysicists.

Rüger, A. (1997). P-wave reflection coefficent for transversely isotropic models with vertical and horizontal axis of symmetry. *Geophysics*, 62(3):713–722.

Rüger, A. (2002). *Reflection Coefficients and Azimuthal Avo Analysis in Anisotropic Media*. Geophysical Monograph Series, No. 10. Society of Exploration Geohysicists.

Schumskii, P. A. (1964). *Principles of structural geology*. Dover Publications, New York.

Schwerzmann, A. (2006). *Borehole analyses and flow modeling of firn-covered cold glaciers*. PhD thesis, Versuchsanstalt für Wasserbau, Hydrologie und Glaziologie der ETH Zürich.

Seddik, H., Greve, R., Placidi, L., Hamann, I., and Gagliardini, O. (2008). Application of a continuum-mechanical model for the flow of anisotropic polar ice to the EDML core, Antarctica. *J. Glaciol.*, 54(187):631–642.

Sheriff, R. and Geldart, L. (1995). *Exploration Seismology*. Cambridge University Press.

Slichter, L. B. (1932). The Theory of the Interpretation of Seismic Travel-Time Curves in Horizontal Structures. *Physics*, 3(6):273–295.

Smith, A. and Murray, T. (2008). Bedform topography and basal conditions beneath a fast-flowing West Antarctic ice stream. *Quat. Sci. Rev.*

Smith, A. M. (1997). Basal conditions on Rutford Ice Stream, West Antarctica, from seismic observations. *J. Geophys. Res.*, 102(B1):543–552.

Smith, A. M. (2007). Subglacial bed properties from normal-incidence seismic reflection data. *J. Environ. Eng. Geophys.*, 12(1):3–13.

Steinhage, D., Nixdorf, U., Meyer, U., and Miller, H. (1999). New maps of the ice thickness and subglacial topography in Dronning Maud Land, Antarctica, determined by means of airborne and radio-echo sounding. *Ann. Glaciol.*, 29:267–272.

Sunder, S. S. and Wu, M. S. (1994). Crack nucleation due to elastic anisotropy in polycrystalline ice. *Cold Reg. Sci. Technol.*, 18:29–47.

Svensson, A., Bigler, M., Blunier, T., Clausen, H. B., Dahl-Jensen, D., Fischer, H., Fujita, S., Goto-Azuma, K., Johnsen, S. J., Kawamura, K., Kipfstuhl, S., Kohno, M., Parrenin, F., Popp, T., Rasmussen, S. O., Schwander, J., Seierstad, I., Severi, M., Steffensen, J. P., Udisti, R., Uemura, R., Vallelonga, P., Vinther, B. M., Wegner, A., Wilhelms, F., and Winstrup, M. (2013). Direct linking of Greenland and Antarctic ice cores at the Toba eruption (74 ka BP). *Climate of the Past*, 9(2):749–766.

Telford, W., Telford, W. M., Geldart, L., and Sheriff, R. (1990). *Applied Geophysics*. Monograph series. Cambridge University Press.

Thiel, E. and Ostenso, N. A. (1961). Seismic studies on antarctic ice shelves. *Geophysics*, 26(6):706–715.

Thomsen, L. (1986). Weak elastic anisotropy. *Geophysics*, 51(10):1954–1966.

Thomsen, L. (1993). *Weak anisotropic reflections*, volume 8 of *Offset-dependent reflectivity - Theory and Practice of AVO Analyses, Investigations in Geophysics Series*. Society of Exploration Geophysicists.

Thorsteinsson, T., Kipfstuhl, J., and Miller, H. (1997). Textures and fabrics in the GRIP ice core. *J. Geophys. Res.*, 102(C12):26583–26599.

Thyssen, F. (1966). Die Temperaturabhängigkeit der P-Wellengeschwindigkeit in Gletschern und Inlandeis. *Zeitschr. f. Geophysik*, 33:65–79.

Tsvankin, I. (1997). Anisotropic parameters and P-wave velocity for orthorombic media. *Geophysics*, 62(4):1292–1309.

Tsvankin, I. (2001). *Seismic signatures and analysis of reflection data in anisotropic media*, volume 29 of *Handbook of geophysical exploration, seismic expolration*. Pergamon.

Vaughan, D. G. and Comiso, J. C. (2013). Observations: Cryosphere. In Bamber, J., Huybrechts, P., and Lemke, P., editors, *Climate Change 2013: The Physical Science Basis. Contribution of Working Group I to the Fourth Assessment Report of the Intergovernmental Panel on Climate Change*. Draft Version.

Vogt, C., Laihem, K., and Wiebusch, C. (2008). Speed of bubble-free ice. *J. Acoust. Soc. Am.*, 124(6):3613–3618.

Voigt, W. (1910). *Lehrbuch der Kristallphysik: (mit Ausschluss der Kristalloptik)*. Bibliotheca mathematica Teubneriana ; 12. Johnson, New York.

Wagner, S. (1996). *Dreidimensionale Modellierung zweier Gletscher und Deformationsanalyse von eisreichem Permafrost*. PhD thesis, Versuchsanstalt für Wasserbau, Hydrologie und Glaziologie der ETH Zürich.

Wallbrecher, E. (1986). *Tektonische und Gefügeanalytische Arbeitsweisen*. Ferdinand Enke Verlag.

Wesche, C., Eisen, O., Oerter, H., Schulte, D., and Steinhage, D. (2007). Surface topography and ice flow in the vicinity of the EDML deep-drilling site. Antarctica. *J. Glaciol.*, 53(442–448):182.

Wesche, C., Riedel, S., and Steinhage, D. (2009). Precise surface topography of the ground ice ridges at the Ekströmisen, Antarctica, based on several geophysical data sets. *ISPRS Journal of Photogrammetry and Remote Sensing*, 114:381–386.

Wilhelms, F. (1996). *Leitfähigkeits- und Dichtemessung an Eisbohrkernen / Measuring the Conductivity and Density of Ice Cores (in German)*, volume 191 of *Berichte zur Polarforschung*. Alfred-Wegener-Institut für Polar- und Meeresforschung.

Wilson, C. J. L., Russell-Head, D. S., and Sim, H. M. (2003). The application of an automated fabric analyzer system to the textural evolution of folded ice layers in shear zones. *Ann. Glaciol.*, 37:7–17.

Woodcock, N. H. (1977). Specification of fabric shapes using an eigenvalue method. *Geol. Soc. Am. Bull.*, 88:1231–1236.

Yilmaz, O. (2001). *Seismic data processing*, volume 2 of *Investig. Geophys.* Society of Exploration Geophysicists.

Zillmer, M., Gajewski, D., and Kashtan, B. M. (1997). Reflection coefficients for weak anisotropic media. *Geophys. J. Int.*, 129:389–398.

Zillmer, M., Gajewski, D., and Kashtan, B. M. (1998). Anisotropic reflection coefficients for a weak-contrast interface. *Geophys. J. Int.*, 132:159–166.

Abbreviations and nomenclature

AVA	Amplitude Versus Angle
AVO	Amplitude Versus Offset
AWI	Alfred-Wegener-Institut Helmholtz-Zentrum für Polar und Meeresforschung
BHG	BoreHole Geophone
BKG	Bundesamt für Katographie und Geodäsie
bp	bandpass (filter)
CDP	Common Depth Point
CMP	Common MidPoint
COF	Crystal Orienation Fabric
DEP	DielEctric Profiling
DML	Dronning Maud Land
EDML	EPICA Dronning Maud Land (ice core and borehole)
ElViS	Electrodynamic-Vibrator System
EPICA	European Project of Ice Coring in Antarctica
fb	first break (of wavelet)
fk	frequency wavenumber (filter)
GAP	γ-Attenuation Profiling
GPR	Ground Penetrating Radar
HTI	Horizontal Transversly Isotropic
hp	highpass (filter)
IPICS	International Partnerships in Ice Core Sciences
IRH	Internal Reflection Horizonts
KCI	ice core from Colle Gnifetti on the Swiss-Italien border
LIMPICS	Emmy Noether young investigator group
max	maximum (of wavelet)
NMO	Normal MoveOut
ηNMO	ηNMO, 4th-order NMO correction
PETN	Pentaerythritol tetranitrate; explosives
P-wave	compressional wave
RAMdrill	Rapid Air Movment drill
RES	Radio-Echo Sounding
RMS	Root Mean Square
SNR	Signal-to-Noise Ratio
S-wave	Shear wave
SH-wave	Horizontal Shear wave
SV-wave	Vertical Shear wave
TNT	Trinitrotoluene
TWT	Two Way Traveltime
VSM	Vertical Single Maximum

VTI	Vertical Transversly Isotropic
WAIS	West Antarctic Ice Sheet
WGS84	World Geodetic System 1984
zc	zero crossing (of wavelet)

General:

x_1, x_2, x_3	cartesian coordinate system
$\vec{c}$	c-axis orientation
A_{ij}	weighted orientation tensor
W	weighting function
λ_1	COF eigenvalue (with $\lambda_1 \leq \lambda_2 \leq \lambda_3$)
λ_2	COF eigenvalue
λ_3	largest COF eigenvalue
φ	opening angle in x_2 direction
χ	opening angle in x_1 direction
ψ	rotation angle for girdle fabric ψ=0 -> HTI media
ϕ	opening angle in x_1 or x_2 direction
c_{mnop}	elasticity tensor
C_{ij}	elasticity tensor in Voigt notation
s_{mnop}	compliance tensor
S_{ij}	compliance tensor in Voigt notation
σ_{mn}	stress
τ_{op}	strain
ρ	denisty
ρ_{ice}	density for ice
$\mathfrak{T}$	Temperature
$\mathfrak{T}_m$	measured Temperature

Thomsen parameter:

ε	
γ	
δ	
δ_{vel}	δ calculated from velocities
η	anellipticity parameter
ξ	δ or γ
ξ_{eff}	RMS value of ξ
δ_{eff}	RMS value of δ
γ_{eff}	RMS value of γ
η_{eff}	RMS value of η

Seismic:

p	ray parameter
x	offset
z	depth

Z	deppest point
f	frequency of wave
λ_{w}	wavelength
θ	group angle
θ_{out}	group angle for component outside of the symmetry plane
ϑ	phase angle
β	critical angle of total reflection
α	dip angle of tilted reflector
R_{pp}	reflection coefficent for PP-reflection
R_{shsh}	reflection coefficent for SHSH-reflection
R_{svsv}	reflection coefficent for SVSV-reflection

Seismic velocities and traveltimes:

lower case letters	interval velocities/times
upper case letters	RMS-velocities, travletimes for multiple layers
ζ	P- or SH-wave
t	interval TWT
T	RMS TWT for multiple layers
T_{P}	RMS TWT for multiple layers for P-wave
$t_{\zeta 0}$	zero-offset interval TWT for P- and SH-wave
$T_{\zeta 0}$	zero-offset RMS TWT for multiple layers for P- and SH-wave
t_{p0}	zero-offset interval TWT for P-wave
T_{P0}	zero-offset RMS TWT for multiple layers for P-wave
v	isotropic interval velocity
v_{p}	isotropic P-wave interval velocity
v_{s}	isotropic S-wave interval velocity
$v_{\mathrm{p,ice}}$	isotropic P-wave interval velocity for ice
$v_{\mathrm{s,ice}}$	isotropic S-wave interval velocity for ice
v_{A}	isortopic apparent velocity
V_{RMS}	isotropic RMS velocity
V_{NMO}	isotropic NMO velocity
v_{ph}	interval phase velocity (absolute value)
$v_{\zeta}(\vartheta)$	interval phase P- and SH-wave velocity
$v_{\mathrm{p}}(\vartheta)$	interval phase P-wave velocity
$v_{\mathrm{sh}}(\vartheta)$	interval phase SH-wave velocity
$v_{\mathrm{sv}}(\vartheta)$	interval phase SV-wave velocity
$\vec{v_{\mathrm{g}}}$	interval group velocity vector
$v_{\mathrm{g},x_1}, v_{\mathrm{g},x_2}, v_{\mathrm{g},x_3}$	components of interval group velocity vector in x_1, x_2, x_3 direction
v_{g}	interval group velocity (absolute value)
$v_{\zeta 0}$	interval zero-offset P- and SH-wave velocity
v_{p0}	interval zero-offset P-wave velocity
v_{s0}	interval zero-offset S-wave velocity
v_{sh0}	interval zero-offset SH-wave velocity
$v_{\mathrm{nmo},\zeta}$	interval anisotropic P- and SH-wave NMO velocity
$v_{\mathrm{nmo,p}}$	interval anisotropic P-wave NMO velocity
$v_{\mathrm{nmo,sh}}$	interval anisotropic SH-wave NMO velocity
$v_{\mathrm{nmo,sv}}$	interval anisotropic SV-wave NMO velocity

$V_{\mathrm{RMS},\zeta 0}$	zero-offset RMS velocity of $v_{\zeta 0}$
$V_{\mathrm{RMS,P0}}$	P-wave zero-offset RMS velocity of v_{p0}
$V_{\mathrm{RMS,S0}}$	SH-wave zero-offset RMS velocity of v_{sh0}
$V_{\mathrm{RMS,S0}}$	S-wave zero-offset RMS velocity of v_{s0}, valid for cone fabric
$V_{\mathrm{NMO},\zeta}$	anisotropic P- and SH-wave NMO velocity: RMS velocity of $v_{\mathrm{nmo},\zeta}$
$V_{\mathrm{NMO,P}}$	anisotropic P-wave NMO velocity: RMS velocity of $v_{\mathrm{nmo,p}}$
$V_{\mathrm{NMO,SH}}$	anisotropic SH-wave NMO velocity: RMS velocity of $v_{\mathrm{nmo,sh}}$
$V_{\mathrm{ElViS},\zeta}$	P- and SH-wave velocity derived from ElViS data
$V_{\mathrm{ElViS,P}}$	P-wave velocity derived from ElViS data
$V_{\mathrm{ElViS,SH}}$	SH-wave velocity derived from ElViS data

Radar:

ϵ	relative permittivity
ϵ'	dielectric constant
ϵ''	dieletric loss factor
v_{r}	velocity of radar wave
c_0	velocity in vacuum
R_{r}	reflection coefficent for radar wave

List of Figures

List of Tables

A Calculation of polycrystal elasticity tensor

A.1 Connection of eigenvalues to opening angels

The following equations give the connection between the eigenvalues λ_1, λ_2 and λ_3 an the two opening angles φ and χ. The eigenvalues give the size to the main directions of the momentum of inertia describing the fabric. The opening angles give the distribution of the c-axes orientation within the enveloping spanned up by these two angles. How the opening angles are derived from the eigenvalues is described in section 4.2.

For a cone fabric the angle $\varphi = \chi$ is calculated by

$$\begin{aligned} \varphi = \chi &= b_1 \sin(c_1\lambda_3 + d_1) + b_2 \sin(c_2\lambda_3 + d_2) \\ &\quad + b_3 \sin(c_3\lambda_3 + d_3) + b_4 \sin(c_4\lambda_3 + d_4), \end{aligned} \tag{A.1}$$

with

$$\begin{array}{lll} b_1 = 141.9, & c_1 = 6.251, & d_1 = 2.157, \\ b_2 = 139, & c_2 = 10.33, & d_2 = -1.809, \\ b_3 = 90.44, & c_3 = 14.68, & d_3 = 4.685, \\ b_4 = 36.61, & c_4 = 16.9, & d_4 = 12.63. \end{array}$$

For a thick girdle fabric the angle χ are calculated by

$$\chi = p_1\lambda_1^7 + p_2\lambda_1^6 + p_3\lambda_1^5 + p_4\lambda_1^4 + p_5\lambda_1^3 + p_6\lambda_1^2 + p_7\lambda_1 + p_8, \tag{A.2}$$

$$\varphi = 90^\circ, \tag{A.3}$$

with

$$\begin{array}{llll} p_1 = 2.957e+07, & p_2 = -3.009e+07, & p_3 = 1.233e+07, & p_4 = -2.599e+06, \\ p_5 = 3.023e+05, & p_6 = -1.965e+04, & p_7 = 877.6, & p_8 = 2.614. \end{array}$$

For a partial girdle fabric the angle φ are calculated by

$$\varphi = a_1 \sin(b_1\lambda_3 + c_1) + a_2 \sin(b_2\lambda_3 + c_2) + a_3 \sin(b_3\lambda_3 + c_3) + a_4 \sin(b_4\lambda_3 + c_4), \tag{A.4}$$

$$\chi = 0^\circ, \tag{A.5}$$

with

$$
\begin{array}{lll}
a_1 = 118.7, & b_1 = 7.415, & c_1 = -3.517, \\
a_2 = 97.47, & b_2 = 13.68, & c_2 = 1.161, \\
a_3 = 46.57, & b_3 = 18.58, & c_3 = 6.935, \\
a_4 = 7.455, & b_4 = 25.18, & c_4 = 11.47.
\end{array}
$$

A.2 Inverse elasticity and compliance tensor

Here, the calculation of the inverse elasticity tensor and compliance tensor for orthorhombic media is given (Bower, 2010). The inversion of elasticity and compliance tensor is needed for the determination of the Voigt–Reuss bounds calculated in section 4.2.

Hook's law in terms of the elasticity tensor in Voigt notation for orthorhombic media gives: (eq. (3.1)):

$$
\begin{aligned}
\sigma_1 &= C_{11}\tau_1 + C_{12}\tau 2 + C_{13}\tau_3, \\
\sigma_2 &= C_{12}\tau_1 + C_{22}\tau 2 + C_{23}\tau_3, \\
\sigma_3 &= C_{13}\tau_1 + C_{23}\tau 2 + C_{33}\tau_3, \\
\sigma_4 &= C_{44}\tau_4, \\
\sigma_5 &= C_{55}\tau_5, \\
\sigma_6 &= C_{66}\tau_6.
\end{aligned} \tag{A.6}
$$

Hook's law in terms of the compliance tensor in Voigt notation for orthorhombic media gives: (eq. (4.2)):

$$
\begin{aligned}
\tau_1 &= S_{11}\sigma_1 + S_{12}\sigma 2 + S_{13}\sigma_3, \\
\tau_2 &= S_{12}\sigma_1 + S_{22}\sigma 2 + S_{23}\sigma_3, \\
\tau_3 &= S_{13}\sigma_1 + S_{23}\sigma 2 + S_{33}\sigma_3, \\
\tau_4 &= S_{44}\sigma_4, \\
\tau_5 &= S_{55}\sigma_5, \\
\tau_6 &= S_{66}\sigma_6.
\end{aligned} \tag{A.7}
$$

To calculate the elasticity tensor from the compliance tensor ($C_{ij} = S_{mn}^{-1}$) the equations (A.7) are inserted into the equations (A.6). To calculate the compliance tensor from the elasticity tensor ($S_{mn} = C_{ij}^{-1}$) the equations (A.6) are inserted into the equations (A.7). In both cases the system of linear equations needs to be solved. This gives the following results for the elasticity tensor

$$
C_{ij} = \begin{pmatrix}
e/a & -h/a & -k/a & 0 & 0 & 0 \\
-h/a & f/a & -l/a & 0 & 0 & 0 \\
-k/a & -l/a & g/a & 0 & 0 & 0 \\
0 & 0 & 0 & 1/S_{44} & 0 & 0 \\
0 & 0 & 0 & 0 & 1/S_{55} & 0 \\
0 & 0 & 0 & 0 & 0 & 1/S_{66}
\end{pmatrix}, \tag{A.8}
$$

with

$$\begin{aligned} a &= S_{11}S_{22}S_{33} + 2S_{12}S_{23}S_{13} - S_{23}^2S_{11} - S_{13}^2S_{22} - S_{12}^2S_{33}, \\ e &= S_{22}S_{33} - S_{23}^2, \\ f &= S_{11}S_{33} - S_{13}^2, \\ g &= S_{11}S_{22} - S_{12}^2, \\ h &= S_{12}S_{33} - S_{13}S_{23}, \\ k &= S_{13}S_{22} - S_{12}S_{23}, \\ l &= S_{22}S_{11} - S_{12}S_{13}, \end{aligned} \tag{A.9}$$

and for the compliance tensor

$$S_{ij} = \begin{pmatrix} E/A & -H/A & -K/A & 0 & 0 & 0 \\ -H/A & F/A & -L/A & 0 & 0 & 0 \\ -K/A & -L/A & G/A & 0 & 0 & 0 \\ 0 & 0 & 0 & 1/C_{44} & 0 & 0 \\ 0 & 0 & 0 & 0 & 1/C_{55} & 0 \\ 0 & 0 & 0 & 0 & 0 & 1/C_{66} \end{pmatrix}, \tag{A.10}$$

with

$$\begin{aligned} A &= C_{11}C_{22}C_{33} + 2C_{12}C_{23}C_{13} - C_{23}^2C_{11} - C_{13}^2C_{22} - C_{12}^2C_{33}, \\ E &= C_{22}C_{33} - C_{23}^2, \\ F &= C_{11}C_{33} - C_{13}^2, \\ G &= C_{11}C_{22} - C_{12}^2, \\ H &= C_{12}C_{33} - C_{13}C_{23}, \\ K &= C_{13}C_{22} - C_{12}C_{23}, \\ L &= C_{22}C_{11} - C_{12}C_{13}. \end{aligned} \tag{A.11}$$

A.3 Rotation matrices for elasticity and compliance tensor

Here the rotation matrix for the elasticity tensor and compliance tensor following Sunder and Wu (1994) are given. For the calculation of the elasticity tensor for different fabrics the monocrystal elasticity tensor needs to be rotated (sec. 4.2).

The rotation matrix for the elasticity tensor

$$R^{\mathrm{C}} = \begin{pmatrix} l_1^2 & m_1^2 & n_1^2 & 2m_1nl_1 & 2n_1l_1 & 2l_1m_1 \\ l_2^2 & m_2^2 & n_2^2 & 2m_2nl_2 & 2n_2l_2 & 2l_2m_2 \\ l_31^2 & m_3^2 & n_3^2 & 2m_3nl_3 & 2n_3l_3 & 2l_3m_3 \\ l_2l_3 & m_2m_3 & n_2n_3 & m_2n_3 - m_3n_2 & n_2l_3 - n_3l_2 & l_2m_3 - l_3m_2 \\ l_3l_1 & m_3m_1 & n_3n_1 & m_3n_1 - m_1n_3 & n_3l_1 - n_1l_3 & l_3m_1 - l_1m_3 \\ l_1l_2 & m_1m_2 & n_1n_2 & m_1n_2 - m_2n_1 & n_1l_2 - n_2l_1 & l_1m_2 - l_2m_1 \end{pmatrix}, \tag{A.12}$$

and the compliance tensor

$$R^{S} = \begin{pmatrix} l_1^2 & m_1^2 & n_1^2 & m_1 n l_1 & n_1 l_1 & l_1 m_1 \\ l_2^2 & m_2^2 & n_2^2 & m_2 n l_2 & n_2 l_2 & l_2 m_2 \\ l_3 1^2 & m_3^2 & n_3^2 & m_3 n l_3 & n_3 l_3 & l_3 m_3 \\ 2l_2 l_3 & 2m_2 m_3 & 2n_2 n_3 & m_2 n_3 - m_3 n_2 & n_2 l_3 - n_3 l_2 & l_2 m_3 - l_3 m_2 \\ 2l_3 l_1 & 2m_3 m_1 & 2n_3 n_1 & m_3 n_1 - m_1 n_3 & n_3 l_1 - n_1 l_3 & l_3 m_1 - l_1 m_3 \\ 2l_1 l_2 & 2m_1 m_2 & 2n_1 n_2 & m_1 n_2 - m_2 n_1 & n_1 l_2 - n_2 l_1 & l_1 m_2 - l_2 m_1 \end{pmatrix}, \tag{A.13}$$

with the following direction cosines

$$\begin{pmatrix} l_1 & l_2 & l_3 \\ m_1 & m_2 & m_3 \\ n_1 & n_2 & n_3 \end{pmatrix}, \tag{A.14}$$

for rotation around the x_1-axis

$$\begin{pmatrix} 1 & 0 & 0 \\ \cos\phi & -\sin\phi & 0 \\ \sin\phi & \cos\phi & 0 \end{pmatrix}, \tag{A.15}$$

for rotation around the x_2-axis

$$\begin{pmatrix} \cos\phi & 0 & -\sin\phi \\ 0 & 1 & 0 \\ \sin\phi & 0 & \cos\phi \end{pmatrix}, \tag{A.16}$$

and for rotation around the x_3-axis

$$\begin{pmatrix} \cos\phi & -\sin\phi & 0 \\ \sin\phi & \cos\phi & 0 \\ 0 & 0 & 1 \end{pmatrix}. \tag{A.17}$$

A.4 Polycrystal

The derived equations for components of the elasticity tensor and compliance tensor for the polycrystal (eq. (4.6) and (4.7), respectively) with c-axis distribution within the angel ϕ in x_1, x_2 and x_3-direction, calculated using the rotation matrices as given in appendix A.3.

These variables apply for all equations for the calculation of polycrystal:

$$\begin{aligned} b_1 &= \frac{3}{4}\phi_0 + \alpha + \beta, \\ b_2 &= \frac{3}{4}\phi_0 - \alpha + \beta, \\ b_3 &= \frac{1}{4}\phi_0 - \beta, \\ \alpha &= \frac{1}{2}\sin 2\phi_0, \end{aligned}$$

$$\beta = \frac{1}{16}\sin 4\phi_0. \tag{A.18}$$

(A.19)

The components of the polycrystal elasticity tensor with c-axes distribution around the x_1-axis, i.e., within the $[x_2, x_3]$-plane are calculated by:

$$\begin{aligned}
C^{\mathrm{p}}_{11} &= C^{\mathrm{m}}_{11},\\
C^{\mathrm{p}}_{22} &= \frac{1}{2\phi_0}\left[b_1 C^{\mathrm{m}}_{22} + b_2 C^{\mathrm{m}}_{33} + 2b_3(C^{\mathrm{m}}_{23} + 2C^{\mathrm{m}}_{44})\right],\\
C^{\mathrm{p}}_{33} &= \frac{1}{2\phi_0}\left[b_1 C^{\mathrm{m}}_{33} + b_2 C^{\mathrm{m}}_{22} + 2b_3(C^{\mathrm{m}}_{23} + 2C^{\mathrm{m}}_{44})\right],\\
C^{\mathrm{p}}_{44} &= \frac{1}{2\phi_0}\left[(b_1 + b_2) C^{\mathrm{m}}_{44} + b_3(C^{\mathrm{m}}_{22} - 2C^{\mathrm{m}}_{23} + C^{\mathrm{m}}_{33} - 2C^{\mathrm{m}}_{44})\right],\\
C^{\mathrm{p}}_{55} &= \frac{1}{2\phi_0}\left[C^{\mathrm{m}}_{55}(\phi_0 + \alpha) + C^{\mathrm{m}}_{66}(\phi_0 - \alpha)\right],\\
C^{\mathrm{p}}_{66} &= \frac{1}{2\phi_0}\left[C^{\mathrm{m}}_{66}(\phi_0 + \alpha) + C^{\mathrm{m}}_{55}(\phi_0 - \alpha)\right],\\
C^{\mathrm{p}}_{12} &= \frac{1}{2\phi_0}\left[C^{\mathrm{m}}_{12}(\phi_0 + \alpha) + C^{\mathrm{m}}_{13}(\phi_0 - \alpha)\right],\\
C^{\mathrm{p}}_{13} &= \frac{1}{2\phi_0}\left[C^{\mathrm{m}}_{13}(\phi_0 + \alpha) + C^{\mathrm{m}}_{12}(\phi_0 - \alpha)\right],\\
C^{\mathrm{p}}_{23} &= \frac{1}{2\phi_0}\left[(b_1 + b_2) C^{\mathrm{m}}_{23} + b_3(C^{\mathrm{m}}_{22} - 4C^{\mathrm{m}}_{44} + C^{\mathrm{m}}_{33})\right].
\end{aligned} \tag{A.20}$$

The components of the polycrystal elasticity tensor with c-axes distribution around the x_2-axis, i.e., within the $[x_1, x_3]$-plane are calculated by:

$$\begin{aligned}
C^{\mathrm{p}}_{11} &= \frac{1}{2\phi_0}\left[b_1 C^{\mathrm{m}}_{11} + b_2 C^{\mathrm{m}}_{33} + 2b_3(C^{\mathrm{m}}_{13} + 2C^{\mathrm{m}}_{55})\right],\\
C^{\mathrm{p}}_{22} &= C^{\mathrm{m}}_{22},\\
C^{\mathrm{p}}_{33} &= \frac{1}{2\phi_0}\left[b_1 C^{\mathrm{m}}_{33} + b_2 C^{\mathrm{m}}_{11} + 2b_3(C^{\mathrm{m}}_{13} + 2C^{\mathrm{m}}_{55})\right],\\
C^{\mathrm{p}}_{44} &= \frac{1}{2\phi_0}\left[C^{\mathrm{m}}_{44}(\phi_0 + \alpha) + C^{\mathrm{m}}_{66}(\phi_0 - \alpha)\right],\\
C^{\mathrm{p}}_{55} &= \frac{1}{2\phi_0}\left[(b_1 + b_2) C^{\mathrm{m}}_{55} + b_3(C^{\mathrm{m}}_{11} - 2C^{\mathrm{m}}_{13} + C^{\mathrm{m}}_{33} - 2C^{\mathrm{m}}_{55})\right],\\
C^{\mathrm{p}}_{66} &= \frac{1}{2\phi_0}\left[C^{\mathrm{m}}_{66}(\phi_0 + \alpha) + C^{\mathrm{m}}_{44}(\phi_0 - \alpha)\right],\\
C^{\mathrm{p}}_{12} &= \frac{1}{2\phi_0}\left[C^{\mathrm{m}}_{12}(\phi_0 + \alpha) + C^{\mathrm{m}}_{23}(\phi_0 - \alpha)\right],\\
C^{\mathrm{p}}_{13} &= \frac{1}{2\phi_0}\left[(b_1 + b_2) C^{\mathrm{m}}_{13} + b_3(C^{\mathrm{m}}_{11} - 4C^{\mathrm{m}}_{55} + C^{\mathrm{m}}_{33})\right],\\
C^{\mathrm{p}}_{23} &= \frac{1}{2\phi_0}\left[C^{\mathrm{m}}_{23}(\phi_0 + \alpha) + C^{\mathrm{m}}_{12}(\phi_0 - \alpha)\right].
\end{aligned} \tag{A.21}$$

The components of the polycrystal elasticity tensor with c-axes distribution around the x_3-axis, i.e., within the $[x_1, x_2]$-plane are calculated by:

$$\begin{aligned}
C^{\mathrm{p}}_{11} &= \frac{1}{2\phi_0}\left[b_1 C^{\mathrm{m}}_{11} + b_2 C^{\mathrm{m}}_{22} + 2b_3(C^{\mathrm{m}}_{12} + 2C^{\mathrm{m}}_{66})\right], \\
C^{\mathrm{p}}_{22} &= \frac{1}{2\phi_0}\left[b_1 C^{\mathrm{m}}_{22} + b_2 C^{\mathrm{m}}_{11} + 2b_3(C^{\mathrm{m}}_{12} + 2C^{\mathrm{m}}_{66})\right], \\
C^{\mathrm{p}}_{33} &= C^{\mathrm{m}}_{33}, \\
C^{\mathrm{p}}_{44} &= \frac{1}{2\phi_0}\left[C^{\mathrm{m}}_{44}(\phi_0 + \alpha) + C^{\mathrm{m}}_{55}(\phi_0 - \alpha)\right], \\
C^{\mathrm{p}}_{55} &= \frac{1}{2\phi_0}\left[C^{\mathrm{m}}_{55}(\phi_0 + \alpha) + C^{\mathrm{m}}_{44}(\phi_0 - \alpha)\right], \\
C^{\mathrm{p}}_{66} &= \frac{1}{2\phi_0}\left[(b_1 + b_2)C^{\mathrm{m}}_{66} + b_3(C^{\mathrm{m}}_{11} - 2C^{\mathrm{m}}_{12} + C^{\mathrm{m}}_{22} - 2C^{\mathrm{m}}_{66})\right], \\
C^{\mathrm{p}}_{12} &= \frac{1}{2\phi_0}\left[(b_1 + b_2)C^{\mathrm{m}}_{12} + b_3(C^{\mathrm{m}}_{22} - 4C^{\mathrm{m}}_{66} + C^{\mathrm{m}}_{11})\right], \\
C^{\mathrm{p}}_{13} &= \frac{1}{2\phi_0}\left[C^{\mathrm{m}}_{13}(\phi_0 + \alpha) + C^{\mathrm{m}}_{23}(\phi_0 - \alpha)\right], \\
C^{\mathrm{p}}_{23} &= \frac{1}{2\phi_0}\left[C^{\mathrm{m}}_{23}(\phi_0 + \alpha) + C^{\mathrm{m}}_{13}(\phi_0 - \alpha)\right].
\end{aligned} \tag{A.22}$$

The components of the polycrystal compliance tensor with c-axes distribution around the x_1-axis, i.e., within the $[x_2, x_3]$-plane are calculated by:

$$\begin{aligned}
S^{\mathrm{p}}_{11} &= S^{\mathrm{m}}_{11}, \\
S^{\mathrm{p}}_{22} &= \frac{1}{2\phi_0}\left[b_1 S^{\mathrm{m}}_{22} + b_2 S^{\mathrm{m}}_{33} + b_3(2S^{\mathrm{m}}_{23} + S^{\mathrm{m}}_{44})\right], \\
S^{\mathrm{p}}_{33} &= \frac{1}{2\phi_0}\left[b_1 S^{\mathrm{m}}_{33} + b_2 S^{\mathrm{m}}_{22} + b_3(2S^{\mathrm{m}}_{23} + S^{\mathrm{m}}_{44})\right], \\
S^{\mathrm{p}}_{44} &= \frac{1}{2\phi_0}\left[(b_1 + b_2)S^{\mathrm{m}}_{44} + 4b_3(S^{\mathrm{m}}_{22} - 2S^{\mathrm{m}}_{23} + S^{\mathrm{m}}_{33} - \frac{1}{2}S^{\mathrm{m}}_{44})\right], \\
S^{\mathrm{p}}_{55} &= \frac{1}{2\phi_0}\left[S^{\mathrm{m}}_{55}(\phi_0 + \alpha) + S^{\mathrm{m}}_{66}(\phi_0 - \alpha)\right], \\
S^{\mathrm{p}}_{66} &= \frac{1}{2\phi_0}\left[S^{\mathrm{m}}_{66}(\phi_0 + \alpha) + S^{\mathrm{m}}_{55}(\phi_0 - \alpha)\right], \\
S^{\mathrm{p}}_{12} &= \frac{1}{2\phi_0}\left[S^{\mathrm{m}}_{12}(\phi_0 + \alpha) + S^{\mathrm{m}}_{13}(\phi_0 - \alpha)\right], \\
S^{\mathrm{p}}_{13} &= \frac{1}{2\phi_0}\left[S^{\mathrm{m}}_{13}(\phi_0 + \alpha) + S^{\mathrm{m}}_{12}(\phi_0 - \alpha)\right], \\
S^{\mathrm{p}}_{23} &= \frac{1}{2\phi_0}\left[(b_1 + b_2)S^{\mathrm{m}}_{23} + b_3(S^{\mathrm{m}}_{22} - S^{\mathrm{m}}_{44} + S^{\mathrm{m}}_{33})\right].
\end{aligned} \tag{A.23}$$

The components of the polycrystal compliance tensor with c-axes distribution around the

x_2-axis, i.e., within the $[x_1, x_3]$-plane are calculated by:

$$\begin{aligned}
S^{\mathrm{p}}_{11} &= \frac{1}{2\phi_0}\left[b_1 S^{\mathrm{m}}_{11} + b_2 S^{\mathrm{m}}_{33} + b_3(2S^{\mathrm{m}}_{13} + S^{\mathrm{m}}_{55})\right], \\
S^{\mathrm{p}}_{22} &= S^{\mathrm{m}}_{22}, \\
S^{\mathrm{p}}_{33} &= \frac{1}{2\phi_0}\left[b_1 S^{\mathrm{m}}_{33} + b_2 S^{\mathrm{m}}_{11} + b_3(2S^{\mathrm{m}}_{13} + S^{\mathrm{m}}_{55})\right], \\
S^{\mathrm{p}}_{44} &= \frac{1}{2\phi_0}\left[S^{\mathrm{m}}_{44}(\phi_0 + \alpha) + S^{\mathrm{m}}_{66}(\phi_0 - \alpha)\right], \\
S^{\mathrm{p}}_{55} &= \frac{1}{2\phi_0}\left[(b_1 + b_2)S^{\mathrm{m}}_{55} + 4b_3(S^{\mathrm{m}}_{11} - 2S^{\mathrm{m}}_{13} + S^{\mathrm{m}}_{33} - \frac{1}{2}S^{\mathrm{m}}_{55})\right], \\
S^{\mathrm{p}}_{66} &= \frac{1}{2\phi_0}\left[S^{\mathrm{m}}_{66}(\phi_0 + \alpha) + S^{\mathrm{m}}_{44}(\phi_0 - \alpha)\right], \\
S^{\mathrm{p}}_{12} &= \frac{1}{2\phi_0}\left[S^{\mathrm{m}}_{12}(\phi_0 + \alpha) + S^{\mathrm{m}}_{23}(\phi_0 - \alpha)\right], \\
S^{\mathrm{p}}_{13} &= \frac{1}{2\phi_0}\left[(b_1 + b_2)S^{\mathrm{m}}_{13} + b_3(S^{\mathrm{m}}_{11} - S^{\mathrm{m}}_{55} + S^{\mathrm{m}}_{33})\right], \\
S^{\mathrm{p}}_{23} &= \frac{1}{2\phi_0}\left[S^{\mathrm{m}}_{23}(\phi_0 + \alpha) + S^{\mathrm{m}}_{12}(\phi_0 - \alpha)\right].
\end{aligned} \tag{A.24}$$

The components of the polycrystal compliance tensor with c-axes distribution around the x_3-axis, i.e., within the $[x_1, x_2]$-plane are calculated by:

$$\begin{aligned}
S^{\mathrm{p}}_{11} &= \frac{1}{2\phi_0}\left[b_1 S^{\mathrm{m}}_{11} + b_2 S^{\mathrm{m}}_{22} + b_3(2S^{\mathrm{m}}_{12} + 2S^{\mathrm{m}}_{66})\right], \\
S^{\mathrm{p}}_{22} &= \frac{1}{2\phi_0}\left[b_1 S^{\mathrm{m}}_{22} + b_2 S^{\mathrm{m}}_{11} + b_3(2S^{\mathrm{m}}_{12} + 2S^{\mathrm{m}}_{66})\right], \\
S^{\mathrm{p}}_{33} &= S^{\mathrm{m}}_{33}, \\
S^{\mathrm{p}}_{44} &= \frac{1}{2\phi_0}\left[S^{\mathrm{m}}_{44}(\phi_0 + \alpha) + S^{\mathrm{m}}_{55}(\phi_0 - \alpha)\right], \\
S^{\mathrm{p}}_{55} &= \frac{1}{2\phi_0}\left[S^{\mathrm{m}}_{55}(\phi_0 + \alpha) + S^{\mathrm{m}}_{44}(\phi_0 - \alpha)\right], \\
S^{\mathrm{p}}_{66} &= \frac{1}{2\phi_0}\left[(b_1 + b_2)S^{\mathrm{m}}_{66} + 4b_3(S^{\mathrm{m}}_{11} - 2S^{\mathrm{m}}_{12} + S^{\mathrm{m}}_{22} - \frac{1}{2}S^{\mathrm{m}}_{66})\right], \\
S^{\mathrm{p}}_{12} &= \frac{1}{2\phi_0}\left[(b_1 + b_2)S^{\mathrm{m}}_{12} + b_3(S^{\mathrm{m}}_{22} - S^{\mathrm{m}}_{66} + S^{\mathrm{m}}_{11})\right], \\
S^{\mathrm{p}}_{13} &= \frac{1}{2\phi_0}\left[S^{\mathrm{m}}_{13}(\phi_0 + \alpha) + S^{\mathrm{m}}_{23}(\phi_0 - \alpha)\right], \\
S^{\mathrm{p}}_{23} &= \frac{1}{2\phi_0}\left[S^{\mathrm{m}}_{23}(\phi_0 + \alpha) + S^{\mathrm{m}}_{13}(\phi_0 - \alpha)\right].
\end{aligned} \tag{A.25}$$

A.5 Anisotropic phase and group velocities

The anisotropic SV-wave phase velocity is given in Figure A.1 in addition to the P- and SH-wave phase velocities that were shown in section 4.2.1. The group velocities for the different fabrics were calculated using equations (3.30) and (3.31) from the phase velocities derived with equations (3.20), (3.21), (3.22) for P-, SV- and SH-wave, respectively. These group velocities are shown in Figure A.2 for the P-wave, Figure A.3 for the SH-wave and Figure A.4 for the SV-wave.

The subfigure (d) is empty in case of the phase velocity. In case of the group velocity this subfigure shows the velocities calculated for cone fabric with the equations given by Bennett (1968) (sec. 3.3.2). As these velocities are derived from the slowness surface no phase velocities are given here.

The largest differences between group and phase velocity can be observed for the SH-wave. As displayed in Figure 3.2 and discussed in section 3.3.1 a triplication in case of the SH-wave group velocity can be observed.

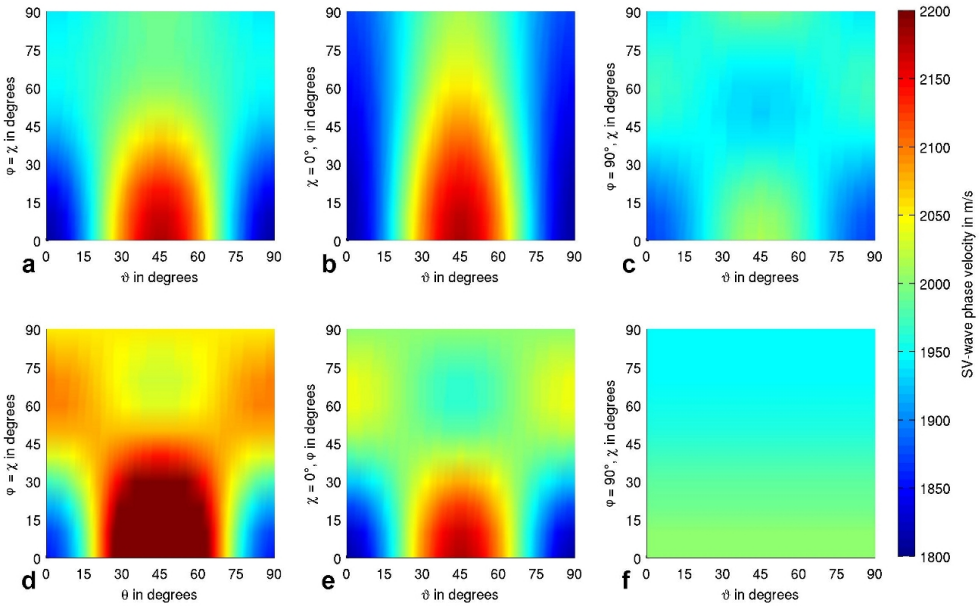

Figure A.1: SV-wave phase velocities over phase angle ϑ for different fabrics. SV-wave velocity for (a) different cone opening angles ($\varphi = \chi$), (b) partial girdle ($\chi = 0°$) and (c) thick girdle ($\varphi = 90°$) within the [$x2$,$x3$]-plane, (e) partial girdle ($\chi = 0°$) and (f) thick girdle ($\varphi = 90°$) within the [$x1$,$x3$]-plane calculated with equation (3.21) given by Daley and Krebes (2004). (d) shows the SV-wave velocity for different cone opening angles ($\varphi = \chi$) calculated with equation (3.35) given by Bennett (1968).

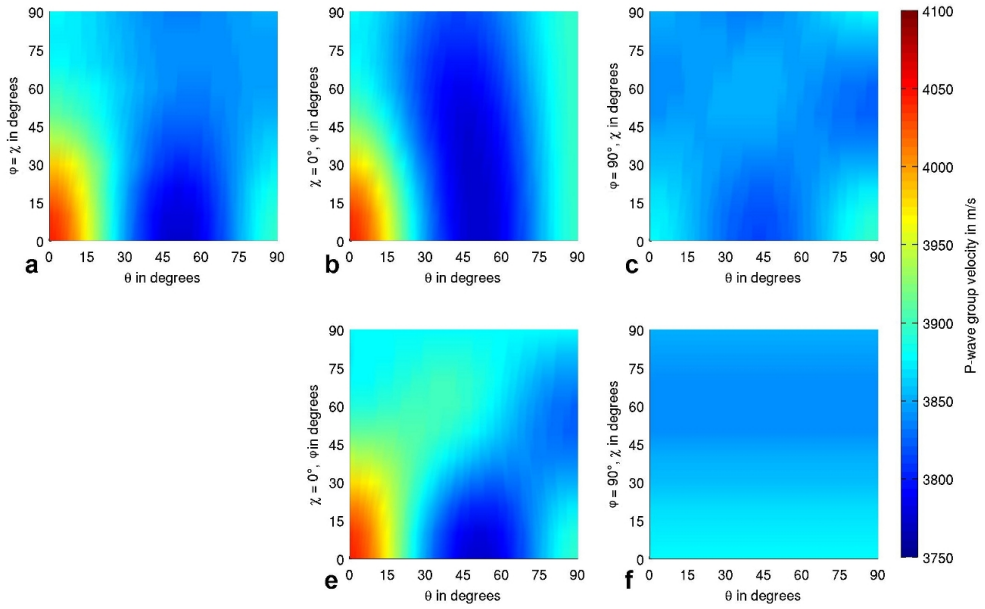

Figure A.2: P-wave group velocities over group angle θ for different fabrics. P-wave velocity for (a) different cone opening angles ($\varphi = \chi$), (b) partial girdle ($\chi = 0°$) and (c) thick girdle ($\varphi = 90°$) within the [$x2$,$x3$]-plane, (e) partial girdle ($\chi = 0°$) and (f) thick girdle ($\varphi = 90°$) within the [$x1$,$x3$]-plane calculated with equations (3.20), (3.30), (3.31).

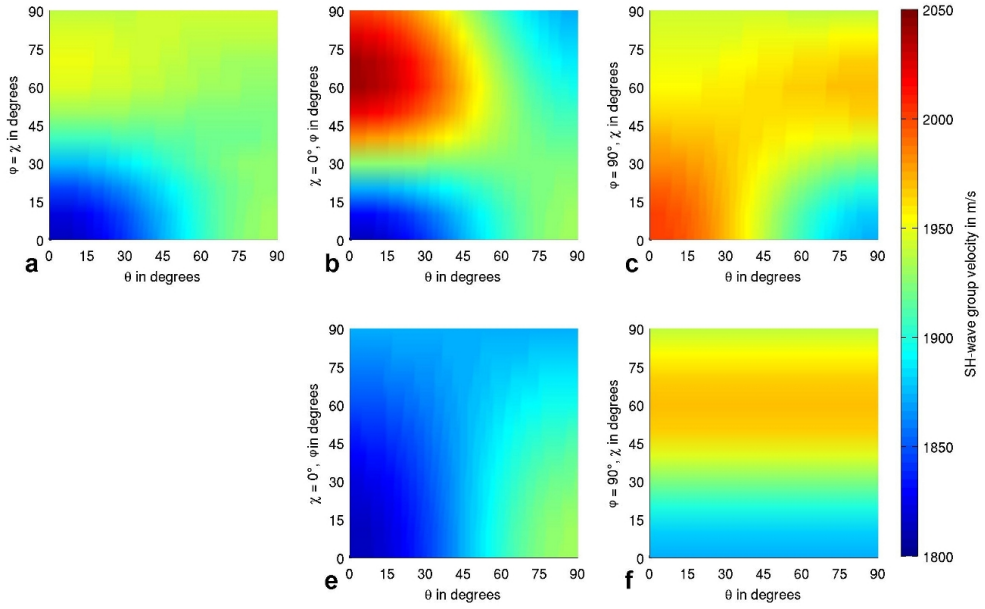

Figure A.3: SH-wave group velocities over group angle θ for different fabrics. SH-wave velocity for (a) different cone opening angles ($\varphi = \chi$), (b) partial girdle ($\chi = 0°$) and (c) thick girdle ($\varphi = 90°$) within the [$x2$,$x3$]-plane, (e) partial girdle ($\chi = 0°$) and (f) thick girdle ($\varphi = 90°$) within the [$x1$,$x3$]-plane calculated with equations (3.22), (3.30), (3.31).

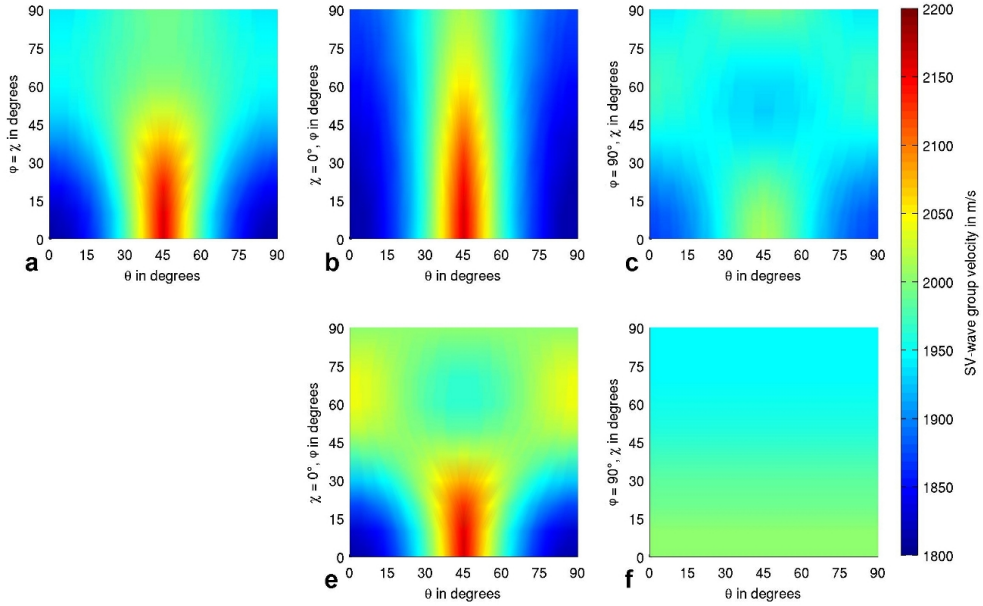

Figure A.4: SV-wave group velocities over group angle θ for different fabrics. SV-wave velocity for (a) different cone opening angles ($\varphi = \chi$), (b) partial girdle ($\chi = 0°$) and (c) thick girdle ($\varphi = 90°$) within the [x2,x3]-plane, (e) partial girdle ($\chi = 0°$) and (f) thick girdle ($\varphi = 90°$) within the [x1,x3]-plane calculated with equations (3.21), (3.30), (3.31).

A.6 Connection of cone opening angle to Thomsen parameter

The following equations give a connection between the opening angle and the Thomsen parameter δ and η. Thus, the anisotropy derived from the seismic data can be given in form of the opening angles for comparison with the ice core data.

For the calculation of a cone opening angle φ from the anisotropy parameter η the following equation is used:

$$\varphi_\eta = 16260 \sin(9.916\eta + 1.475) + 16180 \sin(9.956\eta + 4.612). \tag{A.26}$$

For the calculation of a cone opening angle φ from the anisotropy parameter δ the following equation is used:

$$\varphi_\delta = 264.1 \sin(16.88\delta + 2.443) + 209.4 \sin(19.92\delta - 0.3875). \tag{A.27}$$

B Seismograms

B.1 Comparison of different shooting techniques at Kohnen station

During the measurements carried out at Kohnen station different shooting techniques were used. We used explosives with different charge sizes on the surface and within different borehole depth, deployed in form of boosters and detonation cord. Additionally we used a vibrator source (EnviroVib). The different sources that were used at Kohnen on lines parallel and perpendicular to the ice divide are listed in Table B.1.

The raw and processed seismograms are plotted together for the different charges to directly compare the influence of processing. For each source one representative shot is shown. The seismograms show large differences in the strength of the excited surface and diving waves. The sources on the surface, additionally, excite strong air waves. Thus, the visibility and resolution of the ice-bed interface is quite different for the different sources.

The following main differences can be observed:

- Diving waves are extremely strong in the shots with sources over an extended area at the surface, i.e., the booster and the detonation cord shot, but also visible in the perp-vib and perp-exp-12m (5.6 kg) shots.
- Surface waves are strongest for the sources excited at the surface and in the 12 m deep borehole with a charge size of 5.6 kg explosive, i.e., the para-vib, perp-vib, booster, detonation cord and perp-exp-12m (5.6 kg) shot.
- Strong air waves can be observed in the data with sources excited on the surface, i.e., para-vib, perp-vib, booster and detonation cord shots.
- The bed reflection is visible in the raw data of the detonation cord, the perp-vib, the perp-exp-12m (0.4 kg) and the perp-exp-30m (5.6 kg) shot.
- The best SNR can be observed for the perp-exp-30m (5.6 kg) shot.

Name	year	survey no	survey	orientation	charge	charge size	charge position
para-vib	2013	20130571	wideangle	parallel	vibroseis	10–220 Hz	surface
perp-vib	2013	20130572	wideangle	perpendicular	vibroseis	10–220 Hz	surface
booster	2012	20120511	profile	-	booster	1600 g	surface
detonation cord	2012	20120511	profile	-	detonation cord	1800 g	surface
para-exp-12m (0.4 kg)	2012	20120501	profile	parallel	booster	400 g	12 m borehole
perp-exp-12m (0.4 kg)	2012	20120502	profile	perpendicular	booster	400 g	12 m borehole
para-exp-12m (5.6 kg)	2012	20120531	wideangle	parallel	booster	5.6 kg	12 m borehole
perp-exp-12m (5.6 kg)	2012	20120532	wideangle	perpendicular	booster	5.6 kg	12 m borehole
perp-exp-30m	2012	20120537	wideangle	perpendicular	booster	5.6 kg	30 m borehole

Table B.1: Seismic surveys carried out at Kohnen station.

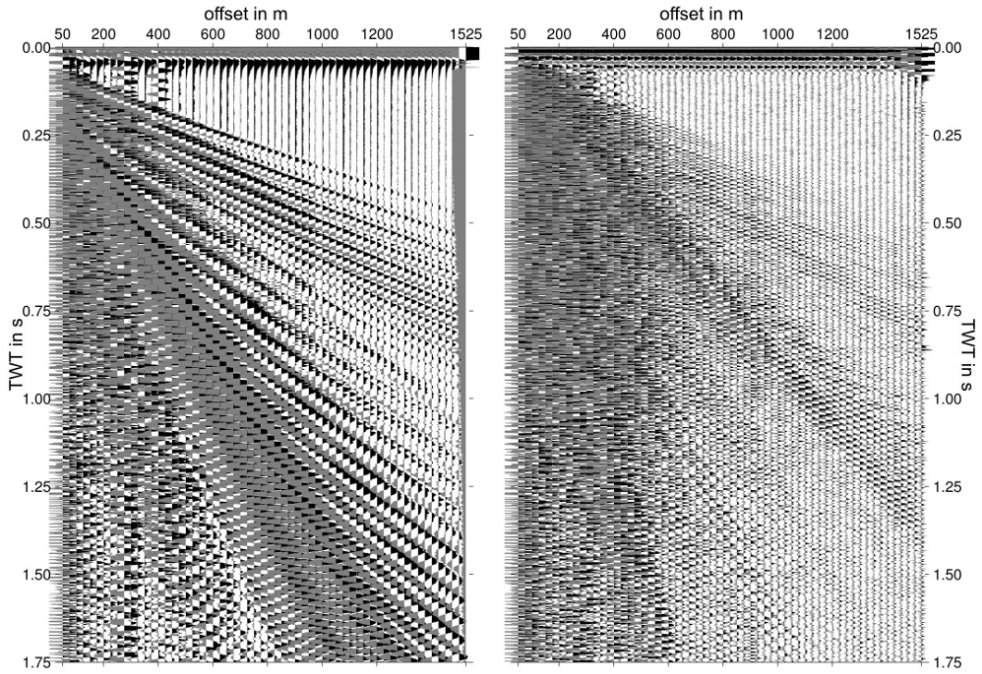

Figure B.1: Raw & processed data booster survey: Booster on surface, 4 times 0.4 kg on the edges of a 10 x 10 m square (1.6 kg). Processing included a 40/50 Hz highpass (*hp*) filter and an narrow *fk*-filter to reduce the influence of the surface wave. (Left figure: raw shot; right figure: processed shot)

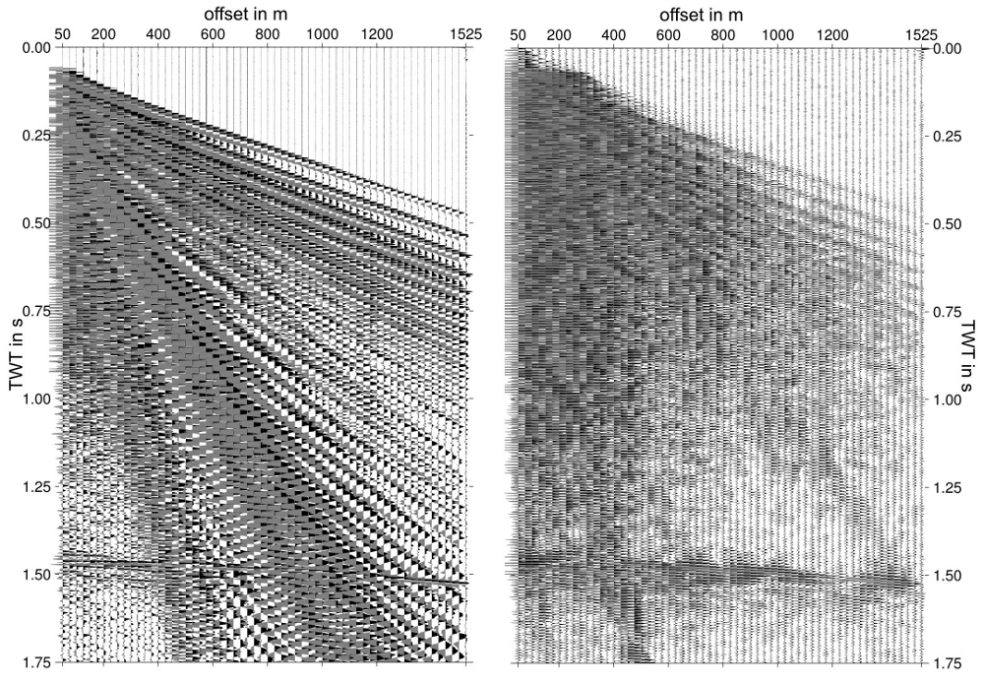

Figure B.2: Raw & processed data detonation cord survey: Detonation cord array on the surface, 9 times 10 m detonation cord in a comp shaped form resulting in a 10 x 10 m square (1.8 kg). Processing included a 35/40 Hz *hp*-filter and an narrow *fk*-filter to reduce the influence of the surface wave. (Left figure: raw shot; right figure: processed shot)

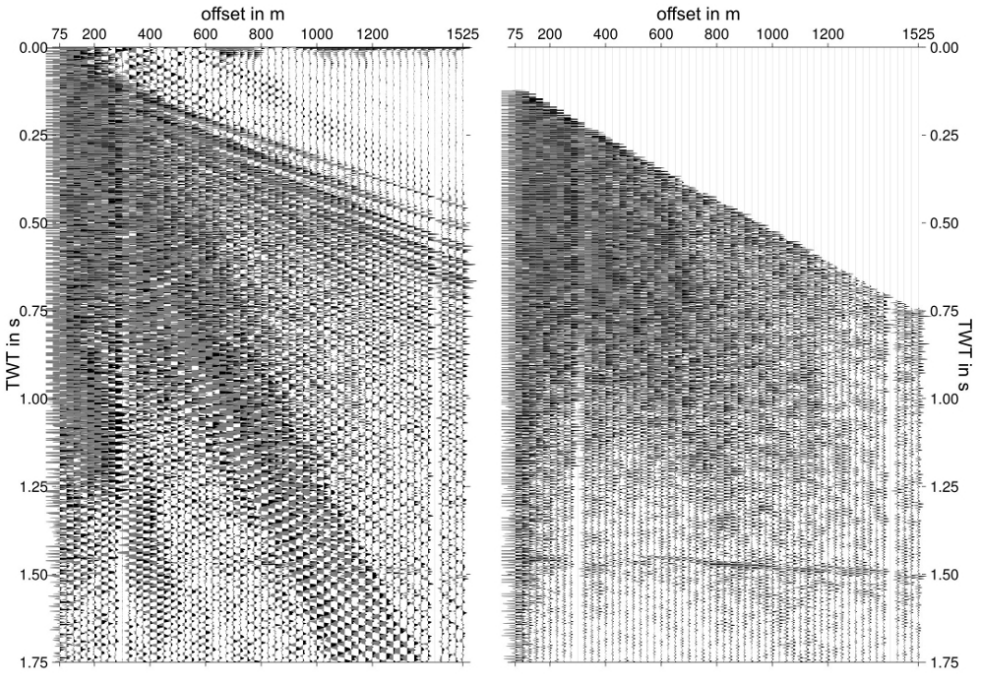

Figure B.3: Raw & processed data perp-vib survey: vibroseis data, 1st shot of wideangle survey perpendicular to ice divide, linear upsweep 20–220 Hz, duration 10 s, taper 500 ms. Processing included the correlation with the sweep, some muting and editing and an 80/90 Hz *hp*-filter. (Left figure: raw shot; right figure: processed shot)

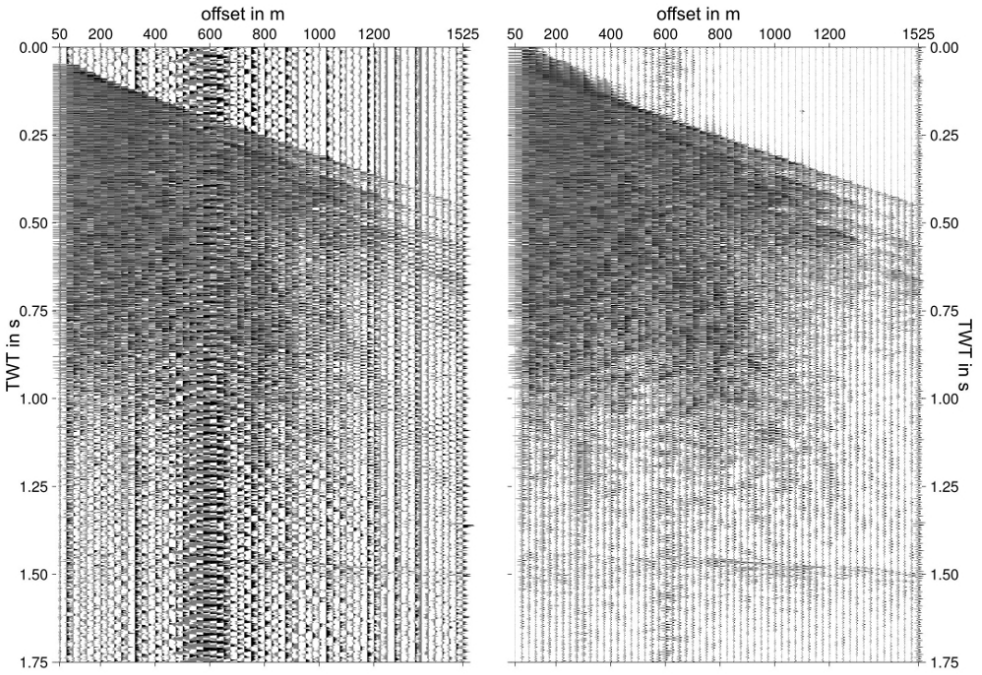

Figure B.4: Raw & processed data perp-exp-12m (0.4 kg) survey: 1st shot of the profile survey, perpendicular to the ice divide, with 0.4 kg booster charge in a 12 m deep borehole. The borehole was not filled with snow. Processing included an 110/120–380/390 Hz *bp*-filter. (Left figure: raw shot; right figure: processed shot)

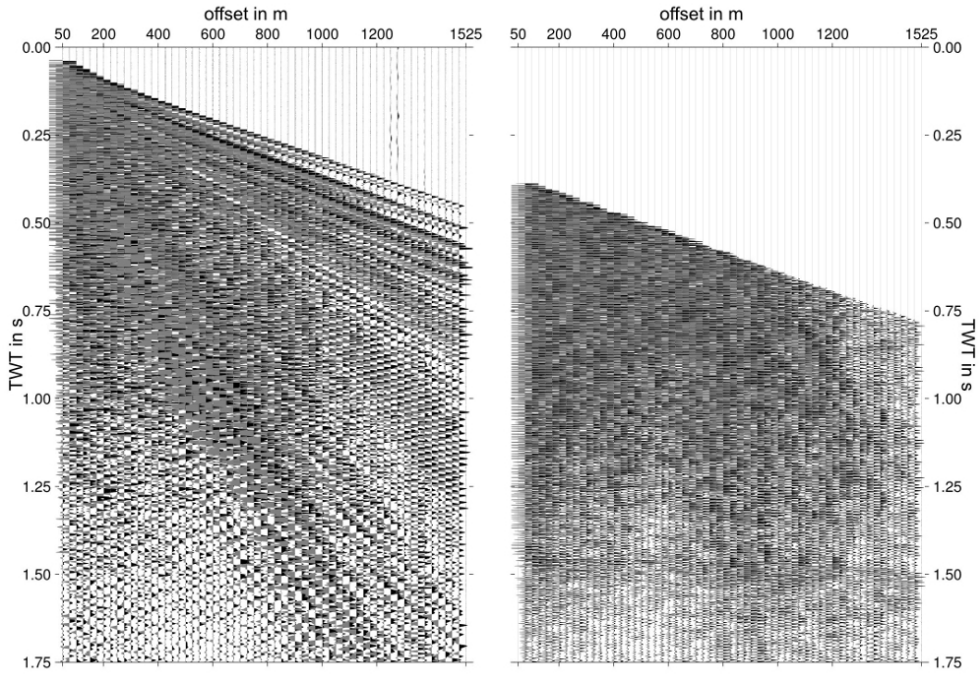

Figure B.5: Raw & processed data perp-exp-12m (5.6 kg) survey: 1st shot of wideangle survey perpendicular to ice divide, with 5.6 kg booster charge in a 12 m deep borehole. Processing included some editing and muting, a 30/50-300/400 Hz *bp*-filter, an 70/90 Hz *hp*-filter and a 90 Hz notch filter. (Left figure: raw shot; right figure: processed shot)

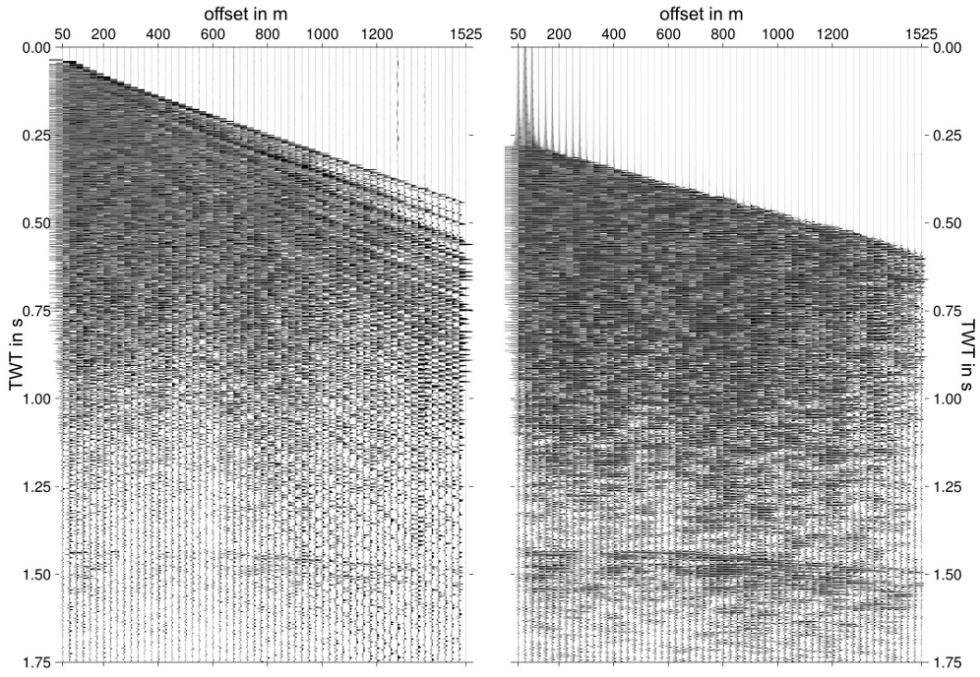

Figure B.6: Raw & processed data perp-exp-30m (5.6 kg) survey: 1st shot of wideangle survey perpendicular to ice divide, with 5.6 kg booster charge in a 30 m deep borehole. Processing included some editing and muting, a 40/50-550/600 Hz *bp*-filter and an 70/90 Hz *hp*-filter. (Left figure: raw shot; right figure: processed shot)

B.2 Wideangle data, Kohnen station

Seismic wideangle surveys were carried out at Kohnen station on two lines, parallel and perpendicular to the ice divide, centered close to the dill location of the ice core EDML (Figure 6.11). The survey was shot in January 2012 using explosives in boreholes of 12 m depth, para-exp-12m (5.6 kg) and para-exp-12m (5.6 kg), Figure B.7 and Figure B.8. Additionally, charges were places on the first three shot positions in 30 m deep boreholes on the perpendicular line, para-exp-12m (5.6 kg), Figure B.9. This was not carried out for larger offsets and on the parallel line due to a breakdown of the drilling unit. The survey was reshot in January 2013 using the EnviroVibe as source, para-vib and perp-vib, Figure B.10 and Figure B.11, respectively. Here, multiple sweeps were done at one location. The different sweeps of the locations were stacked to enhance the SNR ratio. The shooting specification used for the surveys are given in Table B.1.

The bed reflection can be followed for all data sets up to the largest shot offset. For large offsets the vibroseis data (Figure B.10 and B.11) show clearer signals from the bed reflection than the explosive data (Figure B.7 and B.8). Here, an *fk*-filter worked extremely well to reduce the diving waves and see a clear bed reflection signal.

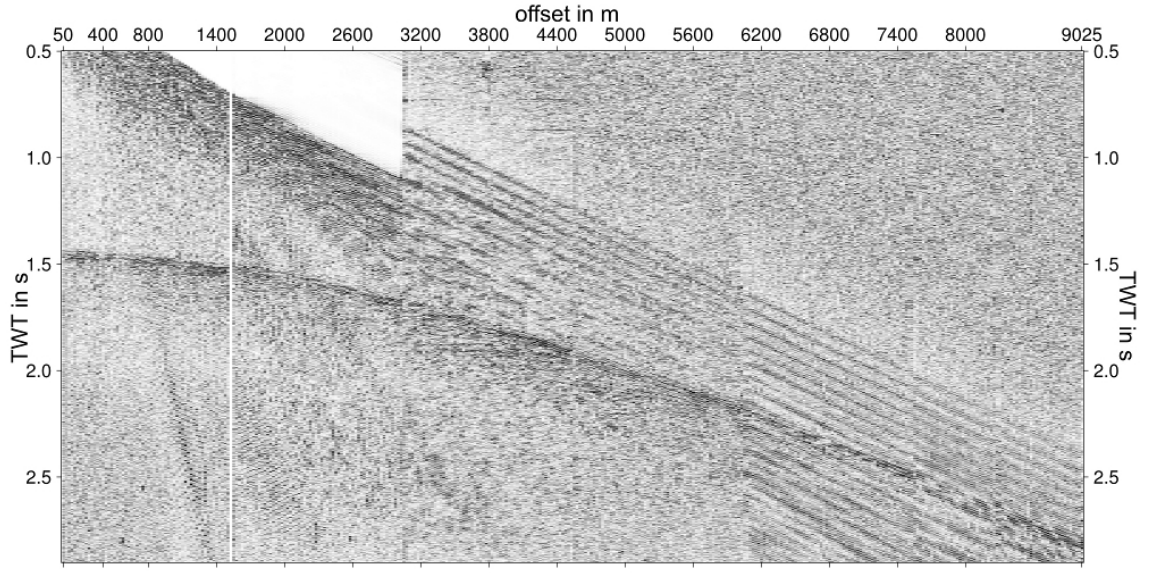

Figure B.7: Wideangle survey para-exp-12m (5.6 kg): parallel to ice divide, 5.6 kg booster, shots placed in 12 m deep boreholes (AGC 1000 ms). The bed reflection can clearly be seen for the complete offset.

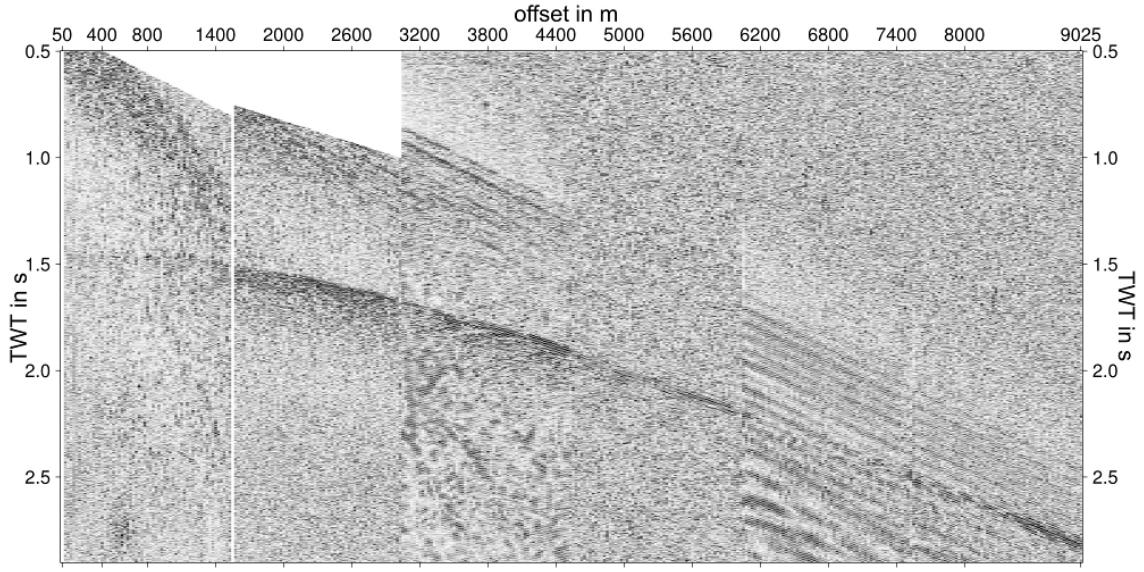

Figure B.8: Wideangle survey perp-exp-12m (5.6 kg): perpendicular to ice divide, 5.6 kg booster, shots placed in 12 m deep boreholes (AGC 1000 ms). The bed reflection can clearly be seen for the complete offset.

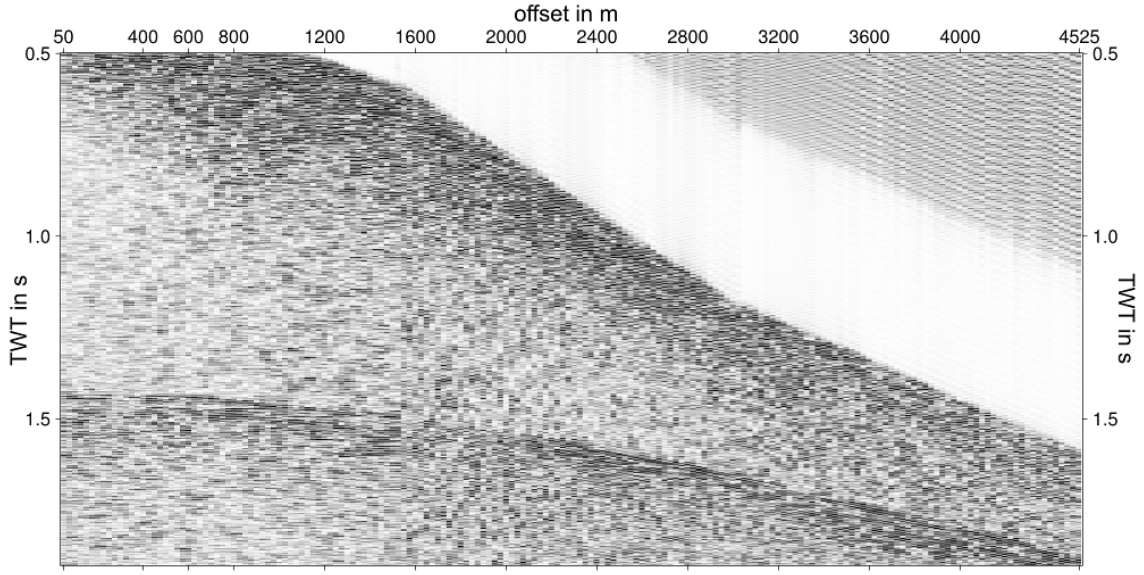

Figure B.9: Wideangle survey perp-exp-30m (5.6 kg): perpendicular to ice divide, 5.6 kg booster, shots placed in 30 m deep boreholes (AGC 1000 ms). This survey shows a clearer bed reflection for the small offsets (<800 m) compared to the shots placed in 12 m deep boreholes. This is due to weaker surface and diving waves.

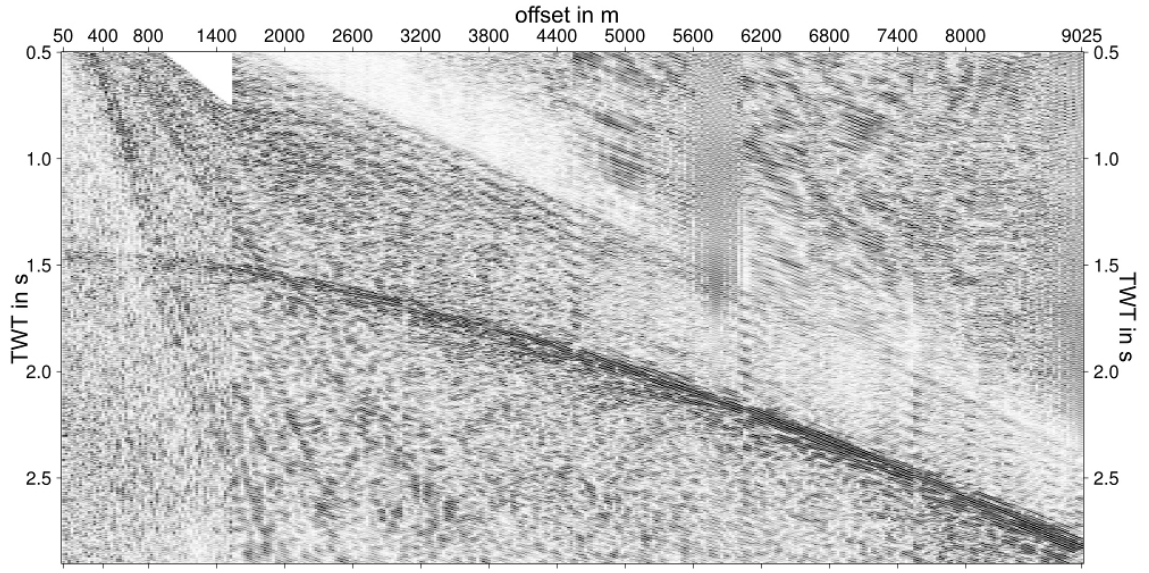

Figure B.10: Wideangle survey para-vib: Vibroseis source parallel to ice divide, the sweep was set to 10 s, 20–220 Hz, taper 500 ms (AGC 1000 ms). Multiple shots per shot position (SP) are stacked here (SP1, SP2, SP3: 2 shots, SP4, SP3:3 shots, SP5:5 shots, SP6:4 shots). A clear bed reflection can be seen, also for the largest offsets.

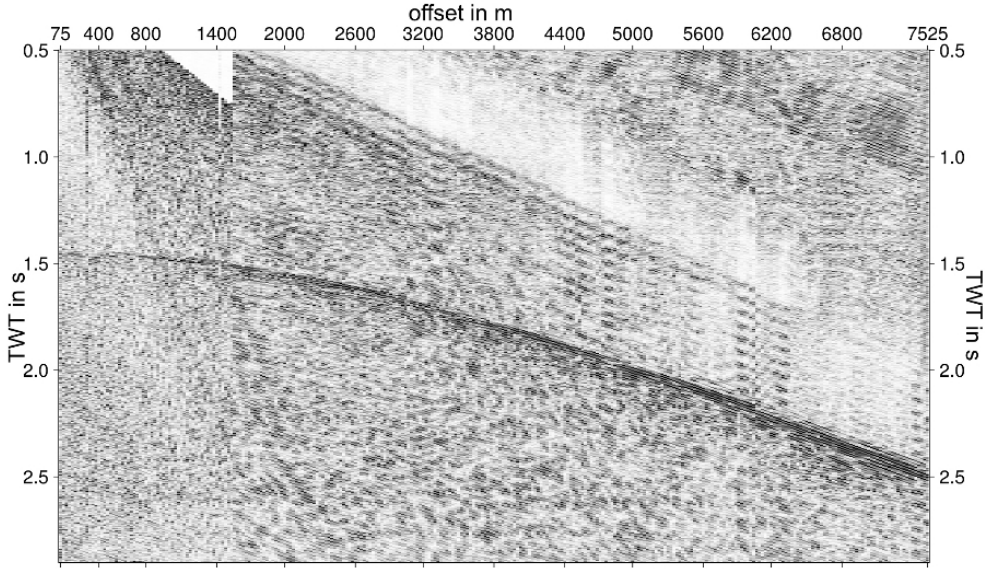

Figure B.11: Wideangle survey perp-vib: Vibroseis source perpendicular to ice divide, the sweep was set to 10 s, 20–220 Hz, taper 500 ms (AGC 1000 ms). Multiple shots per shot position (SP) are stacked here (SP1: 3 shots, SP2, SP3:3 shots, SP4:6 shots, SP5:5 shots). A clear bed reflection can be seen, also for the largest offsets.

B.3 Stacked processed data, Kohnen station

Figure B.12 shows stacked traces as given in Figure 8.5. Here, the data was frequency and fk-filtered before the traces were stacked, while Figure 8.5 shows the stacked raw traces.

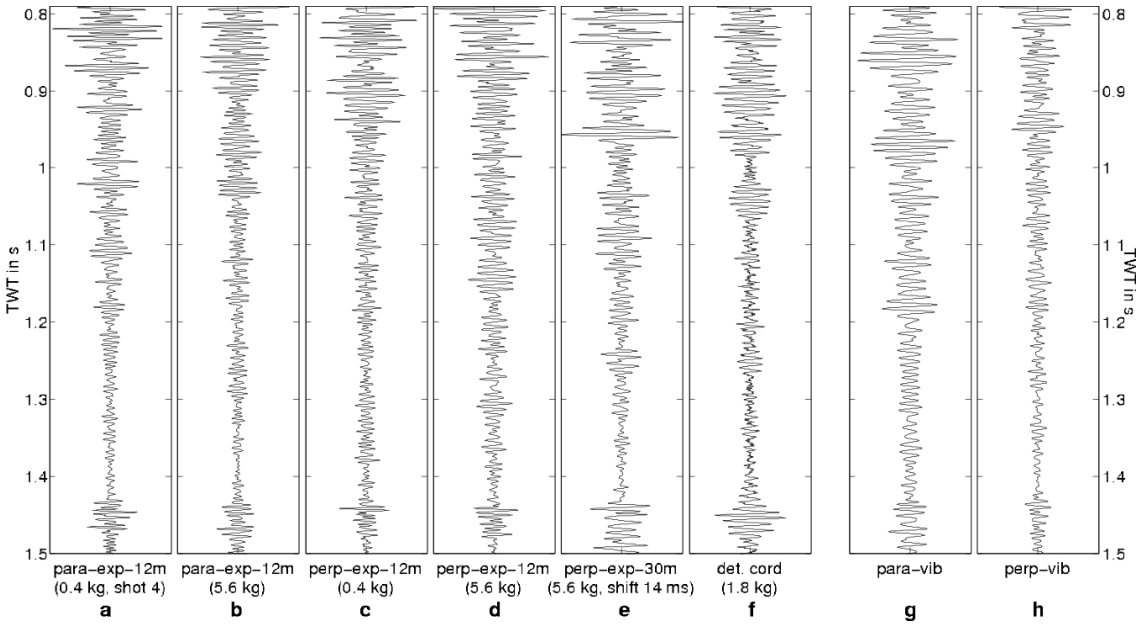

Figure B.12: Stacked traces from different shots with different sources after frequency and fk-filtering. The source settings for the wideangle surveys (b, d, e, g, h) are listed in Table 6.3. The shot para-exp-12m (0.4 kg; a) and perp-exp-12m (0.4 kg; c) are part of the profiles shot parallel and perpendicular to the ice divide, respectively, with 0.4 kg charge size in 12 m deep boreholes. The first shot of the profile survey parallel to the ice divide (a) has very strong noise. Thus, it is not representative for this line and Shot 4 (2250 m SSE of the center) was used instead. In (f) the stacked trace of a shot with detonation cord as source is displayed. Nine parallel lines of 10 m detonation cord were placed 1 m apart from each other (comp-shaped) and connected with detonation cord as lead in to one detonator. This shot is about 9 km ESE of the Kohnen station. The vibroseis data were correlated before stacking, with additional stacking of two shots for para-vib (g) and three shots for perp-vib (h) from the same location. Scaling is individual for each trace.

B.4 Zoom bed reflection, Kohnen station

During the analysis of the NMO-velocities of the bed reflection at Kohnen from the parallel and perpendicular line the possibility of a tilted bed had to be investigated. A possible effect of a tilted bed is a jump in the traveltime of reflections between the different shot positions of the wideangle survey (sec. 9.3.2).

In the para-vib survey (Figure B.13) a possible jump to smaller traveltimes can be observed (red bar) between geophone 60 of shot 1 and geophone 1 of shot 2. This would indicate a negative dip, i.e., a decrease in depth from shot to geophone. In the perp-vib survey (Figure B.14) a possible jump to larger traveltimes can be observed (red bar) between geophone 60 of shot 1 and geophone 1 of shot 2. This would indicate a positive dip, i.e., a increase in depth from shot to geophone.

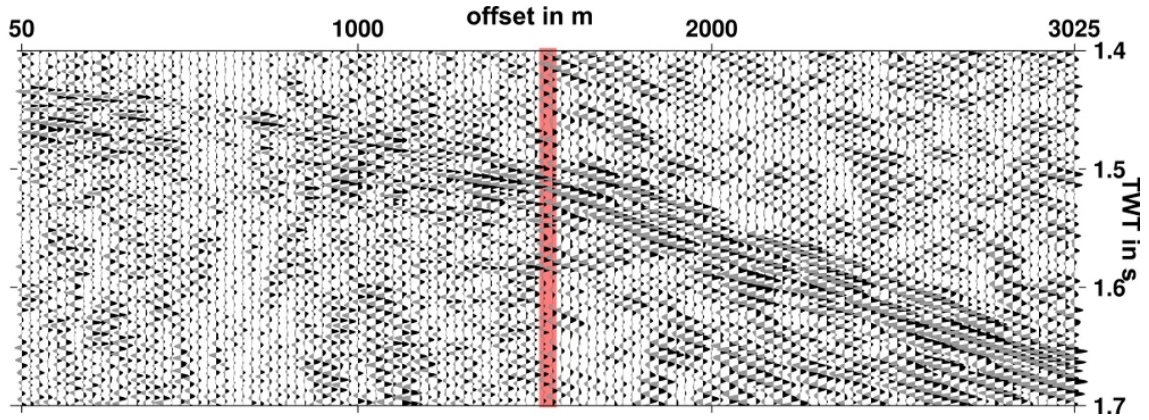

Figure B.13: Zoom on the bed reflection for the first two shot positions of the para-vib wideangle survey to investigate the possibility of a tilted layer at Kohnen. The red area marks the transition from the trace belonging to the last geophone of the first shot position to the trace belonging to the first geophone of the second shot position.

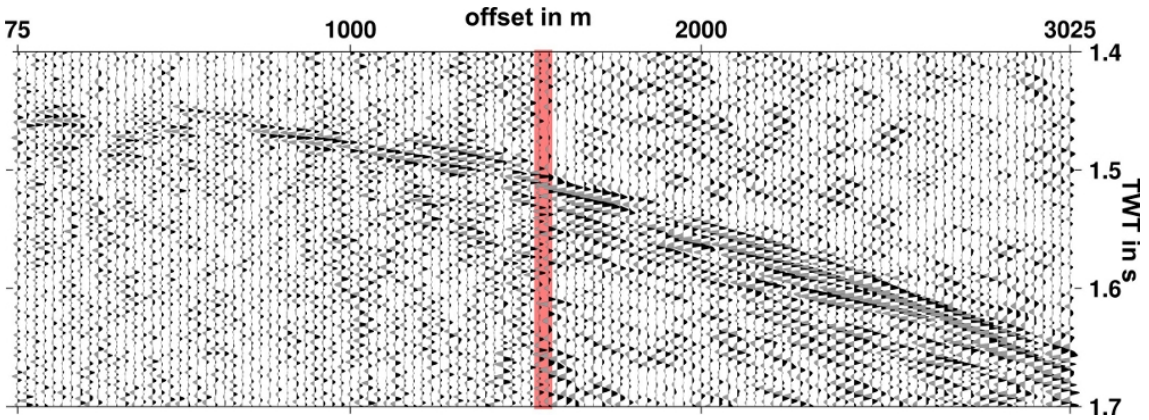

Figure B.14: Zoom on the bed reflection for the first two shot positions of the perp-vib wideangle survey to investigate the possibility of a tilted layer at Kohnen. The red area marks the transition from the trace belonging to the last geophone of the first shot position to the trace belonging to the first geophone of the second shot position.

'Erst seit gestern und nur für einen Tag auf diesem Planeten weilend, können wir nur hoffen, einen Blick auf das Wissen zu erhaschen, das wir vermutlich nie erlangen werden.'

Saussure

Danke!

Mein ganz besonderer Dank gilt dir, Olaf, für die fantastische Betreuung. Ich habe es nie als Nachteil empfunden, dass wir oft per E-Mail kommunizierten. Wann immer ich Fragen hatte bekam ich sofort Antworten von dir. Wenn ich nicht mehr weiter wusste hattest du immer hilfreiche Ideen und Anregungen. Ich bin wirklich froh, dass du diese Arbeit betreut hast.

Vielen Dank für eure Unterstützung, Coen, Pascal und Reinhard, auch wenn sich die LIMPICS Gruppe selten bis nie gemeinsam an einem Ort befunden hat.

Die Zeit meiner Doktorarbeit war eine ganz besondere, da ich an vielen tollen Expeditionen teilnehmen durfte, in denen die LIMPICS Gruppe tatsächlich mal in der ein oder anderen Konstellation zusammen war. Jede dieser Reisen war ganz anders und etwas besonders. Mit Coen, Pascal, Reinhard und Günther durfte ich auf sicheren Wegen vom Colle Gnifetti zur Monte Rosa Hütte absteigen. Unvergesslich war die Woche mit Coen, Sverrir, Yngve und Rick, eingeschlossen in unserem gelben Container während eines Schneesturmes am Halvfarryggen. Eine wirkliche entspannte Kampagne gab es mit Astrid, Christoph, Henry, Olaf und vor allem ElViS an Kohnen, darunter auch eine unglaubliche VSP Messung und Stunden im Trench. Nicht zu vergessen sind hier Piggeldy und Frederik, die seither auf jede Reise mitkommen. In der letzten Kohnen Saison lief nicht alles ganz so wie geplant.

Coen, Rick und Pascal, ihr habt nie aufgehört daran zu glauben, dass der EnvrioVibe sich doch noch vom Fleck bewegt. Unfassbar lustig waren die Fahrten mit Pascal im Pistenbully, um den Streamer von einem Ort zum nächsten zu ziehen. Lustige Abende gab es auch mit Stefanie und Katharina in unserem Container. Vielen Dank für all diese großen und kleinen Abenteuer!

Die Seismikdaten für diese Arbeit hätte es nicht gegeben ohne die Unterstützung der AWI Logistik. Im Besonderen möchte ich mich bedanken bei Cord für minütliches an- und abhängen des Generators vom Netz, Holger für stundenlanges 'groomern' und Jens für die Südseeinsel.

Auch wenn ich nur ab und an am AWI war, hab ich dort immer Antworten auf meine glaziologischen Fragen bekommen. Ilka bin ich sehr dankbar für die vielen COF Messungen, ohne die keiner der Vergleiche in dieser Arbeit möglich gewesen wäre. Gefreut habe ich mich auch immer über die netten Übernachtungsmöglichkeiten in Bremerhaven bei Kerstin und Katharina.

Mein Dank gilt auch Ulrich, der die ElViS-Daten vom Colle Gnifetti prozessiert und die Geschwindigkeitsprofile bestimmt hat, deren Analyse ein wichtiger Bestandteil dieser Arbeit war.

Die meiste Zeit während der Doktorarbeit war ich allerdings in Karlsruhe. Vielen Dank auch dir, Thomas, dass du mir die Möglichkeit gegeben hast während meiner Doktorarbeit am GPI zu sein und mir als 'Exot' einen Platz in deiner Arbeitsgruppe gegeben hast. So hatte ich immer einen Ansprechpartner für die vielen kleinen geophysikalischen Fragen. André, Anna, Ines, Lisa, Martin, Simone, Stefan und Sven, ihr seid eine fantastische Arbeitsgruppe. Es hat mir viel Spass gemacht mit euch zusammen zu arbeiten und Feierabende zu verplanen.

Vielen Dank, Sven, für die vielen kleinen Fragen, die du mir zwischendurch beantwortet hast und die vielen netten Ablenkungen, die das Arbeiten so viel einfacher gemacht haben.

Nachdem ich die Diplomarbeitszeit ohne 'meine Jungs', Tobias, Zacharias, Sven und Martin hinter mich bringen musste, war ich wirklich froh während der Doktorarbeit wieder mit euch zusammen zu arbeiten. Zur Zeit verteilen wir uns räumlich immer mehr, trotzdem hoffe ich, dass wir uns nicht aus den Augen verlieren werden.